University of Alberta

AN EXPERIMENTAL STUDY ON OIL SAND LUMP ABLATION

by

Mahshad Pazouki

A thesis submitted to the Faculty of Graduate Studies and Research
in partial fulfillment of the requirements for the degree of

Doctor of Philosophy
in
Chemical Engineering

Department of Chemical and Materials Engineering

Spring 2013
Edmonton, Alberta

Abstract

The surface mining of oil sand ore requires the use of huge shovels and 400-tonne capacity trucks to transfer the mined ore to the slurry preparation plant, where water and additives are added to the crushed ore. The oil sand slurry is then transported to the extraction section and simultaneously conditioned through a hydrotransport pipeline. The term ″conditioning″ refers to oil sand lump reduction, bitumen liberation and air attachment. There is a tremendous economic and environmental incentive to reduce or eliminate the use of the trucks; thus, many oil sands companies are actively considering processes where the oil sand is conditioned and separated right at the mine face. Unfortunately, this would require an accelerated rate of oil sand conditioning over what is provided today by the relatively long oil sand hydrotransport pipelines used in the industry. This research is focused on the first step in the conditioning: lump ablation. The motivation for this study is the fact that any changes in the current conditioning method need to be supported by a fundamental understanding of the oil sand lump ablation process, because slurry temperature, initial lump size and temperature, pipeline diameter and length, slurry flow rate and shear stress influence the lump ablation.

In this study, an experimental method is developed and the effects of slurry velocity and concentration as well as slurry temperature on the ablation of oil sand lumps are investigated. Artificial oil sand lumps manufactured with similar dry density to actual oil sand are used. Experiments were conducted using a 104mm pipeline loop built at Saskatchewan Research Council Pipe Flow Technology

Centre™ where different slurry velocities (1 to 3m/s) and slurry concentrations (0 to 30 vol %) were achieved. Strain gauge technology was applied to measure the mass loss and drag force acting on the oil sand lump on-line and in real time. The results of the experiments clearly show that an increase of velocity or temperature increases the ablation rate of an oil sand lump. Slurry concentration does not have a significant effect on ablation at 45°C. A predictive model which relates the oil sand lump ablation rate to the surface shear stress and slurry temperature is proposed. The model was validated using the experimental data collected during this study.

Acknowledgments

I would like to thank all staffs at Saskatchewan Research Council Pipe Flow Centre™ for assisting me to design and build the experimental apparatus and supporting me during the experiments. My special thanks go to Dr. R. Gillies, Dr. M. McKibben and P. Schergevitch for their patience and guidance.

I also would like to send my gratitude to Dr. Rick Chalaturnyk for his generous support and guidance in finding the right artificial oil sand lump. I cannot thank enough Gilbert Wong and other staffs at Geotechnical Engineering Lab in Civil Engineering Department for teaching me to manufacture the oil sand lumps and providing assistance whenever I needed.

I am so grateful to Dr. Sean Sanders for accepting me as his graduate student and coaching me throughout this program. I would like to thank him so much for his patience and support during difficult times. I am so proud to be his student.

I would like to thank so much Dr. J. Masliyah and Dr. Tony Young for their consistent support and guidance during my PhD program. I am so grateful to Artin Afacan and the staffs at Chemical Engineering Machine shop for assisting me during the work at University of Alberta.

I am very much thankful to summer students Baurzhan Primkulov and Ethan McKibben who assisted me during summer 2010 and 2011 in manufacturing the oil sand lumps and executing experimental tests.

I am indebted to my dearest parents Mrs. B. Geranghadr and Mr. A. A. Pazouki for teaching me hard work and integrity and always supporting me to achieve my goals. I am very much grateful to my husband Arash Khodabandeh for his support, patience and guidance during years of my education.

Financial support from Canada's Natural Sciences and Engineering Research Council (NSERC) and from the sponsoring companies of the NSERC Industrial Research Chair in Pipeline Transport Processes is gratefully acknowledged. Finally, thank you to my other family members and friends for their love and support.

Table of Contents

List of figures

List of tables:

List of symbols

Symbol	Description	Unit
A	Area	m^2
A_P	Pipe cross section	m^2
A_P'	Reduced pipe cross section	m^2
Ar	Archimedes number	---
A_{PC}	Solid object cross section	m^2
B	Constant	---
C	Solid volume concentration	---
C′	Ratio of mass of solid to mass of carrier fluid	---
C_D	Drag coefficient	---
C_f	Skin drag coefficient	---
C_{mass}	Mass concentration	---
C_{max}	Maximum sand volume concentration	---
C_p	Heat capacity	$J\ kg^{-1}\ K^{-1}$
C_P	Pressure drag coefficient	---
C_μ	Constant in Equation 4.20	---
D	Pipe diameter	m
d	Solid object diameter	m
d_p	Particle diameter	m
d_{50}	Mean particle diameter	m
d^+	Dimensionless particle diameter	---
$-\frac{dp}{dz}$	Pipe axial pressure drop	$Pa\ m^{-1}$
E	Excitation voltage	V
F	Force	N
F_B	Buoyancy force	N
F_f	Skin drag force	N
F_D	Total drag force	N

F_{SG}	Force measured with strain gauge	N
f	Gauge factor	---
f_f	Fanning friction factor	---
f_s	Solid friction factor	---
h	Heat transfer coefficient	$Wm^{-2}\,K^{-1}$
Δh	Thickness of softened layer that is ablated	m
k	Turbulence kinetic energy for particle-free flow	$m^2\,s^{-2}$
k'	Turbulence kinetic energy for slurry flow	$m^2\,s^{-2}$
k_t	Thermal conductivity	$W\,m^{-1}K^{-1}$
L	Length	m
L_R	Strain gauge length	m
l	Turbulence length scale	m
m_0	Lump initial mass	kg
m_i	Lump mass at time i	kg
$\dot{m}$	Ablation rate	$kg\,min^{-1}$
Nu	Nusselt number	---
p	Pressure	Pa
Pr	Prandtl number	---
Q	Volumetric flow rate	m^3s^{-1}
Q_q	Heat flux	W
R_r	Resistance	Ωm
Re	Reynolds number	---
R	Radius	m
s	Distance from pipe center	m
s^+	Dimensionless distance from pipe center	m
T	Temperature	°C
T_{0L}	Lump initial temperature	°C
T_∞	Ambient temperature	°C
t	Time	s
u_b	Velocity of the lump surface layer	ms^{-1}
V	Bulk velocity	ms^{-1}

V_s	Solid object velocity	ms^{-1}
V_{Act}	Pipe actual (increased) velocity	ms^{-1}
V_c	Deposition velocity	ms^{-1}
V_∞	Infinite dilution settling velocity	ms^{-1}
v	Local velocity	ms^{-1}
$\bar{v}$	Average local velocity	ms^{-1}
V^+	Dimensionless local velocity	ms^{-1}
v'	Local fluctuation velocity	ms^{-1}
v^*	Friction velocity	ms^{-1}
v_c	Circuit output voltage	V
$\forall$	Volume	m^3
w	Width	m
Y	Constant in Equation 2.3	---
δ	Thickness	m
σ	Turbulence intensity	---
ε	Turbulent kinetic energy dissipation	$m^{-2}s^{-3}$
$\bar{\epsilon}$	Average pipe energy dissipation	$m^{-2}s^{-3}$
λ	Linear concentration	---
μ	Viscosity	Pa.s
$\mu^{(t)}$	Eddy viscosity	Pa.s
ρ	Density	kg m^{-3}
τ	Shear stress	Pa
τ_w	Wall shear stress	Pa
τ_{wp}	Wall shear stress on solid object	Pa
$\tau^{(t)}$	Turbulent shear stress	Pa
ϑ	Kinematic viscosity	m^2s^{-1}

Subscripts

1	Top layer
2	Bottom layer
12	Interface
B	Bitumen
circum	Circumference
f	Carrier fluid
i	Specific time
Lum	Lump
m	Mixture
R	Resistance
r	Relative
s	Solid particle

1. Background

1.1. Water-based extraction

According to Masliyah (2008), about 15-20% of the Canadian oil sands reserve, containing 140 billion barrels of bitumen can be found at a depth less than 75m where, surface mining is economically feasible. The remaining 80-85% is buried at lower depths, which can possibly be recovered with underground type mining and with in-situ techniques (Masliyah, 2008). In 1967, the Great Canadian Oil Sands (GCOS), now known as Suncor Energy Inc., developed an open-pit mine, a hot water extraction plant, and an upgrading complex (Masliyah, 2008). Their operation was followed in 1979 by Syncrude Canada Ltd.'s open-pit mine at Mildred Lake. Currently, Suncor Energy Inc., Syncrude Canada Ltd., Albian Sands Energy and Canadian Natural Resources Ltd. employ surface mining (Masliyah, 2008).

The typical current surface mining operation (shown in Figure 1.1) includes the following steps (Flint, 2005; Masliyah, 2008):

1) Removal of about 30m overburden using shovels and trucks
2) Mining oil sand with hydraulic or electric shovels
3) Transport of oil sand ore from the mine face to the crushers with trucks
4) Crushing of oil sand large lumps into parts less than 12 inch in size
5) Oil sand conditioning
6) Gravity separation of bitumen froth
7) Diluted froth treatment to separate water and solids
8) Supplemental solvent recovery from tailings
9) Dewatering and concentrating the tailings

Oil sand conditioning includes the following steps (Masliyah et al., (2004); Sanders et al., 2007):

i. Oil sand lump ablation or size reduction
ii. Liberation of bitumen from sand grains
iii. Aeration of bitumen droplets

Originally, oil sand ore carried from the mine with conveyors was conditioned with rotating drums (tumblers) (Masliyah, 2008). Starting from the 1990's, hydrotransport pipelines were employed to simultaneously transport and condition the oil sand ore (Sanders et al., 2004). The use of hydrotransport pipelines significantly improved the oil sand conditioning process at lower process temperatures (Masliyah, 2008). The efficiency of the conditioning process highly influences the final recovery of the bitumen (Sanders et al., 2007; Masliyah 2008); thus achieving a highly-efficient conditioning has always been the target among oil sand producers.

Since the start of extraction of bitumen from oil sands, reducing the production cost and greenhouse gas emissions have been ongoing targets among the bitumen producers (Masliyah, 2008). Continued process improvements have led to more economic bitumen production and reduced environmental footprint (Friesen et al., 2004). Presently, oil sand companies aim to eliminate the use of trucks to transport the oil sand ore to the slurry preparation plant, and wish to condition the oil sand slurry at the mine face (Flint, 2005). This consequent reduction of pipeline length (Flint, 2005) would potentially cause incomplete conditioning and could especially affect lump ablation (Sanders, 2008). In order to resolve this problem an accelerated conditioning process would be required (Sanders, 2008). Before implementing any significant changes in the oil sand conditioning, the fundamentals of oil sand lump ablation must be better understood.

In the subsequent sections of this chapter, the history of the development of hydrotransport pipelines and the potential areas for further improvements in the conditioning process are discussed. An introduction to the greenhouse gas emissions during open-pit mining and its relevance to this study are also provided. Overall, this study aims to provide a better understanding of the phenomenon of

oil sand lump ablation inside the hydrotransport pipeline. In addition, it is targeted to identify a number of parameters which might improve the performance of existing or future hydrotransport systems in the oil sands industry.

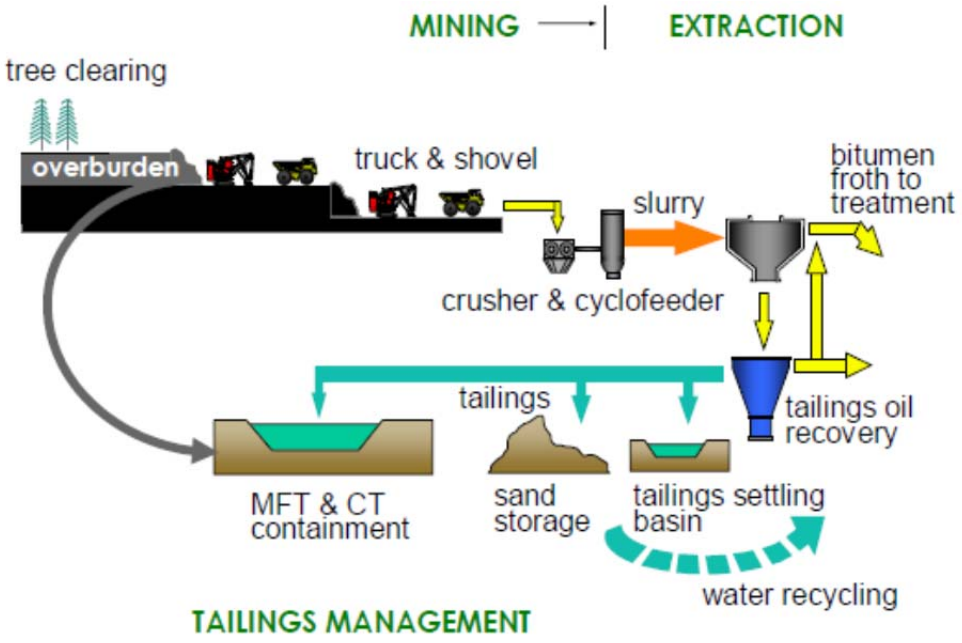

Figure 1.1 Major steps for bitumen production in mining-based recovery
(Flint, 2005)

1.2. Lump ablation in hydrotransport pipelines

Based on the reports of Sanders et al. (2000; 2007), investigations into the possibility of replacing conveyors and tumblers with pipelines began at the Syncrude Research Center in the early 1980's. The idea was originally based on examination of the pipelines transporting tailings from the separation vessels to the tailings ponds. Subsequently, a large scale prototype of an oil sand hydrotransport system, known as the Extraction Auxiliary Production System (EAPS) was commissioned in 1993. This unit became a successful commercial unit that could digest up to 5000 tonnes of oil sands per hour. Since then, hydrotransport pipelines have been used in other commercial extraction plants to

simultaneously transport and condition oil sands ore. Currently, roughly 60 000 tonnes of oil sand, flowing as slurry of about 60% (wt.) solids, is digested per hour to produce ½ million barrels of bitumen per day (Qiu, 2010; Sanders et al., 2007).

Commercial application of hydrotransport pipelines enabled the conditioning process to be carried out at considerably lower temperatures (Masliyah et al., 2004). Syncrude–Aurora now operates their 5km hydrotransport lines at 35-40ºC (Schaan et al., 2007). Typically, a 40–55°C slurry temperature is used in the current operations (Masliyah et al., 2004).

The crushed and screened oil sand lumps, whose sizes range from 50 to 150mm, are ablated (digested) inside the hydrotransport pipeline; ablation is known as the first step of conditioning, as mentioned earlier (Sanders et al., 2004). As Masliyah et al. (2004) describe, ablation of an oil sand lump occurs because of dual effects of heat transfer and mechanical energy. Generally, bitumen acts as a glue to hold the matrix of sand grains together. The viscosity of bitumen is highly temperature-dependent so once the oil sand lump is exposed to the hot slurry medium, the viscosity of bitumen on the surface layer of the lump reduces significantly. The softened surface layer is then sheared away due to shearing inside the hydrotransport pipeline, and a new lump surface is exposed to the hot medium. The new surface is again heated and sheared away with the same mechanism, and this process repeats itself to the point that the entire lump is ablated.

The rate of ablation is controlled by heat transfer from the slurry and by lump contact with other lumps and with the pipe wall (Shook et al., 2002). Therefore, slurry temperature and composition, initial lump size and temperature (Masliyah, 2008) and mechanical shear imparted to the lump are the parameters which most affect the oil sand lump ablation (Masliyah, 2008, Shook and Roco, 1992).

As part of the ongoing target of the industry to reduce the cost and environmental concerns of oil sand production, some companies wish to have the bitumen

extraction process located at the mine face and eliminate the trucks. This leads to reduction of the length of the hydrotransport pipelines. In order to modify the existing process, a better understanding of the lump ablation process is required. This study is to contribute to better understanding of the lump ablation process. Reduction of pipe length may cause incomplete ablation of oil sand lumps; therefore, some modification to the existing conditioning process may be required to compensate for the short ablation time. In order to fulfill this target, it is necessary to identify different parameters that affect the oil sand lump ablation and recognize the way each one influences the ablation process. The oil sand conditioning process can be improved by changing one or more of these factors and ultimately applying to shorter pipelines where accelerated ablation and conditioning are required. A full description of the effect of each of these parameters and lump ablation can be found in Chapter 2.

1.3. Greenhouse gas (GHG) emissions in surface mining

According to Flint (2005), carbon dioxide (CO_2), methane (CH_4) and nitrous oxide (N_2O) are three major GHGs which are emitted in the oil sands industry, with CO_2 being the primary gas released. Carbon dioxide typically accounts for 85-95% of the total emissions. Although the end user of gasoline and fuels is the largest contributor to GHG emissions, the emissions from heavy crude industries (i.e. bitumen and derived synthetic crude) produce higher GHG emissions than conventional oil production.

It is difficult to obtain an exact estimate for GHG emissions for bitumen production with open-pit mining technology (Flint, 2005). Figure 1.2 demonstrates the estimated CO_2 emissions from mining and extraction in open-pit mining technology. According to this figure, about 40kg of CO_2 is emitted in mining and extraction to produce one barrel of synthetic crude oil; close to 5kg of the total emissions seems to be related to diesel fuel consumption. According to the Alberta Energy website (http://www.energy.alberta.ca/oilsands/791.asp), bitumen production in Alberta is predicted to be 37 billion barrels by 2020; thus,

assuming GHG emissions per barrel remains unchanged and identical for all producers, the total CO_2 emitted would be 3.5 billion tonnes per year. Thus emissions because of diesel usage would be 189 million tonnes CO_2. Therefore, CO_2 emission from fuel energy is one of the largest contributors to the GHG emissions. If the use of trucks is eliminated or reduced, CO_2 emissions are reduced significantly.

Even though improvements in the bitumen production process over the last few decades has led to a significant reduction of GHG emissions, the CO_2 emissions will continue to increase because such dramatic increases in production rates are planned (Masliyah, 2008).

It is concluded that the development of GHG emission reduction strategies or technologies is of critical importance for the oil sands industry.

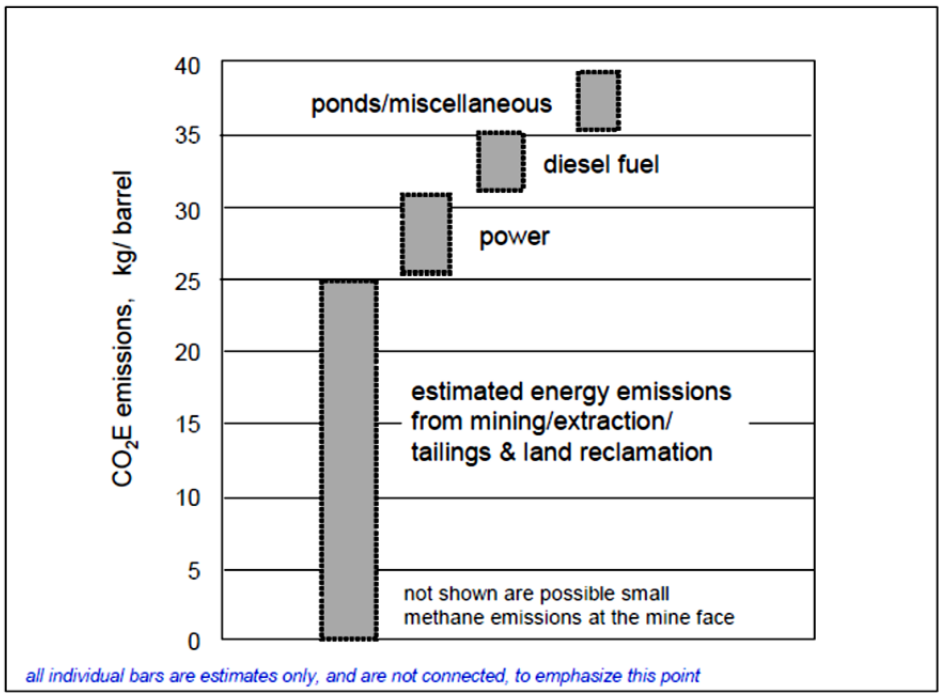

Figure 1.2 Estimated GHG emissions for mining-based bitumen production
(Flint, 2005)

1.4. Technology development to address GHG emission challenges

The introduction of ″At-face″ mining would reduce GHG emissions (Flint, 2005). When this new approach is implemented, trucks used for transporting oil sand ore to the slurry preparation plant are eliminated and therefore a significant source of GHG emissions would be reduced. ″At-face″ mining and its relevance to the current research is discussed further in the next section.

1.5. Research motivation and objectives

The oil sand industry has always relied on continuous technology improvement and new technology adoption to improve bitumen recovery, and reduce environmental foot print and production costs (Flint, 2005; Masliyah, 2008).

Many oil sand companies are actively considering processes where oil sand is conditioned and possibly separated right at the mine face. One benefit of ″At-face″ mining is the reduction of GHG emissions because of the elimination of haul trucks; another result will be the use of considerably shorter hydrotransport pipelines (Flint, 2005). The advantage of using short hydrotransport pipelines is a substantial decrease of the maintenance costs and the likely drawbacks include poor ablation and incomplete conditioning (Sanders, 2008). Maintenance of shorter hydrotransport pipelines cost significantly less; and the cost of maintenance is one of the factors that influences mining costs per barrel of bitumen produced (Flint, 2005). Maintenance is responsible for 50% of the operating cost due to high wear rates in the long hydrotransport pipelines (Schaan et al., 2007). Cost of maintenance and energy requirements are considered as two of the greatest challenges in the oil sand extraction and hydrotransport processes (Flint, 2005).

Recall that ablation of oil sand lumps in a hydrotransport pipeline occurs because of the heat transfer from the slurry to the lump surface, softening of the lump surface layer and its removal due to exposure to shear forces. In other words, heat

transfer and mechanical energy are the two important phenomena in the oil sand lump ablation (Masliyah, 2008).

The Saskatchewan Research Council conducted lump ablation tests using a 264mm pipeline loop. Ablation tests for soft oil sand lumps (T_{0L} = 10°C) at T = 50°C showed that ablation in a 1km pipeline is complete up to 70% whereas it is 95% complete when the pipeline length is increased to 5km (Masliyah, 2008; Shook et al., 2002). The comparison is illustrated in Figure 1.3. It is concluded from this comparison that for a certain operating condition and lump type, lump ablation highly depends on the length of the hydrotransport pipeline or time of ablation.

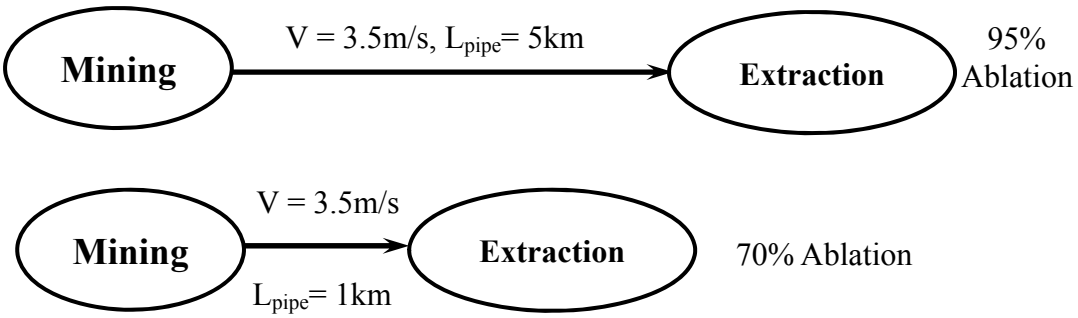

Figure 1.3 Comparison of completion of ablation of oil sand lump in 1km with 5km hydrotransport pipeline
(Based on SRC ablation tests: D=264mm, T=50°C and T_{0L}=10°C)

If one desires to achieve complete oil sand lump ablation in a short pipeline, current operating conditions must be modified. One of the solutions to the incomplete ablation that is likely to occur in ″At-face″ processes is through accelerated oil sand conditioning, referred to here as high-shear, short duration conditioning (Sanders, 2008). The purpose of the proposed process is to increase the mechanical energy to which oil sand lumps are exposed and thus enhance their ablation rate.

In order to develop a high-shear, short duration conditioning process, a better understanding of each of the steps of the conditioning process is required. Oil sand lump ablation, as the first step of the conditioning process, has not received much attention from researchers. No one has fully studied the parameters which affect the lump ablation process. Thus conducting thorough investigations on oil sand lump ablation in order to achieve a better understanding of the process seems to be necessary.

The aim of the current study is to provide some knowledge in the area of oil sand lump ablation. In order to investigate the oil sand lump ablation and the way operating parameters influence this process, the objectives of this research were defined as:

- Establish a reliable experimental method to study oil sand lump ablation
- Measure oil sand lump ablation rates at different operating conditions (slurry velocity and concentration)
- Develop a model of oil sand lump ablation

To study the ablation of individual artificial oil sands lumps, a 104mm pipeline loop was designed and built at the Saskatchewan Research Council Pipe Flow Technology Centre™. Slurries containing sand particles with a median diameter of 0.190mm were used for the ablation tests. Artificial oil sand lumps, manufactured based on similar dry density to the actual oil sand, were used for the tests. The mass loss from an oil sand lump and the drag force acting on the ablating lump were measured on-line and at real time at different slurry temperatures, velocities and concentrations. The mass loss and force measurements were made using strain gauge technology. The results of these tests constitute one of the first studies on the effect of various operating conditions on the digestion of individual oil sand lumps inside a hydrotransport pipeline.

A simplified model that predicts the ablation rate at the initial stages of mass loss with respect to the shear force acting on the lump was developed. The model was validated using the experimental data obtained in this study.

2. Literature review

In this chapter, different parameters that are known to influence the ablation of oil sand lumps are introduced. Previous studies of oil sand lump ablation are described and important areas that have not been covered by these researchers are identified. Some background theory needed in the development of improved ablation models is also introduced in this chapter.

2.1. Effect of different operating parameters on ablation

As described by Masliyah (2008), ablation of oil sand lumps happens because of two important phenomena: heat transfer and shear forces. Once an oil sand lump is exposed to the hot slurry medium, heat from the slurry is transferred to the lump surface and because of the dependence of bitumen viscosity on temperature the surface layer of the lump softens. The soft thin surface layer is then ablated as a result of shearing inside the hydrotransport pipeline. This process repeats itself to the point that the entire oil sand lump is ablated.

Any factors that change the two above-mentioned phenomena; namely, heat transfer and shear forces, would affect the ablation of oil sand lumps. The most important of these parameters, which include slurry temperature, initial lump size, pipeline diameter and pipeline velocity are discussed here.

2.1.1. Effect of slurry temperature

Since the first commercial oil sand mining and bitumen extraction operation was commissioned, attempts to reduce bitumen production costs and environmental impacts have driven process improvements and flowsheet changes (Masliyah et al., 2004). One way to simultaneously reduce both is to operate at lower slurry temperatures.

Slurry temperature is known as the most important parameter in the extraction of bitumen from Athabasca oil sands, as it affects all three steps of oil sand conditioning: oil sand lump ablation, bitumen liberation and air attachment

(Masliyah et al., 2004). Bitumen, because of its high viscosity, holds the mixture of sand grains and fine minerals together within an oil sand lump (Masliyah et al., 2004). Bitumen viscosity decreases sharply with increasing temperature, as shown in Figure 2.1. According to this plot, at room temperature (T = 20°C) the bitumen viscosity is about 2×10^5mPa.s. At this temperature, bitumen looks like a solid and it is essentially impossible to separate bitumen from the sand grains (Masliyah, 2008). However, when the temperature increases to T = 50°C, bitumen viscosity reduces more than one order of magnitude, i.e. to 10^4mPa.s. It is known that at this temperature the separation of bitumen from sand grains occurs relatively quickly. Based on studies of Masliyah et al. (2004) and Wallwork et al. (2004), in order to effectively reduce the lump size and liberate bitumen from sand grains, lower bitumen viscosities must be attained. Froth quality and bitumen recovery are also highly temperature-dependent because slurry temperature affects the air bubble-bitumen attachment.

Although oil sand producers might ultimately wish to operate hydrotransport pipelines at low temperatures because of the reduced operating costs and environmental impacts, they are aware that a balance between the bitumen recovery and temperature reduction must be reached. The oil sands industry found a temperature range that represents a compromise between cost, GHG emissions and bitumen recovery. Operating temperatures between 40 and 55°C are common (Masliyah et al., 2004).

2.1.2. Effect of initial lump size

Recall that heat transfer to the lump is an important factor in ablating oil sand lumps (Eskin et al., 2002). Under similar thermal conditions, the thickness of the layer that is softened and ablated away is essentially equal for all lump sizes; therefore, the fraction of lump mass that is removed decreases as the lump size increases. In other words, the time necessary for complete digestion of a lump increases as the oil sand lump initial size increases (Masliyah, 2008).

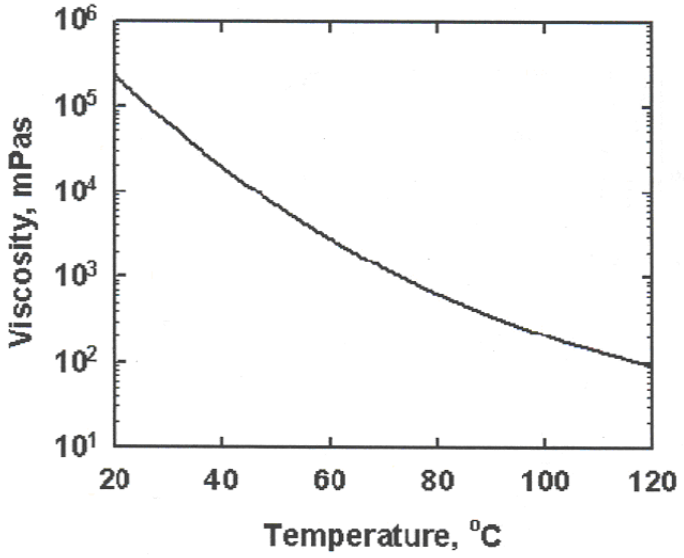

Figure 2.1 Viscosity of Athabasca bitumen as a function of temperature
(Masliyah, 2008)

2.1.3. Effect of pipeline diameter

Pipeline diameter is also a key parameter in the ablation of an oil sand lump. For a certain slurry flow rate, more energy is dissipated in a smaller diameter pipe and this leads to the higher inter particle shear stresses (Masliyah, 2008). The relationship between energy dissipation and pipe diameter is given as (Hesketh et al., 1987):

$$\bar{\epsilon} = \left(2 f_f V^3\right)/D \qquad (2.1)$$

where:

$\bar{\epsilon}$ = Volumetric average of pipe energy dissipation (m^2/s^3)

V = Bulk velocity (m/s)

D = Pipe diameter (m)

f_f = Fanning friction factor

According to this equation, energy dissipated in a pipe inversely varies with diameter of the pipe. Therefore, higher energy dissipation is expected in smaller pipelines and this leads to higher ablation rates.

On the other hand, at a constant slurry flow rate, the bulk velocity is higher in the pipe with the smaller diameter; therefore, the residence time of an oil sand lump inside this pipe will be shorter. According to Masliyah (2008), shorter residence times result in lower ablation rates.

In summary, in order to achieve a desirable ablation rate, a balance must be sought between the oil sand lump residence time and energy dissipation.

2.1.4. Effect of shear stress

An oil sand lump moves at a different velocity than the surrounding slurry and contacts with the pipe wall and other lumps present in the slurry. These create a shear stress at the lump's surface (Masliyah, 2008).

A lump also breaks down or digests more rapidly if it passes through a pump; however, this effect is not the focus of the current study.

In a pipeline, the surface shear force acting on the lump is expected to increase with increasing mixture velocity and concentration. Higher slurry concentrations promote particle-particle interactions and particle-wall interactions (Masliyah, 2008; Sanders et al., 2007).

All stages of the oil sand slurry conditioning process appear to depend on the velocity of the slurry in hydrotransport pipelines (Qiu, 2010). However, more research has been conducted to study the effect of shear exposure on bitumen liberation and bitumen aeration than on the lump ablation. More investigation is required in this area.

The effects of slurry temperature, oil sand lump initial size, pipe diameter and shear stress in the hydrotransport pipeline on oil sand lump ablation were

discussed here. The effect of slurry temperature on ablation has been experimentally investigated before and is well understood. The effects of pipe diameter, lump initial size and shear stress on lump ablation have never been experimentally studied. It is concluded that slurry temperature is an important factor in oil sand lump ablation and no experimental study on lump ablation can be conducted without considering slurry temperature. Lump initial temperature influences the ablation rate; therefore it must be recorded and used for further analysis. Slurry velocity and concentration are the two important parameters that affect the shear stress acting on the oil sand lump in the hydrotransport pipelines; thus, to investigate the effect of shear exposure on the lump, these two parameters need to be considered. It must be noted that residence time of the oil sand lump decreases when slurry velocity increases and this should be considered when interpreting the experimental results.

2.2. Previous studies of oil sand lump ablation

Previous experimental and modelling studies of lump ablation are listed and briefly discussed in this section. The parameters considered by each researcher are summarized here and the parameters which need further investigation are also identified. Note that only the first study described here, that of Traynis (1970), does not involve oil sand lump ablation directly.

2.2.1. Traynis wheel test stand

Traynis (1970) studied the grinding or crushing of coal particles using a wheel test stand. In a separate series of experiments, Traynis showed that pressure loss for slurry in a wheel test stand agrees well with that in a horizontal pipeline. He pointed that this agreement was a result of the similarities in energy dissipation mechanisms of moving solid particles in both systems. According to Traynis (1970), the mechanism of energy dissipation determines the process of the particle crushing; thus, when the energy dissipation mechanism of the two systems is identical the size reduction process will be identical too.

The tests were completed using a wheel test stand made of a D = 200mm pipe. Three runs were repeated with a wheel stand made of D = 300mm pipe to investigate the effect of pipe size on particle crushing or grinding. Prior to the experiments, with the intention of starting with a smooth pipe, pipes were polished using abrasive materials (quartz). The wheel test stand was filled up to 1/3 of the total volume with a mixture of water and coal. For each run using the smaller wheel test stand, 10-40kg of coal was loaded. Coal particles from two different hydraulic mines were utilized for the experiments. At certain time intervals, the degree of size reduction of the coal particles was determined by measuring the particle size distribution (PSD) of the remainder of the coal particles. To re-confirm that the wheel test stand system is representative of the horizontal pipeline, a number of experiments were repeated by recirculating slurry in 4km and 1.3km pipelines. The effect of slurry velocity and concentration, pipe diameter, coal particle size, existence of abrasive rocks, pipe length and mechanical properties (strength and hardness) of the coal particles on the size reduction of the coal particles was investigated.

These experiments showed that:

1) The results obtained using short pipelines (~ 10km) agreed with those of the wheel test stand. But transporting the coal particles for a long distance (> 20-50km) resulted in faster crushing. This is probably because the mixture passed through the feed pump many times. This caused more rapid size reduction of the coal particles. This effect was more evident when the initial coal particle size was large.
2) The slurry velocity was changed from 1.8 to 6m/s for experiments with different coal types. In all cases, velocity had an insignificant effect on the crushing of coal particles.
3) Slurry concentration varied from 1:16 to 1:2, mass of solid to mass of liquid. These experimental runs showed that size reduction of the coal particles was independent of slurry concentration.

4) The pipe size of the wheel test stand did not affect the extent of size reduction of the coal particles.
5) For coal particles initially 3-6mm or 50-100mm in diameter, the degree of size reduction was only affected by the initial particle size. For particles smaller than 3mm, increasing the initial particle size resulted in more visible increase in the intensity of crushing.
6) The existence of abrasive rocks in the slurry caused more rapid size reduction of particles, which were 50-100mm in diameter initially but were crushed to the 3-6mm size range. Considerable crushing was observed within the first 10-15km.
7) The crushing rate was higher in the first few kilometers of the pipe and it decreased as coal particles moved along the pipeline. This must be because of the fact that shear stress decreases as particle size decreases, which would be expected when the particle slip velocity decreases. Rounding of the edges of the particles within the first kilometers of the pipe might be another reason for reduction of the crushing rate with pipeline length.
8) Experiments using coal particles with initial size 6-13mm showed that as the strength factor of the coal particles increased, the crushing rate decreased. Strength factor is an indicator of the grindability of the coal particles.

One of the strengths of this study is that it introduces a new experimental method for studying the mass loss of solid particles. In addition, this is the only study done on the effect of slurry velocity and concentration on the particle mass loss in slurry pipelines. However, one cannot directly apply the results of this research to oil sand hydrotransport pipeline because the nature of coal particles is very different from oil sand lumps.

Coal is brittle organic sedimentary rock that contains varying amounts of carbon, hydrogen, nitrogen, oxygen, and sulfur (Speight, 2005). On the other hand, oil sand contains bitumen, sand grains, clays and small amount of water; and the

viscosity of bitumen highly varies with temperature (Maliyah, 2008). As coal is brittle, coal particles tend to break down into smaller particles when they are exposed to the shear forces; however, mass loss from oil sand lumps occurs by gradual mass removal from the surface of the lump. The amount of oil sand lump mass loss depends on many parameters but temperature seems to be the most important factor. Thus, one cannot study oil sand lump ablation without considering the slurry temperature. Additionally, because the nature of the two materials is different, the effect of slurry concentration and velocity on their mass loss is envisioned to be different.

2.2.2. Law, Masliyah and Nandakumar experimental study

Law et al. (1987) examined the ablation of frozen mixtures of water and paraffin wax (octadecane) with solid particles such as kaolinite clay, titanium oxide, aluminum powder and sand. Because the ablation of oil sand samples was complex they chose to study the ablation of less complex materials. This investigation was conducted with the purpose of obtaining information from a well-controlled system and applying it for designing the rotating drums, which at that time were used for oil sand lump ablation. A turbulent axisymmetric water jet, whose velocity varied between 1.7 and 2.8m/s, was used; the temperature of jet was changed from 32 to 60°C depending on the material being tested. The water temperature was chosen based on the sample's melting point, which is 26-29°C for octadecane. Cylindrical (L = 150mm, d = 11mm) samples were manufactured and immediately frozen in liquid nitrogen. The samples were then placed in front of the jet using a sliding platform. The sliding platform moved up and down by using a stepping motor. Before the start of the experimental run, the front of the sample that was to be exposed to the jet was placed in-line with a certain point, determined as the melt front pointer. During an experimental run, the sample was never moved from this point. Instead, the sliding platform was lowered at a speed equal to the ablation rate of the frozen sample. The downward movement of the sliding platform against time was recorded and plotted and the slope of this line, for each set of the experiments, was considered to be the

ablation rate. It was observed that for each operating condition, the slope of the plotted line remained constant with time. The results of this study showed that (Law et al., 1987):

1) For all of the samples, an increase of the jet temperature significantly increased the ablation rate. For instance, ablation rate of lumps made from octadecane and 60 (vol%) sand at V = 2.8m/s and T = 60°C was equal to 4.4×10^{-3}m/s whereas it was equal to 3×10^{-3}m/s at T = 50°C.
2) Increasing the jet velocity from 1.7 to 2.8 m/s increased the ablation rate equivalent to that of raising the jet temperature by approximately 10°C (from 50 to 60°C). It is because surface shear stress on the sample is proportional to V^2.
3) Addition of solid particles to the samples affected the ablation rate in a complex way. The effect depended on the type of the solid particles and the lump material because thermal conductivity of the solid particles was different so the heat transfer coefficient within the sample differed depending on the solid particles. In the case of octadecane-kaolinite samples, at a certain jet velocity and temperature (V = 2.06m/s, T = 50 and 60°C), ablation rate gradually increased for solids content up to 17 vol% and then ablation rate increased considerably for solids content beyond 17%. The reasons for this observation were mentioned to be: (i) the increase of the heat transfer area due to the roughening of the melting surface and (ii) ablation of the sample as clusters instead of layers at high solid contents. This discussion indicates that ablation also depends on the type and components of the sample or oil sands ore.

This research gave a good indication of the way different parameters influence ablation but the study had a number of limitations:

i. Viscosity of the samples was far different from that of bitumen.
ii. Sample was stationary and was exposed to water only from one face.
iii. Only ablation with water was investigated.

iv. The number of experimental runs using samples manufactured with sand particles was very limited and the effect of clay-size solid particles on ablation was instead explored.

More investigations need to be conducted on actual oil sand lump ablation using a system that better represents the actual conditioning medium. These experiments are necessary for developing a predictive model applicable for all operating conditions.

2.2.3. Saskatchewan Research Council experimental study

In 1996, an experimental study on the ablation of actual oil sand lumps was completed at the Saskatchewan Research Council Pipe Flow Technology Centre™ (Shook et al., 2002). Lump ablation at various operating conditions was investigated by loading a certain amount of lumps to a 264mm pipe loop using a feeder close to the discharge of the pump. At certain time intervals, lumps were trapped by a basket before discharging into the storage tank and were weighed and put back into the loop (Masliyah, 2008; Gillies and Mckibben, 2011). The SRC experiments showed that:

1) For all types of the oil sand lumps the required time, i.e. pipeline length, to reach a certain ablation rate was strongly dependent on the slurry temperature (Masliyah, 2008; Shook et al., 2002). As shown in Figure 2.2, for soft lumps the time of complete ablation at T = 50°C was one third of that at T = 30°C and 18°C. It is noteworthy that the effect of temperature on the ablation rate was found to be qualitatively similar for all types of the oil sand ore (Masliyah, 2008; Shook et al., 2002).
2) As presented in Figures 2.3 (a and b), for ablation at T = 18°C, lump initial temperature had no effect on the time of ablation. However, at higher slurry temperatures (T = 30 and 50°C) the ablation occurred slightly faster for lumps with lower initial temperature. The temperature of oil sand lumps generally varies between 5°C in summer to -5°C in winter (Masliyah, 2008). It can be concluded that temperature difference between

slurry and oil sand lump is an important driving force for the lump ablation: the higher the temperature difference, the faster the ablation.

This experimental study, as the first available research on the ablation of actual oil sand lumps, is very valuable. Unfortunately, the effect of other important parameters such as slurry velocity and concentration on ablation was not investigated by the researchers.

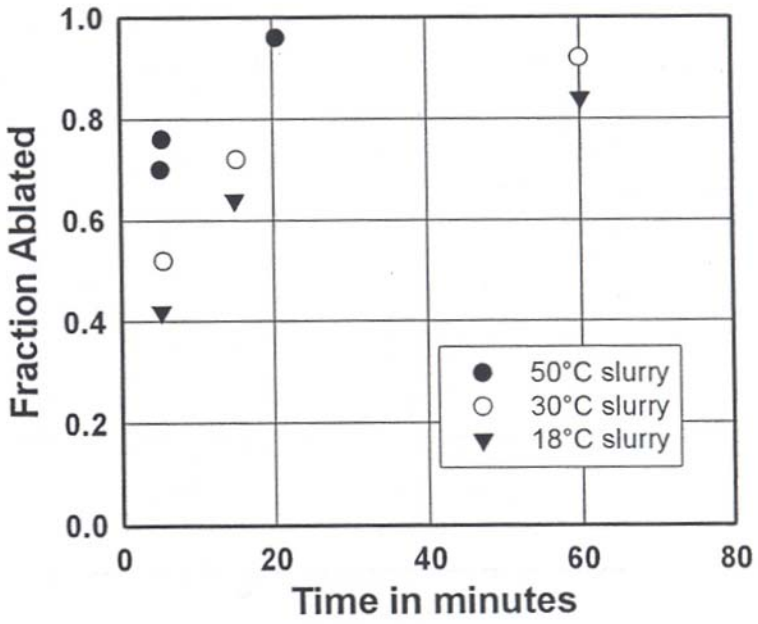

Figure 2.2 SRC Experimental result: effect of slurry temperature on the ablation time of soft lumps: T_{0L}=10°C:D=264mm
(Shook et al., 2002)

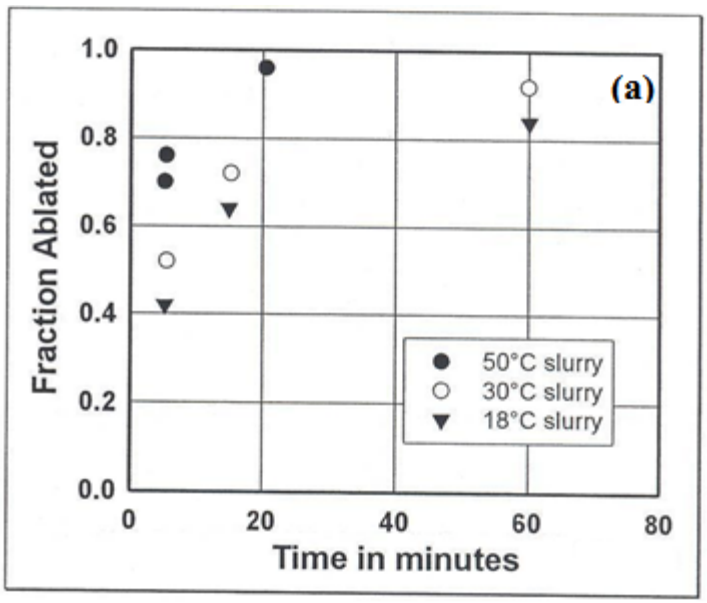

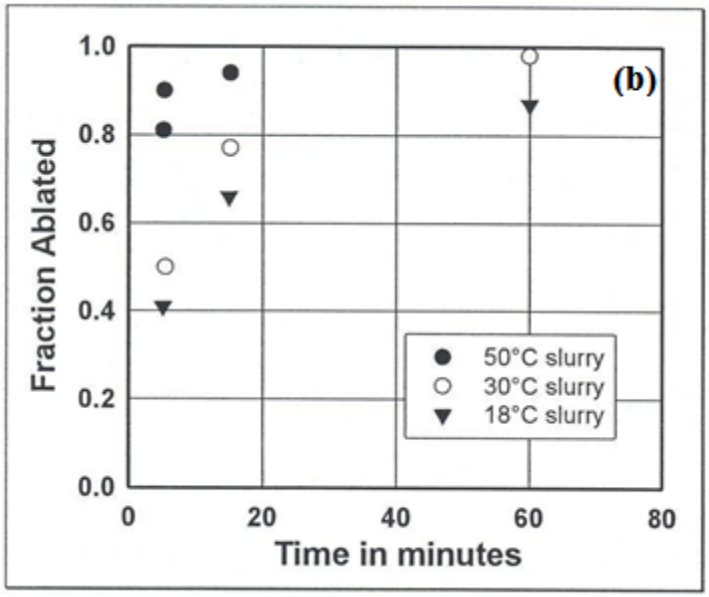

Figure 2.3 SRC experimental result: effect of lump initial temperature on the ablation of soft lumps for (a) T_{0L}=10°C and (b) T_{0L}= -7° C: D=264mm
(Shook et al., 2002)

2.2.4. Bara and Masliyah ablation model

In 1997, Bara and Masliyah developed a model for the ablation of oil sand lumps. The model was developed based on the fact that crushed oil sand lumps and sand particles form a moving layer at the bottom of the pipe, while fine solids and water, collectively known as the carrier fluid, exist within the whole pipe cross-section. The height of the bottom layer reduces with axial position along the pipeline when lump size reduces. It was assumed that the surface layer of the lump heats and softens and is peeled off because of the shear stress inside the pipe. They presumed that this process repeats up to the point that the entire sample (which was defined as 95% of the lump's mass) is removed. The SRC Two-Layer model was used to estimate the velocities of the top and bottom layers of the flow. Shear stress on the lumps was then calculated using the slurry viscosity and the flow axial velocity (Masliyah, 2011; Masliyah et al., 2004). Bara and Masliyah validated their model with the only available experimental data, collected by Saskatchewan Research Council PipeFlow Centre™ in 1996.

Masliyah (2008, 2011) demonstrated the predicted effects of mixture velocity, pipeline diameter, slurry temperature, initial lump size, slurry density and pipeline length using this model:

1) Raising the slurry velocity slightly enhanced the oil sand lump ablation rate (Figure 2.4). It appears that the beneficial effects of velocity increase are offset by the reduced residence time of the lump (Masliyah, 2008).
2) At T = 25°C, as the pipeline diameter increased, lumps were digested more slowly in a way that longer pipelines were needed for complete ablation. For example, in a 12inch pipeline the ablation was nearly completed after 3km, while the digestion of lumps in a 30inch pipeline was not completed even after 5km (Figure 2.5 (a)). However, according to the model predictions, illustrated in Figure 2.5 (b), at T = 50°C the effect of pipeline diameter diminished considerably (Masliyah, 2008). This probably is because heat transfer is the dominant factor in the ablation of

an oil sand lump. At high temperatures, the viscosity of the bitumen decreases tremendously and the surface shear stress required for consequent removal of the soft surface layer reduces significantly; and therefore it is achieved in both small and large pipes.

3) At 40°C, increasing the slurry density from 1463 kg/m^3 to 1544 kg/m^3 resulted in a slight increase in the ablation rate (Figure 2.6). For the purpose of modelling, change of slurry density was determined by changing water flow rate for a fixed amount of dry oil sand input. The oil sand lump ablation reduces as the slurry density reduces when more water is added to the system, since the total slurry flow rate increases and residence time reduced (Masliyah, 2011).
4) Smaller oil sand lumps ablate more rapidly. As shown in Figure 2.7, a 2inch oil sand lump completely ablated in a 3km pipe length but ablation of a 6inch lump would be just 50% complete in a 4km pipe. This is because " a given mass of oil sands ore in the form of smaller lumps will digest much faster than the same mass of ore in the form of larger lumps due to the larger surface area of the former" (Masliyah, 2011).

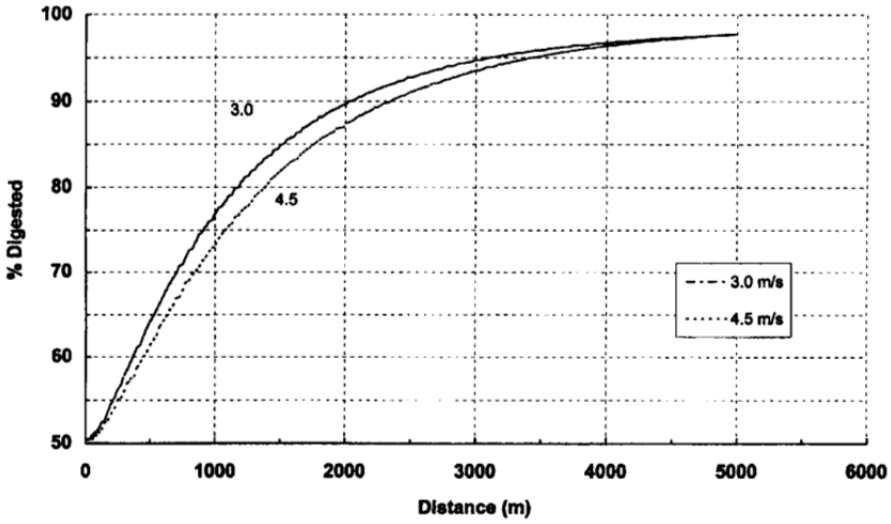

Figure 2.4 Masliyah and Bara oil sand lump ablation model predictions showing the effect of mixture bulk velocity on the oil sand lump ablation: T=50°C;T_{0L}=5°C;V=3.8m/s; d=20mm (Masliyah, 2008)

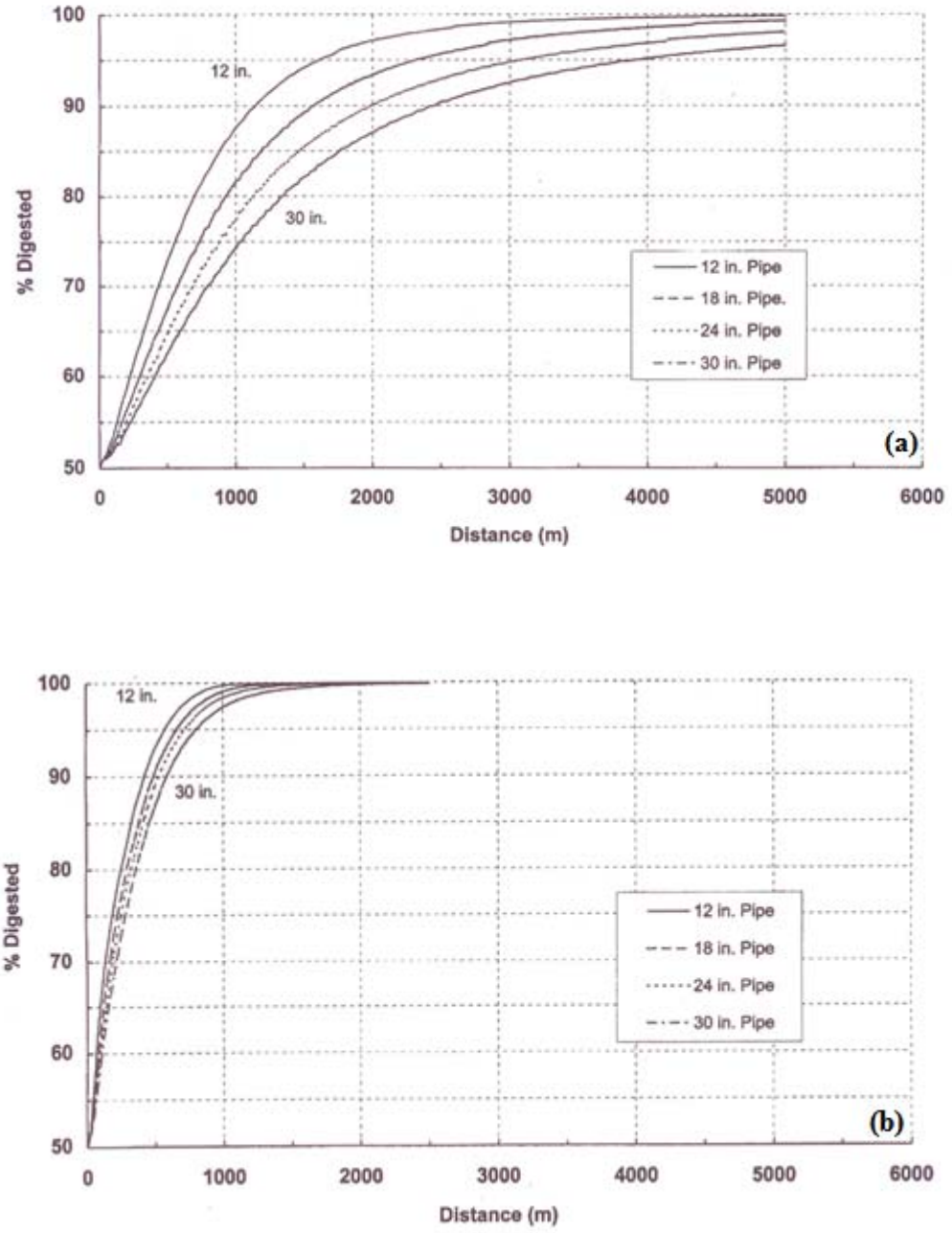

Figure 2.5 Masliyah and Bara oil sand lump ablation model predictions showing the effect of pipe diameter on the ablation of oil sand lumps: T_{0L}=5°C; V= 3.8m/s; ρ_m=1550kg/m^3; d=20mm (a) T=25°C and (b) T=50°C
(Masliyah, 2008)

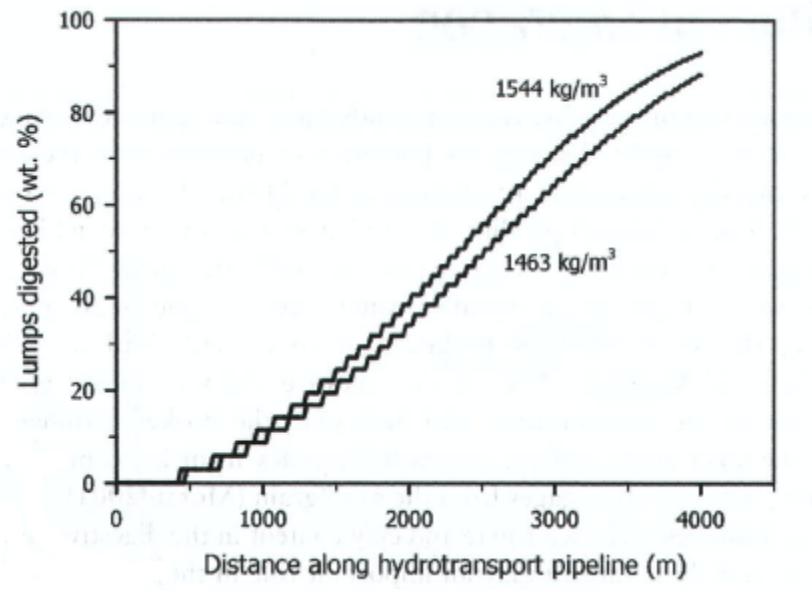

Figure 2.6 Masliyah and Bara oil sand lump ablation model predictions showing the effect of slurry density on the ablation of oil sand lumps: T_{0L}=0°C; D=710mm; d=100mm and T=40°C
(Masliyah, 2011)

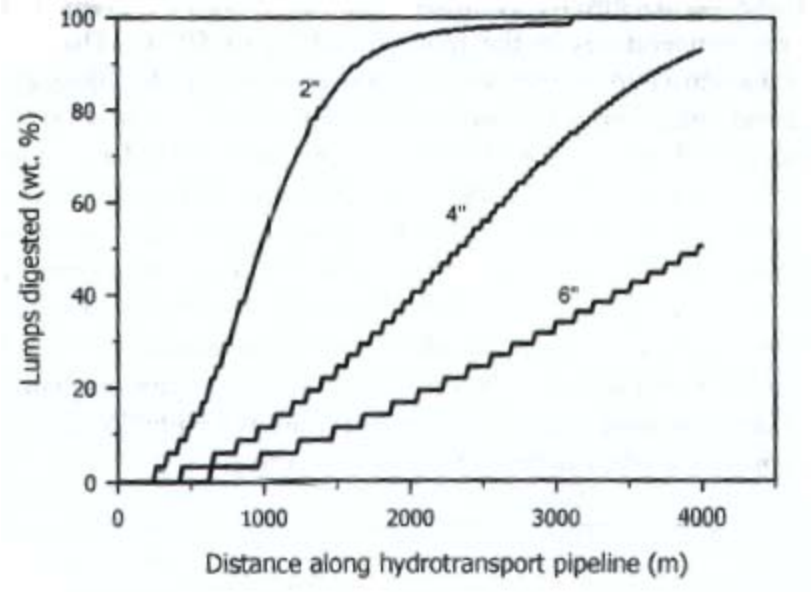

Figure 2.7 Masliyah and Bara oil sand lump ablation model predictions showing the effect of initial lump size on the ablation of oil sand lumps: T_{0L}=0°C; D=710mm; ρ_m=1548kg/m^3 and T=40°C
(Masliyah, 2011)

The method of estimating surface shear force on the lumps has not yet been verified. Masliyah (2008, 2011) mentioned that the velocity of the top and bottom layers were estimated using SRC Two-Layer model and then shear stress within the pipeline was estimated using the slurry viscosity and flow axial velocity. This approach seems to have some limitations:

i. The version of the SRC Two-Layer model that was used at that time was developed based on existing experimental data and the general knowledge of slurry pipelines that existed at that time. Since then, this model has significantly improved but these improvements were never integrated into the Bara and Masliyah's ablation model.

ii. It appears that for developing this model, shear stress on the oil sand lumps was assumed to be equal to the shear stress at the interface of two the layers and was calculated using the bulk velocity. In order to better understand this method, SRC PipeFlow Model 2003 was used to estimate the velocities of the two layers for a system with properties similar to the existing hydrotransport pipelines. Pipeline diameter was assumed to be 762mm and bulk velocity of V = 3.5m/s. Table 2.1 shows the inputs to the model.

Table 2.1 Inputs for SRC PipeFlow 2003 Model

Pipe Wall Roughness (mm)	Coarse Solids Vol Fraction in Settled Bed	Total Solids Vol Fraction in Delivered Mixture	Particle Density (kg/m^3)	Liquid Density (kg/m^3)	d_{50} of Coarse Particles (mm)	Fines (fraction of total solids)	Carrier Fluid Viscosity (Pa·s)
0.050	0.63	0.350	2650	988	0.200	0.150	0.0009

For this system, the SRC PipeFlow Model 2003 predicted the velocity of the top layer at V_1 = 3.68m/s and the lower layer velocity at V_2 = 0.156m/s; thus, the relative velocity (V_1-V_2) = 3.52m/s that is very close to the slurry bulk velocity. In other words, for a system similar to this,

Bara and Masliyah's model uses the slurry bulk velocity to calculate the shear stress acting on the oil sand lump(s). However, according to Gillies and McKibben (2011), the velocity of high-density large solid particles (such as oil sand lumps) in slurry is about 0.9V. This means that the relative velocity causing the shear stress on the lump is in fact 0.1V. Therefore, the shear stress used in the Bara and Maliyah's model might be overestimated.

iii. Only one set of experimental data was available for validating this model. Additionally, the SRC experimental data used for this purpose were limited to a certain pipeline size and velocity.

Thus more research is required to quantify the effects of slurry velocity on ablation. Furthermore, Bara and Masliyah model is not publicly available, so most researchers and engineers have no ability to evaluate for themselves the effects of temperature, velocity, initial lump size, and pipeline length or residence time on lump ablation rate.

2.2.5. Eskin, Leonenko, Lezhnin and Vinogradov ablation model

Eskin et al. (2002) modeled the ablation of an individual spherical oil sand lump using a hypothesis similar to that of Bara and Masliyah (1997) for lump ablation. The model was developed utilizing a number of assumptions:

1) The effect of shear stresses and heating was integrated as some surface (critical) temperature. The critical temperature remained constant during the ablation and was related to the minimum adhesive strength of bitumen; it was determined using the experimental results of Law et al. (1987).
2) They also presumed that the lump retains its spherical shape during ablation.

By using these assumptions, the problem was reduced to one dimensional heat conduction for a shrinking sphere. The critical temperature was used as an input

to the applied convection boundary condition. After simplifying the boundary condition equations, one formula that related the sphere size reduction to the critical temperature was obtained. This equation was solved simultaneously with the heat conduction equation. The value of the critical temperature was assumed to be equal to the digestion rate obtained by Law et al. (1987). They used the ablation rate for ablation at 3-4m/s (Eskin et al., 2002). The authors applied this model to study the effect of lump size and initial temperature on oil sand lump ablation.

Although the fundamentals of this model agree with general hypothesis of how individual oil sand lumps ablate, their way of integrating shear stress to a critical temperature, only available for octadecane-sand lumps, seems to be questionable. Additionally, the effects of slurry velocity and slurry concentration on ablation were not investigated by the authors and, in fact, the model does not allow one to investigate these effects. This is because the model is developed based on one set of shear stress indicators that was obtained for specific experimental runs, which had a number of limitations. Furthermore, the model was never validated against any experimental data.

2.3. Theory and modelling

In order to estimate the ablation rate of the oil sand lumps inside the hydrotransport pipeline, the shear stress acting on the lumps and the temperature profile of the lump at different times must be determined. One can think of the following methods for estimating the shear stress acting on an oil sand lump:

1) SRC Two-Layer model
2) Shear stress decay law
3) Surface shear stress as a percentage of drag force on a solid particle

In this section, the first two methods are discussed in details and the benefits and drawbacks of each method are investigated. The third method is discussed in

Chapter 5 because it is the method that is used by author for calculating the shear stress for validating ablation model.

2.3.1. Estimating lump surface shear stress using SRC Two-Layer model

Recall that Masliyah and Bara (1997) used an early version of SRC model to estimate the shear stress acting on the oil sand lump(s) for developing their ablation model. If one intends to use a similar approach, it would be advisable to use a more recent version of SRC Two-Layer model. In this section, the theory behind the development of the SRC Two-Layer model is explained. Additionally, the validity of this approach for calculating the shear stress acting on a lump is discussed.

In a slurry pipeline similar to the hydrotransport pipeline, fine particles (particles < 0.074mm, or perhaps < 0.044mm) augment the viscosity and density of the suspending liquid; coarse particles that are suspended by fluid turbulence are assumed to be at a constant volume fraction throughout the flow domain; and coarse particles that are not effectively suspended by fluid turbulence transmit their immersed weight to the pipe wall and these particles are found in the lower layer and contribute Coulombic (sliding bed) friction (Shook and Roco, 1992).

For the purpose of Two- Layer model formulation and specifically to write force balance equations, the continuous coarse particle concentration profile was simplified to a step-change, i.e. two layers. The velocity within each layer was assumed to be constant. Figure 2.8 shows the idealized concentration and velocity distributions.

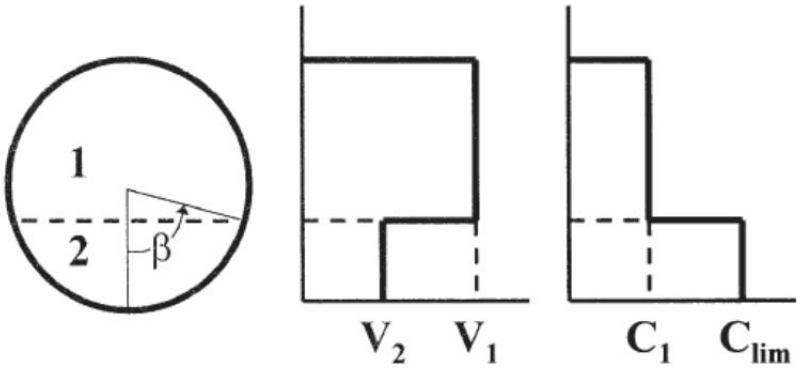

Figure 2.8 Idealized concentration and velocity distributions used in the SRC Two-Layer model
(Gillies et al., 2004)

The SRC Two-Layer model was developed using mass and force balances for, the two layers of the slurry. The force balance produces an equation for the axial pressure gradient in horizontal slurry as a function of friction losses in top, and bottom layers and the interface between the two layers (Gillies et al., 2004).

To estimate the ablation rate of an oil sand lump, the actual shear stress on the lump needs to be estimated. If one assumes an oil sand lump is located at the interface between the two layers, the surface shear stress acting on this lump can be assumed to be equal to the shear stress at the interface. The shear stress at the interface is calculated using (Shook and Roco 1992):

$$\boldsymbol{\tau_{12} = \frac{1}{2} f_{12}(V_1 - V_2)|V_1 - V_2|\rho_1} \qquad (2.2)$$

where ρ_1 denotes the slurry density in the upper layer, and f_{12} can be estimated from a modified Colebrook friction factor equation:

$$\boldsymbol{f_{12} = \frac{2(1+Y)}{[4\ \log_{10}(D/d)+3.36]^2}} \qquad (2.3)$$

where $Y = 0$ for $d/D < 0.0015$ and Y is calculated using the following equation when $0.0015 < d/D < 0.15$:

$$Y = 4 + 1.42 \log_{10}(d/D) \qquad (2.4)$$

Equation (2.4) has been formulated from data taken at Ar < 3×10^5 (Shook and Roco, 1992).

It is inferred from Equation (2.2) that the shear stress acting on the lump is proportional to $(V_1\text{-}V_2)^2$. Calculating velocity of the layers using the SRC Two-layer model showed that V_2 is small compared to V_1 (recall the discussion presented in Section 2.2.4). Therefore, $(V_1\text{-}V_2)$ is approximately equal to the slurry bulk velocity. On the other hand, other research conducted at the Saskatchewan Research Council showed that the velocity of a large particle in horizontal slurry flow was about 0.9V (where V is slurry bulk velocity) (Gillies and McKibben, 2011). In summary, shear stress on the oil sand lump would be proportional to $(0.1V)^2$ which is considerably smaller than $(V_1\text{-}V_2)^2$. This means that the shear stress calculated using Equation 2.2 might overestimate the shear stress acting on an individual lump.

2.3.2. Preliminary estimation of the effects of slurry velocity and concentration on pipe local shear stress using shear stress decay law

In order to estimate the effects of increases of slurry velocity and concentration on pipe local shear stress and consequently oil sand lump ablation, the simplified approach shown below was taken.

If one assumes a stationary solid particle in a slurry pipe flow where:

- Slurry flow has reached steady state, and
- Density is constant throughout the pipe

the local shear stress where the solid particle is located in the hydrotransport pipeline can be estimated using the shear stress decay law (Shook and Roco, 1992):

$$\tau_{rz} = \frac{2s\,\tau_w}{D} \qquad (2.5)$$

where:

s = Distance from pipe axis (m)

τ_{rz} = Shear stress at y (Pa)

τ_w = Pipe wall shear stress (Pa)

D = Pipe diameter (m)

Hence for a known wall shear stress, the shear stress at any radial position of the pipe can be calculated. However, calculating the wall shear stress for a hydrotransport pipeline is complex because wall shear stress and flow density are not constant around the pipe.

Recall that flow is not uniform throughout the cross-section in a hydrotransport pipeline and significant concentration and velocity gradients can exist particularly when operating at velocities just higher than the deposition velocity (Shook et al., 2002). However, Gillies et al. (2004) experimentally investigated the concentration and velocity distributions and pressure loss of sand (d_{50} = 0.190 and 0.270mm) slurry flows. They showed that for highly concentrated settling slurries at velocities significantly higher than the deposition velocity, the concentration profile is nearly uniform. They also concluded that for these slurries, Coulombic friction is negligible relative to kinematic friction. Also, according to Shook et al. (2002), Coulombic friction is typically negligible as long as the particle diameter is not too large ($d_{50} \leq 0.3$mm) and the mixture velocity is high (say, $V > 2Vc$). It is also appropriate for vertical flows of sand slurries where the particle diameter is less than 0.300mm or so (Adane et al., 2012).

It is therefore worthwhile to consider the so-called kinematic friction loss component of the SRC Pipe Flow model, given below as Equations 2.6 and 2.7, to calculate the wall shear stress for such systems. Using the SRC model, the kinematic friction loss component is determined so that it accounts for the friction associated with the flow of the carrier fluid, and the friction related to particle collisions and the tempering effect of near-wall lift (Shook et al., 2002). If the

Coulombic friction can be assumed to be negligible, then only kinematic friction is important and the wall shear stress, τ_w, is calculated using:

$$\boldsymbol{\tau_w = 0.5\, V^2\left(f_f\, \rho_f + f_s\, \rho_s\right)} \qquad (2.6)$$

Gillies (2012) developed a correlation for calculating f_s:

$$\boldsymbol{f_s = \lambda^{1.25}[A\, Ln(d^+) + B]} \qquad (2.7)$$

where,

$$\boldsymbol{d^+ = \frac{d\, v^* \rho_f}{\mu_f} = \frac{d\,(f_f/2)^{0.5} V\, \rho_f}{\mu_f}} \qquad (2.8)$$

and,

$$\boldsymbol{\lambda = [\left(\frac{C_{max}}{C}\right)^{1/3} - 1]^{-1}} \qquad (2.9)$$

for $d^+ \leq 21$: $A = -1.1 \times 10^{-4}$ *and* $B = 4.2 \times 10^{-4}$

and $d^+ \geq 21$: $A = -5.6 \times 10^{-5}$ *and* $B = 2.6 \times 10^{-4}$

The kinematic friction loss calculation (described above) provides a tool for realistic assessment of the effect of slurry velocity and concentration on the local shear stress. An arbitrarily-chosen model system, whose properties are described in Table 2.2, is considered here. The local shear stress, plotted as a function of mixture velocity and for two different solid concentrations, is shown in Figure 2.9.

Table 2.2 Input parameters for estimating shear stress inside the pipe

Term	Value
D (mm)	103
s (mm)	20
ρ_f(kg/m^3)	1000
μ_f (Pa.s)	0.001
d_{50} (mm)	0.120
ρ_s (kg/m^3)	2650

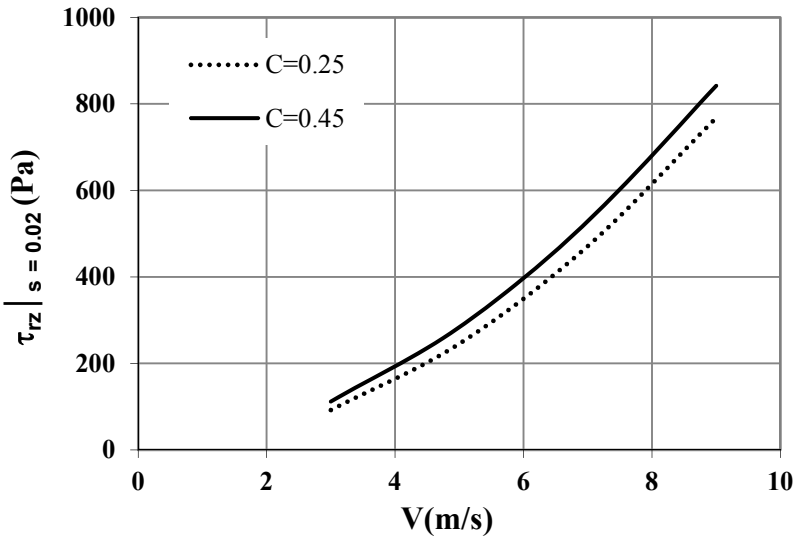

Figure 2.9 Pipeline local shear stress at different slurry velocities and concentrations

This graph indicates that for a solid particle placed 20mm from the center of a 103mm (diameter) pipe, the surface shear stress on the particle increases substantially at higher mixture velocities. Figure 2.10 illustrates the percent increase of the pipe local shear stress as result of concentration increase at different slurry velocities. Based on this graph, it appears that increase of slurry concentration at lower slurry velocities has more significant effect on the local shear stress.

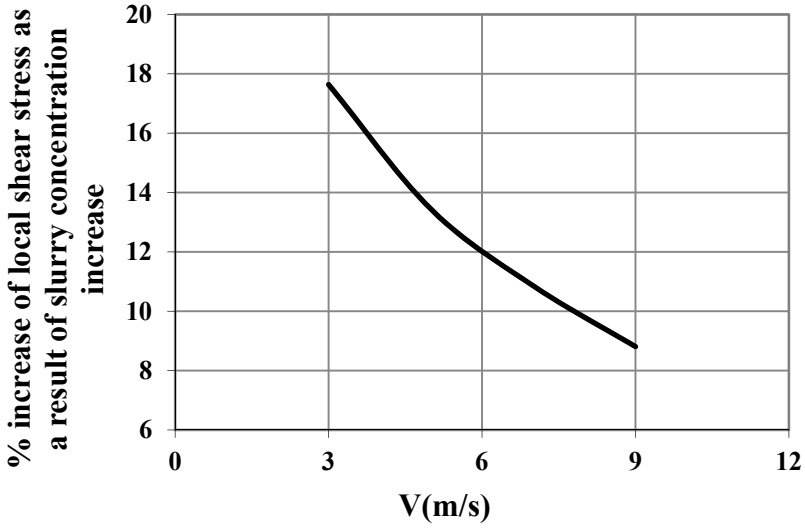

Figure 2.10 Increase of local shear stress in a slurry pipeline as a result of slurry concentration increase from 25% to 45% (by volume)

It should be noted that these graphs qualitatively indicate the effect of velocity and concentration on shear stress and do not represent the actual shear stress on the oil sand lumps. This example was done for a simplified case where the solid particle is stationary but in the actual hydrotransport pipelines, oil sand lumps move along the pipe axis; thus, in order to estimate the shear stress acting on the lump, lump slip velocity must be considered.

2.4. Summary

A limited number of studies on the ablation of large particles exist. Among these studies only few looked at the effect of velocity and concentration on the ablation. Traynis (1970) showed that slurry concentration and velocity have no effect on the grinding or crushing of the coal particles. Law et al. (1987) proved that for a stationary sample, increase of velocity significantly increases the ablation rate. Masliyah (2008) used the Bara and Masliyah model to show that slurry velocity has a small effect on oil sand lump ablation because at a constant flow rate, the residence time decreases as the slurry velocity increases. Additionally, an estimate

of pipe local shear stress showed that increasing slurry velocity enhances the shear stress inside the pipeline and this is an indication of increasing oil sand lump ablation. An increase in slurry concentration appears to have a more significant effect on the increase of local shear stress at low slurry velocities.

No research has been done to experimentally study the effect of slurry velocity and concentration on the ablation of actual oil sand lumps. Additionally, a publicly available model that is capable of estimating the ablation rate of the oil sand lump as a function of shear stress forces is required for scientific and engineering use.

2.5. Implications for experimental design, test execution and modelling

It was found that in order to develop a model that accurately predicts lump ablation rate, surface shear stress on the lump must be properly approximated or measured. Thus, an appropriate force measurement technique must be developed. It was decided to test the ablation of a stationary individual oil sand lump in order to measure the actual forces acting on the lump. Once a reliable experimental and measurement technique is available, investigating the effect of different operating parameters, i.e. velocity and concentration, on the oil sand lump ablation becomes possible.

3. Experimental method

The goals of this research are to develop an experimental method for studying the oil sand lump ablation, study the effect of slurry velocity and concentration on the lump ablation and develop a model for lump ablation.

In order to determine the important factors that must be taken into account in designing and building an experimental apparatus, to identify an appropriate oil sand lump for completing the tests and to plan the actual experiments, a small and much less expensive apparatus, referred to here as the ″prototype apparatus″, was set up at the University of Alberta. A series of much less time-consuming experiments was conducted using the prototype apparatus. The findings from the prototype experimental runs were used in the design and fabrication of a much larger-scale apparatus which was located at the Saskatchewan Research Council PipeFlow Technology Centre™. The larger-scale apparatus, referred here as the SRC apparatus, was used to investigate the effects of slurry temperature, slurry velocity and concentration on lump ablation. Cylindrical artificial oil sand lumps, manufactured such that they had similar dry density to actual oil sand lumps, were used for the tests conducted with the SRC apparatus. The oil sand lumps were anchored inside a vertical section of a 104mm (diameter) pipe. Oil sand lump mass loss and drag force acting on the lump were measured using a series of wall-mounted strain gauges.

In this chapter, details about the experiments completed at the University of Alberta using the prototype apparatus are given. In addition, the findings from these tests, which were critical to planning, designing and executing the experiments using the SRC apparatus, are discussed. Details of the apparatus, procedures and material used for the SRC experiments are also described.

3.1. Prototype lump ablation apparatus and experiments

3.1.1. Objectives and overview

Preliminary experiments were conducted at the University of Alberta using an existing pipeline loop, which was modified specifically for these trials. Two different oil sand lumps and octadecane-sand lumps were tested using this apparatus. The main objectives of these experiments were to:

- Determine the specifications of the equipment that are appropriate for lump ablation experiments, including size, geometry, flow rates and residence times;
- Test and select a method for anchoring the oil sand lump within the pipeline loop
- Choose a reliable measurement method to track lump mass loss and to measure forces acting on the lump
- Find or produce oil sand lumps with standard characteristics. Samples had to be strong enough so that their ablation under different operating conditions could be tested; this included high velocity and high temperature flows.

In order to fulfill the objectives, experimental runs with three different samples were conducted at University of Alberta. Table 3.1 describes types of the samples used for the tests, the results of the experiments and the actions taken based on the results.

At the end of these experiments it was found that the best way to hold an oil sand lump in place is to locate it within a basket. An idealized oil sand lump with reproducible properties was identified and produced. Additionally, the idea of using strain gauges for measuring lump mass loss and forces acting on the lump was formed at the end of these experiments.

Table 3.1 Summary of experiments conducted using the prototype apparatus

Series #	Ablating sample	Results/Issues	Action(s)
1	Hand-formed oil sand lump	- No repeatability of the ablation rate data was observed - Issue can be with apparatus or samples	A new sample with known repeatability behavior must be identified
2	Octadecane (Parrafin wax) lump	- Repeatable ablation rate data was obtained - Issue was not with apparatus	A new oil sand-based sample with standard characteristic must be identified
3	Cylindrical artificial oil sand lump	- Repeatable ablation rate data were obtained - Method of holding the sample in place was identified	- These lumps were selected for the tests to be conducted with the SRC apparatus - Permanent apparatus must be a pipe loop with the ability to recirculate high slurry flow rates

3.1.2. Apparatus

Figure 3.1 provides a schematic of the apparatus tested at the University of Alberta. The storage tank was filled with water at the desired operating temperature. Water was pumped with a Moyno 1000 progressing cavity pump (Model No. A2FCDQ 3AAA) equipped with 7.5hp motor (BALDOR INDUSTRIAL MOTOR, Model No. M3710T) through the 26.5mm diameter pipeline and into the funnel-shaped test cell. A flexible 26.5mm hose was used to connect the carbon steel pipeline with the test cell. The test cell was placed inside a plastic barrel, which was used to collect water overflowing from the test cell.

Water was then recirculated to the storage tank using a sump pump (BURCAM, 1/4 HP All-purpose submersible utility pump, Model No. 300507P) placed at the bottom of the barrel. The flow rate and temperature of the water were measured with a Coriolis flow meter (Krohne, Model No. MFM4085K 300G+) installed downstream of the pump on the steel section of the loop.

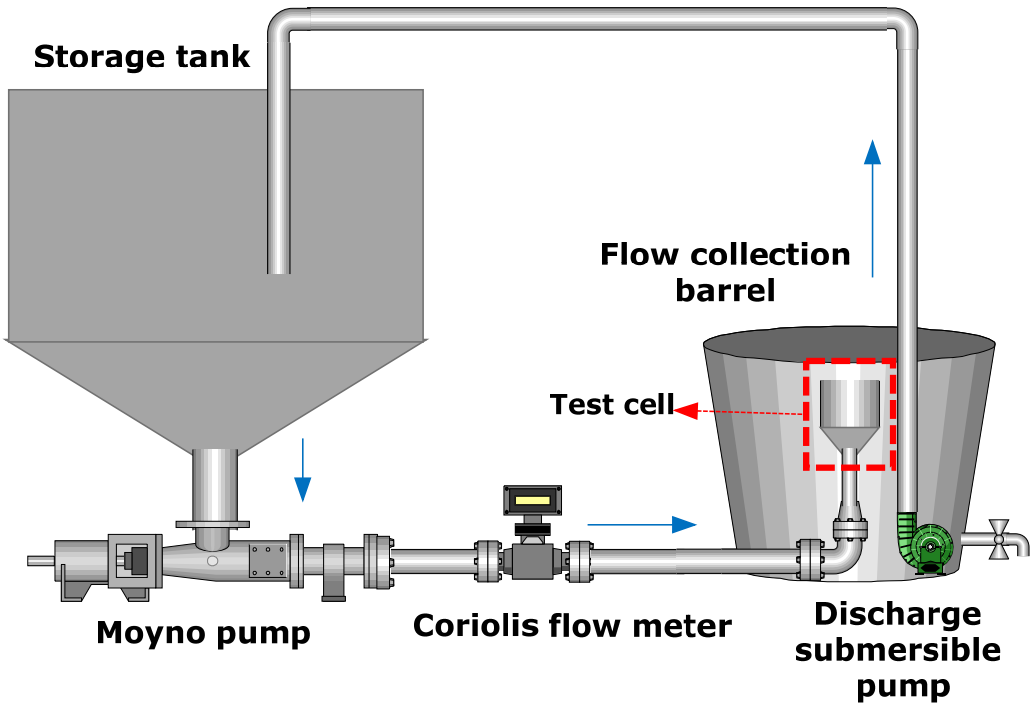

Figure 3.1 Schematic of University of Alberta prototype apparatus

A schematic illustration of the test cell itself is shown here as Figure 3.2. The funnel-shaped test cell was made from steel and consisted of a conical bottom section and a cylindrical top part. The diameter of the cone varied from 26mm to 152.4mm and its total height was about 200mm. The height of cylindrical section was 154mm. The diameter of the cone was determined so that the upward water velocity at each point balances the calculated terminal velocity of the lump at different stages of ablation. This was done to ensure that the samples remained suspended within the cone throughout the entire ablation process. On the other hand, the tall cylindrical part of the cell was designed for the cases where the samples were heavy and their suspension inside the cell was impossible; in these

cases, the sample was placed in a basket in horizontal orientation and was held within the cylindrical section of the test cell. The basket, hand-made from 1mm metal wire, was tied to a support stand positioned on a table beside the barrel. For these tests, the conical section of the cell was filled with ring packing to smooth the flow and facilitate a more uniform flow distribution upstream of the anchored sample. An impingement plate and a screen mesh were also implemented to help the flow distribute evenly within the funnel-shaped test cell, especially for the tests conducted without the ring packing.

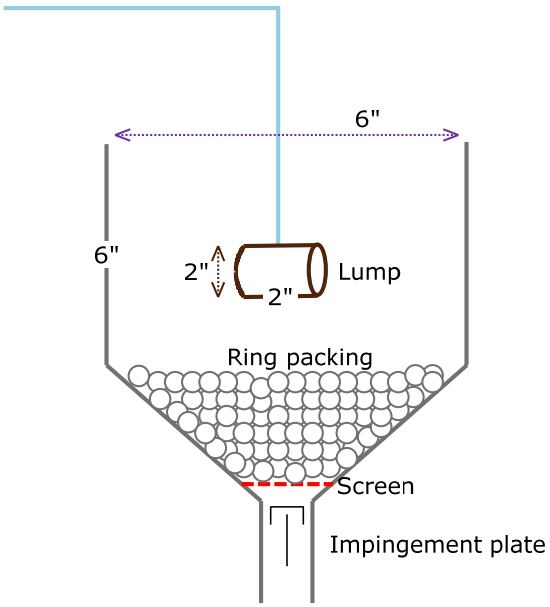

Figure 3.2 Schematic of test cell

3.1.3. Materials

1) Hand-formed oil sand lumps

Homogenized oil sand ore, used for making spherical oil sand lumps, was supplied by Syncrude Canada Ltd. Table 3.2 shows the characteristics of the oil sand ore. To make 9 or 19g lumps, ore was first weighed and then rounded by

hand until a sphere was formed. The diameter of each lump was either 19mm (9g) or 25.4mm (19g).

Table 3.2 The properties of homogenized oil sand ore supplied by Syncrude Canada Ltd.

Oil sands specifying code	MA(09-01-29)
Bitumen (wt%)	8.5
Water (wt%)	3.2
Solids (wt%)	88.2
Fraction of total solids <44μm	39%
d_{50} (μm)	79

2) Octadecane (Paraffin wax) lumps

Law and Masliyah (1987) used cylindrical rods of octadecane-solids for their ablation tests. Here, a similar procedure was used to manufacture spherical octadecane-sand samples. A mixture of octadecane and sand was prepared by melting octadecane (purity: 99+% ACROS ORGANICS) and mixing it with 5% (vol.) of 0.090mm silica sand (Lane Mountain, Valley, Washington, USA). A (700mm×550mm×250mm) mould made from PVC was used for manufacturing the samples. The mould consisted of two rectangular prisms with a hemispherical hole (d = 25.4mm) in the center of each rectangular prism. The two parts of the mould were first tightened together using a pair of screws embedded on its two sides (refer to Figure 3.3); after the screws were tightened, the spherical mould was ready to be filled. About 14.5g of the hot mixture was then poured into the mould using a small diameter hole at the top of the mould. A small plastic lid was used to seal the small hole. The mould assembly was then transferred to the liquid nitrogen bath for instant freezing. It took about 30-60s for the mould to freeze; after this time, the PVC mould was disassembled.

It was necessary to freeze the octadecane-sand lump very rapidly using the liquid nitrogen to avoid settling of the sand particles inside the mould. In one set of tests, the sample was frozen more slowly in a freezer, and the bottom half of the sphere was darker than the upper half, indicating that sand particles had settled before the lump was frozen. The settling was noticeable because the sand particles were slightly darker than paraffin wax. Photographs of the PVC mould are shown in Figure 3.3. Images of a set of paraffin-sand spheres (before and after ablation) are illustrated in Figure 3.4.

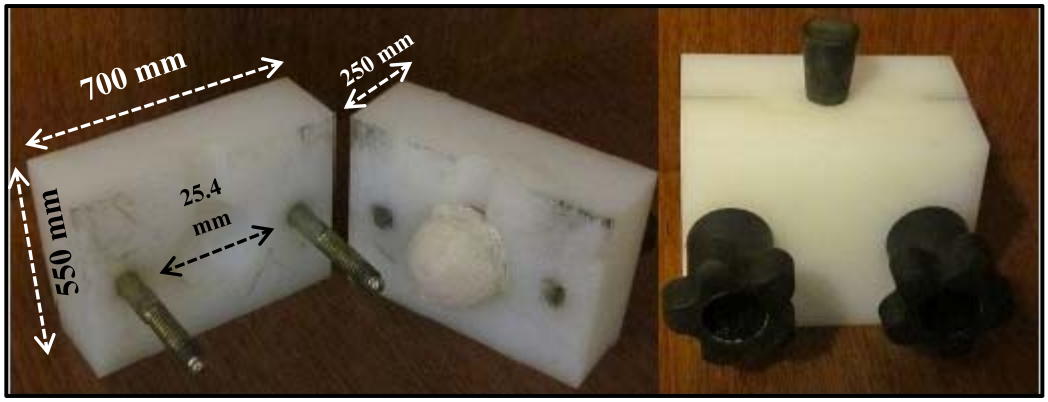

Figure 3.3 PVC mould used for producing 25.4mm octadecane-sand spherical samples

Figure 3.4 Octadecane-sand lumps (before and after ablation)

3) Artificial oil sand lumps

Artificial oil sand lumps were manufactured based on the criterion that they must have a similar dry density and consistent material strength as actual oil sand lumps (Chalaturnyk, 2009) using a time-consuming, labour-intensive, and difficult method developed by Scott et al. (2001).

In general, the steps involved in the manufacturing of the artificial oil sand lumps are (Scott et al., 2001):

1) Saturation of sand with water
2) Sand densification
3) Mould assembling
4) Bitumen injection
5) Immediate freezing
6) Mould disassembling

A detailed description of the aforementioned steps for manufacturing the artificial oil sand lumps is given in Appendix 2.

Bitumen and sand from oil sand tailings are the raw materials needed to manufacture the artificial oil sand lumps. Depending on the type of bitumen and particle size distribution of the sand used to manufacture the lump, the characteristics of the lumps may differ. If tailings sand is used, lumps are similar to actual oil sand lumps. Bitumen that is similar in properties (e.g. composition, density and viscosity) to the bitumen found in actual oil sand is difficult to obtain so different types of bitumen were tested. Three different bitumen supplies were provided by Syncrude Ltd. for manufacturing the oil sand lumps. Two of the bitumen supplies were atmospheric topped bitumen and one was vacuum topped bitumen. It was found that the vacuum topped bitumen was highly viscous and therefore impossible to be used for manufacturing the oil sand lumps. Although the atmospheric topped bitumen samples were supplied by the same company and were from the same production line, their viscosities were different, as shown in Table 3.3. Bitumen viscosity was measured with a HAAKE RS150 (RheoStress RS150) viscometer. The viscometer operating procedure is presented in Appendix 3.

Table 3.3 Viscosity of Atmospheric Topped Bitumen (ATB)

	Viscosity (Pa.s)		
Bitumen	**40°C**	**60°C**	**80°C**
ATB-1	63	5.3	1.1
ATB-2	86	8.6	1.6

The viscosity of the two samples can be correlated as a function of temperature. Figure 3.5 shows the data and trendline plotted for each bitumen supply. The correlations obtained from the measured viscosities are:

ATB-1: $$\boldsymbol{Ln(\mu_B) = 127.69 \left(\frac{1}{T}\right)^{0.662}} \quad (3.1)$$

ATB-2: $$\boldsymbol{Ln(\mu_B) = 111.96 \left(\frac{1}{T}\right)^{0.62}} \quad (3.2)$$

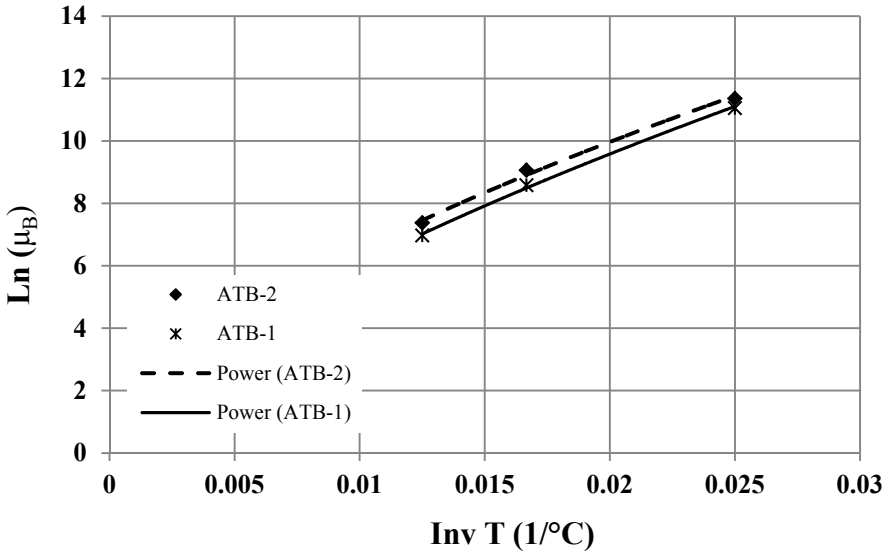

Figure 3.5 Viscosity of Atmospheric Topped Bitumen: ATB-1 and ATB-2

Both (ATB-1) and (ATB-2) supplies were used for manufacturing oil sand lumps.

The particle size distribution (PSD) of washed Syncrude tailings sand, appropriate for lump manufacturing is given as Figure 3.6. Tailings sand was washed before use to remove the fines; fines will fill out the pores and prevent bitumen to fully disperse through the stack of sand.

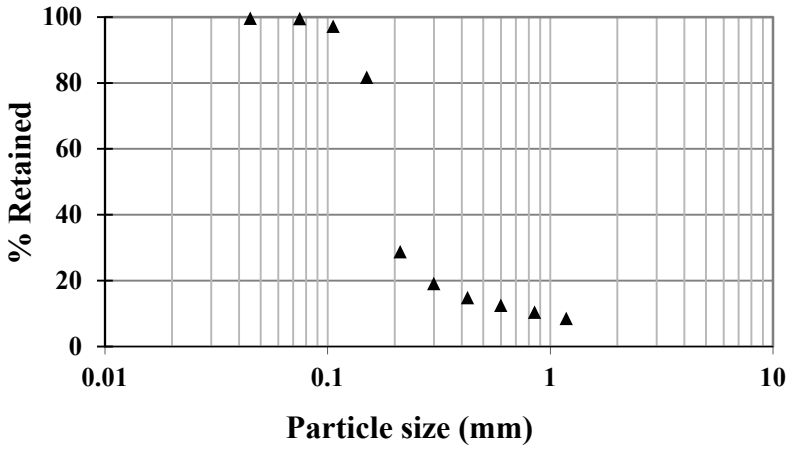

Figure 3.6 Particle size distribution- Syncrude tailings sand

For Syncrude tailings sand, the d_{50} was about 0.180mm with C_{max} = 0.61. The method of measuring C_{max} is given in Appendix 4. A number of oil sand lumps were manufactured using Syncrude tailings sand and because of shortage of supply of the actual tailings sand, some oil sand lumps were produced using a mixture of two different commercially-available sands. The mixed sand called "Artificial Tailings Sand" (AT sand) had the same PSD as Syncrude tailings sand but C_{max} = 0.54.

The "AT sand" was prepared using the following procedure:

- Lane Mountain sand (LM# 70 (d_{50} = 0.190mm); Lane Mountain, Valley, Washington, USA) and Granusil Silica Filler (Sil7; GHP Systems Inc., USA) were screened and divided into different size ranges.
- Based on the PSD of the actual tailing sand, the appropriate amount of each size was weighed and mixed.

It was found that the commercially-available sand contained only small amounts of fine particles (< 44 microns) so they did not require pre-washing. The PSD of the LM#70 Lane Mountain sand and Sil 7 industrial quartz are presented in Figure 3.7.

Two different artificial oil sand lumps were manufactured for the current study; one was made from artificial tailings sand and ATB-2 (Type A), and the other was made from the actual tailings sand and ATB-1 (Type B).

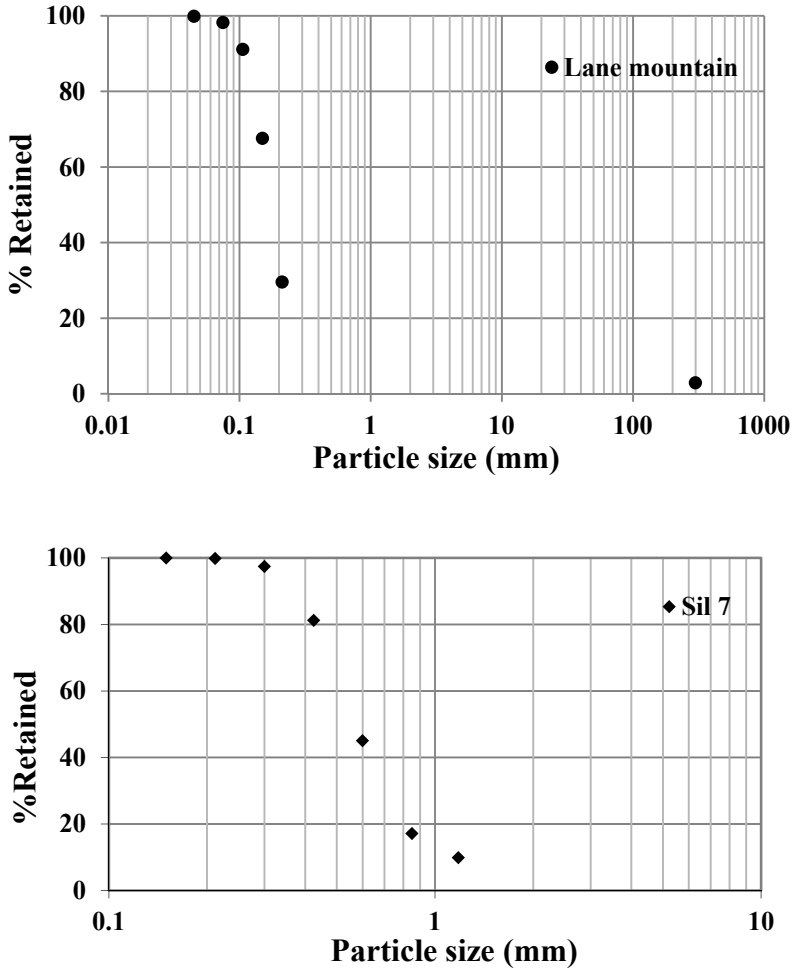

Figure 3.7 Sand particle size distribution: LM#70 Lane Mountain and Sil 7 industrial quartz

Lumps (m_0 = 200g, d = 50.8mm, L = 50.8mm) were prepared in an aluminum split mould (ID = 50.8mm L = 50.8mm). The amount of sand used for each sample was calculated based on the desired porosity of the lump. Porosity of the Type B lumps was equal to 36% so the amount of sand was determined from the following calculations:

$$\forall_t = \frac{\pi}{4} \times 0.0508^2 \times 0.0508 = 0.000103 \text{ m}^3$$

$$\forall_{sand} = 0.000103 \times (1 - 0.36) = 65.92 \times 10^{-6} \text{ m}^3$$

$$m_{sand} = 2650 \times 65.92 \times 10^{-6} = 0.175 \text{ kg}$$

The amount of sand used for Type A lump was about 0.158kg which results in porosity equal to 42%. The mass of sand in this case was found experimentally; when about 0.175kg sand was used, injection of bitumen into the sand bed became impossible, resulting in incomplete injection and failure of the lump manufacturing process. The amount of sand was decreased to allow for easier injection of the bitumen into the sand bed. The average amounts of bitumen and water in Type B samples were 39 and 5.5g, respectively; and about 45g and 12.9g for Type A samples.

3.1.4. Procedures

Ablation of three different lump types (19mm and 25.4mm hand-formed spherical oil sand lumps, 25.4mm spherical octadecane (paraffin wax)-sand samples and idealized artificial oil sand lumps were tested. A summary of the experimental conditions for the three series of experiments is presented in Table 3.4.

The use of the prototype apparatus was limited in the following ways:

- It was not fitted with a temperature control/ heat exchanger system, thus temperature changed ±5°C during the runs;

- The recirculation system operated only with water because the sump pump was not able to pump slurries; also, the flow collection barrel was not equipped with a mixer.

Table 3.4 Experimental conditions used for prototype experiments

Series #	Sample	Flow rate (L/s)	Temperature range (°C)
1	Hand-formed oil sand lump	0.7	21-24
2	Spherical octadecane-sand lump	0.55	29-30
3	Cylindrical artificial oil sand lump	0.7 and 1.1	21-24

Experimental Series #1 and 2:

The procedure for completing experiments with hand-formed spherical oil sand lump and octadecane (paraffin wax)-sand sample was:

1) Fill the storage tank with water until it contains about 2/3 of its total volume. The water temperature is controlled by measuring the tank contents and adjusting the flow rates of hot and cold water into the tank as required.
2) Start the pump and adjust the flow rate to the desired value by simultaneous increasing the pump speed and checking the flow rate on the flow meter. Check the water temperature using the Coriolis flow meter; if required, add hot or cold water to adjust the temperature. Check the water temperature before each run and adjust the temperature if needed.
3) Wait one minute for fully developed, steady flow to occur through the pipeline and the test cell. Start the sump pump to recirculate the water collected inside the barrel.

4) Weigh the sample using a top-loading balance (Sartorius, Model No. TE6101, 0.1g accuracy).
5) Release the sample within the test cell and record the time.
6) At the desired time, remove the sample from the test cell, weigh it and put it back. Continue to repeat this step until 90-95% of the sample is ablated (this number was chosen according to Masliyah (2008)). Record the time of ablation versus mass of the sample. Make sure to wear latex gloves at all times and cover the scale's weighing surface with aluminum-paper wrap to prevent excessive sticking of material to the surface.

Experimental Series #3:

The procedure for conducting Series # 3 is:

1) Repeat the first three steps listed above, for Series #1 and 2.
2) Weigh the oil sand lump and record the mass.
3) Place the oil sand lump in the basket and weigh; record the mass again.
4) Repeat steps 5 and 6, mentioned above; use basket to remove the sample from the cell to measure the weight.

3.1.5. Findings

Prototype experiments were completed in three series using three different samples. For the first sets of experiments, hand-formed spherical oil sand lumps were tested. The second (using octadecane-sand spheres) and third (using artificial oil sand lump) phases were planned with the intention of resolving the problems encountered during the first set of experiments. A lack of reproducibility of the data and rapid ablation of the spherical oil sand lumps were the two critical issues encountered with the first two samples.

For each run, the fraction digested was plotted against time of ablation. The fraction of the lump that was digested/ ablated was calculated using:

$$\textbf{Fraction Digested} = \left[\mathbf{1} - \frac{\boldsymbol{m_i}}{\boldsymbol{m_0}}\right] \qquad (3.3)$$

where m_0 and m_i represent lump initial mass and lump mass at time i, respectively. Before starting the actual experiments, ablation of each sample was tested twice to obtain an idea of the approximate time to complete ablation for that sample. The time intervals for mass measurement were then determined based on the time required for complete ablation; at least three data points were required to accurately plot the fraction digested versus time for each sample. In order to examine the reproducibility of the experimental runs, each run was repeated more than twice.

At the end of the prototype experiments, it was found that experiments conducted with the artificial oil sand lumps were reproducible and these lumps were strong enough to be tested in vigorous experimental environment. The results of each series of preliminary experiments are given in this section.

1) Spherical oil sand lumps

Hand-formed spheres (25.4mm and 19mm in diameter) were tested using the prototype set up. The results of these tests are presented in Figures 3.8 and 3.9. In these figures the fraction digested, calculated using Equation 3.3, is plotted against time of ablation for Q = 0.7L/s and T = 21-24°C. With the purpose of examining the repeatability of the tests, each experimental run was repeated five times; each set of data is shown as a different data series. The raw data are presented in Appendix 5.

From the results of these tests it is concluded that:

- The repeatability of the tests was unsatisfactory since the time to reach complete ablation could not be reproduced.

- Ablation rate was relatively high even at very low flow rates, indicating that it would be nearly impossible to study ablation of these samples at higher slurry temperatures and velocities.
- The method of handling the lumps for weight measurement was impractical. A significant amount of oil sand adhered to the gloves and to the bench top balance during the sample mass measurement step, causing significant errors and uncertainty in fractional mass loss data.

Based only on the results of the ablation tests conducted with the spherical (hand-formed) oil sand lumps and the prototype apparatus, it was not possible to diagnose the source(s) of variability. However, it seemed that two possible causes could be (i) that the oil sand lumps do not have similar properties and (ii) that there is a systematic problem with the prototype apparatus; specifically, that measurable conditions are identical but some unmeasured parameters are varying. An example of the latter could be the development of the flow inside the test cell. In order to investigate this further, a set of experiments was conducted using lumps comprised of octadecane and sand (Series #2). Cylindrical rods of octadecane-solids were used in the study of Law and Masliyah (1987) and were proven to yield highly reproducible results. The ablation results obtained with these samples and prototype apparatus are described in the following section.

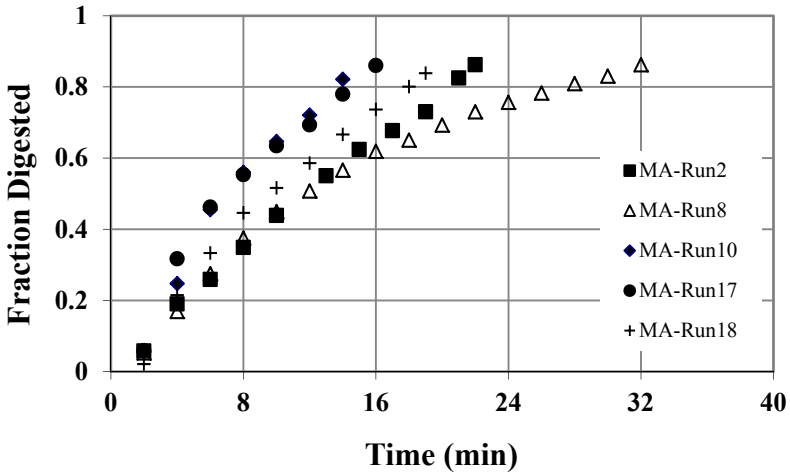

Figure 3.8 Ablation of 25.4mm spherical lumps: Q=0.7L/s; T≈ 21-24°C; T_{0L}≈21°C

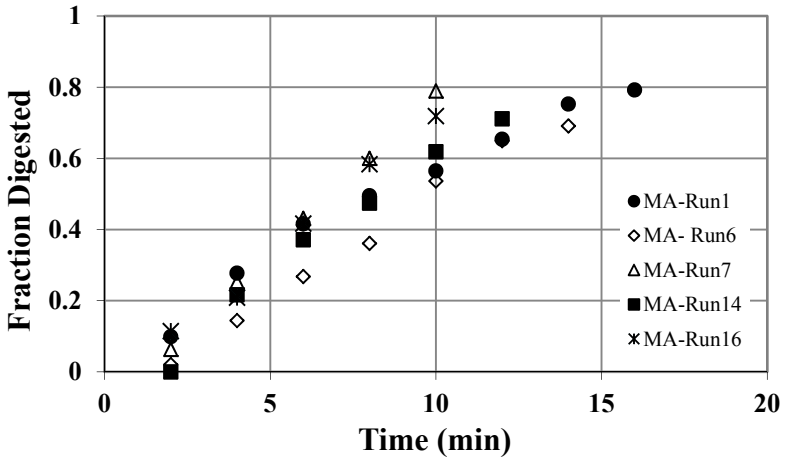

Figure 3.9 Ablation of 19mm spherical lump: Q=0.7L/s; T≈ 21-24°C; T_{0L}≈21°C

2) Spherical octadecane (paraffin wax)-sand lumps

In order to examine whether the problem of non-repeatability, observed in Series #1, was because of issues with the prototype set up, the ablation of a new type of lump using the same apparatus was tested. The flow rate of water was adjusted to 0.55L/s and the test temperature changed from 29 to 30°C for these tests. Ablation of the three identical octadecane-sand samples, stored at room temperature, was examined. The fraction digested, calculated using Equation 3.3, is plotted versus time of ablation for the three runs and is given as Figure 3.10. The raw data are presented in Appendix 5.

Because of the rapid ablation of these lumps, the tests had to be completed at low flow rates. From the results of these tests it was concluded that:

- The prototype set-up functioned well; meaning that flow was distributed uniformly within the test cell.

- Lack of repeatability of the data could be attributed to the inconsistent/uncontrolled characteristics of the hand-formed oil sand lumps.

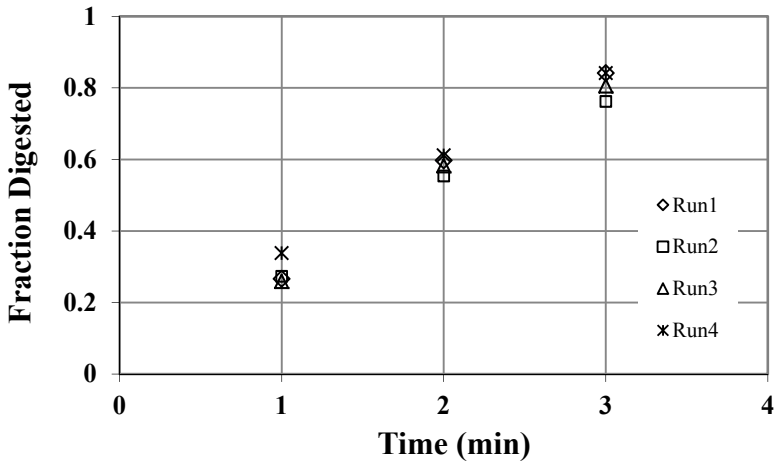

Figure 3.10 Ablation of 25.4mm octadecane-sand lumps: Q=0.55 L/s; T≈ 21-24°C; T_{0L}≈21°C

3) Artificial oil sand lumps

The ablation of artificial oil sand lumps was also tested using the prototype apparatus. In order to investigate the repeatability of the tests, identical runs were repeated three times. Figure 3.11 displays a plot of fraction ablated against time of ablation for the artificial oil sand lumps. These data were collected at Q = 1.1L/s, and water temperature decreased from 24 to 21°C during these tests. Fraction digested was calculated using Equation 3.3. It can be understood from this figure that the ablation of the three artificial oil sand lumps occurs with the same rate; meaning that using the artificial oil sand lump for ablation tests results in reproducible data.

In order to test the effect of water flow rate on the ablation of the artificial oil sand lumps, another set of ablation tests was conducted at a lower flow rate (Q = 0.7L/s) and similar temperature range. The fraction ablated is plotted in Figure 3.12 as a function of time for the two different flow rates. This figure shows that

an increase of water flow rate enhances the oil sand lump ablation. Raw data are given in Appendix 5.

Additionally, a method for anchoring the oil sand lump in place was determined. Artificial oil sand lumps (200g) were much heavier than the other two samples so suspending them within the test cell required very high water velocities that were not achievable with the prototype apparatus. Many different anchoring methods were tested and many of these tests were failures. For example, a lump was tied with string (cotton or plastic) and suspended in the tests cell. In these cases, the lump was always cut all the way through along the position, where the string was located, causing the two pieces of lump to drop down into the test cell. This occurred on numerous occasions and forced the premature end of each ablation test. It was found that the best way to hold the lump in place was using a basket to anchor it within the test cell.

Based on the ablation tests conducted with the artificial oil sand lumps and the prototype apparatus, it was concluded that:

- Acceptable repeatability can be achieved using artificial oil sand lumps;
- Ablation of the artificial oil sand lumps is slow enough to enable ablation testing under more severe operating conditions;
- The ablation of the cylindrical lump seems to be highly dependent on the water flow rate (Figure 3.12); more investigation is necessary to better understand the effect of velocity on the oil sand lump ablation;
- The time that oil sand lump begins losing mass does not coincide with the start of experiment, and depends (at least) on the water velocity, as shown in Figure 3.12;
- The use of a basket to hold the lump allows one to remove the lump from the test cell, weigh it and return it to the test cell without introducing error to the mass loss measurements through incidental handling of the lump.

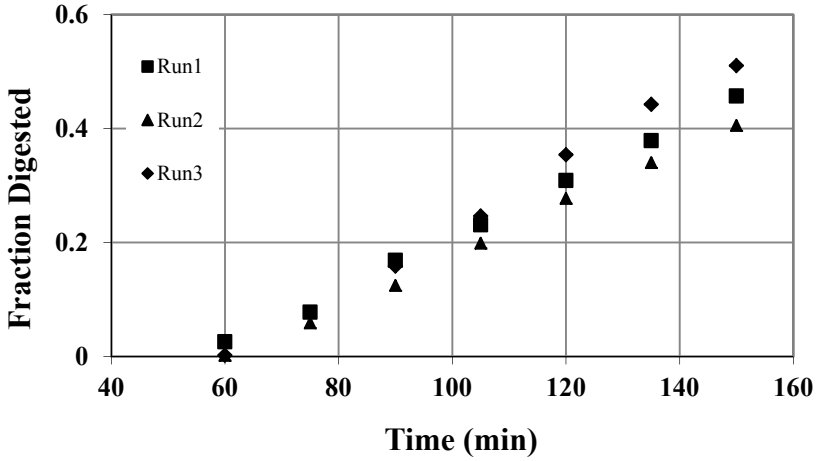

Figure 3.11 Ablation of artificial oil sand lumps using prototype apparatus: Q=1.1L/s; T≈ 21-24°C; T_{0L}≈-20°C

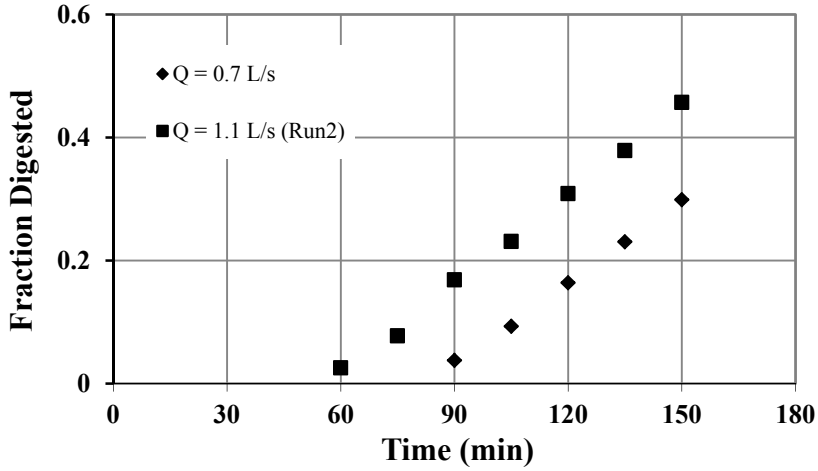

Figure 3.12 Effect of water flow rate on ablation of artificial oil sand lump using prototype apparatus: T≈ 21-24°C; T_{0L}≈-20°C

3.1.6. Lessons learned

Findings from the experiments conducted at University of Alberta using the prototype apparatus can be summarized as follows:

- Artificial oil sand lumps are appropriate for conducting ablation experiments because they provide satisfactory reproducibility of the tests. They are also strong enough to provide the capability of completing experiments at high velocities, concentrations and temperatures.
- Attempting to capture the lump followed by handling it for mass loss measurements introduces an unacceptably large experimental error. This can be eliminated by placing the sample in a large mesh basket for ablation tests.
- Based on the limited number of experiments conducted using artificial oil sand lumps, velocity appears to have a significant effect on the lump ablation rate.
- In order to conduct the experiments with water and slurry at high velocities, a new apparatus must be designed. The new set-up should be designed so as to pump and recirculate volumes of water or slurry.

A pipeline loop with a storage tank provides the capability of recirculating slurry and water. However, when a pipeline loop is used, the oil sand lump should be anchored inside the pipe meaning that removal for mass loss measurements would be difficult. A device that enables the operator to remotely measure the mass must be designed. Strain gauges mounted on the outside of the pipe wall can be used for mass and drag force measurements. Based on these findings, a pipeline loop was designed and built at Saskatchewan Research Council Pipe Flow Technology Centre™. Details about this apparatus and the subsequent experimental program are given in the following pages.

3.2. SRC lump ablation test loop

3.2.1. Apparatus

The schematic of the SRC apparatus is presented as Figure 3.13. A photograph of the apparatus is given as Figure 3.14. The pipeline loop was constructed from carbon steel pipe with 104mm internal diameter. The storage tank consisted of a cylindrical section (D = 1816mm, L = 1829mm) and a frustum cone section (L = 813mm). The total volume was 5.5m^3. The tank was loaded to the height of 1340mm (total volume 2.2m^3) for the lump ablation experiments. A mixer (Cleveland Eastern, model number unknown) with a 40hp motor, controlled by a Square D Variable Frequency Drive (model VSD57VD46S66) was used to mix the slurry in the tank.

Flow was produced by a Warman 6/4AH centrifugal pump, which was powered by a 60hp (575volts, 57.8AMPS) motor. The motor was connected to a 60hp variable frequency drive (Relcon, Model AFR 7060 ACT) which provided the ability to adjust pump speed, thus allowing for operation of the loop at a range of mixture velocities.

At the discharge of the pump, a 13mm discharge pipe was embedded for sampling. The length of the vertical section of the pipe between the Tee and basket containing the oil sand lump was 40D to ensure that flow was fully developed at that point. A pipe over pipe heat exchanger section, 3m in length, was built on the vertical section. A separate flow system containing a mixture of ethylene glycol and water was circulated through the annulus of the heat exchanger for temperature control. The central boiler and chiller of the SRC Pipe Flow Centre were used to heat and cool the glycol mixture. A flow control valve (Belimo 5, 20Nm, 24 VAC/AC) looped with the temperature probe, was used for temperature control.

The oil sand lump was placed in a basket that was anchored within the strain gauged spool. The strain gauged spool was equipped with four foil strain gauges,

which provided the on-line force measurements. The gauged spool is discussed in greater detail in the following pages. The water or slurry flow produced in the loop passed by the strain-gauged basket apparatus in the vertical flow section of the loop and then discharged into the storage tank through a larger pipe (D=254mm) whose other end was located under the liquid level in the tank.

A resistance temperature detector (RTD) probe (Aircom Industries, model number unknown) is embedded downstream of the sampling line. Downstream of the temperature probe is a magnetic flow meter (Foxboro 4" Flow tube, Model No. 9304-S1BA-PHJ-GL). The temperature, flow rate and strain gauge data signals are sent to a computer to be recorded on a data acquisition system using Dasylab 10.0 software. For these lump ablation tests, unless otherwise cited, 60s averages were recorded. Data were automatically transferred to an Excel sheet to be saved and subsequently analyzed.

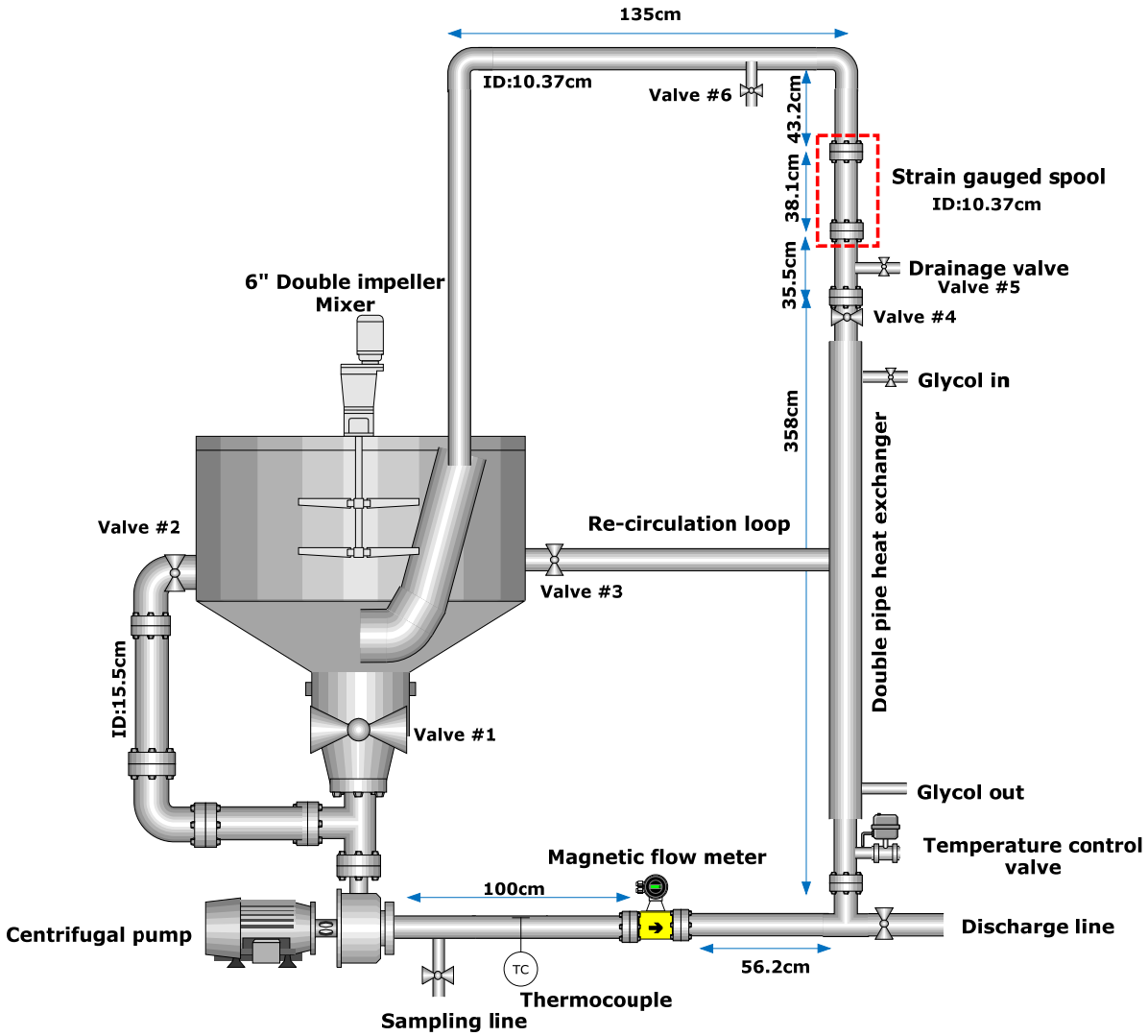

Figure 3.13 Schematic of SRC apparatus

Figure 3.14 Experimental apparatus at Saskatchewan Research Council Pipe Flow Technology Centre™

Strain gauged spool

Strain gauges were used for on-line measurement of the oil sand lump mass and to measure the forces to which the oil sand lump is exposed. The oil sand lump was placed in a basket that was anchored within the pipe. The spool in which the basket was anchored is referred to as the "strain gauged spool". The strain gauges were mounted on the outside of the spool on a narrow disk. A schematic illustration of the spool from two different views is presented as Figure 3.15. A photograph of the spool is given as Figure 3.16.

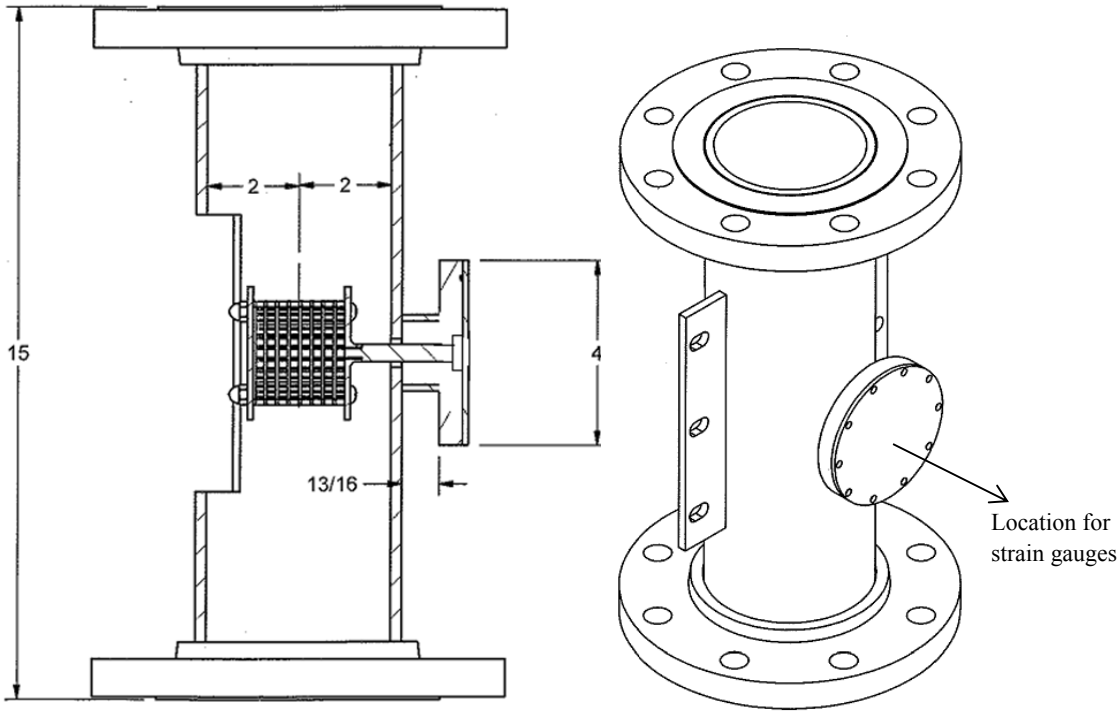

Figure 3.15 Schematic of strain gauged spool
(Dimensions in inches)

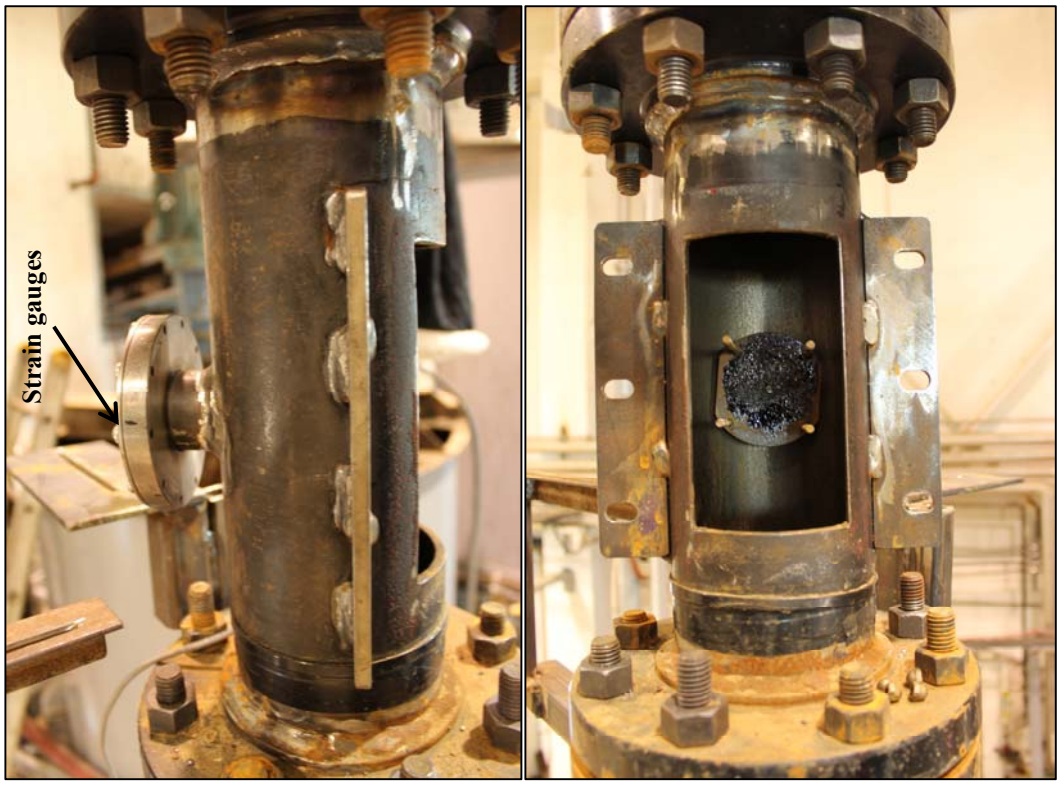

Figure 3.16 Strain gauged spool

According to Window and Holister (1982), strain gauges are used in a wide range of applications in civil and mechanical engineering measurements. Several different foil strain gauge designs exist. When they are mounted on a particular machine part or structural element, they adhere to the surface and deform with the part as it is loaded. The resulting change in the resistance of the gauge filament provides means for measuring the average axial strain over the region upon which the strain gauge is mounted. If the strain gauge is small in size, this measurement approximates the axial strain at a point on the body. The gauge factor, *f*, of a strain gauge is expressed mathematically as:

$$\boldsymbol{f} = \frac{\boldsymbol{dR_r/R_r}}{\boldsymbol{dL_R/L_R}} \qquad (3.4)$$

where R_r and L_R indicate, respectively, the initial resistance and initial length of the strain gauge filament, and dR_r and dL_R denote the small changes in resistance and length. Changes occur as the gauge is strained along with the surface to which it is bonded. The gauge factor is a measure of the relative resistance change for a given strain and is thus an index of the strain sensitivity of the gauge. The higher the gauge factor, the more sensitivity and the greater the electrical output for recording purposes. Performance of the strain gauge is absolutely dependent on its bond with the test part (Perry and Lissner, 1962; Window and Holister, 1982). In order to make accurate use of the strain gauges, small changes in the resistance of the strain gauge (dR_r) must be detected. Here, dR_r is measured using a Wheatstone bridge circuit, shown here as Figure 3.17.

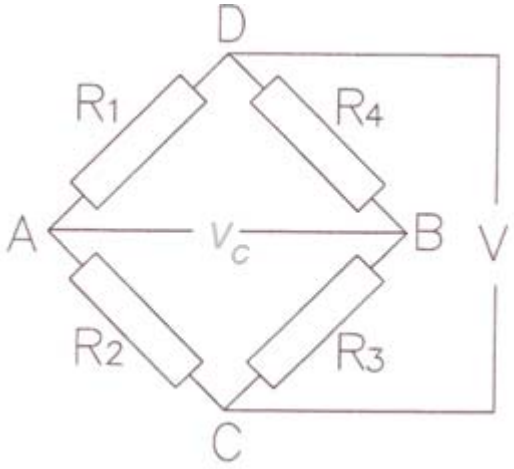

Figure 3.17 Wheatstone bridge circuit with input voltage V and output voltage v_c
(Perry and Lissner, 1962)

In practice, R_1 is a strain gauge, and depending on the instrumentation used, R_2, R_3 and R_4 may be additional strain gauges or may be resistances inside the strain indicator. Three basic types of configurations exist for Wheatstone bridge: quarter bridge, half bridge and full bridge (Perry and Lissner, 1962).

Based on Equation 3.5, bridge output voltage is related to the excitation voltage given to the bridge and to the change in resistance:

$$v_c = \left(\frac{dR_r}{R_r}\right) E \qquad (3.5)$$

The magnitude of the excitation voltage (*E*) applied to the bridge is very important, and it is difficult to find the appropriate excitation voltage. The excitation voltage needs to be enough to enable the user to measure the desired range of forces and yet small enough to prevent or minimize heating of the strain gauges. The appropriate excitation voltage is found through trial and error, starting from low excitation voltages and increasing until a slow, steady increase in the output voltage reading is observed.

The "voltage creep" continues until maximum voltage is reached (http://www.intertechnology.com/Vishay/pdfs/TechNotes_TechTips/TN-502.pdf). General purpose strain gauges (MICRO-MEASUREMENTS & SR-4®, EA-06-062AQ-350) were used in this study; specifications are given in Table 3.5.

Table 3.5 Specifications of strain gauges used in this study

Grid resistance (Ohms)	350 ± 0.15%
Gauge factor @ 24°C	2.115 + 0.5%
TC of gauge factor, %/100°C	+1.3 ± 0.2%

In order to achieve temperature compensation for the strain gauge measurements and to create a high signal-to-noise ratio, a full bridge configuration was chosen for this study. The maximum excitation voltage for the current system was found to be about 2.1V, which was supplied with a Vishay 2100 amplifier (Intertechnology Inc.). The method of installing strain gauges is fully explained in Appendix 1.

An oil sand lump was placed in a basket that was attached to a circular plate, referred to here as the membrane. Strain gauges were installed on the outside of the membrane. The baskets used for the ablation experiments are described in detail in the following pages. It is very important to install the strain gauges on a clean and chemical-free surface. The gap between the strain gauges, determined based on the recommendations of the manufacturer, must be accurate. Soldering

must be done very carefully because any disconnections create errors and noise in the measurements. Images of a proper strain gauge installation, i.e. clean surface, equal gap between gauges, and clean soldering are given as Figures 3.18 and 3.19.

The basket was anchored to the membrane using a rod/arm (D = 9.525mm, L = 50.8mm) with a threaded end. The stress caused by forces acting on the basket causes the deformation of the rod and that deforms the thin (δ = 1.587mm) steel plate (membrane). Use of a longer lever arm results in a larger reaction moment at the wall for a certain force on the basket (moment = force × distance). A larger reaction moment at the membrane results in larger deformation, which is then shown as higher voltage reading from the strain gauges. The membrane was constructed of high quality stainless steel (17-4PH) to prevent permanent deformation of the plate, which can occur if the basket/arm/plate system is exposed to very large forces during an experiment, e.g. high velocity slurry flow tests. The membrane was installed in a way that strain gauges were located perpendicular to the flow direction.

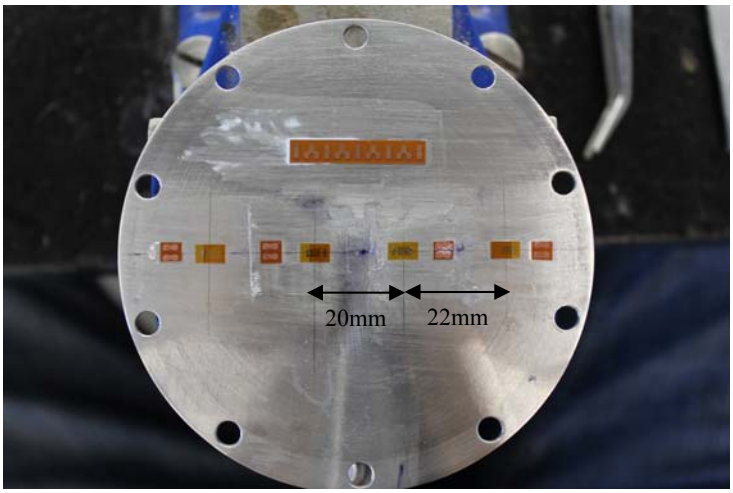

Figure 3.18 Four encapsulated strain gauges mounted on the membrane

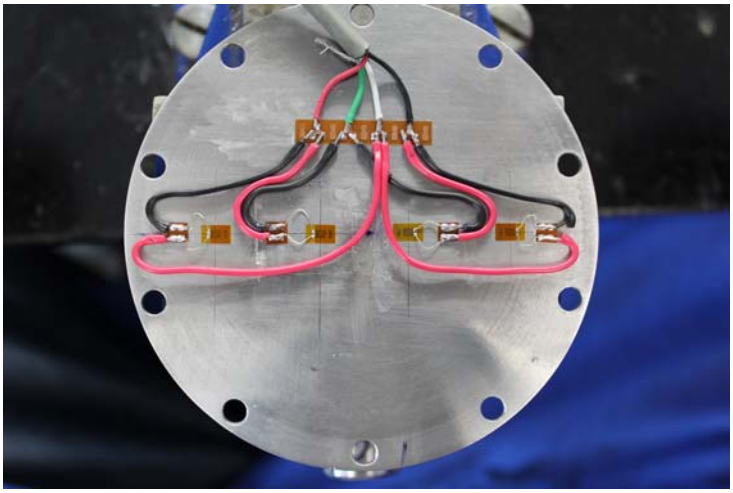

Figure 3.19 Soldered strain gauges on the membrane

Baskets

Baskets with two different mesh sizes were chosen for the purpose of anchoring the oil sand lumps in the center of the strain gauge spool. The mesh sizes were chosen based on the lump size expected in the final stages of ablation. In other words, the mesh openings must be small enough to hold the lump after it is 95% ablated. At a later stage of the experiments, it was decided to repeat some of the runs with a different basket to study the effect of basket mesh size and shape on the lump ablation rate. In order to ensure that the basket remained stable under high flow rates and severe flow conditions, two edge-rounded rectangular plates (73.29mm × 63.47mm, δ = 2.95mm) made from carbon steel were placed at the two ends of the baskets; the two ends were connected together using welded screws.

Most of the ablation experiments were completed with Basket#1 (25mm^2 square shape openings, δ_{wire} = 1.46mm) and a few runs were done with Basket#2 (20.83mm × 8.38mm diamond shape openings, δ_{wire} = 3.15mm). Images of the two baskets are given as Figure 3.20.

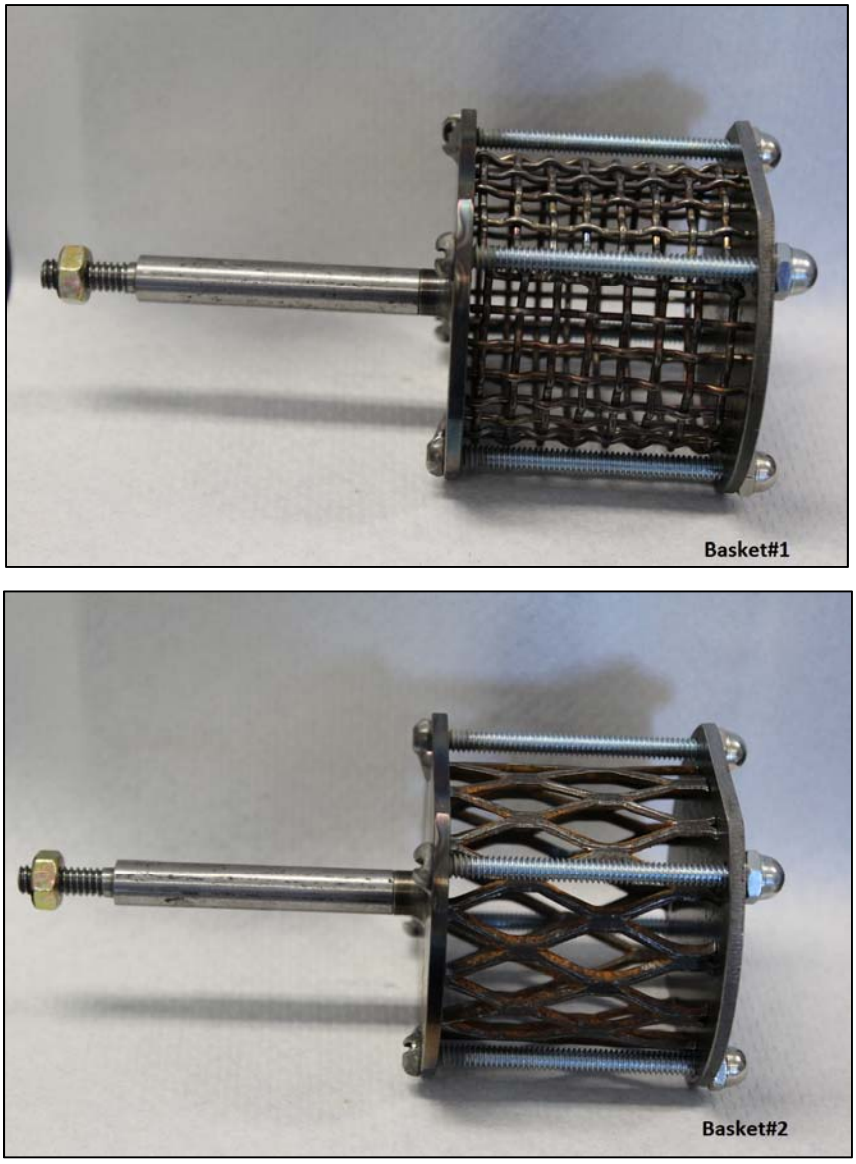

Figure 3.20 Baskets to hold oil sand lump during ablation: SRC apparatus

3.2.2. Materials

Artificial oil sand lumps

Materials used for manufacturing artificial oil sand lump were discussed in section 3.1.

Sand slurry

Industrial quartz (d_{50} = 0.190mm, Granusil Silica Fillers, GHP systems Inc., USA) was used for slurry preparation. This sand is commonly used at the SRC Pipe Flow Technology Centre to represent the sand component of oil sand (Gillies and McKibben, 2011; Schaan et al., 2007).

3.2.3. Experimental procedure

As mentioned in Chapter 2, the slip velocity of a large high-density particle in horizontal slurry flow is about 0.1V, where V is the slurry bulk velocity. Therefore, the slip velocity for large oil sand lumps flowing in the actual hydrotransport pipelines operating at V = 3-5.5 m/s (Schaan et al., 2007), is about 0.3-0.55m/s.

One way to increase the shear exposure on the lump is to increase the slip velocity of the lump simply by increasing the mixture bulk velocity. In the current study, the lump was stationary; thus the slip velocity was equal to the slurry velocity. It was also shown in Chapter 2 that increasing the slurry concentration enhances the pipe local shear stress inside the slurry pipelines, especially at low slurry velocities. In order to examine the effect of slurry concentration on lump ablation, experiments were completed at three different slurry concentrations. The highest concentration (30 vol%) most closely resembles the slurry concentration of the actual hydrotransport pipelines (Sanders et al., 2004). Ablation was examined at 45°C to evaluate the effect of "typical" operating temperatures on the ablation of oil sand lump. Ablation was also tested at 30°C, as industry sponsors have long indicated their desire to operate hydrotransport pipelines at lower temperatures. It is therefore important to understand the effect of slurry velocity and concentration

on lump ablation at low temperatures. Table 3.6 illustrates the operating conditions tested during the SRC experiments.

Table 3.6 Experimental conditions for SRC lump ablation experiments

Slurry temperature (°C)	30			45	
Slurry velocity (m/s)	1	1.5	2	2.5	3
Slurry sand conc'n (vol %)	0		15		30
Slurry sand size (d_{50}) (mm)	0.190				
Lump initial temperature (°C)	-8				

The total volume of the pipeline loop and the tank (filled to the level of 1340mm) was kept at 2.2m^3 for all tests. Since the density of sand is 2650 kg/m^3, 872.4kg sand was added to prepare slurry (C = 15%), and another 872.4kg was added to prepare slurry (C = 30%).

The experimental procedure can be summarized as follows:
(1) Start up the system, (2) Take drag force and mass loss data and (3) Shut down the system. Over the next few pages, each step is described in greater detail.

1) Start up the system

Working with sand slurry systems is complicated because if enough consideration is not put into the procedure, system plugging and subsequent emergency shutdown can occur very easily. A number of steps must be taken at the start up and shutdown of the system to avoid potential problems. Most importantly, enough water must be present in the system to prevent sudden introduction of large amounts of sand to the pump and pipes. Other important parameters in starting up this system are initial system temperature adjustment, measuring lump initial mass using strain gauges, placing the sample in the basket and assembling the gauged spool. The steps taken to start up the SRC apparatus can be summarized as follows:

- Ensure that enough water is loaded to the tank and Valves #1 and #2 (Figure 3.13) are closed.
- Turn on data acquisition system and open a new file.
- Start up the mixer and continue mixing for about 5min. It is better to gradually increase the speed, especially when the concentration is high. Maximum required speed depends on the concentration and volume of the slurry and must be determined experimentally. The optimal mixing speed occurs when the sand slurry in the tank is well-mixed while simultaneously avoiding the creation of a vortex, which occurs at higher mixer speeds and causes air to be entrained in the slurry.
- Open Valve #2 and start the pump. When pump speed is set such that the mixture velocity is 1m/s, open Valve #1 and close Valve #2 (this action prevents the pump from plugging). When running experiments with water, pump plugging is not expected to happen; therefore, Valve # 1 can remain open during the start-up. Adjust the pump speed to reach the desired velocity. For the purpose of heating/cooling of the slurry, V = 2.5 m/s is reasonable. While heating/cooling, make sure Valve #3 remains open and Valve #4 is closed.
- Open the valves that circulate the hot/cold glycol mixture through the pipe-over-pipe heat exchanger.
- Adjust the temperature controller to the desired temperature.
- While waiting for the system to reach the desired (specific) temperature, first adjust the strain gauge reading to zero using the knob on the amplifier box and record the reading (a value near zero is acceptable). Then tighten the empty basket in place and take another reading (a reading averaged over 10s is sufficient). This determines the mass of the empty basket. Disassemble the empty basket; ensure the strain gauge reading returns to the original value (zero).
- Retrieve the oil sand lump from freezer and place it inside the basket.
- Fix the basket in place within the gauged spool. This needs to be done via the window on the side of the spool.

- Take a reading of the strain gauge voltage to determine the initial mass of the lump.
- Tighten the 6 screws that hold the door of the window in place. To prevent leakage, a washer must seal the gap between the body of the spool and the door. Take another reading to ensure that closing the window and tightening the screws did not affect the strain readings. The lump installation procedure takes about 8-10min.

2) Drag force and lump mass measurements

Drag force is measured under flowing conditions, i.e. during the ablation experiments. However, to measure the lump mass, flow must be stopped or diverted from the gauged spool and water/slurry must be drained from the spool. If the spool is filled with water, the true lump mass cannot be measured. A number of valves are installed in the loop to provide the ability to make these specific measurements. The procedure for lump mass measurement can be summarized as follows:

- Open Valve # 4 and simultaneously close Valve #3.
- As soon as there is flow through the system and specifically through the strain gauged spool, record the time with a stopwatch and start collecting data via the acquisition system. These data are used to calculate the drag force.
- Collect the slurry velocity, temperature and strain gauge voltage with 60s averaged readings.
- For on-line measurement of lump mass, simultaneously close Valve #4 and open Valve #3: this diverts the flow from the gauged spool to the tank using the circulation loop. Depending on the operating condition, the time interval required for mass measurements varies between 5-20min.
- Before taking the strain gauge voltage, immediately open Valve #6 and drain the water/slurry inside the spool using Valve #5 (to accurately measure gravity force).

- Take a reading of the strain gauge voltage. This gives the mass of the lump at each time.
- Close Valves #5 and 6.
- Open Valve #4 and immediately close Valve #3. Resume the drag force measurements and the ablation experiment.
- Repeat these steps until the strain gauge reading, with no flow through the spool, approaches the reading for empty basket (indicates lump mass equal to zero). The criteria for complete ablation is taken to be the time when 90-100% oil sand lump is sheared away.
- To weigh the empty basket open Valve #3 and shut off Valve #4.
- Take another reading of the strain gauge voltage. This is to take into account the potential change in the zero reading that can occur because of noise or deformation of the membrane. If this reading differs from the reading taken initially with the empty basket, this difference should be considered for converting the strain gauge voltage to force. Details about calculations are given in the following sections.
- Save the Excel file on the computer.

Calibrating strain gauges

In order to convert the amplified strain gauge readings (in Volts) to force, the output voltage must be calibrated prior to the measurements. A schematic illustration of the calibration apparatus is given as Figure 3.21. Depending on the direction of the force exposed, negative or positive voltages might be detected. Therefore, strain gauges were calibrated for both positive and negative slopes; this was done by turning the spool upside down.

The procedure for calibrating the strain gauges is as follows:

- Bolt a carbon steel rod (D = 9.525mm, L = 76.2mm) to the membrane.
- Hang a heavy duty wire from the rod. Fasten the wire to the rod so that it stays at the centre of the spool.

- Zero the strain gauge reading and record it.
- Hang pre-weighed weights on the rod one by one and record the reading. When heavy weights are needed use a bucket to hold the weights. Make sure to take the bucket's weight into account.
- Continue this step until the output voltage reaches the excitation voltage. This indicates the maximum voltage/ force that can be measured with the strain gauges.
- Remove the weights one by one and record the output voltage after each mass reduction. If the reading deviates from the original value of zero when no force is applied, steel deformation has occurred. In this case repeat all the steps for a lower maximum weight.
- Plot output voltage versus force (kg).

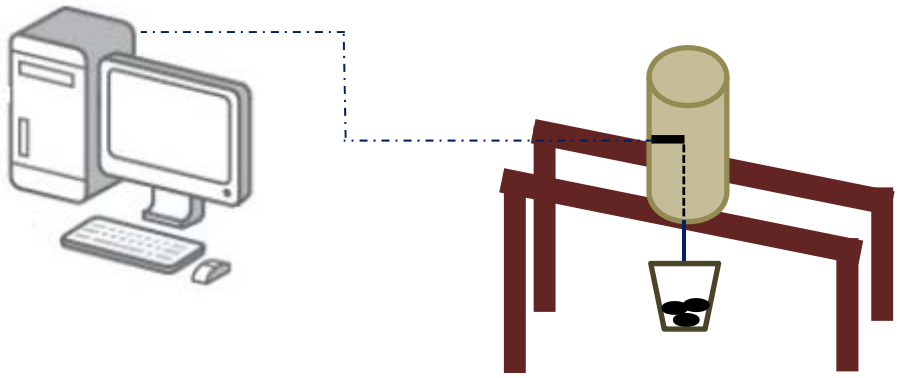

Figure 3.21 Schematic of spool set-up for calibration

In this study, calibration was conducted for both small and large forces. This was to ensure the accuracy of force measurements when small mass loss is detected. The current system was capable of measuring forces as large as 6kg or 59N. The graphs (shown in Appendix 6) show that strain gauge voltage changed linearly with force and their relation can be defined with the following correlations:

$$\boldsymbol{F(kg) = -3.1513\, v_c - 0.0038} \quad \text{(Negative voltage)} \quad (3.6)$$

$$\boldsymbol{F(kg) = 3.192\, v_c + 0.0136} \quad \text{(Positive voltage)} \quad (3.7)$$

Converting strain gauge readings to forces

Strain gauge readings, collected as averaged 60s intervals, were converted to drag force on the ablating lump. Recall that, the strain gauges were calibrated such that downward forces were considered negative and upward forces were positive. The drag force was calculated from the total force measured with strain gauges using the following equation:

$$\boldsymbol{F_D = F_{SG} + F_B} \qquad (3.8)$$

where, F_{SG} and F_B symbolize force measured with strain gauge and buoyancy force, respectively.

The procedure used to convert strain gauge readings to forces is shown below:

- Calculate difference in the zero detected by strain gauges from the desired value for zero (-0.0012 for negative reading and -0.0043 for positive reading. Refer to Equations 3.6 and 3.7).
- Add the value from previous step to the total voltage collected at each time.
- Convert the voltage to force using the calibration equations shown previously.
- Calculate lump mass at each step using Equation 3.6.
- Calculate lump and basket buoyancy using:

$$\boldsymbol{F_B\ (kg) = m_{basket}(1 - \rho_m/\rho_{steel}) + m_{lum}(1 - \rho_m/\rho_{lum})} \qquad (3.9)$$

- Use Equation 3.8 to calculate the total drag force acting on the oil sand lump.

Since lump mass was known at the beginning and end of each interval/step, for the moments between the two it can be calculated with either of these methods:

- Plot lump mass as a function of time and interpolate for mass at any time

- Use the average of initial and final lump mass for all the moments between them. Buoyancy force is normally considerably smaller than F_{SG}, thus the error resulting from this simplification is within the acceptable range.

3) Shut down the system

It is critical that a very specific and well-planned procedure is followed to shut down a slurry flow loop to ensure that plugging does not occur anywhere in the system. Plugging can occur extremely quickly. The steps in the procedure followed here are:

- Open Valve#2 and then close Valve #1.
- Shut down the mixer and wait for 2-5min while continuing to have flow through the loop and back into the mixer.
- Slowly decrease the pump speed to about 1m/s. Continue to operate the system at this low velocity for about 2min. This helps to wash sand particles from the loop.
- Turn off the pump and close the valves for the heating/cooling flow.

Carrier fluid viscosity measurements

Abrasion of sand particles of the slurry results in fines being generated (Traynis, 1970), and fine particles augment the viscosity of the carrier fluid. Therefore, samples of carrier fluid were collected daily using the sample port described earlier. The viscosity of the carrier fluid of each sample was measured. For these tests, it was found that the carrier fluid viscosity remained constant at 0.007Pa.s. Details of the carrier fluid viscosity measurements are given in Appendix 3.

Visualization measurements

In order to conduct the visualization tests, the strain gauged spool was first replaced with a spool of identical size but made from acrylic. The oil sand lump was placed in the basket and was mounted within the acrylic section using a

threaded rod that is tightened to the wall from outside of the spool. The oil sand lump ablation process was then recorded with a high speed camera (TroubleShooter HR Mono Maximum Memory) or a digital camera (Canon EOS 500D).

The procedure followed for the visualization tests is:

- Load fresh water to the system to ensure that water flowing past the system is not dirty or rusty.
- Start the pump and adjust the water temperature to the desired value, following a procedure similar to that used when the strain gauged spool is in place.
- Remove the strain gauged spool.
- Place the frozen oil sand lump inside the basket. It takes about 20 to 30min for one to remove the sample from freezer, place it within the spool and assemble it in place.
- Anchor the basket within the acrylic spool.
- Tighten the acrylic spool in the place in the loop.
- Start the flow following a similar start up procedure described earlier for water tests and record the ablation process.

3.2.4. Drag force measurement on non-ablating objects

Use of strain gauge technology enables one to measure the drag force acting on ablating and non-ablating objects. In order to develop a method of calculating drag force on a large solid object in slurry, a number of runs were conducted using non-ablating spheres and cylinders anchored alone within a basket. Details of the materials and procedures used for these tests are given in this section.

Materials

Size of the spheres and cylinder used for drag force measurements is given in Table 3.7.

Table 3.7 Solid objects tested at different slurry bulk velocity for assessing effect of basket

Cylinder	Diameter (mm) 50.8		Length (mm) 50.8	
Sphere diameter (mm)	50.8	44.9	35	27

The objects were anchored within the gauged spool by bolting a rod/arm (D = 9.53mm) to the membrane; the length of the arm changed according to the sample size (L = 55.56, 57.86, 63.5 and 67.47mm) to ensure sphere/cylinder was positioned at the centre of the spool.

Slurries that were prepared for ablation experiments were also used for these tests.

Procedures

The procedures of mounting the non-ablating objects within the loop, starting up and shutting down the system were the same as those followed for the ablation tests. The drag force measurement procedures were also similar to those described for the measurement of the drag force on oil sand lumps.

4. Experimental results and discussion

The effects of slurry velocity, concentration and temperature on oil sand lump ablation were investigated. Table 4.1 shows the operating conditions, determined using parameters given in Table 3.6, for each experimental run. The lump ablation experiments, done using the SRC apparatus, are divided into three different categories, in terms of slurry concentration. Sand with d_{50} = 0.190mm was used to prepare the slurries. At each slurry concentration, lump ablation over a range of slurry velocities and two operating temperatures was investigated. As mentioned in Chapter 3, the maximum force measurable with the current strain gauge system was 59N so the experimental conditions were determined such that the force measured with the strain gauge was always less than 59N. For example at 30% sand and V = 3m/s, the force was greater than 59N; thus, this test was eliminated. The other limiting factor was the strength of the artificial oil sand lump. For example, at V > 2m/s and T = 45°C, the lump ablated very rapidly and tracking the mass loss became impractical. Therefore, the range of experimental parameters tested was affected by this limitation. The conditions actually studied using the SRC test apparatus are summarized in Table 4.1. Artificial oil sand lumps (Type A) with identical size at T_{0L} = -8°C were used for all runs.

For each ablation test, artificial oil sand lump mass loss and the drag force acting on the ablating lump were measured as functions of time. The mass loss and drag force data were considered together to understand the effect of each operating parameter on lump ablation.

In this chapter, the results of visualization tests are given first, since the images taken of the oil sand lump during ablation enable one to better interpret the quantitative ablation data presented consequently. Prior to the start of the ablation test program, a number of steps were taken to validate and assess the measurement and experimental techniques used. Strain gauge measurements were validated by comparing (i) the weigh scale mass measurement with the strain

gauge measurement and (ii) the measured drag force on non-ablating objects with the calculated (predicted) drag force. One method for modelling the drag force on large objects in slurries was identified.

Table 4.1 Experimental runs: SRC apparatus

Slurry temperature (°C)	Slurry velocity (m/s)	Slurry sand concentration (vol %)		
		0	15	30
30	1	R-W1	R-15-1	R-30-1
	1.5	R-W2	R-15-2	R- 30-2
	2	R-W3	R- 15-3	R- 30-3
	2.5	R-W4	R-15-4	R-30-4
	3	R-W5	R-15-5	-----
45	1	R-W6	R-15-6	R-30-5
	1.5	R-W7	R-15-7	R-30-6
	2	R-W8	R-15-8	R-30-7

As discussed in the previous chapter, an oil sand lump was placed inside the basket during the ablation tests. The effect of the basket on drag force measurements was determined by comparing the measured drag force on an individual non-ablating object with the measured drag force on the same object placed inside the basket. Fluctuations of the strain gauge and flow meter measurements were analyzed and the measurement error for water and for slurries was determined. The effect of basket mesh size on ablation was investigated by repeating some of the experimental runs using Basket#2 and comparing the results with identical runs completed using Basket#1. Recall that the specifications of each basket are given in Chapter 3. The ablation results using Type A lumps were validated by repeating some of the tests using Type B lumps which were manufactured with different components. This was done to determine the effect of the lump components on the lump ablation rate and how the effect of slurry temperature and velocity changes when lump characteristics changes.

Repeatability of the results was examined by repeating the runs three times and comparing the results.

4.1. Visualization tests

Some might still question Masliyah's hypothesis on the mechanism of lump ablation in layers from the surface of the lump. In order to determine if an oil sand lump breaks into parts or ablates layer-by-layer, and to better analyze the results of the strain gauge measurements, a number of visualization tests were conducted using a clear, acrylic spool. The strain gauged spool was replaced by the visualization section for these experiments.

The visualization tests were conducted only with water at T = 30°C because:

- The sand slurry is opaque so it was impossible to see through the visualization section during tests involving slurries;
- At higher temperatures, visualization became more difficult due to condensation of water vapor on the wall of the acrylic section; and
- Ablation occurred very rapidly at slurry temperatures of T = 45°C and recording the ablation process became very difficult.

Images shown as Figure 4.1 were taken with a digital camera (Canon EOS 500D) during a Type B lump ablation test in water at V = 0.5m/s and T=30°C. These photographs show that after some time, the lump starts to ablate and its shape changes from cylindrical to approximately spherical. The visualization test was continued until the lump reached approximately 0-10% of its original size.

Since the process of assembling the visualization section took 20-30min, which was longer than that for the gauged spool (8-10min), ablation occurred more rapidly in the former case than the latter. After 20-30min, the entire lump reaches room temperature (refer to Chapter 5) and the ablation rate increases because thicker layers of the lump can be sheared off because overall the bitumen viscosity is much lower

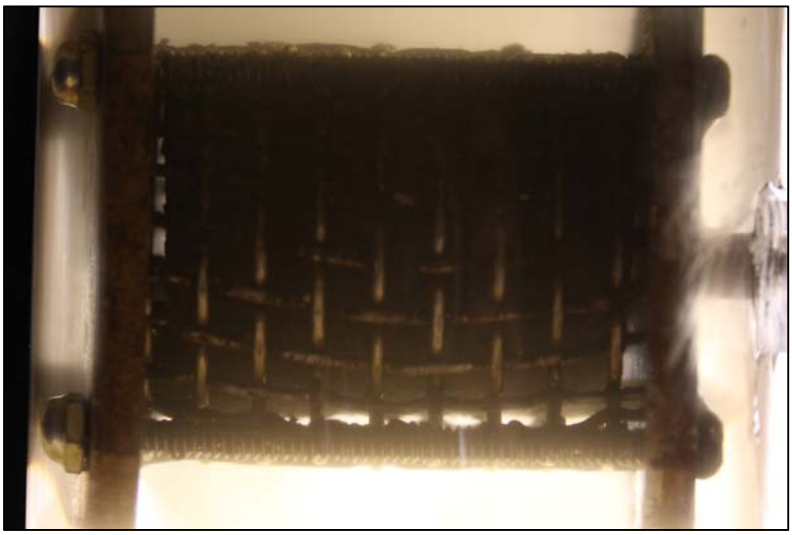

t = 1min

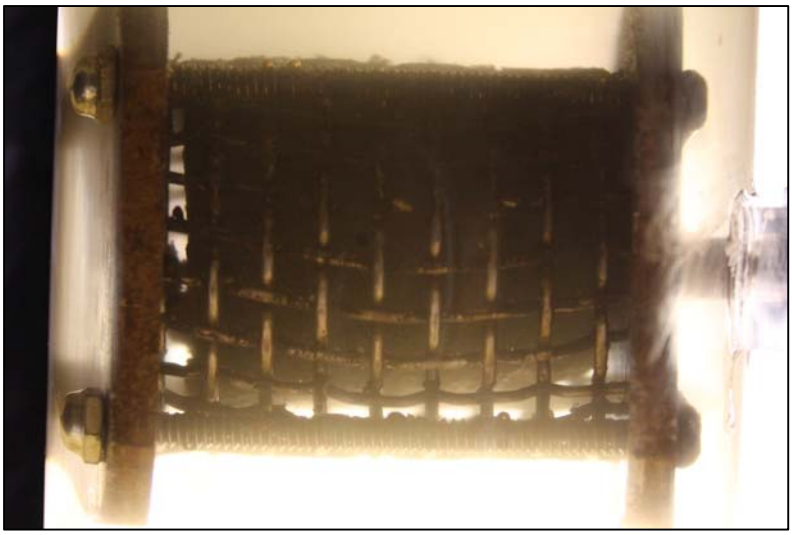

t = 5min

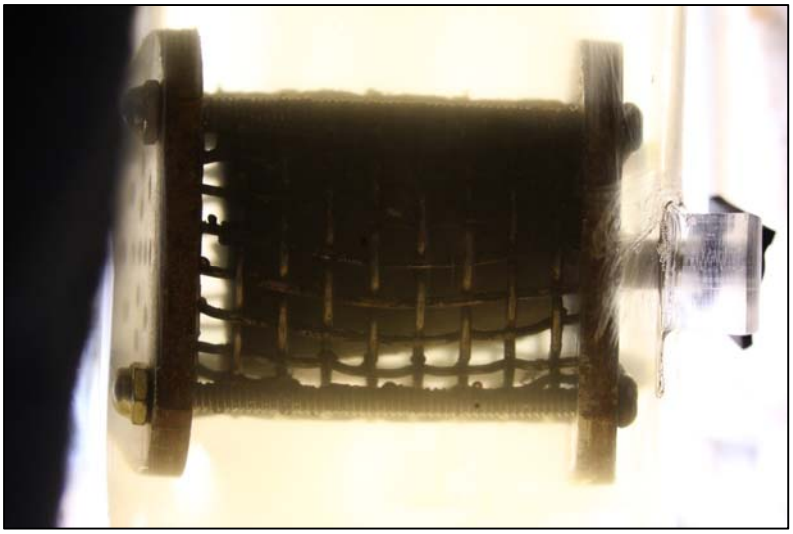

t = 10min

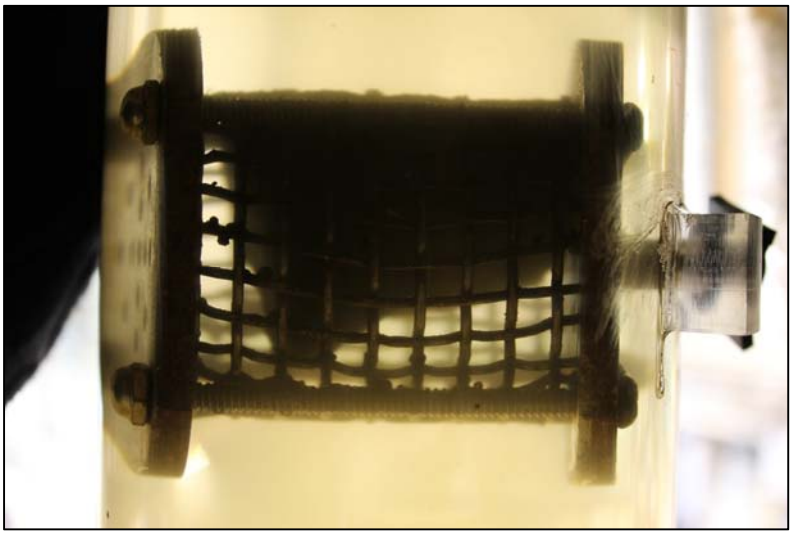

t = 25min

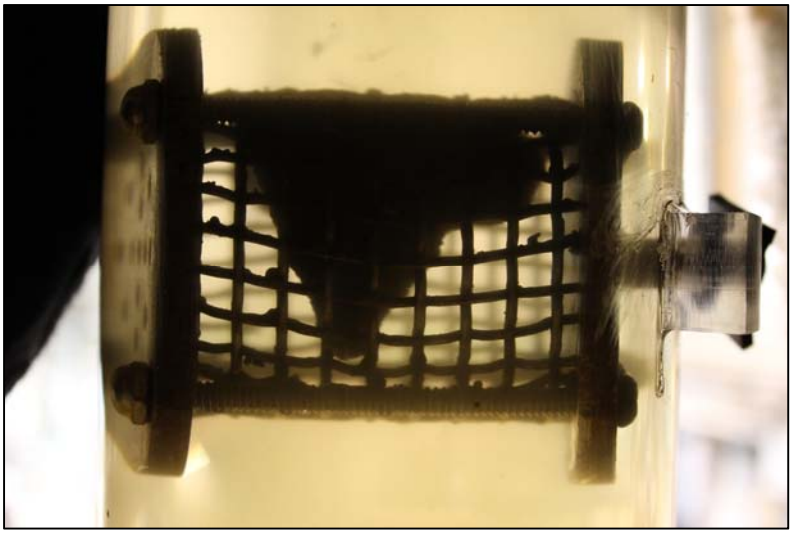

t = 40min

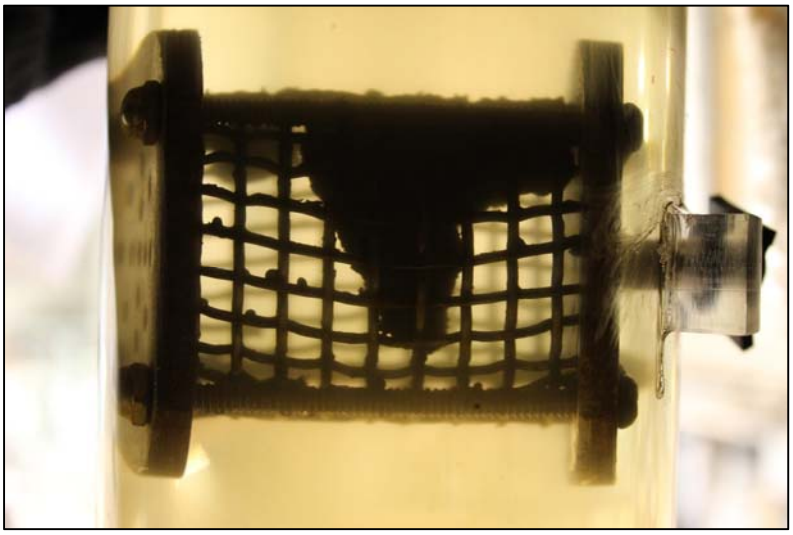

t = 60min

Figure 4.1 Visualizing ablation of Type B lump in water: T=30°C and V=0.5m/s

The time required for an oil sand lump to ablate completely depended on the operating conditions. For example, for water flowing at V = 1m/s and T = 30°C, the lump remained almost unchanged after 70min. However, for runs at higher flow rates and/or higher temperatures, complete ablation occurred in a much shorter time. Recall that complete ablation was indicated by examining the size of the lump remaining; once the size of the lump was within 0-10% of its original size, flow was stopped and the ablation process was assumed to be complete. It

was observed that the lump remaining in the basket at the end of each ablation test was approximately spherical (as shown in Figure 4.2). In this figure, the large un-ablated lump is related to the experimental run done using a Type A lump in water at V = 1m/s and T = 30°C. It is clear that ablation at this condition did not completely happen.

Figure 4.2 Oil sand lumps remaining after different ablation experiments

Ablation of a Type B oil sand lump in water flowing at V = 1.5m/s and T = 30°C was also recorded using a high speed camera (specification is given in Chapter 3). This video clearly shows that the oil sand lump ablates in layers and does not tumble inside the cage even when it becomes very small. A copy of the video recorded during this run is appended to each bound version of this thesis.

4.2. Strain gauge measurements

The novel strain gauge measurement technique, used here to obtain real-time drag force and on-line lump mass measurements, was validated using the following methods: (i) assessing the mass measurements and (ii) validating the drag force measurements. The mass measurements obtained using the strain gauge method were compared with the actual weigh scale measurements. The drag force

measured on non-ablating objects in water was also compared with the calculated drag force. The drag force on solid objects in slurries was measured and a method of modelling drag force in slurries was developed. In addition, the effect of the basket on the drag force measurements was investigated.

Another assessment was conducted to estimate the errors in mass and drag force measurements resulting from the fluctuations caused by external noise. The strain gauge measurements were found to be very sensitive to the vibration of the loop and to high-speed operation. Details of these studies are given in this section.

4.2.1. Validation of lump mass measurements

Oil sand lumps were weighed after preparation and before storage. The mass of each lump was also measured at the start of each experiment using the strain gauges. The two measurements were compared to evaluate the accuracy of the lump mass measurements obtained using the strain gauge technique. Figure 4.3 illustrates results typical of this comparison. The error of each measurement is also plotted on this graph. Based on data of Figure 4.3, the strain gauges normally underestimated the lump mass, as the data points fall mostly below the parity line. However, the maximum error of the measurements was about 4.5%. Considering the fact that these experiments were performed using a large pipeline loop in a pilot plant environment, the amount of error in the measurements was felt to be satisfactory. Raw data are given in Appendix 6.

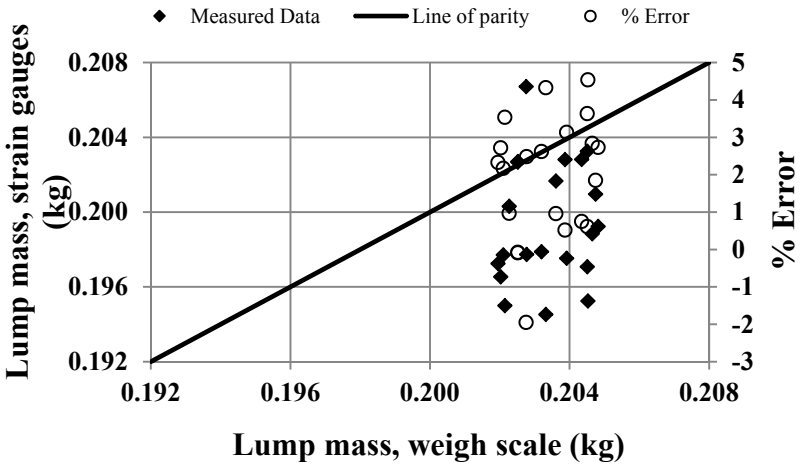

Figure 4.3 Lump mass measurements with weigh scale in comparison with strain gauges measurements

4.2.2. Validation of drag force measurements

In order to validate the strain gauge measurements, the drag force acting on a number of spheres of different size was measured and compared with the calculated drag force. The method of calculating drag force acting on smooth spheres is very well-understood. The comparison of the two sets of data was done with attention to the point that the spheres were anchored using a steel rod. It is understood that the rod contributes to the total measured drag force and the amount of rod contribution is expected to become more pronounced once its size is comparable to the sphere size.

Drag forces acting on the aluminum spheres (with sizes given in Table 3.7) in water flowing at V = 1, 1.5, 2, 2.5 and 3 m/s were measured. The water temperature varied from 26 to 30°C. Since the temperature and strain gauge output were recorded, the drag force calculated for any time "t" was based on the temperature measured at time "t".

Drag force calculation

Bodies immersed in a moving fluid experience a resultant force due to the interaction between the body and the fluid; this can be described as the object wall shear stress, τ_{wp}, due to the viscous effects and normal stresses due to the pressure, p (Young et al., 2004). The resultant force in the direction of flow velocity is referred to as the ″drag force″ and the resultant force normal to the upstream velocity is the ″lift force″. For a small element of the surface of a body shown in Figure 4.4, the drag and lift forces are defined (Young et al., 2004):

$$\boldsymbol{F_D = \int dF_x = \int p \cos\theta \, dA + \int \tau_{wp} \sin\theta \, dA} \qquad (4.1)$$

$$\boldsymbol{F_L = \int dF_y = -\int p \sin\theta \, dA + \int \tau_{wp} \cos\theta \, dA} \qquad (4.2)$$

The first term of right hand side of Equation 4.1 is the pressure drag and the second term is referred to as the friction drag. The definitions (above) indicate that drag and lift force can be calculated providing that wall shear stress and pressure distributions are known. The latter can rarely be obtained analytically for blunt bodies or high Reynolds numbers; hence experimental tests or numerical methods are needed (Young et al., 2004).

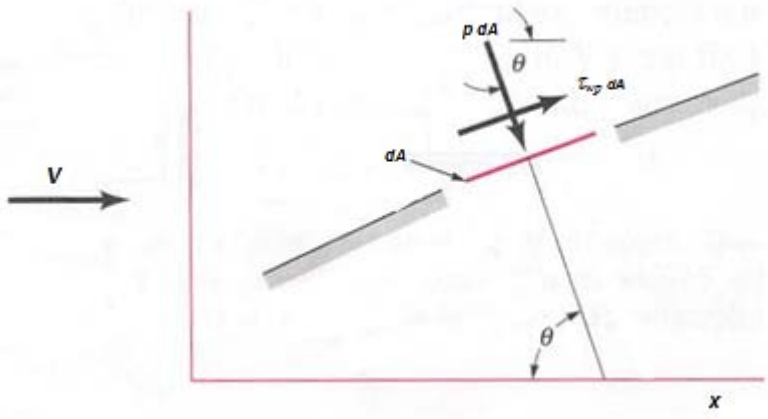

Figure 4.4 Pressure and shear forces on a small element of the surface of a body in a moving fluid
(Young et al., 2004)

For most cases, the pressure and shear stress effects are considered together and drag force for an object which is larger than boundary layer thickness, is defined as (Shook and Roco, 1992):

$$\boldsymbol{F_D = \frac{1}{2}\, C_D \rho\, A_p V^2} \qquad (4.3)$$

where C_D and V denote drag coefficient and bulk velocity, respectively. The drag coefficient, C_D, is a function of particle Reynolds number and the relative roughness of the surface (Young et al., 2004). For a smooth sphere and circular cylinder the drag coefficient can obtained from the available correlations or from a graph such as the one shown here as Figure 4.5.

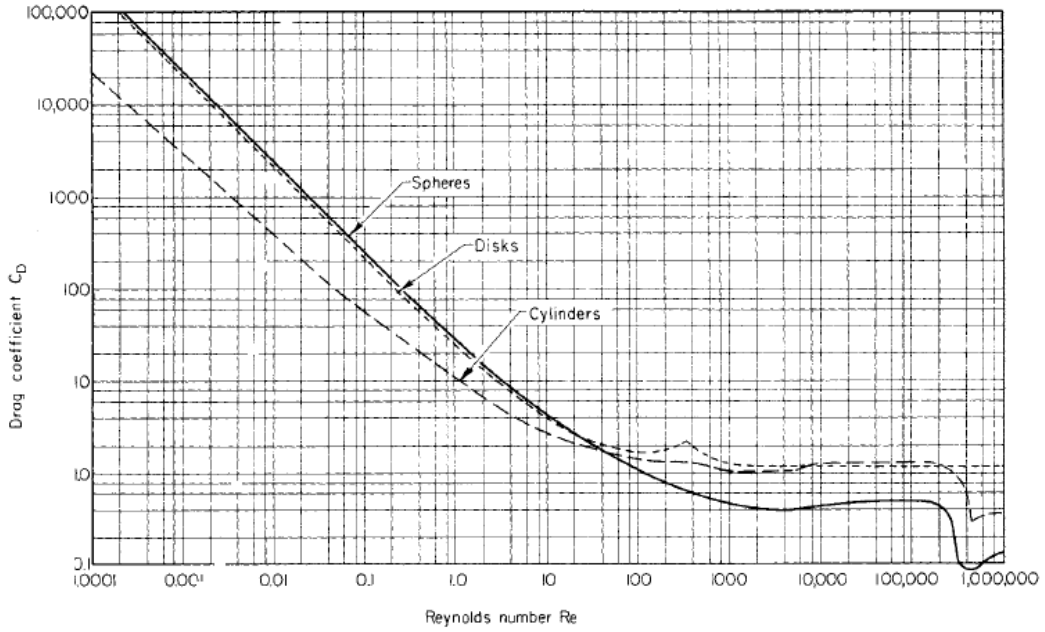

Figure 4.5 Drag coefficient for smooth cylinder and sphere
(Young et al., 2004)

Calculation of the drag force on an aluminum sphere

The drag force acting on a smooth sphere can be calculated using Equation 4.3. However, four important points must be considered when calculating drag forces on the spheres used in these experiments:

1) The spheres were large relative to the pipe cross section, so wall effects must be considered. The wall effect can be taken into consideration by substituting the bulk velocity in Equation 4.3 with the actual velocity. The actual velocity is greater than the bulk velocity and can be calculated from (Young, 2004):

$$\boldsymbol{V_{Act} = (A_P/A'_P)\, V} \qquad (4.4)$$

where, A_P and A'_P indicate pipe cross section and pipe reduced cross section.

2) The drag coefficient introduced here is related to the drag in a quiescent fluid but flow in this system is turbulent. Over the last decades many researchers have studied the way turbulence intensity affects drag acting on the objects; however, their results did not always agree. Some researchers showed that drag force increases in turbulent flow and others showed that it decreases in turbulent flow. Zhou et al (2009) studied the terminal settling velocity of spheres of two different sizes (d = 6.35 and 7.94mm) in turbulent flow. They showed that the drag coefficient in turbulent flow is greater than that in stationary flow. They plotted their experimental data on the standard drag coefficient plot for comparison, here shown in Figure 4.6. Doroodchi et al. (2007) studied the settling of Teflon and Nylon particles (d = 2.4-8mm) in turbulent flow and showed that the ratio of the drag force in quiescent flow to that in turbulent flow might increase or decrease depending on the particle diameter, its density and Stokes number. However, they did not provide a correlation to show the dependency. Kawanisi and Shiozaki (2008) investigated the effect of turbulence on the settling of particles with different densities and diameter and showed that at high turbulence intensity the relative settling velocity increases with the increasing relative turbulence intensity regardless of the Stokes number. At intermediate turbulence intensity and large Stokes number, settling of particles tend to be slowed, but the settling velocity of particles is increased at small Stokes number. In summary, based on the

existing literature, it is difficult to quantify the effect of turbulence in the current system on the drag coefficient. It must be noted that there might be some error associated with the correlation used to determine the drag coefficient.

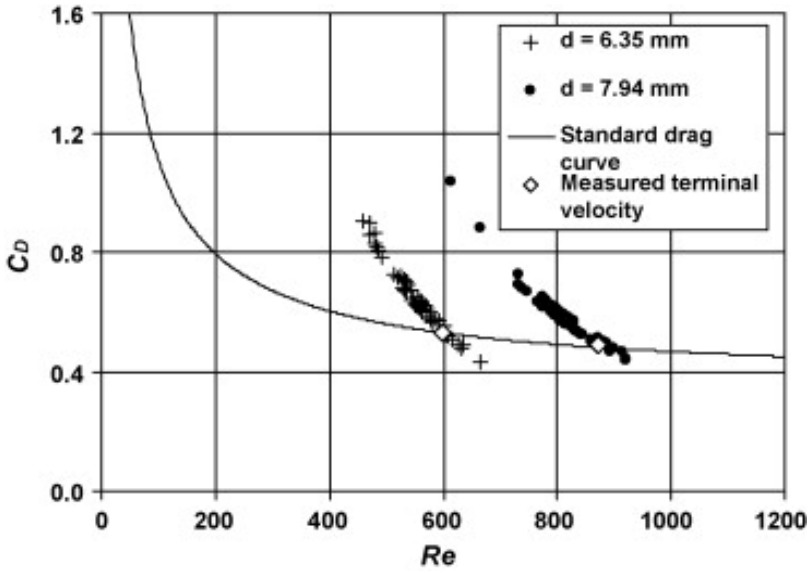

Figure 4.6 Turbulent-affected drag coefficient in comparison with drag coefficient in quiescent fluid
(Zhou et al., 2009)

3) In Equation 4.3, it is assumed that the velocity to which the stationary object is exposed to is equal to the average bulk velocity. However, when a large object is placed in the center of a pipe with turbulent flow, it is exposed to a velocity distribution. Thus, the velocity distribution within a pipe must be considered to calculate the drag force acting on an object placed within the pipe.

   The velocity distribution (far from the pipe wall) for turbulent pipe flow of a Newtonian fluid (Re > 2×10^4) can be calculated using (Bird et al., 1960):

$$\boldsymbol{v^+ = (ln\, s^+)/0.36 + 0.38} \qquad (\text{for } s^+ \geq 26) \qquad (4.5)$$

$$\boldsymbol{v^+ = v_z/v^*} \qquad (4.6)$$

$$s^{+} = (s\, v^{*}\, \rho_m)/\mu_m \qquad (4.7)$$

where v^{+}, v_z , v^{*}, s and R denote the dimensionless velocity, local velocity, friction velocity, distance from the pipe centre and pipe radius, respectively. Figure 4.7 shows the way R and s are defined.

For example, the local velocity of 15% slurry flowing in a pipe (D = 104mm) at T = 28°C and V = 1 to 3 m/s at any radial point was calculated by substituting $s+$ and $v+$ (Equations 4.6 and 4.7) into Equation 4.5. This calculation showed that the local velocity (v_z) was independent of the bulk velocity and it changed as a function of the distance from the pipe centre (s). The dimensionless local velocity (v_z/V), for the system described above, was plotted as a function of dimensionless distance from the pipe center (s/R) in Figure 4.8. When the spheres tested here are placed within the pipe, values of s (defined as the distance from wall of the sphere to the pipe centre) vary from 13.5mm to 25mm, meaning that s/R changes from 0.26 to 0.49. Thus, according to this graph the spheres are exposed to a velocity that is 1.2 to 1.27 times greater than the bulk velocity, refer to the lines shown in red in Figure 4.8. Equation 4.3 must be modified to accommodate the changes given in points (1) and (3):

$$F_D = \frac{1}{2}\, C_D \rho\, A_p (1.3 V_{Act})^2 \qquad (4.8)$$

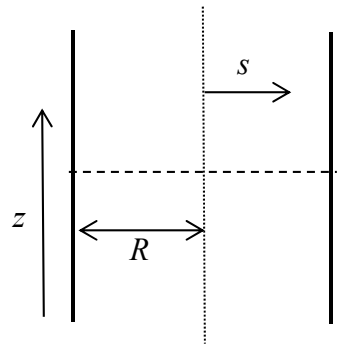

Figure 4.7 Distance from pipe centre (s) and pipe radius (R)

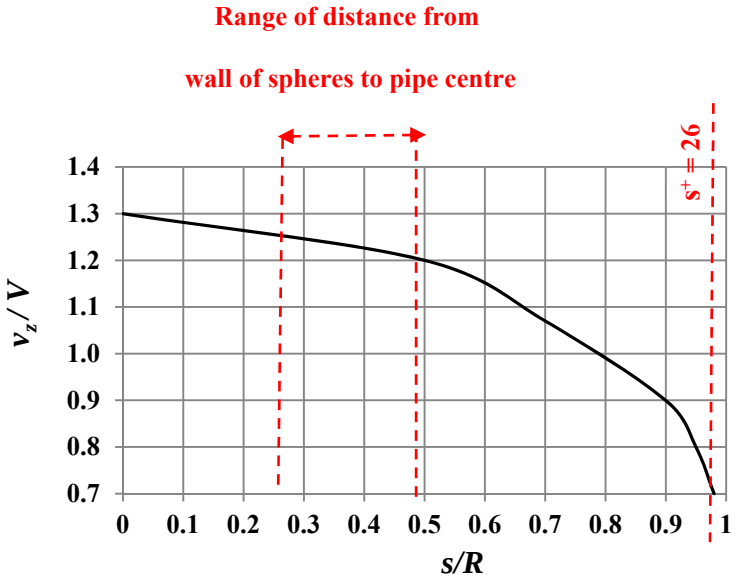

Figure 4.8 Velocity profile for turbulent flow in a pipe D=104mm: slurry (C=0.15); T= 28°C

4) A rod is used to hold the sphere within the pipe, which contributes to the total drag force measurements. If one assumes the assembly of sphere and rod as a body that is exposed to the flow bulk velocity, then the drag acting on the assembly is sum of the drag acting on the rod and that acting on the sphere:

$$F_{D(sphere)} = F_{D(total)} - F_{D(rod)} \qquad (4.9)$$

In this study, by comparing the total drag measured on the rod-sphere assembly with the calculated drag on the sphere, it was found that the effect of rod can be ignored for 50.8 and 44.9mm spheres. This is because considerably shorter rods were used to anchor these spheres, and the diameter of the rod was much smaller than the diameter of these spheres; so the drag force acting on the rod was insignificant compared to the drag force on the large spheres.

The drag force acting on each rod was measured by anchoring it individually within the strain gauged spool and flowing slurry or water at a velocity equal to the actual velocity. In other words, it was assumed that the rod is attached to the sphere and therefore, it is exposed to a velocity

higher than the bulk velocity. Raw data of the measurements and calculations are provided in Appendix 6.

Validation results

The "adjusted" drag force acting on each sphere was calculated by subtracting the drag force on the rod from the total drag force on the rod-sphere assembly. The "adjusted" drag force was then compared with the calculated or predicted drag force for each sphere. The data for the three different spheres are plotted in Figures 4.9 (a, b and c). These figures show that for most of the cases, the calculated drag force, shown as a solid line, is in agreement with the "adjusted" drag force. A slight difference between the "adjusted" drag force and the calculated drag force is observed at the higher bulk velocities. The deviation might be because of the potential error in drag force measurements on the rods. However, the error in measurement at high velocities is still less than -10%. In summary, this investigation showed that strain gauges could satisfactorily be used for drag force measurements.

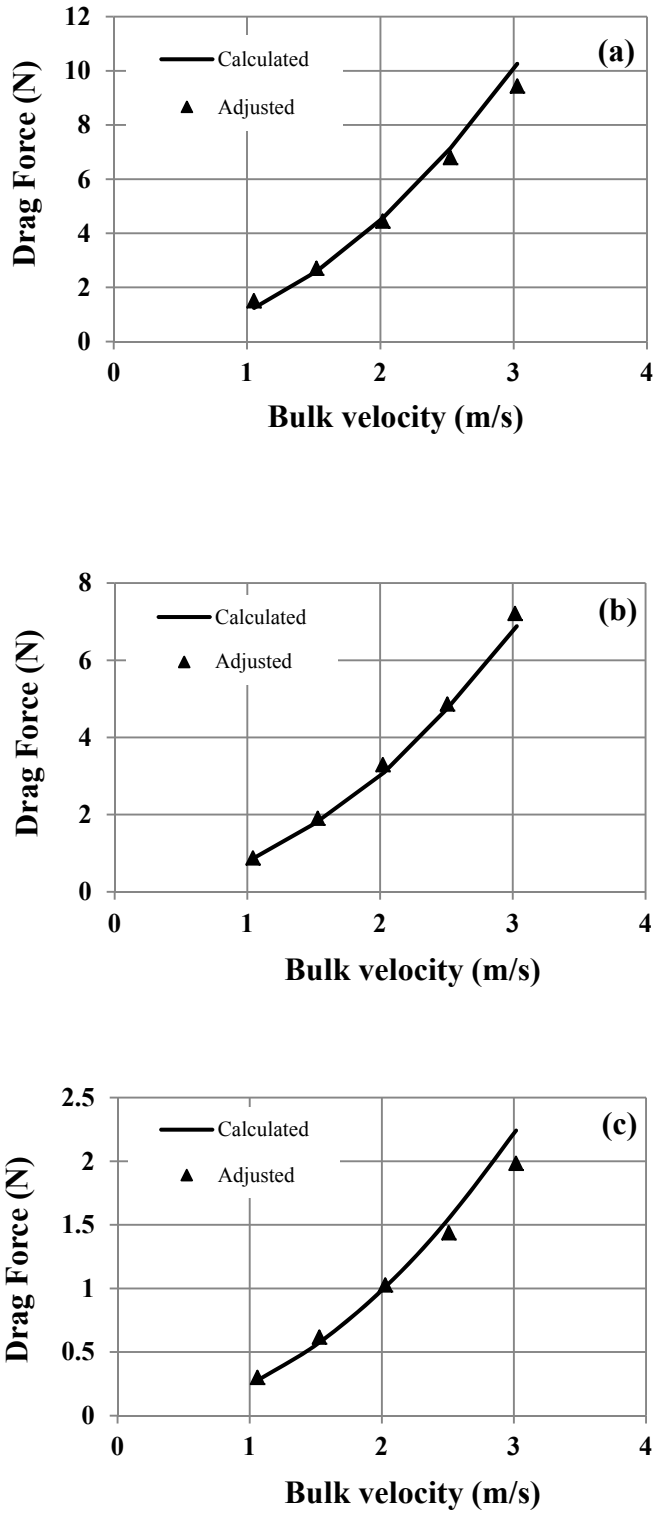

Figure 4.9 "Adjusted" drag force in comparison with calculated drag force for (a) d=50.88mm, (b) d=44.9mm and (c) d=27mm sphere: water at T=26-30°C

4.2.3. Analysis of the effect of the basket on measured drag forces

Oil sand lump ablation experiments were conducted using baskets to anchor the lump. It was not possible to conduct these tests without placing the ablating lump within a basket. The basket has the following effects: (i) it most likely impairs the ablation process because the surface area of the lump that is exposed to the flow is reduced (the amount of the surface reduction depends on the opening size of the basket); (ii) the way sand particles interact with a lump might be different (when a lump is placed inside the basket, a sand grain might contact the basket and returns back into the flow or it might contact the surface of the lump that is not covered with the basket mesh) and (iii) it contributes to the total drag force acting on the lump. For this study, however, a basket is used for every ablation test, so its effect on the lump mass loss can be ignored when mass loss at different operating conditions are compared relative to each other. Here, the effect of the basket on the drag force measurements in water and in slurry flow was investigated and quantified.

The visualization tests showed that a cylindrical oil sand lump ablates and becomes approximately spherical, retaining this shape until it completely disappears. Based on this observation, the drag forces acting on non-ablating cylinders and spheres placed in Basket#1were measured. Drag forces acting on an anchored aluminum cylinder and different sizes of aluminum spheres (dimensions given in Table 3.7), resembling lump at different ablation stages, was also measured using the strain gauges. The drag force measured for each individual solid object was subtracted from the drag force measured for the basket-solid object assembly and the result was interpreted as the effect of the basket on the drag force measurements. Additionally, tests were conducted using the empty Basket#1 and the drag force acting on the basket at different slurry or water velocities was measured. The basket effect obtained from the method mentioned above was compared with the drag force measured on the empty basket. Table 4.2 shows an example of the data obtained for the 50.8mm sphere in slurry (C = 0.15) at different velocities. Table 4.3 presents the measured drag force acting on the

empty basket at the same operating conditions. By comparing the "basket effect" obtained through subtraction (Table 4.2) with that obtained by making drag force measurements for the empty basket (Table 4.3), it is possible to evaluate the validity of subtracting the drag force of the basket alone from that measured for the basket-object assembly. The difference between the two measurements was +6 to -12% when all the spheres and cylinder sizes were considered. In the case of slurry (C = 0.30), the greatest difference between the two measurements was estimated to be -12%; however, the greatest difference for measurements in water was -5.83%. It appears that the greatest difference in the "basket effect" occurs for slurry flow. It is probably related to the differences in the interaction of sand particles with the empty basket from the interaction of sand particles with the solid object-basket assembly. In summary, considering all of the cases, the difference between the two methods for estimating the drag force on the basket seems to be relatively small. The "basket effect" obtained from these two methods, for all of the solid objects, is plotted against mixture (water or slurry) velocity in Figures 4.10 (a, b and c). On these figures, data related to the drag force measurements on the empty basket are plotted as solid black lines. Once again, the figures indicate that the drag forces measured with the two methods are in good agreement.

Table 4.2 Effect of basket on drag force measurements: slurry (C = 0.15); d = 50.8mm sphere

Bulk velocity (m/s)	**Drag force (N)**	**Drag force (N)**	**Drag force (N)**
	d=50.8mm sphere in basket	d=50.8mm sphere only	basket effect
1.09	9.5	2.1	7.4
1.38	16	4	12
1.95	30	6.4	23.6
2.49	45.3	8.5	36.8
2.98	61.2	13.1	48.1

Table 4.3 Measured drag force on empty basket: slurry (C = 0.15)

Bulk velocity (m/s)	Drag force measured on empty basket (N)
1.17	8.7
1.58	15.4
2.17	26.2
2.59	33.6
3.05	44.4

Table 4.4 Difference between drag force on basket, measured using sphere (d=50.8mm)-basket assembly and empty basket

Basket effect on drag force (N)	Drag force on measured on empty basket (N)	% Difference from average drag force
7.4	8.7	-3.69
12	15.4	-6.00
23.6	26.2	-2.60
36.8	33.6	2.31
48.1	44.4	2.02

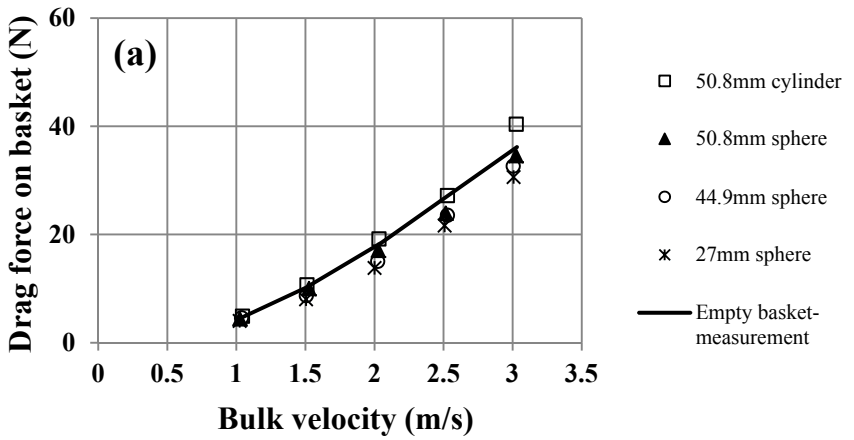

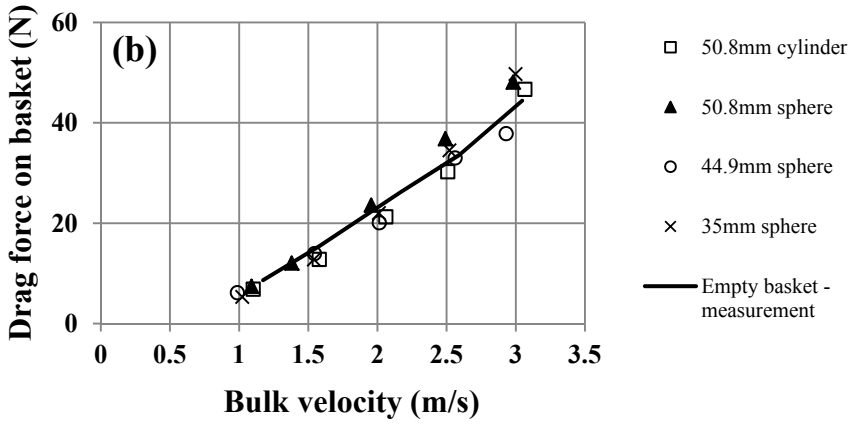

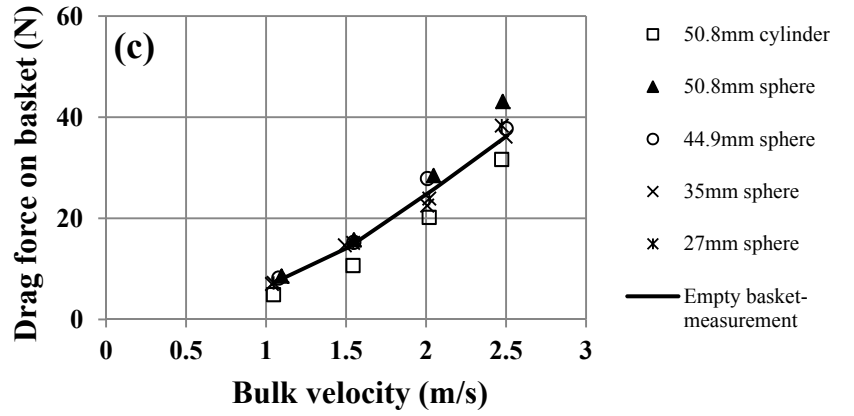

Figure 4.10 Effect of basket on drag force measurements in (a) water; (b) slurry (C=0.15) and (c) slurry (C=0.30)

It is concluded from this analysis that the drag force acting on an oil sand lump, which is placed in a basket, can be calculated by subtracting the drag force acting on the empty basket from the total drag force acting on the lump-basket assembly.

4.2.4. Modelling drag force in slurry

A model for estimating the drag force acting on a large solid particle (such as an oil sand lump) in slurries was proposed by measuring the drag force on different non-ablating objects and comparing them with the calculated drag force. Different calculation methods were tested and it was found that equivalent flow model can be used to model the drag force acting on large solid objects in slurries.

The measured drag force acting on each solid object in every slurry concentration and velocity was divided by the cross sectional area of the object ($Z_{exp} = (F_D)_{Exp}/A_{PC}$) and Z_{exp} was then plotted against V^2_{Act} (V_{Act} calculated using Equation 4.4). Slurry flow inside a vertical pipe at velocities higher than the particle settling velocity is homogeneous and therefore slurry density and viscosity can be calculated using the equivalent fluid model. Based on the equivalent fluid model, density, ρ_m, and viscosity, μ_m, of the mixture can be calculated using (Gillies & Shook, 2000):

$$\boldsymbol{\rho_m = \rho_s C + \rho_f (1 - C)} \qquad (4.10)$$

$$\boldsymbol{\mu_r = \mu_m / \mu_f = 1 + 2.5C + 0.16\lambda^2} \qquad (4.11)$$

where λ is defined using Equation 2.9.

The density and viscosity of the slurries tested here were calculated and substituted in Equation 4.3 to calculate $Z_{cal} = F_D/A_{PC}$ for a stationary solid object within a pipe:

$$\boldsymbol{Z_{cal} = \frac{F_D}{A_{PC}} = \frac{1}{2} \rho_m C_D V^2_{Act}} \qquad (4.12)$$

Data obtained for Z_{cal} were also plotted against V^2_{Act} on the same graph as Z_{exp}. Both the calculated and experimental data are shown in Figure 4.11. The symbols

shown on these figures illustrate Z_{exp} for different non-ablating objects and the solid line represents Z_{cal}. The Z_{cal} results were independent of the solid object size so only one set of the data was plotted. As shown in these figures, the measured data (Z_{exp}) are in good agreement with the calculated data (Z_{cal}). This observation indicates that drag force on the large objects in slurries can be estimated using the equivalent flow model. Raw data are given in Appendix 6.

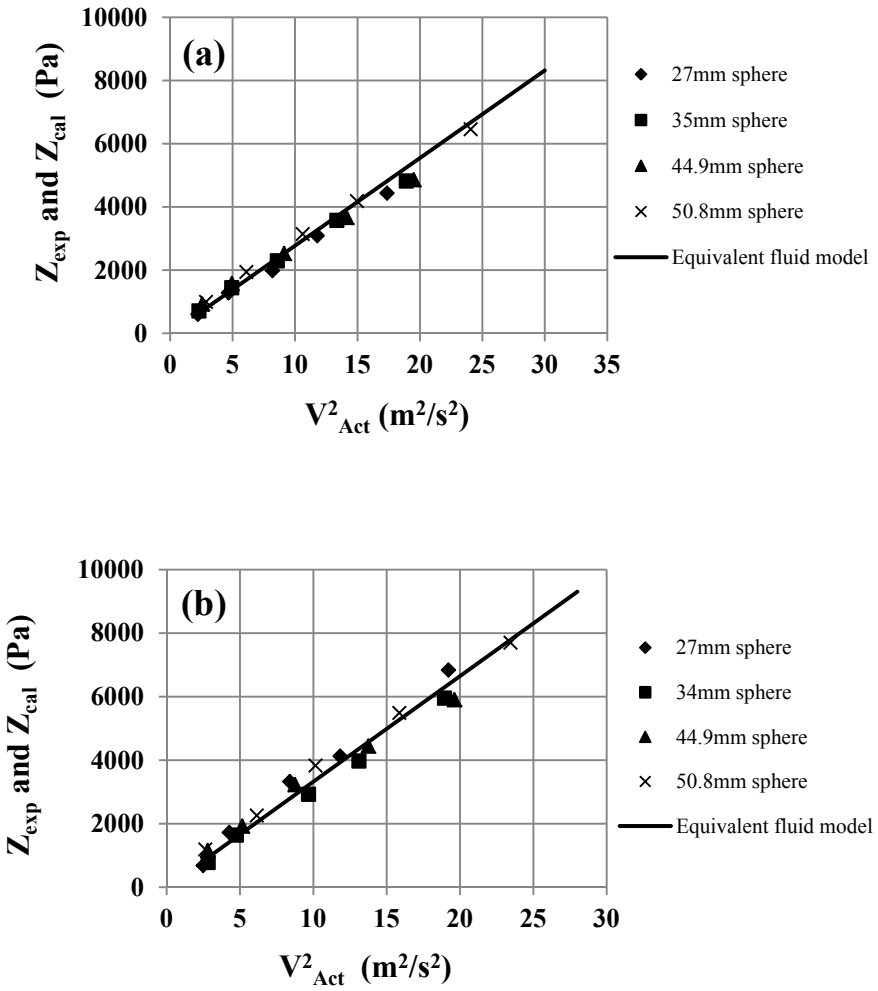

Figure 4.11 Modelling drag force on large solid objects in (a) slurry (C=0.15) and (b) slurry (C=0.30)

4.2.5. Analysis of strain gauge and flow meter measurement fluctuations

Data from the magnetic flow meter and strain gauges were collected using a data acquisition system (Dasylab 10.0). As mentioned earlier, 60s averages of readings from each instrument were recorded. Strain gauges are extremely sensitive to noise from the surroundings, which causes their output voltage to fluctuate. It was observed that slurry flow causes more fluctuations in the strain gauge and flow meter readings compared to water. It was necessary to quantify these fluctuations and determine the measurement errors resulting from the fluctuations. The steps taken for this evaluation were as follows:

- An aluminum cylinder, with dimensions identical to a new (un-ablated) oil sand lump, was placed inside the basket which was then anchored within the strain gauged spool.
- At each slurry concentration and mixture velocity, flow meter and strain gauge data were collected for 5-15min.
- At certain times, the strain gauged spool was bypassed to measure the oil sand lump mass loss during ablation. At certain slurry velocities, flow was redirected for 10s and was then returned to the original flow configuration through the test spool. The drag force acting on the sample was measured 5min before and after redirecting the flow to determine the effect this had on the drag force measurement.

Figure 4.12 shows the fluctuations of the drag force measurement in water flowing at a nominal (target) velocity of 1m/s. Each data point (black diamond) on this graph shows the drag force on the basket-cylinder assembly at a certain time. The solid line represents the average drag force measured at this operating condition. The average drag force was 6.83N; the measured drag force deviates from the average drag force by approximately -1.7 to +2%. Flow meter readings were converted to bulk velocities and were plotted against time in Figure 4.13. This figure illustrates that velocity changed between 1.036 to 1.043m/s which shows slight deviation from nominal 1m/s.

Similar tests were completed for water flowing at target velocities of 1.5, 2, 2.5 and 3m/s, and the percent difference between the minute-by-minute readings and the average drag force was calculated for all of the tests. The percent difference for the measured drag force on the basket-aluminum cylinder assembly at each water velocity is shown in Figure 4.14. It is understood from this graph that the error in the drag measurements at the range of water velocity considered here varies between -1.75 to +2.2%. Raw data are given in Appendix 6.

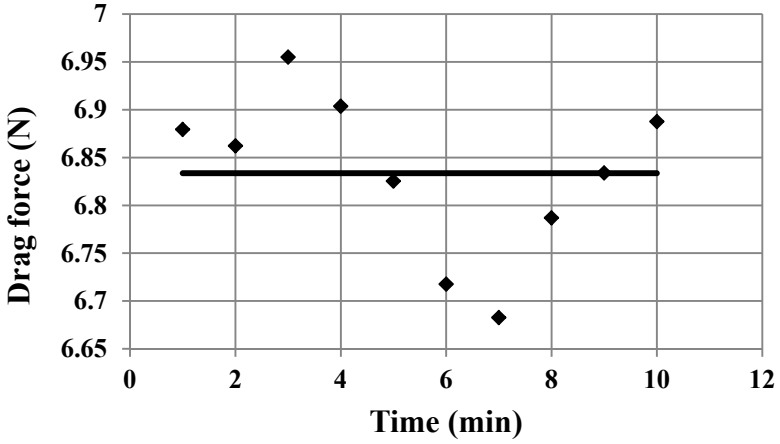

Figure 4.12 Fluctuation of drag force measurement on basket-aluminum cylinder assembly in water: V=1m/s and T=26°C

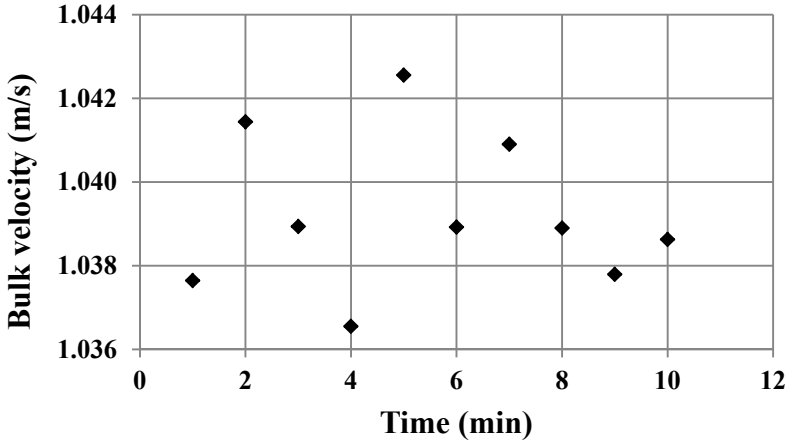

Figure 4.13 Fluctuation of bulk velocity: water at V=1m/s and T=26°C

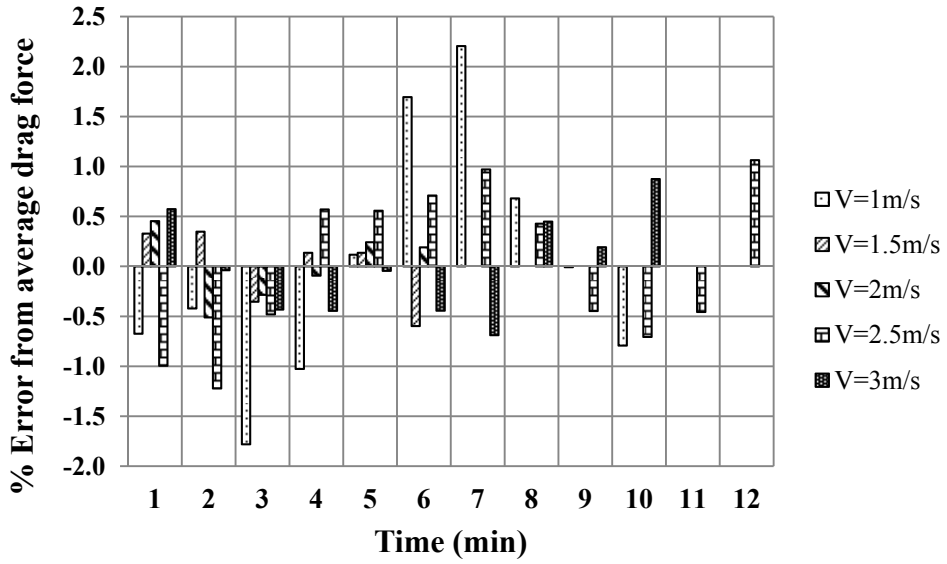

Figure 4.14 % Error of measured drag force from average drag force on basket-aluminum cylinder assembly: water at T=26°C

Strain gauge and flow meter measurements were also evaluated for sand slurry (C = 0.15) flowing at nominal (target) velocities of 1, 1.5, 2, 2.5 and 3m/s. Figure 4.15 presents the measured drag force for V (target) = 2m/s as a function of time.

White diamonds on this graph show drag force measured after flow is stopped and redirected. In this case, the average drag force was calculated equal to 30.67N and the maximum error for the drag measurements was found to be about ±1.6%. The bulk velocity, calculated from the measured slurry flow rate, was also plotted against time as shown in Figure 4.16. The slurry bulk velocity varied between 1.96 to 2.09m/s for the slurry target velocity at 2m/s. The deviation is again viewed to be acceptable for pilot scale experimental studies in terms of the possible effect on the lump drag force measurements. The percent error of the drag force measurements from the average drag forces at different slurry velocities were plotted in Figure 4.17. According to Figure 4.17, % error of drag measurement in slurry (C = 0.15) varies between -8% to +9% for different slurry velocities. This is still in the acceptable range relative to the magnitude of the total drag force acting on the basket-aluminum cylinder assembly at different slurry bulk velocities.

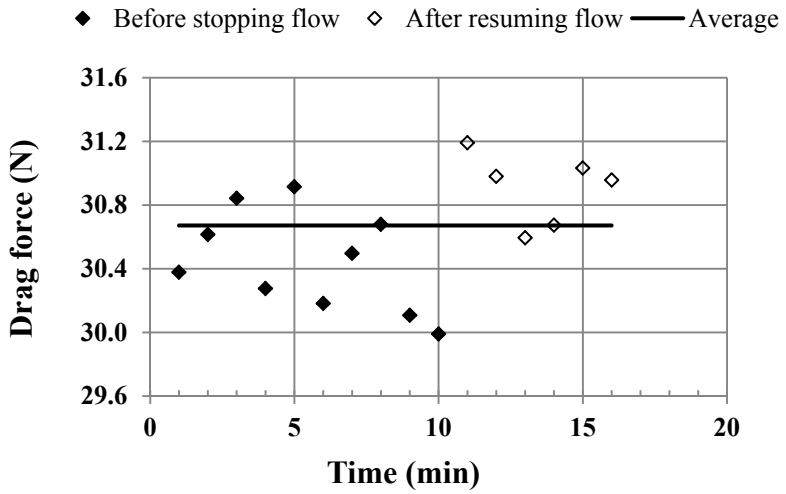

Figure 4.15 Fluctuation of drag force measurement on basket-aluminum cylinder assembly in slurry (C=0.15): V=2m/s and T=26°C

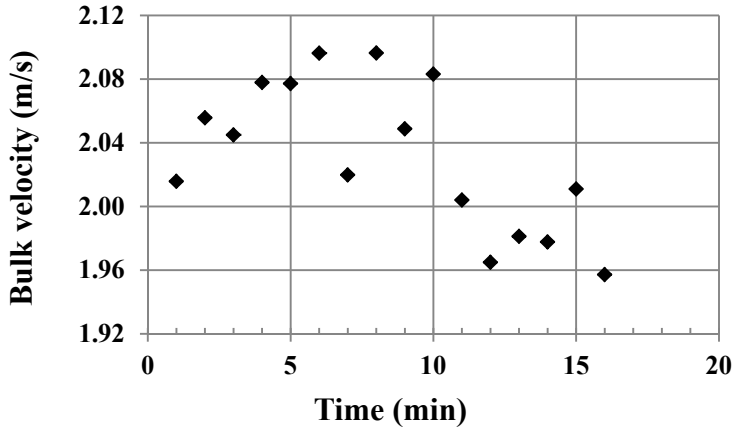

Figure 4.16 Fluctuation of bulk velocity: slurry (C=0.15) at V=2m/s and T=26°C

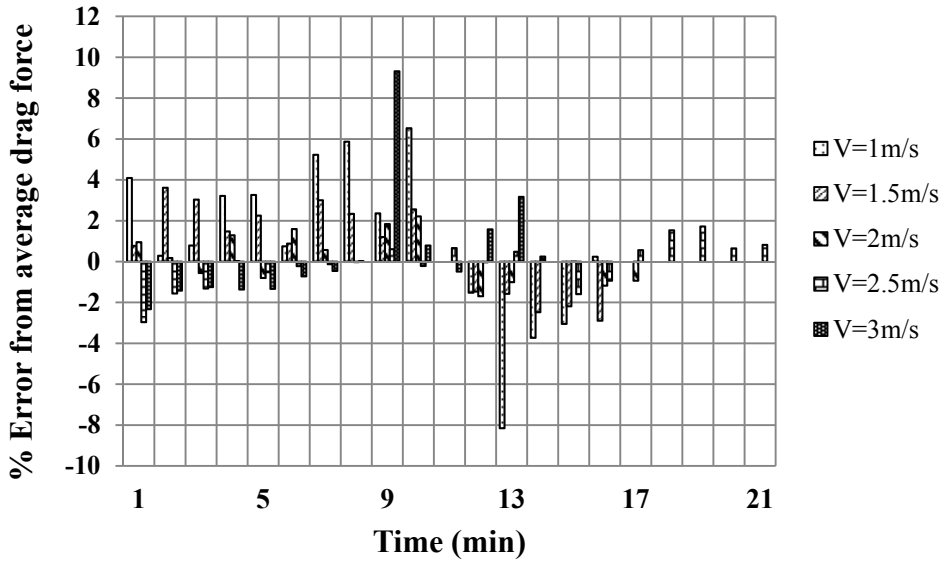

Figure 4.17 % Error of measured drag force from average drag force on basket-aluminum cylinder assembly in slurry (C=0.15) at T=26°C

Additionally, fluctuation tests were completed for slurry (C = 0.30) for t = 5min at different slurry velocities. The results for a target (nominal) velocity of 1.5m/s are given in Figure 4.18; here the symbols show the measured drag force as a function of time and the solid line shows the average drag force at this velocity. The

average drag force was found equal to 18.9N and the percentage error was measured about -1.66 to +0.2%. Fluctuations in measured slurry bulk velocity for a target velocity of 1.5m/s are shown in Figure 4.19. The slurry bulk velocity varied from 1.45 to 1.55m/s at a target velocity of 1.5m/s. Similar to the previous cases, percent error of the measured drag force from the average drag force at different slurry velocities was plotted for comparison (Figure 4.20). From this comparison it can be seen that the maximum error occurs at a target velocity of 1m/s, with the % error ranging from -18.9 to +17%. The % error at the other slurry velocities was relatively small, from -6 to +2.7%. The reason for the large error in the drag force measurement at V = 1m/s is most likely related to the fact that the bulk velocity is very close to the deposition velocity (V_c) for the slurry. The deposition velocity for the horizontal section of the pipe was calculated, using PipeFlow 10, to be 1.2m/s. Therefore at V = 1m/s, 0.190mm sand particles tend to settle and this causes fluctuations in the drag force measurements using the strain gauges.

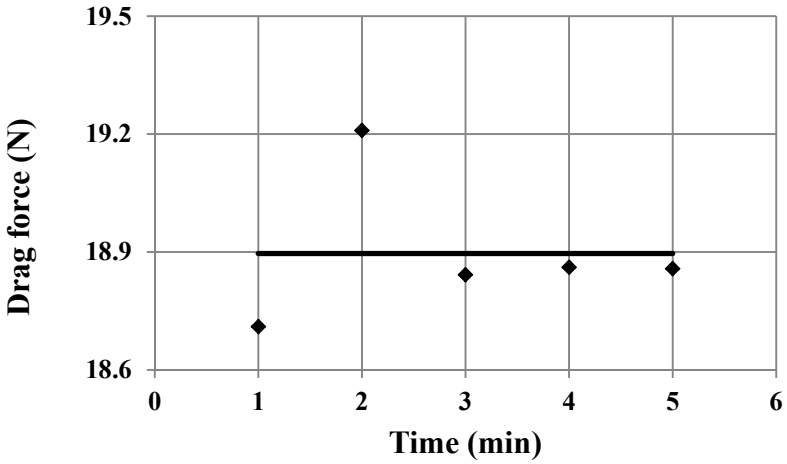

Figure 4.18 Fluctuation of drag force measurement in slurry (C=0.30): V=1.5m/s and T=26°C

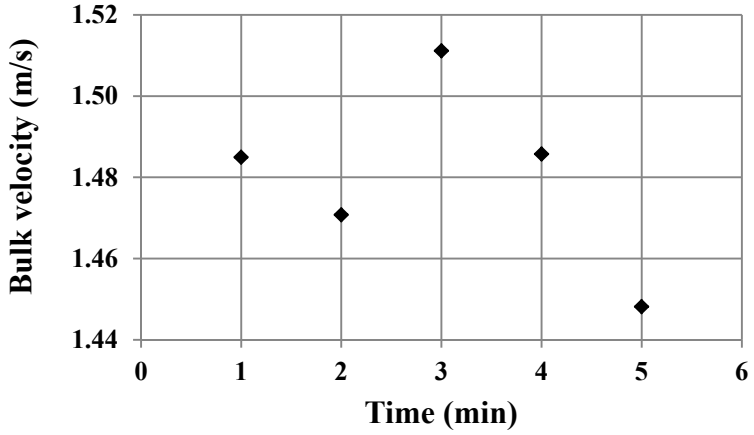

Figure 4.19 Fluctuation of bulk velocity: slurry (C=0.30) at V=1.5m/s and T=26°C

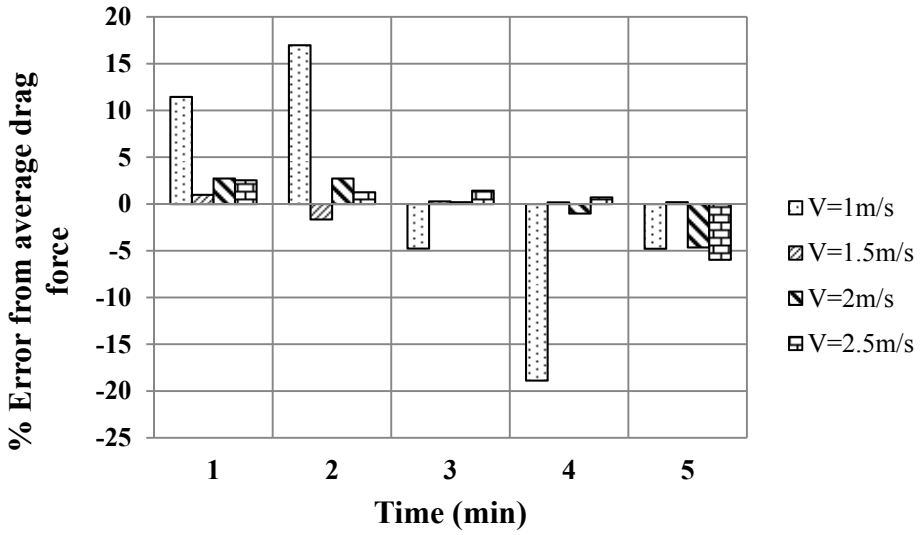

Figure 4.20% Error of measured drag force from average drag force on basket-aluminum cylinder assembly in slurry (C=0.30) at T=26°C

It is concluded that in nearly all cases, the measurement error is less than ± 10%. The percent error is less than ± 20% for slurry (C = 0.30) flow at 1m/s which is most likely because at this operating condition, the bulk velocity in the horizontal section of the flow loop is very near the slurry deposition velocity.

4.3. Assessing repeatability of ablation tests

A number of runs were repeated three times to examine the repeatability of ablation tests conducted with the SRC apparatus. Figures 4.21 to 4.24 show some of the results of the test repeats. At each condition, the fraction of lump digested was plotted against time for three identical tests. Raw data from additional tests are presented in Appendix 6.

It can be seen from these tests that the ablation of all three lumps was completed at the same rate and within the same time frame. These results show that the lump ablation tests conducted for this study were reasonably repeatable.

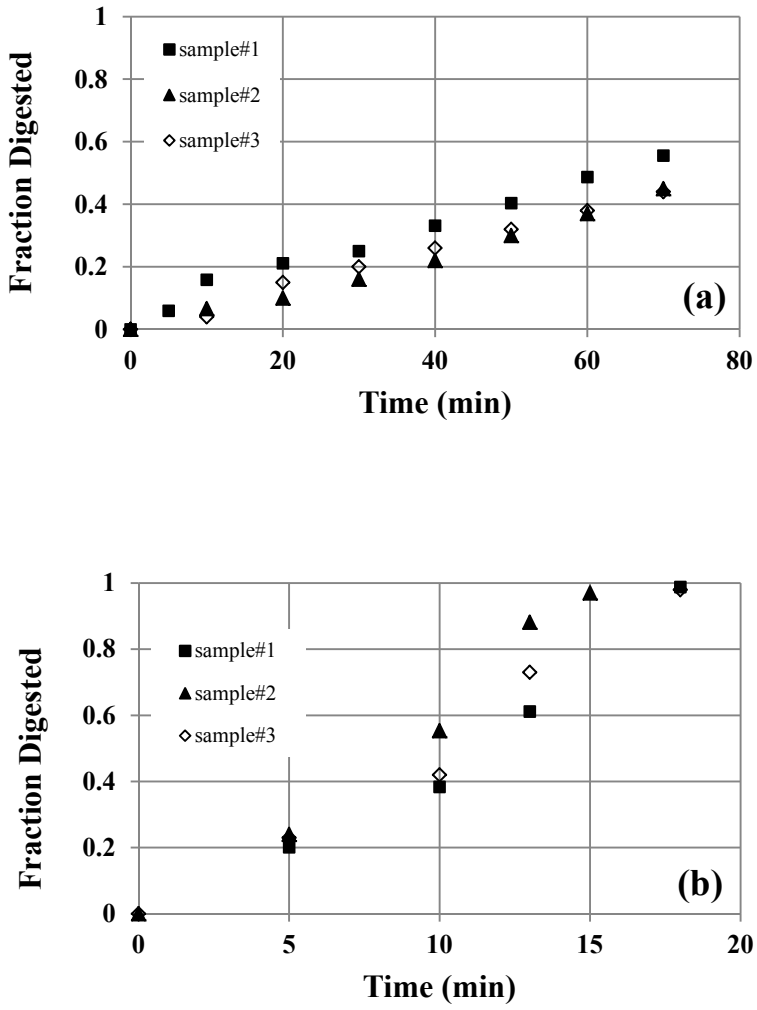

Figure 4.21 Repeatability tests for Type A lumps ablated in water at V=2m/s: (a) T=30°C and (b) T=45°C

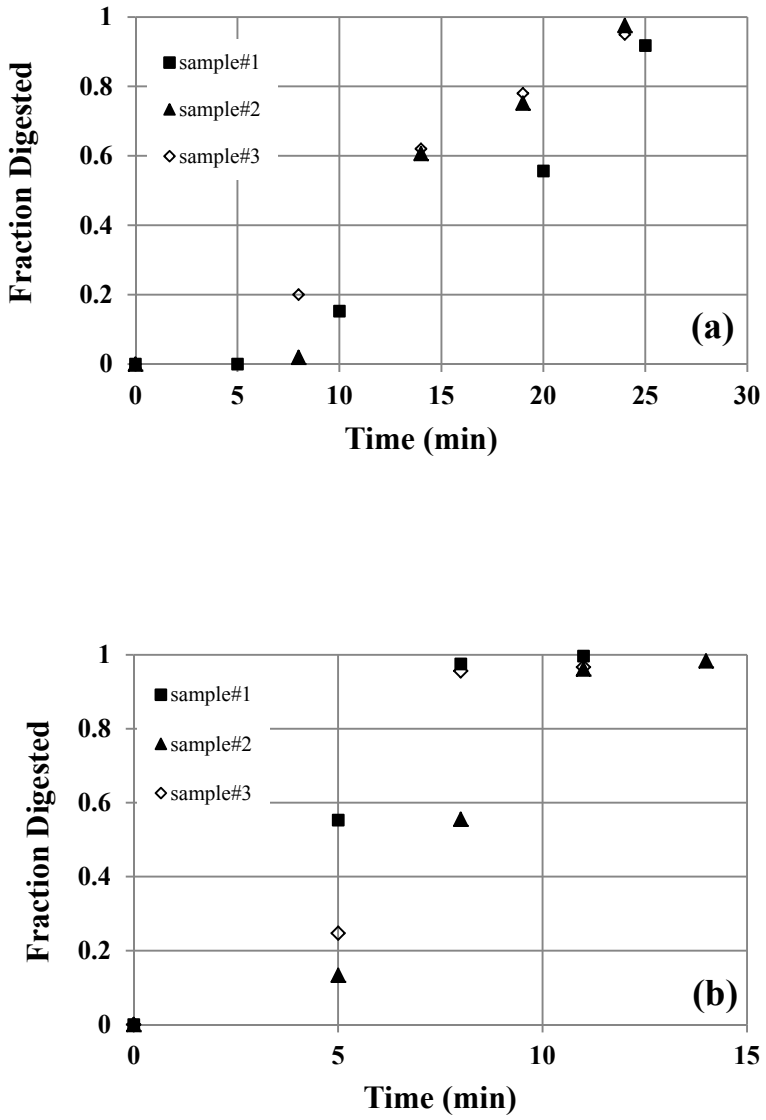

Figure 4.22 Repeatability tests for Type A lumps ablated in slurry (C = 0.15) at: (a) V=2.5m/s, T=30°C and (b) V=2m/s T=45°C

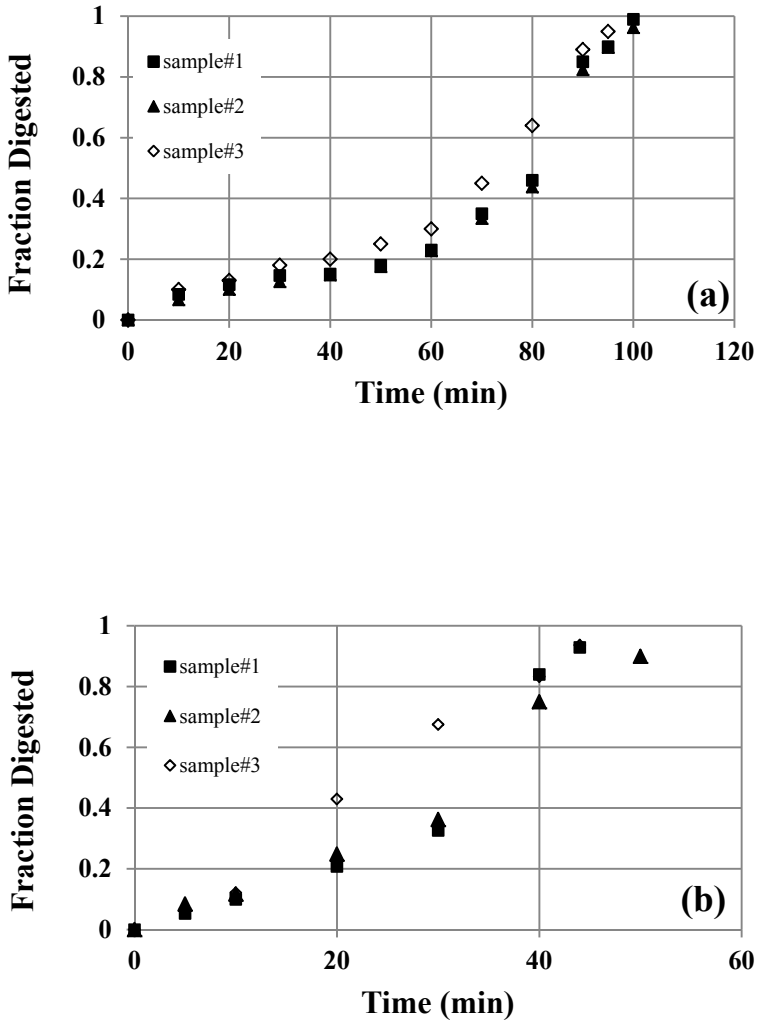

Figure 4.23 Repeatability tests for Type A lumps ablated in slurry (C=0.30) at T=30°C: (a) V=1.5m/s and (b) V=2m/s

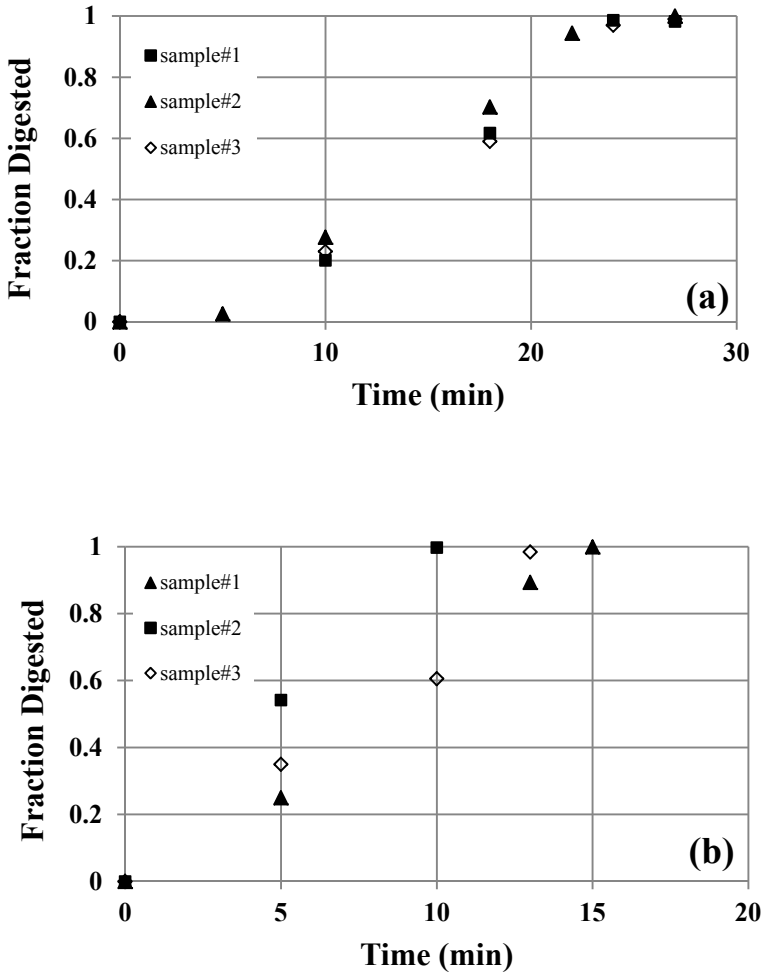

Figure 4.24 Repeatability tests for Type A lumps ablated in slurry (C=0.30) at T=45°C: (a) V=1.5m/s and (b) V=2m/s

4.4. Effect of basket mesh size on ablation

The effect of the basket mesh size on oil sand lump ablation was investigated by repeating a number of the experimental runs conducted with Basket#1, this time using Basket#2. Recall that the only difference between the two baskets was the mesh size. Lump ablation was examined for water at T = 30°C and V = 1.5 m/s and 2m/s. For each run, the fraction digested was plotted versus time of ablation, as shown in Figure 4.25 (a). According to the results of Figure 4.25 (a), time of ablation, ablation rate and fraction digested for the two lumps are identical up to 100min; however, the last data point shows considerably greater mass loss for the test using Basket#2. Close examination of the lump remaining after the completion of the ablation test using Basket#2 showed that a relatively large portion of the lump was missing. Generally, it was found during the visualization tests that once an oil sand lump was exposed to low flow rates for considerably long periods of time it lost strength and did not necessarily ablate through the same mechanism as a fresh lump. After a long period of exposure to flow, the lump becomes saturated with water and can easily break into pieces. In the case of this test, perhaps because the mesh size of Basket#2 was relatively large, piece(s) of the broken lump were swept from the basket, causing a significant mass loss between readings.

Similarly, ablation of two oil sand lumps were examined in slurry (C = 0.30) at T = 30°C and V = 1.5 m/s using the two different baskets. Figure 4.25 (b) illustrates the comparison of these two tests. It is observed that the ablation rate, time of ablation and fraction ablated are similar, especially up to 80min. Beyond this time, ablation occurred slightly more rapidly in Basket#2 than in Basket#1, which is the reverse what is observed in Figure 4.25 (a). The reason for this is not clear. As was seen for the ablation tests with water, the basket mesh size did not significantly affect oil sand lump ablation. Raw data are given in Appendix 6.

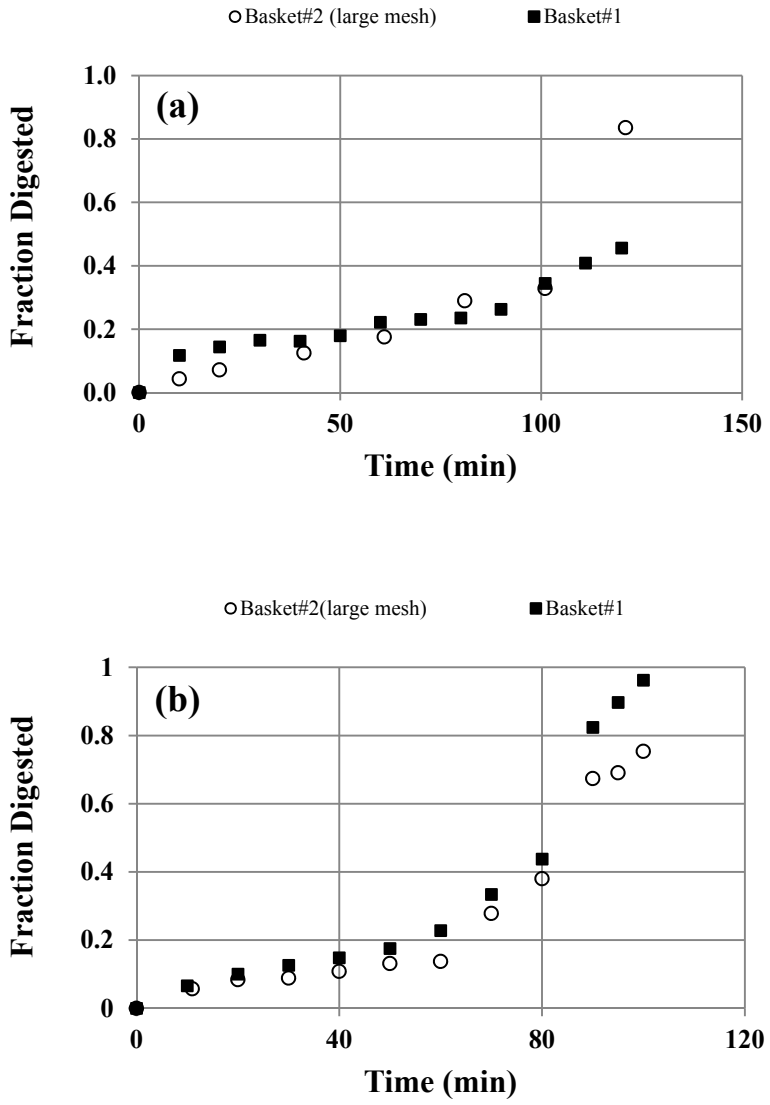

Figure 4.25 Effect of type of basket on ablation of Type A lumps at T= 30C and V=1.5m/s: (a) water and (b) slurry (C=0.30)

The effect of basket mesh size on ablation was also examined at higher slurry velocity and T = 30°C. The fraction digested was plotted against time of ablation for both ablation tests, and presented here as Figure 4.26. This graph shows that at a higher slurry velocity, ablation occurs more rapidly when using Basket#2.

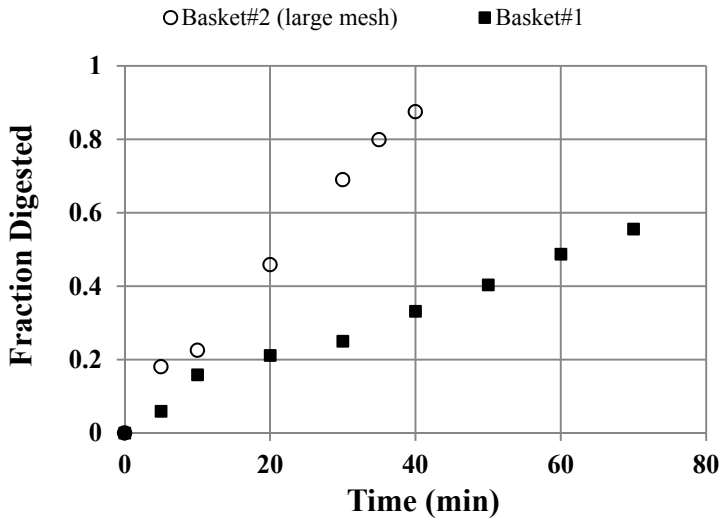

Figure 4.26 Effect of type of basket on ablation of Type A lump in water at T=30°C and V=2m/s

In the current study it was decided to use Basket#1 to investigate the effect of slurry velocity and concentration on ablation because ablation occurred more slowly when using Basket#1, especially at high flow rates. This provided the capability to expand the range of the slurry velocities and concentrations that were tested. In addition, as long as the results of tests conducted using Basket#1 are compared together, the analysis is valid.

4.5. Effect of slurry velocity on oil sand lump ablation

Recall that bitumen producers wish to eliminate the use of trucks and complete oil sand conditioning at the mine face. This change would result in the use of short hydrotransport pipelines compared to the existing design, which could potentially lead to incomplete lump ablation. One way to improve ablation is to increase the shear stress acting on the lumps by increasing the slurry velocity as long as the lump residence time remains unchanged. The purpose-built SRC apparatus was used to examine the effect of slurry velocity on oil sand lump ablation using artificial oil sand lumps. The effect of slurry velocity on ablation was investigated for water flow and two different slurry flows at two temperatures. For each run, fraction of lump digested, calculated using Equation 3.3, was plotted as a function

of time. The results are presented here as Figures 4.27 and 4.28 for T = 30 and 45°C, respectively. The effect of slurry velocity on the oil sand lump ablation rate was also investigated.

Figures 4.27 (a, b and c) illustrate the fraction of lump digested as a function of time for water and slurries (C = 0.15 and 0.30) at T = 30°C. The oil sand lump ablation in water flowing at V = 1, 1.5, 2, 2.5 and 3m/s are compared in Figure 4.27 (a). The results presented in this figure show that the ablation process is very slow for V ≤ 2m/s: it takes about 125min for the lump to ablate to half of its initial size. However, at V = 3m/s, ablation occurs much more rapidly and is complete in about 25min. Figure 4.27 (b) shows the data related to the fraction of lump digested against time of ablation for ablation in slurry (C = 0.15). Similar to ablation in water, lump ablation occurs more slowly at V = 1m/s than at V = 3m/s. It takes about 38min for the lump to ablate by 35% for slurry flowing at V = 1m/s whereas at V = 3m/s, it takes less than 5min to ablate by the same amount and only 10min to ablate completely. As shown in Figure 4.27 (c), ablation in slurry (C = 0.30) is very slow at V < 2m/s; for example, when slurry flows at V = 1.5m/s, complete ablation happens after 100min. However, when the velocity is increased to 2 or 2.5m/s, complete ablation occurs at much shorter times. Ablation is 100% complete in 20min when slurry flows at 2.5m/s.

Experimental data for lump ablation in water and slurries at T = 45°C are presented as Figures 4.28 (a, b and c). Generally, the dependency of lump ablation on velocity is similar to that of lump ablation at T = 30°C. Ablation is 80% complete after 90min water flowing at 1m/s. However, it is 100% complete after 45min at V = 1.5m/s and 20min at 2m/s. For the slurry (C = 0.15), the time to complete ablation is cut in half when the velocity is increased from 1.5m/s to 2m/s. Similar behavior was seen for ablation in the more concentrated slurry (C = 0.30).

In summary, these figures show that for all of the cases, lump ablation is highly dependent on velocity, regardless of the sand concentration or slurry temperature.

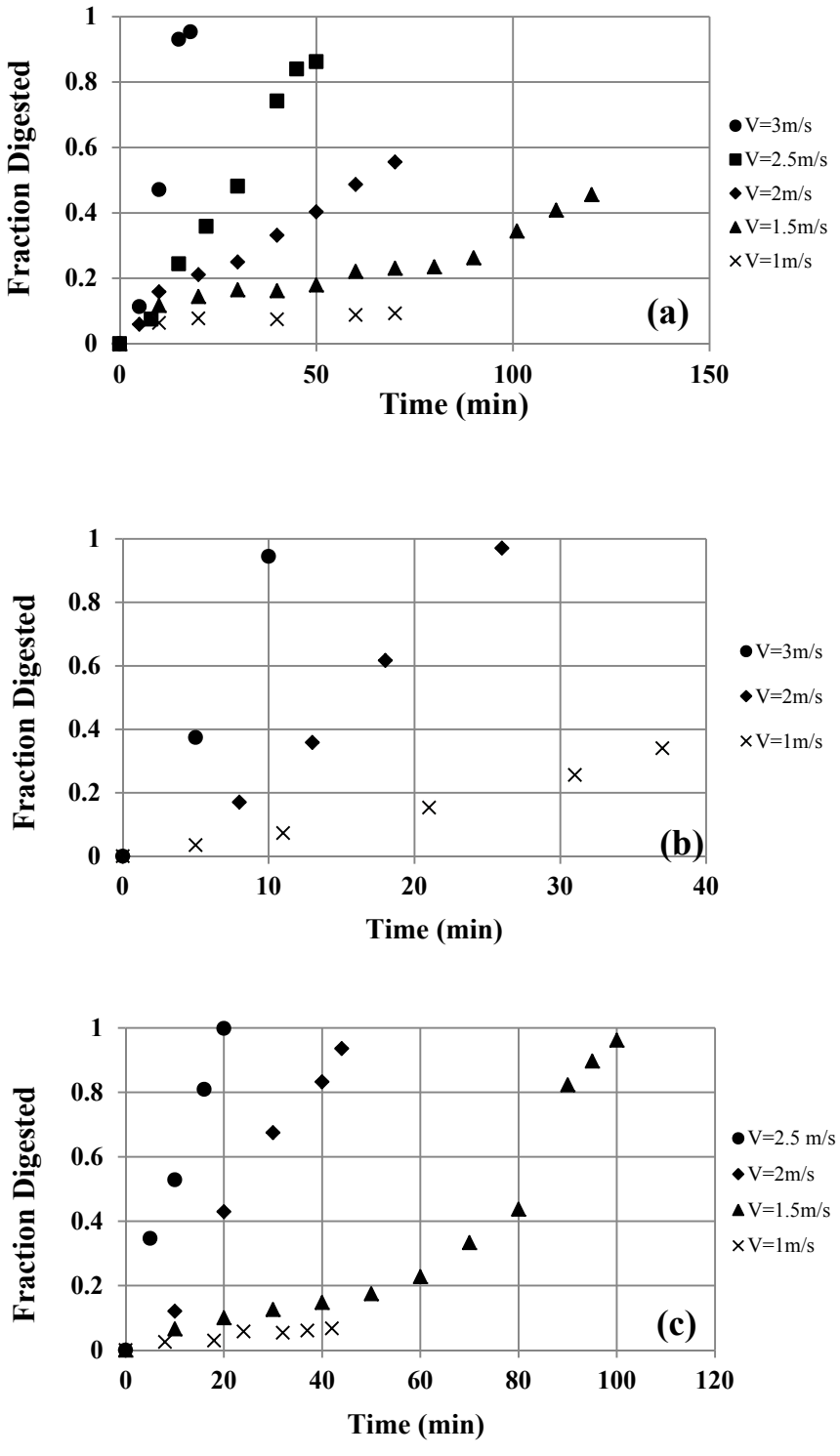

Figure 4.27 Effect of velocity on ablation in (a) water, (b) slurry (C=0.15) and (c) slurry (C=0.30) at T=30°C

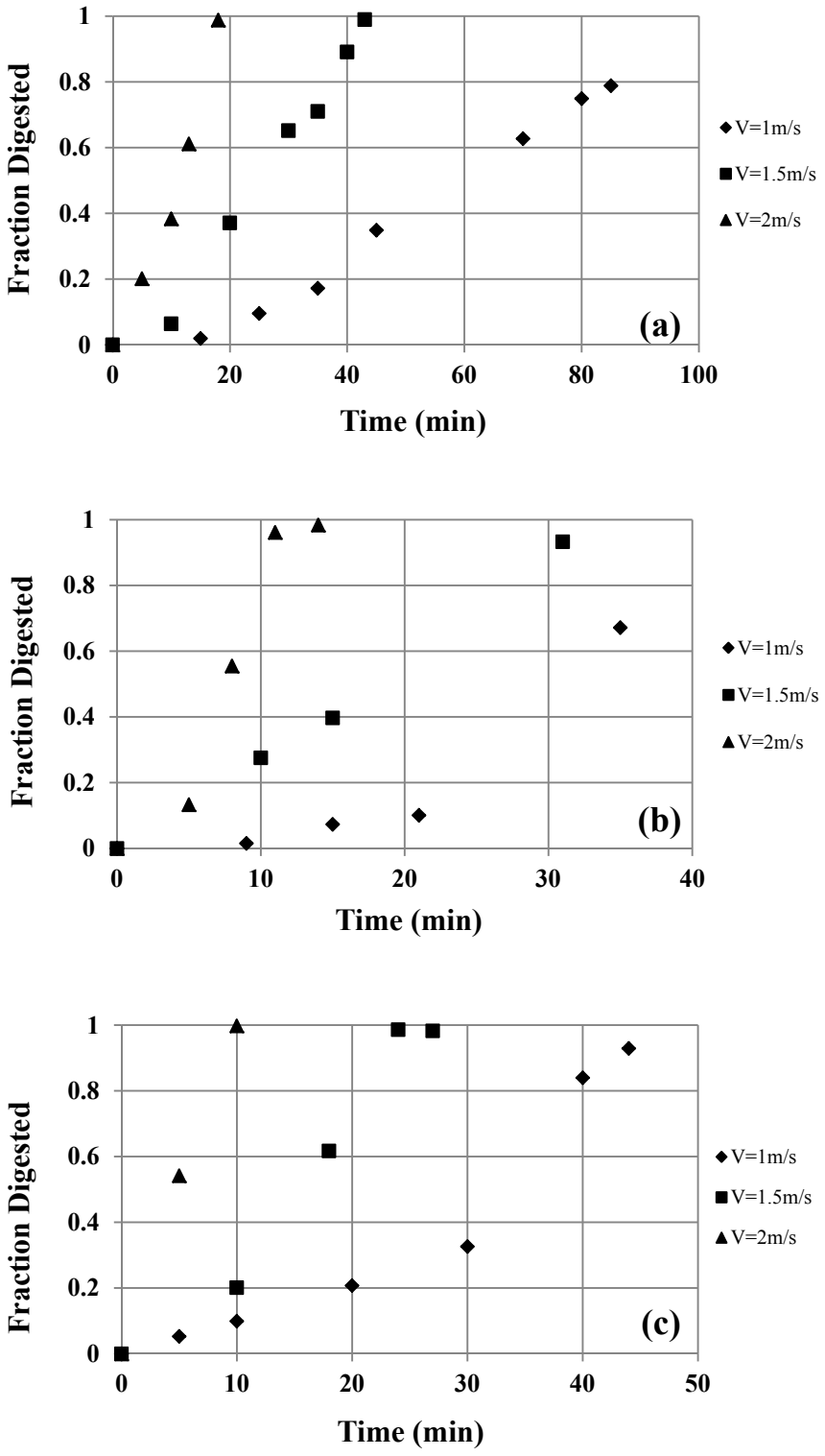

Figure 4.28 Effect of velocity on ablation in (a) water, (b) slurry (C=0.15) and (c) slurry (C=0.30) at T=45°C

In order to quantitatively show how lump ablation is affected by velocity, the ablation rate as a function of flow velocity was investigated. Ablation rate was defined as lump mass loss over a specific period of time and was calculated using:

$$\dot{m} = \left|\frac{(m_{i2} - m_{i1})}{(t_{i2} - t_{i1})}\right| \qquad (4.13)$$

where m_{i1} and m_{i2} denote lump mass at t_{i1} and t_{i2}, respectively.

For each test, lump mass was plotted as a function of time and then ablation rate was calculated for different time segments. It was found that, in most of the cases, ablation rate changed in two steps. It remained unchanged for a relatively short period of time and then increased and remained constant during the remaining time of ablation. It appeared that the first step belongs to the time that heat transfer happens within the oil sand lump; therefore, ablation occurs slowly. It is believed that for the second step of lump ablation, which ablation remains unchanged, lump ablation is more shear stress driven. The fact that lump ablation rate remained constant was different from the results of an experimental study done by SRC in 1996, which showed that ablation rate decreased with decreasing lump size. The difference between the two observations can be explained as:

- For a freely-moving lump, the shear forces acting on the lump decrease as the lump loses mass and becomes smaller. Because lump slip velocity decreases as its size decreases. Also, the smaller lumps are less likely to break up when passing through the pump impeller and thus they lose less mass compared to the larger lumps.
- In the case of the current study, the lump is anchored and therefore lump slip velocity for a constant bulk velocity remains unchanged. Also, lumps do not pass through the pump.

If the ablation rate is linear for the period during which ablation occurs, Equation 4.13 can be simplified as:

$$\dot{m} = \frac{(m_0 - m_f)}{t} \qquad (4.14)$$

where m_0, m_f and t represent lump initial and final mass and time of ablation, correspondingly. Figure 4.29 shows the lump mass plotted against time for ablation in slurry (C = 0.15) at V = 2m/s and T = 30°C (Run No. R-15-3, refer to Table 4.1). According to Equation 4.13, the absolute value of the slope of the trendline is equal to the ablation rate. For this run $\dot{m}_1$ = 0.0042 kg/min and $\dot{m}_2$= 0.0089 kg/min.

Figures 4.30 (a and b) illustrate the lump ablation rate related to the second step of ablation, which is shear stress driven, as a function of velocity for water and slurries (C = 0.15 and 0.30) at T = 30 and 45°C. The trendline for each set of data is given. It seems that lump ablation rate varies as V^n where for ablation at T = 30°C: n = 4- 4.7 and for ablation at T = 45°C: n = 2. This shows that lump ablation at T = 30°C is more mechanical energy driven. However, change of ablation rate for slurry (C = 0.15) at T = 45°C appears to vary with $V^{4.7}$ and the reason for this difference is not clear.

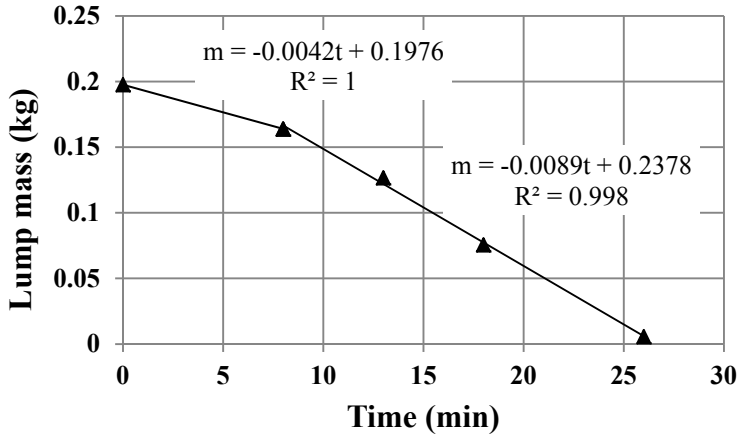

Figure 4.29 Ablation rate: Run No. R-15-3 (Type A lump); V=2m/s and T=30°C

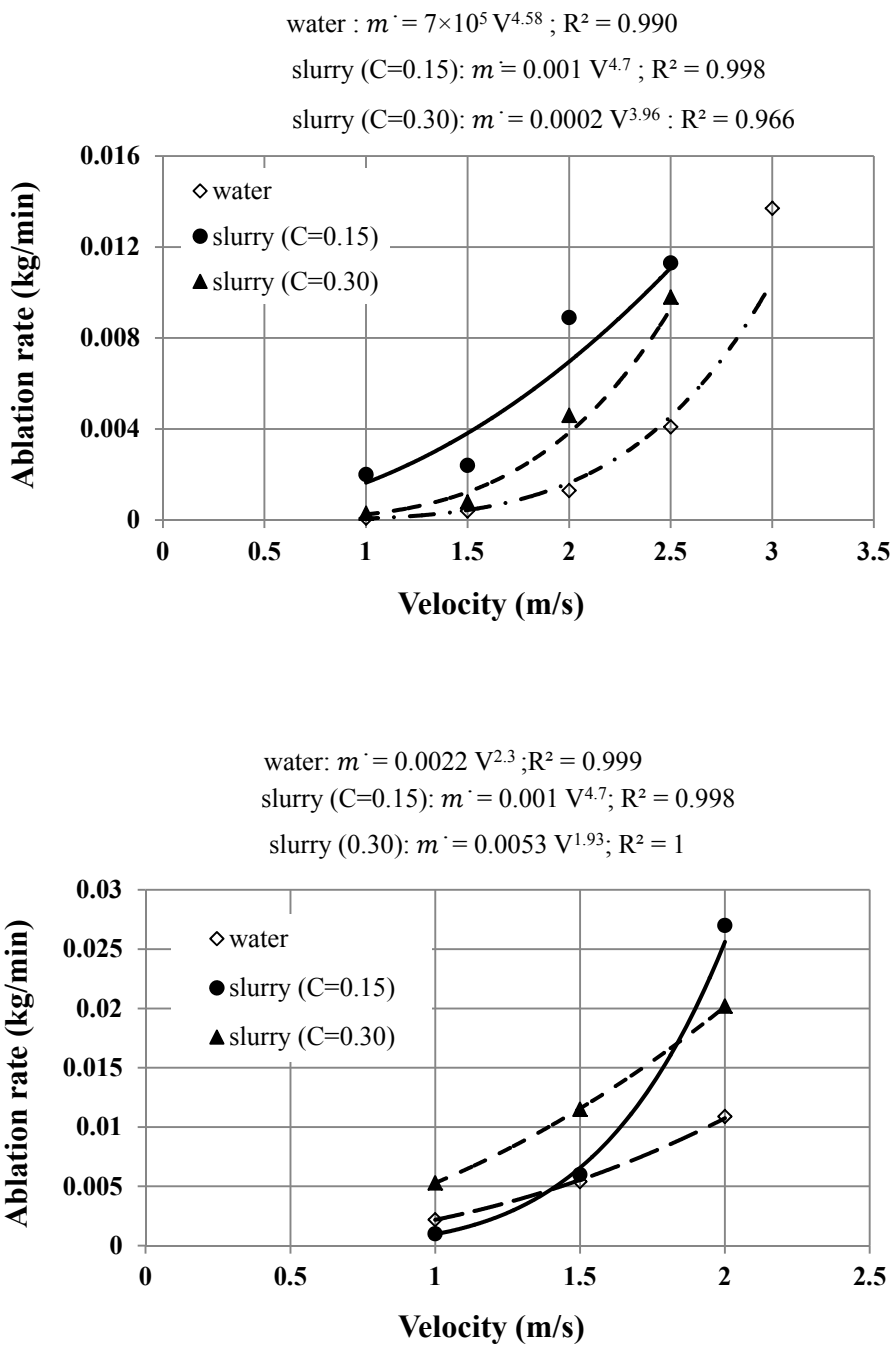

Figure 4.30 Effect of velocity on ablation rate: (a) T=30°C and (b) T=45°C

In summary, the effect of velocity on oil sand lump ablation was investigated using artificial oil sand lumps and the SRC apparatus. These experiments show that lump ablation occurs much more rapidly as velocity increases. Additionally,

it was shown that the lump ablation rate changed in two steps. The first step occurred more slowly, which seemed to be related to the time of heat transfer to lump and the second step appeared to be shear stress driven. Oil sand lump ablation rate varied as a function of V^n where n changes from 2 to 4.7. Lump ablation at the lower slurry temperature is more dependent on velocity. Raw data are given in Appendix 6.

4.6. The effect of slurry concentration on oil sand lump ablation

The calculations done in Chapter 2 showed that with addition of sand to water, the local shear stress increases. During the ablation tests, an increase of ablation rate with increase in slurry concentration was expected.

The observed effects of slurry concentration on lump ablation are shown in Figures 4.31 and 4.32, for T = 30 and 45°C. Each graph shows three different data sets: for water and for two slurry concentrations (C = 0.15 and C = 0.30). Because of limitations in the strain gauge measurements, tests with slurry (C = 0.30) were not conducted for V > 2.5m/s, i.e. maximum strain gauge voltage was reached. According to Figures 4.31 (a, b, c, d and e), ablation in water at T = 30°C was much slower than that in the slurry. However, an increase in the sand concentration, from C = 0.15 to C = 0.30, resulted in a reduction of ablation rate. This phenomenon is more visible at V < 2m/s.

In the case of ablation at T = 45°C, Figures 4.32 (a, b and c), ablation in water is slower than that in the slurry but the increase in slurry concentration seems to have an insignificant effect on the ablation.

It appears that at the lower slurry temperature and high concentration, another factor affects lump ablation. The following possibilities were investigated:

- At high slurry concentration, the chance for adhering sand grains from slurry on the lump increases and it decreases heat transfer and prevents layer-by-layer ablation;

- Sand-water mixture is not properly mixed and this causes the reduction of sand grains contacts with a lump, or
- Turbulence modulation in slurries causes a reduction in surface shear stress.

The first possibility was examined by inspecting an oil sand lump some time (15-20min) after the start of the ablation process in slurry flow (C = 0.30) at low velocities (V = 1 and 1.5m/s). The slurry was stopped and the lump was immediately taken out of the spool and examined closely. No sign of sand grains adhering to the lump was observed. Also, with the assistance of the technicians at the SRC Pipe Flow Centre, mixing of the slurry was checked and it was found that mixing is done properly. Thus, the third possibility, i.e. turbulence modulation, was investigated. It is known that adding solid particles to the turbulent flow modulates the turbulence (Gore and Crowe, 1989) so it is necessary to investigate the way the particulate phase may have influenced the turbulence in this study. Turbulence modulation modifies skin friction and heat transfer (Crowe, 2000; Kim et al., 2005; Zhao et al., 2010). The effect of solid particles on the turbulence/shear stress and heat transfer is discussed in detail in the following sections. Raw data are presented in Appendix 6.

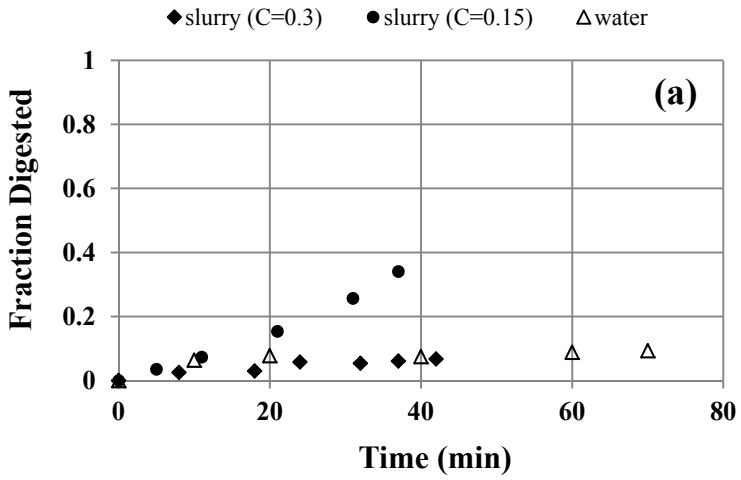

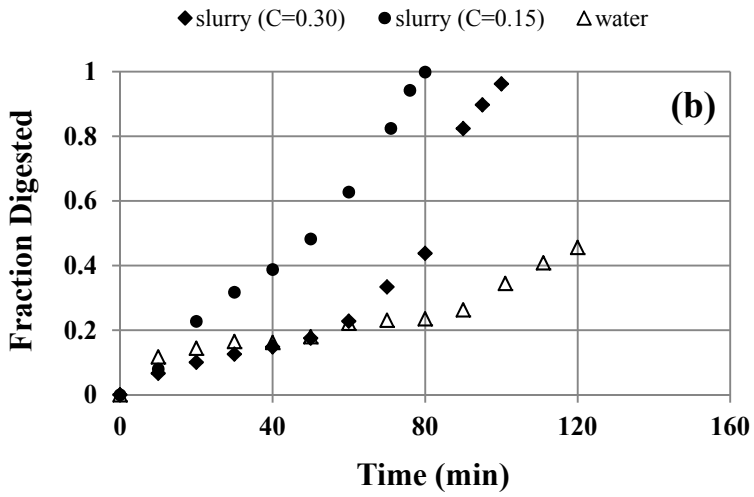
slurry (C=0.30)
slurry (C=0.15)
water
(b)
Fraction Digested
Time (min)
0
0.2
0.4
0.6
0.8
1
0
40
80
120
160

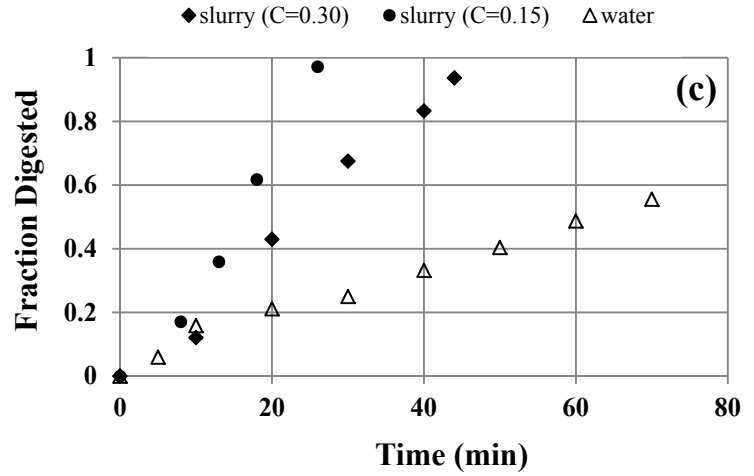
slurry (C=0.30)
slurry (C=0.15)
water
(c)
Fraction Digested
Time (min)
0
0.2
0.4
0.6
0.8
1
0
20
40
60
80

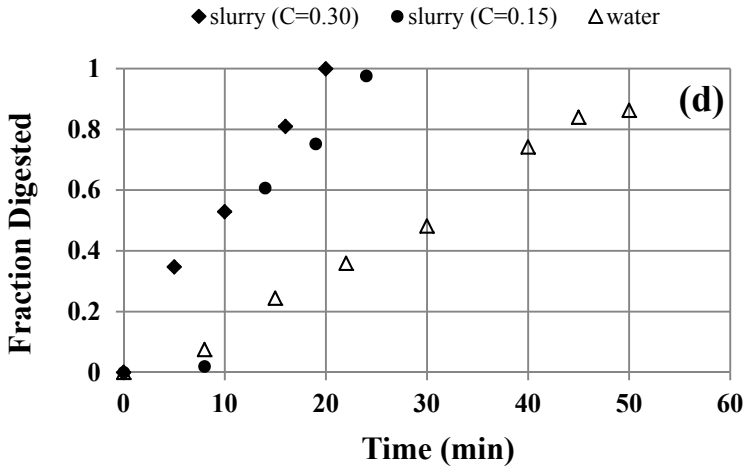
slurry (C=0.30)
slurry (C=0.15)
water
(d)
Fraction Digested
Time (min)
0
0.2
0.4
0.6
0.8
1
0
10
20
30
40
50
60

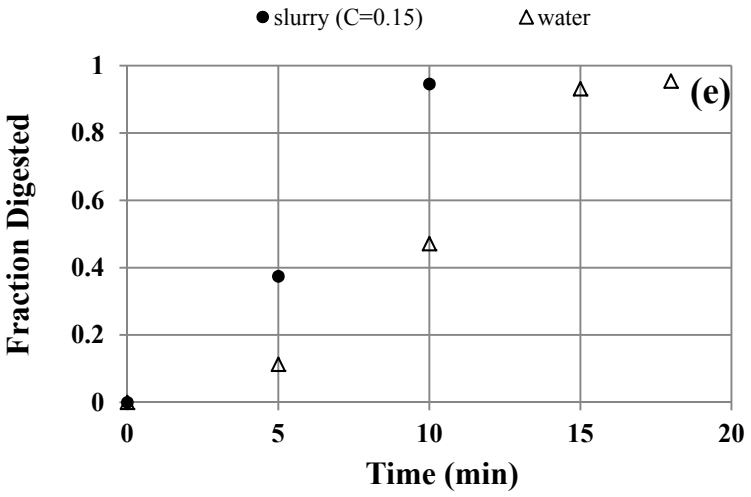

Figure 4.31 Effect of slurry concentration on ablation at T=30°C: (a) V=1m/s; (b) V=1.5m/s; (c) V=2m/s; (d) V=2.5m/s and (e) V=3m/s

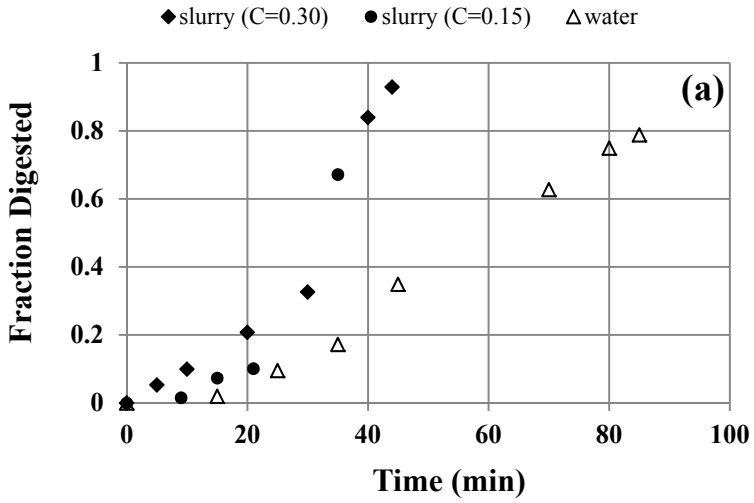

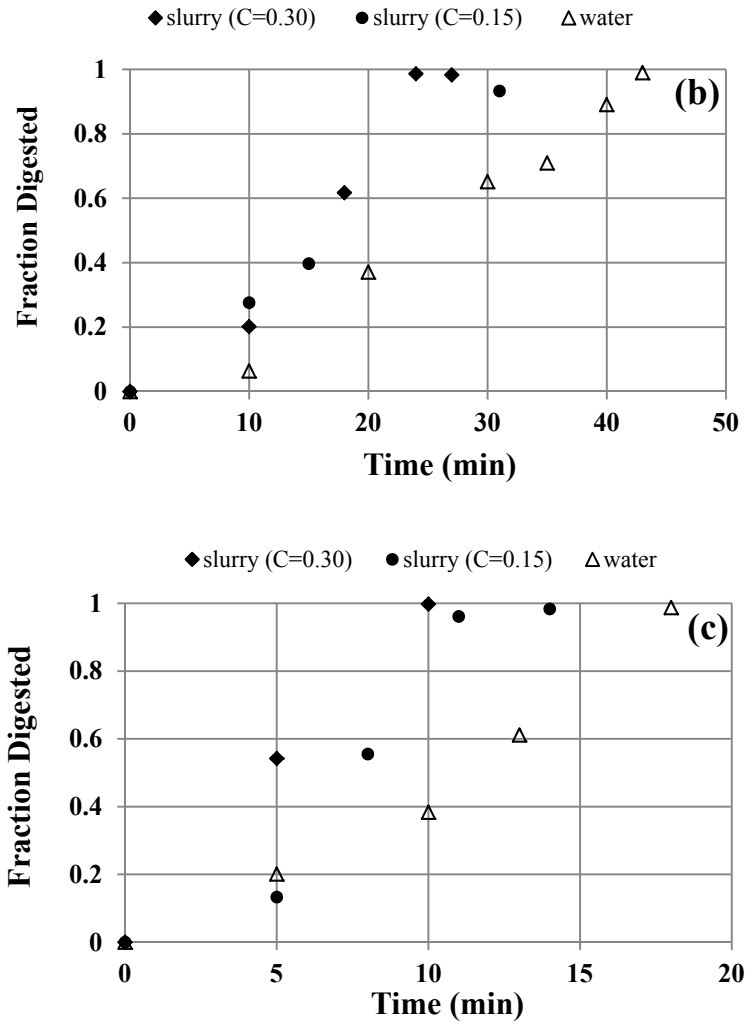

Figure 4.32 Effect of slurry concentration on ablation at T=45°C: (a) V=1m/s; (b) V=1.5m/s and (c) V=2m/s

4.6.1. Estimating shear stress for turbulent flow in a pipe

Previous studies show that addition of small concentrations of solid particles to the flow modifies the turbulence intensity of the carrier fluid (Crowe, 2000). It seems that this is also the case for the current experiments. However, all of the existing studies in the area of turbulence modulation have been completed for extremely dilute mixtures and primarily gas-solid systems. Because findings from previous studies were the only available information on this topic, they were used as a guide to propose a possible effect of sand particles on turbulence intensity in the current study.

For a turbulent flow, velocity measurement as a function of time shows that velocity fluctuates in a chaotic fashion (Bird et al., 1960), as illustrated in Figure 4.33. Thus, the actual local velocity in each direction is the sum of the mean velocity and fluctuating velocity components. For example, in the *z* direction:

$$\boldsymbol{v_z = \overline{v}_z + v'_z} \qquad (4.15)$$

Once the fluctuating velocity is considered, the total average shear stress ($\bar{\tau}$) is calculated as the sum of the viscous momentum flux ($\bar{\tau}^{(v)}$) and the turbulent momentum flux ($\bar{\tau}^{(t)}$). For example, the total shear stress can be written as (Bird et al., 1960; Versteeg and Malalasekera, 1995):

$$\boldsymbol{\bar{\tau}_{yz} = \bar{\tau}_{yz}^{(v)} + \bar{\tau}_{yz}^{(t)}} \qquad (4.16)$$

where, viscous momentum flux is calculated based on Newton's law of viscosity:

$$\boldsymbol{\bar{\tau}_{yz}^{(v)} = \mu \left(\frac{\partial \overline{v_y}}{\partial z} + \frac{\partial \overline{v_z}}{\partial y}\right)} \qquad (4.17)$$

and in analogy with Newton's law of viscosity, the turbulent momentum tensor (turbulent shear flow) is equal to:

$$\boldsymbol{\bar{\tau}_{yz}^{(t)} = \mu^{(t)} \left(\frac{\partial \overline{v_y}}{\partial z} + \frac{\partial \overline{v_z}}{\partial y}\right)} \qquad (4.18)$$

where μ and $\mu^{(t)}$ denote fluid viscosity and turbulent or eddy viscosity.

The total average shear stress is precisely determined if the turbulent momentum tensor and eddy viscosity are known.

Based on the *k*-ε model, the eddy viscosity can be defined as (Versteeg and Malalasekera, 1995):

$$\boldsymbol{\mu^{(t)} = \rho C_\mu \frac{k^2}{\varepsilon}} \qquad (4.19)$$

where, k is the kinetic energy of turbulence that depends on the turbulence intensity (σ) and is calculated as:

$$\boldsymbol{k = \frac{9}{4}\left(\sigma\, v_{ref}\right)^2} \qquad (4.20)$$

and v_{ref} is a reference velocity, here equal to the bulk velocity, and ε denotes the dissipation of the turbulent kinetic energy created by work done by the smallest eddies against viscous shear stress. The dissipation of turbulent kinetic energy can be calculated using:

$$\boldsymbol{\varepsilon = \frac{k^{3/2}}{l}} \qquad (4.21)$$

According to Versteeg and Malalasekera (1995), the constant C_μ in Equation 4.19 is a dimensionless constant that, with comprehensive data fitting, is estimated as 0.09. In Equation 4.21, l is the eddy length scale, which for a fully developed flow in a pipe can be estimated as:

$$\boldsymbol{l = D[0.07 - 0.04\left(1 - \frac{2s}{D}\right)^2 - 0.03\left(1 - \frac{2s}{D}\right)^4]} \qquad (4.22)$$

where s is the distance from centre of the pipe.

It is understood from these equations that to calculate the eddy viscosity and the kinetic energy of turbulence, the turbulence intensity in the slurry must be appropriately estimated (Versteeg and Malalasekera, 1995).

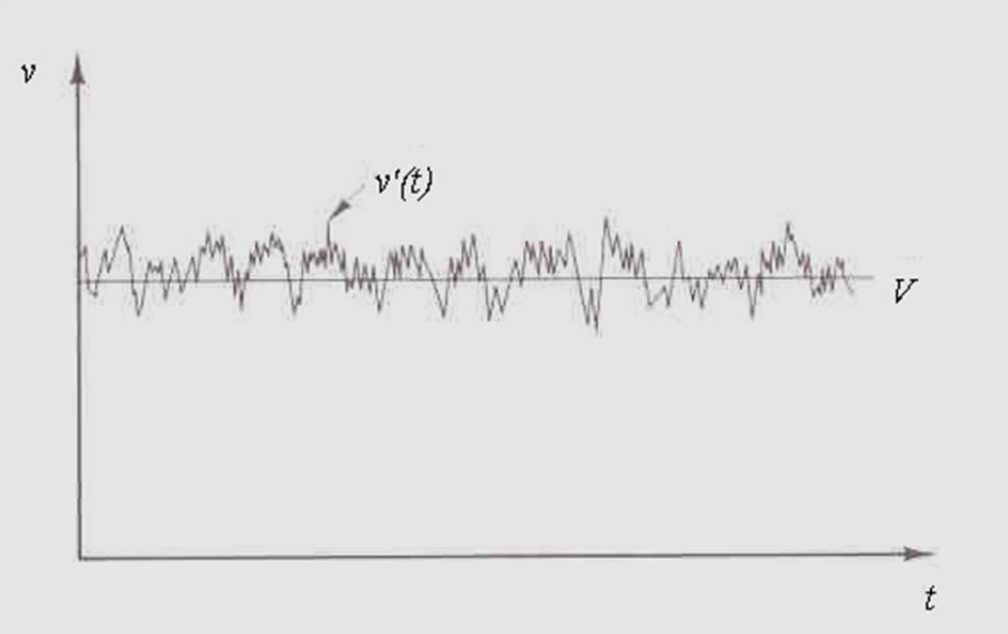

Figure 4.33 Velocity fluctuations of turbulent flow
(Bird et al., 1960)

Addition of particles, even in very low concentrations, to the flow modulates the turbulence intensity of the carrier fluid (Crowe, 2000). Gore and Crowe (1989), using existing experimental studies, defined a critical parameter as the ratio of the particle diameter to the turbulence length scale (d_p/l) to quantify the change of the turbulence intensity because of the addition particles to the flow. Crowe (2000) used the same critical parameter and existing studies to develop a correlation to estimate the change of turbulence intensity because of the addition of particles to the flow. The model was developed based on the volume-averaged equations for kinetic energy of the carrier phase. It is valid for dilute slurries. Equation 4.23 shows the Crowe model, where k' and k are the turbulent kinetic energy for the dilute slurry flow and the particle-free flow, respectively. The ratio of the mass of the dispersed solid phase to the mass of the carrier fluid calculated using Equation 2.24 (Crowe, 2000), is referred to as C′.

$$\frac{k'}{k} = \frac{1+0.55C'\left(gD/V^2\right)^{1.6}\left(\rho_f VD/\mu_f\right)^{0.2}\left(l/D\right)^{1.8}\sigma^{-3}\left(d_p/l\right)^{0.8}}{1+\left(\rho_f/\rho_s\right)^{1/3}C'^{1/3}\left(d_p/l\right)^{-1}} \qquad (4.23)$$

$$C' = \frac{\textbf{Mass of solid phase}}{\textbf{Mass of liquid phase}} \qquad (4.24)$$

It is noteworthy that all the experimental data used by Crowe were collected for extremely dilute gas-solid flows. Figure 4.34 shows the Crowe (2000) model predictions in comparison to the existing experimental data. The only data collected for liquid-solid slurry flow are those of Zisselmar and Molerus (1979). Again this graph suggests that turbulence intensity is highly influenced by solids and its change depends on the slurry concentration and d_p/l. In the current system, most likely addition of sand attenuates the turbulence intensity and this causes the reduction of local shear stress. Based on Equation 4.19, eddy viscosity, $\mu^{(t)}$, is proportional to k^2; thus, if k decreases when solid is added, turbulent shear flow, $\bar{\tau}_{yz}^{(t)}$, and local shear stress, $\bar{\tau}_{yz}$ decrease.

Additionally, Zhao et al. (2010) showed that skin friction decreases with addition of solid particles to the flow. However, to conclude turbulence modulation affects oil sand lump ablation at lower slurry temperature, more investigation is necessary to fully understand the turbulence intensity in concentrated slurries.

The effect of turbulence modulation is also important in slurries at T = 45°C but at the higher slurry temperature, heat transfer seems to be the dominant phenomenon in oil sand lump ablation. Details about the effect of slurry temperature on oil sand lump ablation are discussed in Section 4.7.

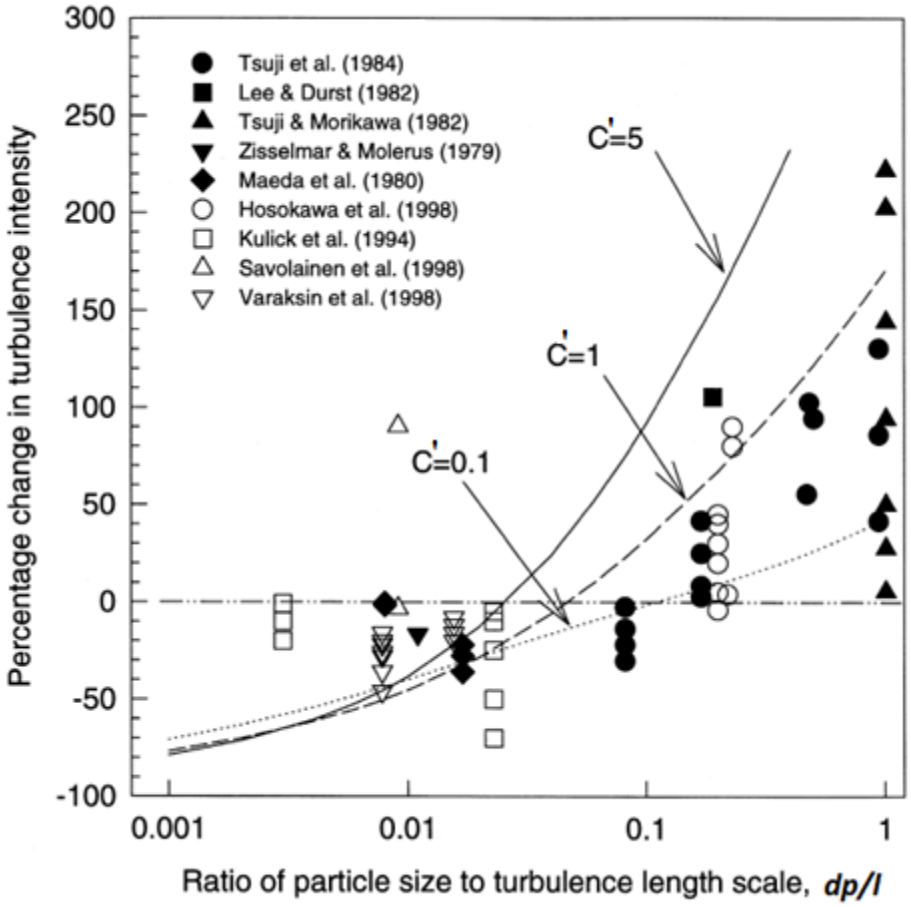

Figure 4.34 Crowe model predictions in comparison with the experimental data
(Crowe, 2000)

4.6.2. Effect of increase of solids concentration on heat transfer

Two processes are critical to the lump ablation: viscosity reduction of the lump because of heat transfer from the flow, followed by the removal of the softened outer layer of the lump as a result of the shear forces acting on the lump surface. One cannot describe or model ablation without discussing heat transfer. In other words, one cannot describe the effect of shear force on lump ablation without first describing the mechanism of viscosity reduction because of heat transfer from the slurry to the lump surface.

Heat transfer from the slurry to the lump occurs by convection and then by conduction within the lump (Masliyah, 2008). Before an oil sand lump is exposed

to the flow, free convection from air occurs; once it is exposed to the slurry flow, heat is transferred to the lump through forced convection. Recall that bitumen viscosity is highly temperature-dependent; therefore, the viscosity of bitumen at each point on the lump surface might differ depending on the temperature. In order to estimate the ablation rate of an oil sand lump for certain operating conditions, the temperature profile of the oil sand lump and consequently the bitumen viscosity of each point must be known.

If one assumes oil sand lumps as a two-dimensional object whose lengths are placed in x and y coordinates, the 2D temperature profile for that oil sand lump can be written as Equation 4.25. When heat convection occurs in both directions, the boundary conditions are defined as Equations 4.26 a and b (Holman, 2010):

$$\frac{\partial^2 T}{\partial^2 x} + \frac{\partial^2 T}{\partial^2 y} = \frac{1}{\alpha}\frac{\partial T}{\partial t} \qquad (4.25)$$

$$hA(T_\infty - T)_{x=0,y} = -k_t A \frac{\partial T}{\partial x}\Big]_{x=0,y} \qquad (4.26\ a)$$

$$hA(T_\infty - T)_{y=0,x} = -k_t A \frac{\partial T}{\partial y}\Big]_{y=0,x} \qquad (4.26\ b)$$

where h, k_t and $\alpha = \frac{k_t}{\rho C_p}$ represent the heat transfer coefficient, thermal conductivity and thermal diffusivity, respectively (Holman, 2010).

The heat transfer coefficient for a smooth cylinder in a fluid flow is calculated using the following correlations:

Free convection:

$$Nu = 0.125\ (Gr\ Pr)^{1/3} \qquad (4.27)$$

$$\text{for} \quad GrPr = 10^7 - 10^{12}$$

where, $Nu = \frac{hd}{k_t}$, $Gr = \frac{g\beta(T_S - T_\infty)d^3}{\vartheta^2}$ and $Pr = \frac{C_p \mu}{k_t}$. Dimensionless numbers must be calculated at $T_f = \frac{(T_S + T_\infty)}{2}$ and $\beta = \frac{1}{T_f}$.

Forced convection:

$$\boldsymbol{Nu = 0.3 + \frac{0.62\, Re^{1/2} Pr^{1/3}}{\left[1+\left(\frac{0.4}{Pr}\right)^{2/3}\right]^{1/4}}\left[1+\left(\frac{Re}{282000}\right)\right]^{4/5}} \quad (4.28)$$

Equation 4.28 is valid for Re = 10^2-10^7 when RePr > 0.2.

While convective heat transfer from a turbulent single-phase flow to a solid object is well understood, there is almost no information available (e.g. heat transfer coefficient) for slurry flows. However, one can approximate the trend of change of heat transfer coefficient for a cylindrical oil sand lump using the existing correlations for heat transfer from the pipe wall to the slurry, or vice versa.

Kiyohashi et al. (1974) studied the heat transfer from homogeneous slurries, of different sizes of limestone, to the pipe inner wall and developed the following correlation for slurries with particle diameter of d_{50} = 0.080-0.150mm (Kiyohashi et al., 1974):

$$\boldsymbol{Nu = 0.00567\, Re^{0.987} Pr^{0.4}} \quad (4.29)$$

where: $Nu = \frac{Dh_m}{k_{tm}}$, $Pr = \frac{C_{pm}\mu_m}{k_{tm}}$, $Re = \frac{VD\rho_m}{\mu_m}$

$$\boldsymbol{C_{Pm} = C_{mass} C_{ps} + (1 - C_{mass}) C_{pf}} \quad (4.30)$$

$$\boldsymbol{\mu_m = \mu_f (1 + 22.4\, C)} \quad (4.31)$$

$$\boldsymbol{k_{tm} = \frac{2k_{tf} + k_{ts} - 2C\,(k_{tf} - k_{ts})}{2k_{tf} + k_{ts} + C\,(k_{tf} - k_{ts})}} \quad (4.32)$$

In these equations, ρ_m denotes the density of the slurry that is calculated using Equation 4.10 and C_{mass}, k_{ts} and k_{tf} are mass fraction of solids in the slurry, the particle heat conductivity and carrier fluid heat conductivity, respectively.

Additionally, Farber and Depew (1963) showed that with addition of 0.200mm particles to water, the ratio of slurry Nusselt number to fluid Nusselt number decreases at low solids concentrations and then reaches a plateau at higher slurry concentrations. Figure 4.35 illustrates their experimental result in comparison with a numerical study done by El-Behery et al. (2011).

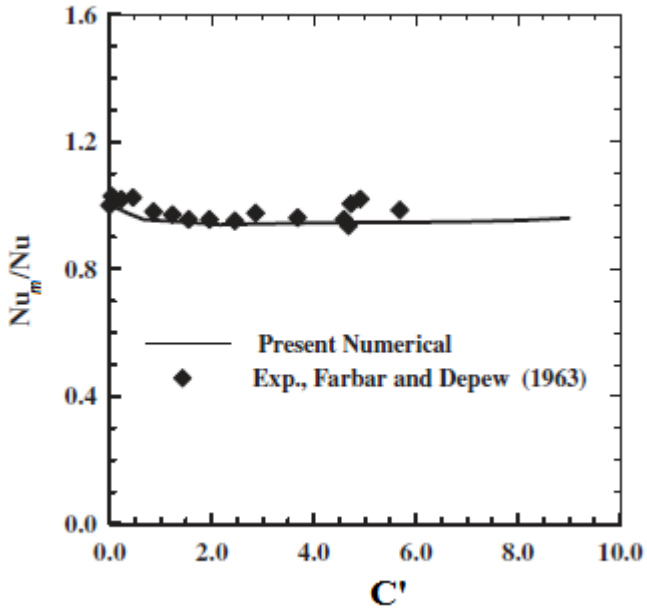

Figure 4.35 Effect of addition of 0.200mm solid particles to water on heat transfer
(El-Behery et al., 2011)

As discussed here, addition of particles to the flow modifies the heat transfer to/from the flow. The effects of mixture velocity and solids concentration on the heat transfer coefficients for the current system were evaluated using the equations given above and the results are presented in Table 4.6. Parameters given in Table 4.5 were used as inputs to calculate Nusselt numbers and heat transfer coefficients. It is understood from Table 4.6 that the heat transfer coefficient for the more concentrated slurry could be expected to be reduced by 22% from that estimated for the lower concentration mixture. The reduction is velocity-independent.

Table 4.5 Input parameters for heat transfer coefficient calculations for slurries (C=0.15 and 0.30)

	Term	Value
	D (m)	0.104
Component properties	k_{ts}(W/mK)	0.2
	Cp_s (J/kgK)	800
	ρ_s (kg/m^3)	2650
Carrier fluid properties	k_{tf} (W/mK)*	0.6
	Cp_f(J/kgK)*	4174
	ρ_f (kg/m^3)	995.7
	μ_f (Pa.s)	8×10^{-4}
Slurry (C = 0.15) properties	k_{tm} (W/mK)	0.5
	Cp_m (J/kgK)	3115
	ρ_m (kg/m^3)	1247.5
	μ_f (Pa.s)	4×10^{-3}
	Pr	27.3
Slurry (C = 0.30) properties	k_{tm} (W/mK)	0.5
	Cp_m (J/kgK)	2381
	ρ_m (kg/m^3)	1494
	μ_f (Pa.s)	8×10^{-3}
	Pr	36.6

* (Holman, 2010)

Table 4.6 Heat transfer coefficient at T=30°C: slurries (C=0.15 and 0.30)

	Slurry (C=0.15)			Slurry (C=0.30)			
Slurry bulk velocity (m/s)	Pipe Reynolds number	Nusselt number	h (W/m^{2}K)	Pipe Reynolds number	Nusselt number	h (W/m^2 K)	% difference
1	2.9×10^4	547	2628	2×10^4	423	2052	22
1.5	4.4×10^4	817	3921	3×10^4	631	3062	22
2	5.9×10^4	1085	5208	4×10^4	839	4068	22
2.5	7.4×10^4	1352	6492	5×10^4	1045	5070	22
3	8.8×10^4	1618	7772	6×10^4	1251	6069	22

Similarly, Figure 4.36 can be used to predict the effect of slurry concentration on the heat transfer coefficient. The ratio of the solid mass to the liquid mass (C') for the slurries (C = 0.15 and 0.30) was 0.47 and 1.13, respectively. According to Figure 4.35, as C' increases from 0.47 to 1.13, the ratio of the slurry Nusselt number to the carrier fluid Nusselt number is reduced slightly. Based on this graph:

At C'= 0.47, Nu_m/Nu = 0.99

At C'= 1.13, Nu_m/Nu = 0.97

thus, with increase of solid particles the Nusselt number ratio decreases by 2%. For both slurries, by substituting k_{tm} from Table 4.4 into the Nusselt number equation $Nu_m = \frac{h_m D}{k_{tm}}$, heat transfer coefficient is calculated. Using this method, it is concluded that heat transfer coefficient decreases by 1% by addition of 15 vol% solid particles to the slurry.

Overall, the two methods described above were originally developed for heat transfer between slurry and the surrounding pipe. However, they were used in this study to directionally indicate how slurry concentration could affect heat transfer to an oil sand lump. From this analysis, it appears that the heat transfer coefficient reduces with increasing slurry concentration-which is another possible cause for the slower oil sand lump ablation in slurry (C = 0.30) at T = 30°C. In the same way, this effect is present in the case of the ablation at T = 45°C but it is less pronounced because at this temperature, the temperature difference between slurry and lump is much higher and the temperature difference is the dominant driving force for the heat transfer (refer to Equations 4.26 (a and b)). It is concluded that the dominant driving force is not affected by the slight change of heat transfer coefficient so the slight decrease of heat transfer coefficient with increasing slurry concentration does not affect ablation at T = 45°C.

4.7. The effect of slurry temperature on oil sand lump ablation

Bitumen holds the sand grains together in an oil sand lump: the lower the bitumen viscosity, the faster the size reduction of the oil sand lump (Masliyah, 2008). Bitumen viscosity is highly temperature-dependent and it significantly reduces with increasing temperature. The Saskatchewan Research Council experiments (Masliyah, 2008; Shook et al., 2002) showed considerable ablation enhancement with increasing slurry temperature. In this study, oil sand lump ablation in water and slurries (C = 0.15 and 0.30) at T = 30 and 45°C, flowing at 1, 1.5 and 2 m/s were tested. The fraction of lump digested as a function of time was plotted for all the experimental runs and the effect of operating temperature on the oil sand lump ablation was investigated.

Figures 4.36 (a, b and c) illustrate the fraction of lump digested as a function of time for lump ablation in water and slurries (C = 0.15 and 0.30) flowing at different velocities. On each graph, data related to tests at T = 30°C are shown with open symbols and those for runs at T = 45°C are represented with black symbols. Comparing the data for ablation in water flowing at V = 2m/s, at two different temperatures, it takes about 70min for a lump to be 60% ablated at T = 30°C while it takes approximately ¼ of that time for a lump to ablate completely at T = 45°C (Figure 4.36(a)). Additionally, complete lump ablation occurs in 25min at T = 30°C whereas it happens in 15min at T = 45°C for tests conducted using slurry (C = 0.15) at V = 2m/s (see Figure 4.36(b)). The time required for complete ablation in slurry (C = 0.30) flowing at V = 2m/s and T = 45°C is about 1/5 of that at T = 30°C, shown on Figure 4.36(c). It appears that the effect of temperature on lump ablation is more pronounced for ablation in water and slurry (C = 0.30) than that in slurry (C = 0.15) and this observation is persistent for ablation at different velocities. In other words, heat transfer is the dominant phenomenon in flows that are postulated to have lower local shear stresses.

Moreover, Figures 4.36 (a) and 4.36 (c) show that lump ablation at V = 1m/s and T = 45°C occurred at a similar rate as at V = 2m/s and T = 30°C. This means that

for water and slurry (C = 0.30), an increase of slurry temperature by 15°C has the same effect on the lump ablation as the increase of velocity by 1m/s. However, Figure 4.36 (b) shows that the lump ablation rate for the runs at V = 1.5m/s and T = 45°C corresponded with the ablation rate for the test at V = 2m/s and T = 30°C. This indicates that in the case of slurry (C = 0.15), an increase of the slurry temperature by 15°C has the same effect on the lump ablation as the increase of velocity by 0.5m/s. Therefore, this again confirms that slurry temperature has a more significant effect on the lump ablation in water and slurry (C = 0.30) than that in the 15% slurry. The raw data are presented in Appendix 6.

It is concluded from these analyses that slurry temperature significantly affects oil sand lump ablation. Increase of water and 30% slurry temperature by 15°C results in the same amount of increase of lump ablation when the velocity increases by 1m/s. However, 15°C increase in slurry temperature and 0.5m/s velocity increase have the same effect on the ablation of an oil sand lump in the 15% slurry.

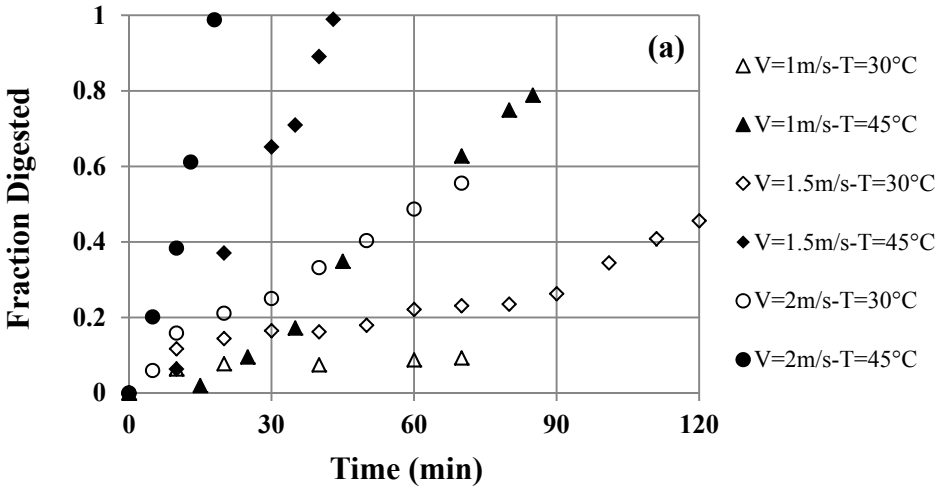

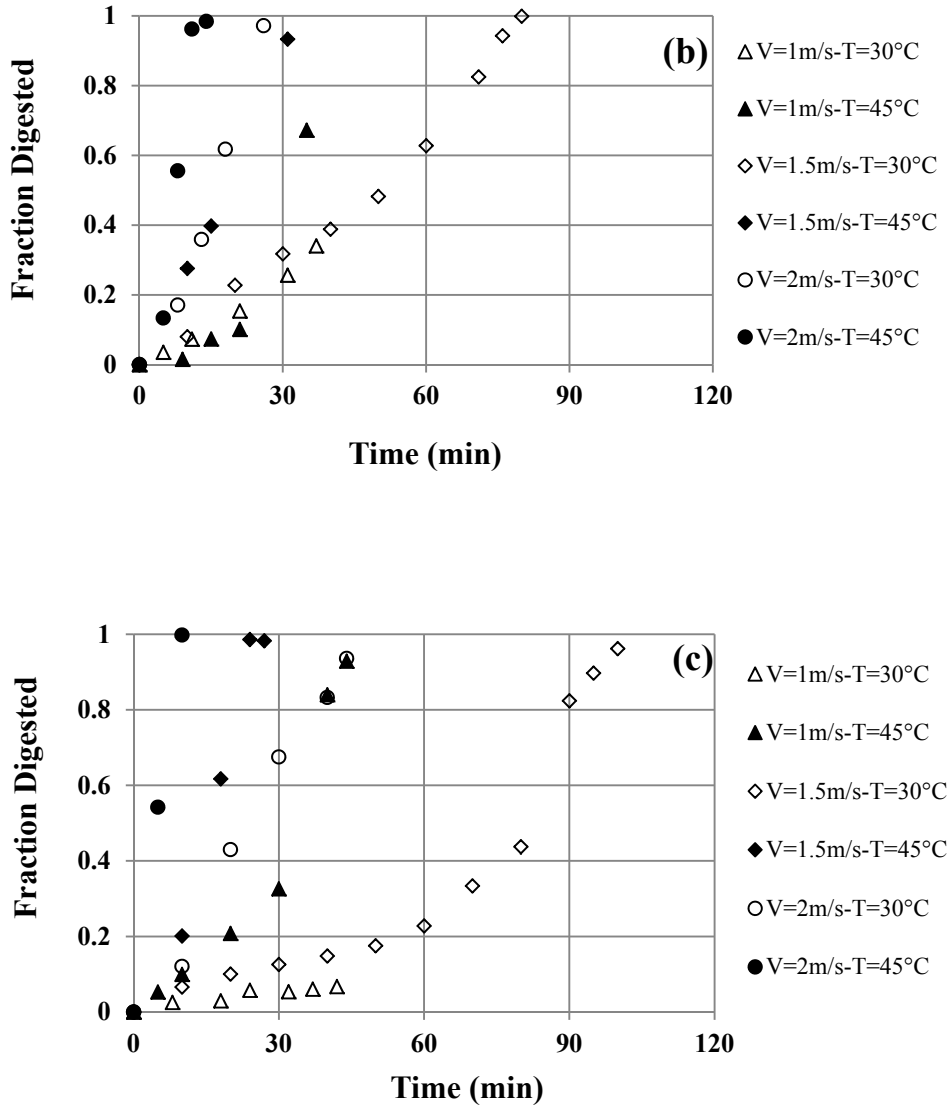

Figure 4.36 Effect of slurry/water temperature on ablation: (a) water; (b) slurry (C=0.15) and (c) slurry (C=0.30)

4.8. Comparison of ablation rates with changes in lump constituents

The two types of artificial oil sand lumps produced for this study were different in terms of their components, i.e. bitumen and sand. Type A oil sand lumps were made using the artificial tailings sand prepared by mixing the commercially available sand grains and ATB-2, which is described in Chapter 3. Type B oil

sand lumps were manufactured using the washed Syncrude tailings sand and ATB-1 bitumen. It must be noted that at all temperatures, the viscosity of ATB-1 was lower than that of ATB-2. The results discussed earlier in this chapter were based on the experiments completed using Type A oil sand lumps; here, a number of experimental runs were repeated using Type B lumps. The fraction digested, calculated using Equation 3.3, was plotted as a function of the time of the ablation for the two identical tests conducted using the two different oil sand lumps. Because a limited number of Type B lumps were available, only a few ablation tests in water were completed for comparison. Additionally, the effects of velocity and temperature on the ablation of Type B lumps were examined.

Figures 4.37 and 4.38 show the results of the experiments conducted using Type A and Type B lumps at identical conditions. In Figure 4.37 (a and b), ablation of the two lumps in water at V = 1 and 1.5m/s and T = 45°C is compared. In Figure 4.38 (a and b) data for water at V = 1 and 1.5m/s and T = 30°C are presented. It can be seen from these figures that for both velocities and temperatures tested, Type B lumps ablate much more rapidly than Type A lumps. This is because the viscosity of the bitumen used in manufacturing Type B lump was significantly lower than the viscosity of the bitumen consumed for manufacturing Type A lump.

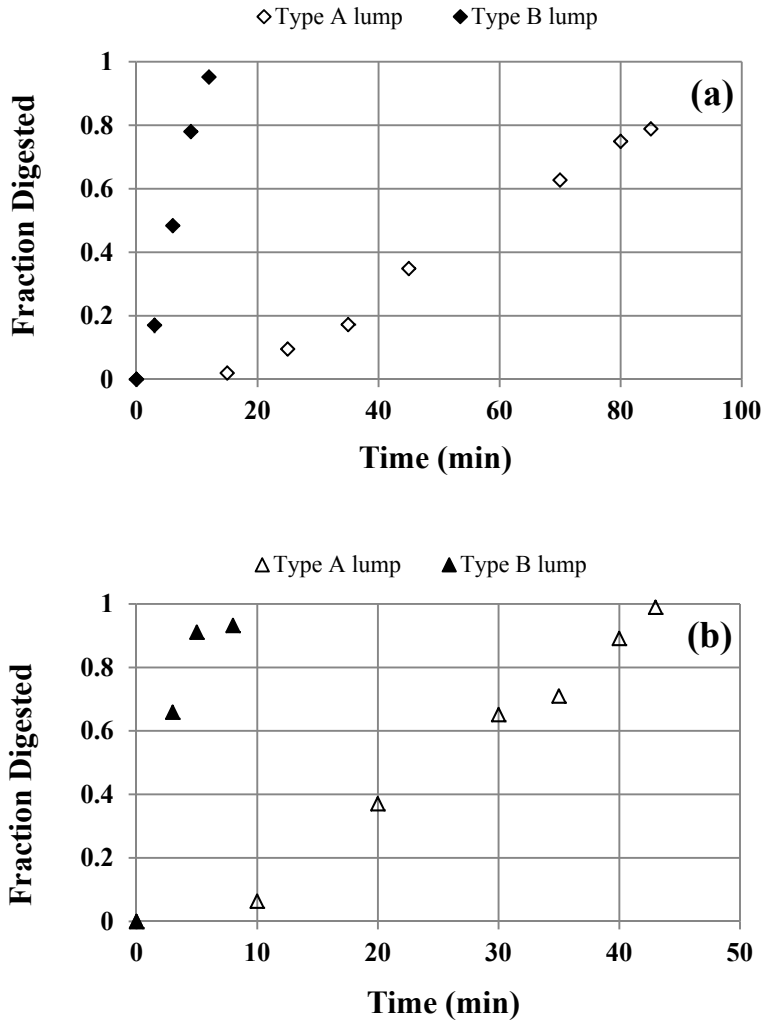

Figure 4.37 Effect of lump material on ablation in water at T=45°C: (a) V=1m/s and (b) V=1.5m/s

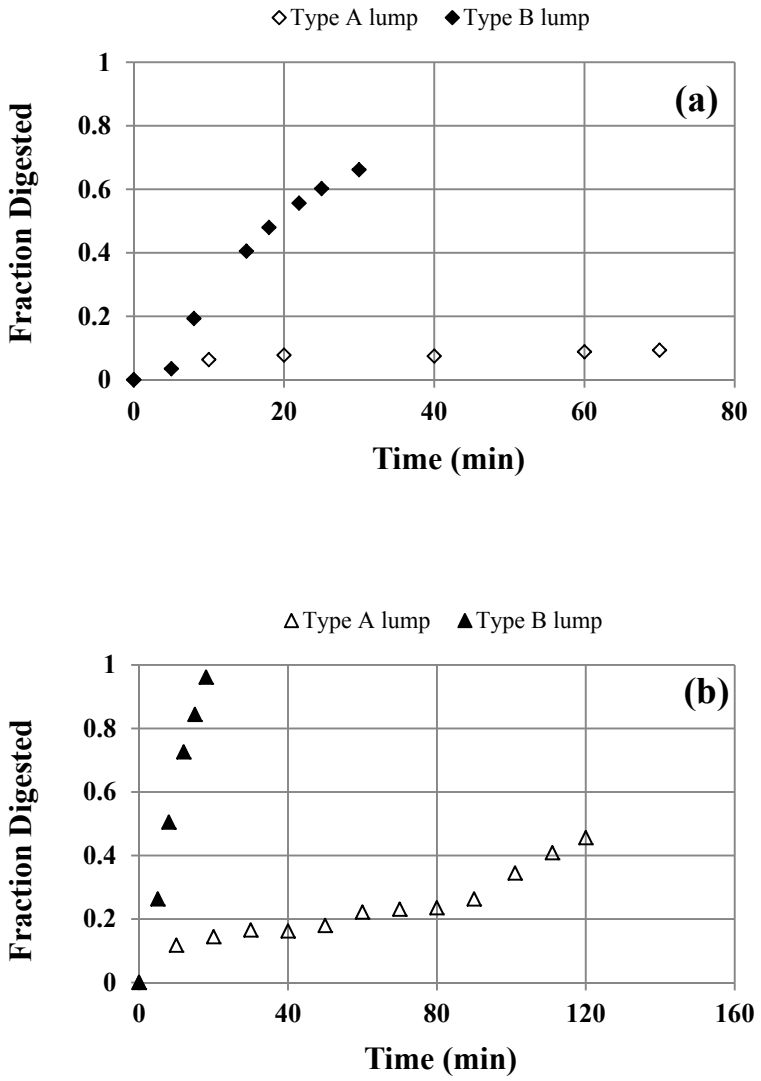

Figure 4.38 Effect of lump material on ablation in water at T=30°C: (a) V=1m/s and (b) V=1.5m/s

The effects of velocity and temperature on the ablation of Type B lumps were also investigated. Figures 4.39 (a and b) and 4.40 (a and b), respectively, show the effects of water velocity and temperature on ablation. In both graphs, the fraction of lump digested is plotted against time of ablation. According to these figures, the ablation rate increases significantly as the water temperature and velocity increases. The time to complete ablation in water flowing at V = 1 and 1.5m/s and at T = 30°C is half that observed for water flowing at T = 45°C. An increase in the

velocity from 1 to 1.5m/s has the same effect and reduces the time to complete ablation by 50%.

It is clear from these results that in general, ablation of a Type B lump occurred much more rapidly than with a Type A lump. However, changes in velocity or temperature seem to have similar effects on the ablation of both samples.

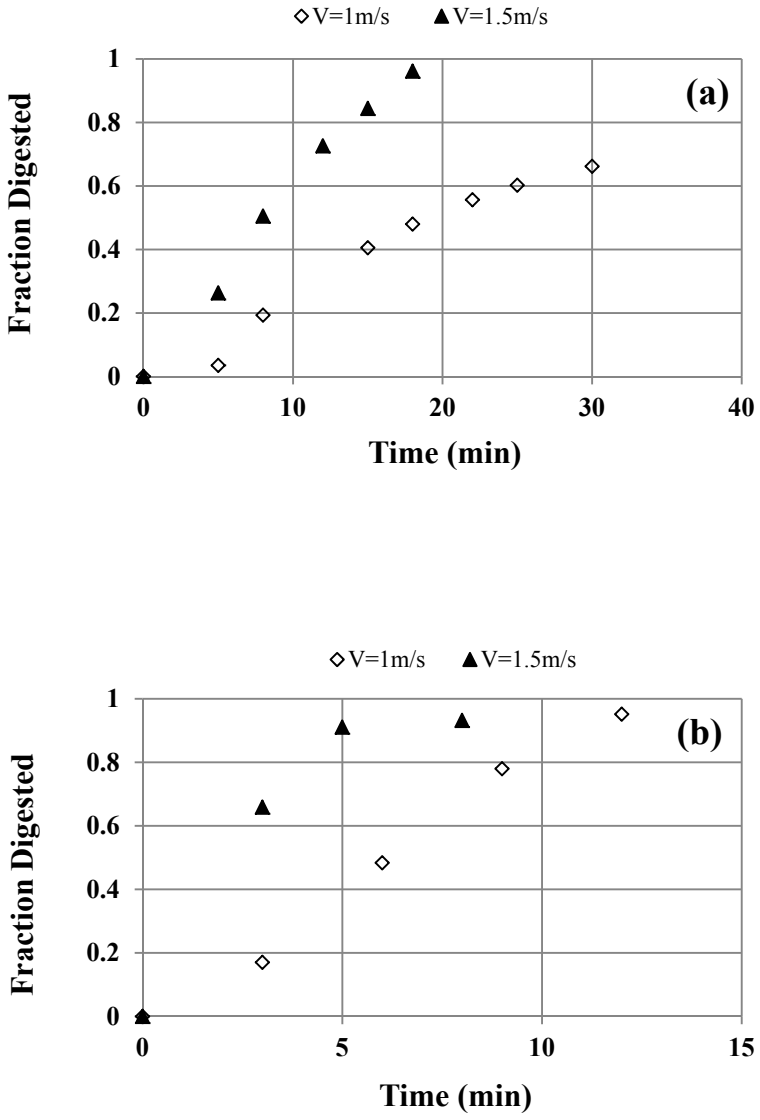

Figure 4.39 Effect of velocity of water on ablation of Type B lump at (a) T=30°C and (b) T=45°C

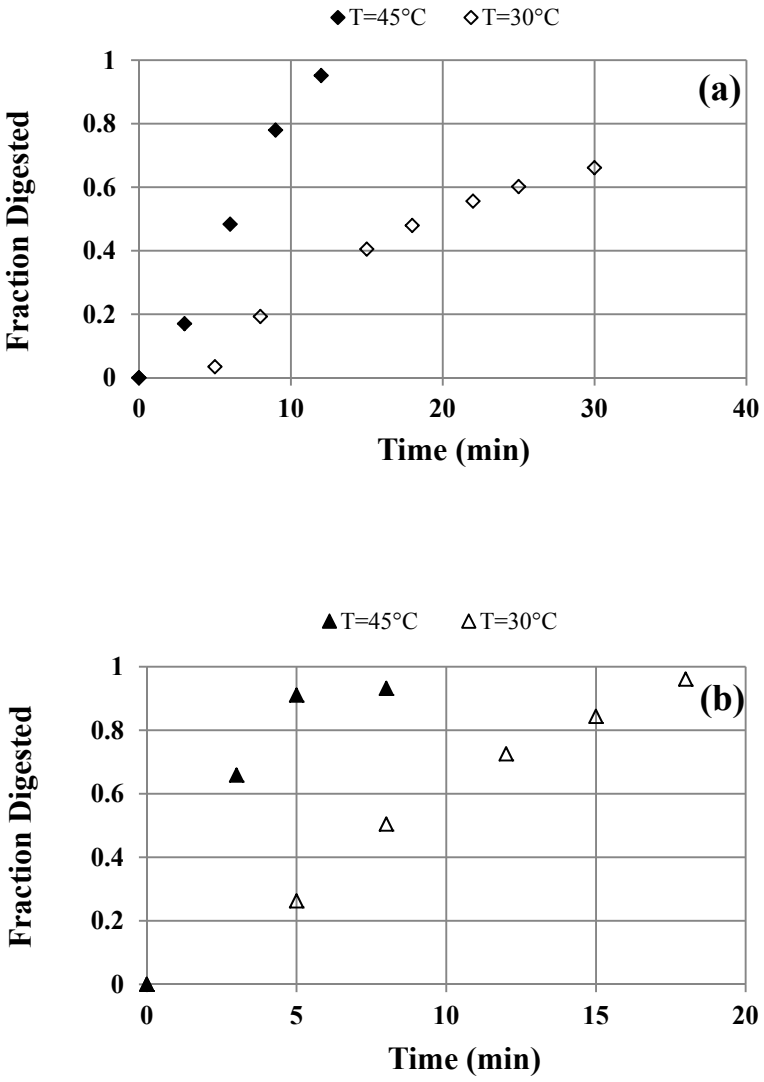

Figure 4.40 Effect of temperature of water on ablation of Type B lump at (a) V=1m/s and (b) V=1.5m/s

4.9. Measurement of drag force on ablating oil sand lump

For each experimental test, the drag force acting on the lump was calculated by subtracting the drag force on the empty basket from the total drag force measured, as described in Section 4.2.3. The drag force acting on the lump was plotted as a function of time on the primary axis and adjusted oil sand lump size was plotted on the secondary axis as a function of time. The adjusted oil sand lump diameter at a certain time was calculated using the strain gauge measurements, lump mass at that time and the oil sand lump density. It was assumed that for some time from start of the ablation process, the oil sand lump retains its cylindrical shape with L/d = 1 and then it becomes spherical. This assumption is based on the observations made in the visualizations tests presented at the beginning of this chapter. The time that change of the lump shape to spherical occurs must be estimated. The procedure used in this study is as follows:

1) It was first assumed that throughout the entire ablation time, a lump remains cylindrical with L/d = 1. Equivalent cylindrical diameter for lump at each time was then calculated using:

$$\boldsymbol{d_i = 2\left(\sqrt[3]{\frac{4\,m_i}{\pi \rho_{lum}}}\right)} \qquad (4.33)$$

where m_i and ρ_{lum} denote lump mass at time i and lump density, respectively.

2) It was then assumed that lump was spherical from the beginning to the end of the ablation process and equivalent spherical diameter for lump at each time was calculated using:

$$\boldsymbol{d_i = 2\left(\sqrt[3]{\frac{3\,m_i}{4\pi\,\rho_{lum}}}\right)} \qquad (4.34)$$

3) The initial equivalent cylindrical diameter was known to be 50.8mm, thus the diameter of the lump at each time of ablation must be smaller than

that. However, comparing the two sets of equivalent diameters showed that from the beginning of the test until some time‘t’, the equivalent spherical diameter was greater than 50.8mm. Within that period of time, the lump was most likely cylindrical and thus the equivalent cylindrical diameter was used as the adjusted lump diameter. As soon as the calculated equivalent spherical diameter was less than the equivalent cylindrical diameter, the lump was assumed to be spherical. From this time until the completion of the ablation process, the equivalent spherical diameter was used as the adjusted lump diameter.

For these calculations, the density of the oil sand lump was calculated by dividing the lump initial volume to its initial mass, measured after preparation. It must be noted that although this method of calculation gives a very good indication of the lump size at each stage, there is still some uncertainty about the exact time of the change of lump shape.

Table 4.7 shows an example of the adjusted lump diameter calculations, for the test with water at V = 3m/s and T = 30°C. The density of the oil sand lump was 1982kg/m^3.

Figures 4.41, 4.42 and 4.43 illustrate the drag force acting on the lump and lump adjusted diameter as a function of time in water or slurry flows at different operating temperatures and velocities. As expected, in all cases, the maximum drag force is measured initially when the lump has its initial (maximum) diameter and reaches a minimum at the end of the ablation process. The minimum drag force is zero once the lump is ablated completely. In addition, the maximum drag force in Figure 4.42 (a) is equal to that in Figure 4.42 (c). This observation is expected because these two experimental runs were similar in terms of slurry velocity and concentration, with the only difference being slurry temperature. It is well-known that drag force does not depend on temperature significantly, since the temperature changes only the density and viscosity of the carrier fluid.

Table 4.7 Calculating lump adjusted diameter for Run R-W5 (water at V=3m/s and T=30°C)

Time (min)	Lump mass (kg)	Lump volume (m3)	Equivalent spherical diameter (mm)	Equivalent cylindrical diameter (mm)	Lump adjusted diameter (mm)
0	0.2040	1.03×10^{-4}	58.17	50.82	50.82
5	0.1752	8.84×10^{-5}	55.29	48.30	48.30
10	0.1044	5.27×10^{-5}	46.54	40.65	46.54
15	0.0136	6.87×10^{-6}	23.61	20.62	23.61
18	0.0091	4.58×10^{-6}	20.62	18.02	20.62

It was also observed that drag force was the greatest for a new lump in slurry (C = 0.30) and the lowest for that in water. The maximum drag force varied from 2N (at V = 1m/s) to 16N (at V= 3m/s) for lump in water and it changed from 3N (at V = 1m/s) to about 30N (at V= 3m/s) in slurry (C = 0.15). The maximum drag force in slurry (C = 0.30) was measured equal to 6N at V = 1m/s and 22N at V = 2.5m/s. Drag force at V = 2.5m/s in water and slurry (C = 0.15) was about 12N and 14N, respectively.

In summary, the drag force acting on the lump increases with increasing slurry concentration. Drag force is sum of pressure drag force and skin friction (Young, 2004). The trend of increase of pressure drag force on the oil sand lump can be envisioned in analogy with the pressure drop within the pipeline. The pipeline pressure drop for a fully-developed steady flow with constant density can be calculated using (Shook and Roco, 1992):

$$\frac{-dp}{dz} = \frac{4\tau_w}{D} \qquad (4.35)$$

Equations 2.6 to 2.9 can be used to calculate pipe wall shear stress for slurry flow in vertical pipes. In the case of a pipeline system with the properties given in Table 4.8, pressure drops for water or slurries (C = 0.15 and 0.30) flowing

through the pipe were 60.8, 62.4 and 65.2Pa. This means that the pressure drop increases with adding sand to water and increasing the slurry concentration. It is expected that the pressure drag force acting on the oil sand lump placed within the pipe follows a similar trend and increases with increasing the solid concentration.

As was discussed in Section 4.6, for the current system, skin friction apparently decreases with addition of 30 vol% solid particles to the flow. However, the amount of reduction of skin friction for the concentrated slurries studied here is not known. It is believed that increase of the pressure drag force, as discussed above, is significant and therefore addition of solid particles to the flow results in higher total drag force at higher slurry concentrations.

Table 4.8 Input parameters for estimating pressure drop inside the pipe

Term	Value
D (mm)	103
V (m/s)	2
ρ_f (kg/m^3)	1000
μ_f (Pa.s)	1×10^3
d_{50} (mm)	0.190
ρ_s (kg/m^3)	2650

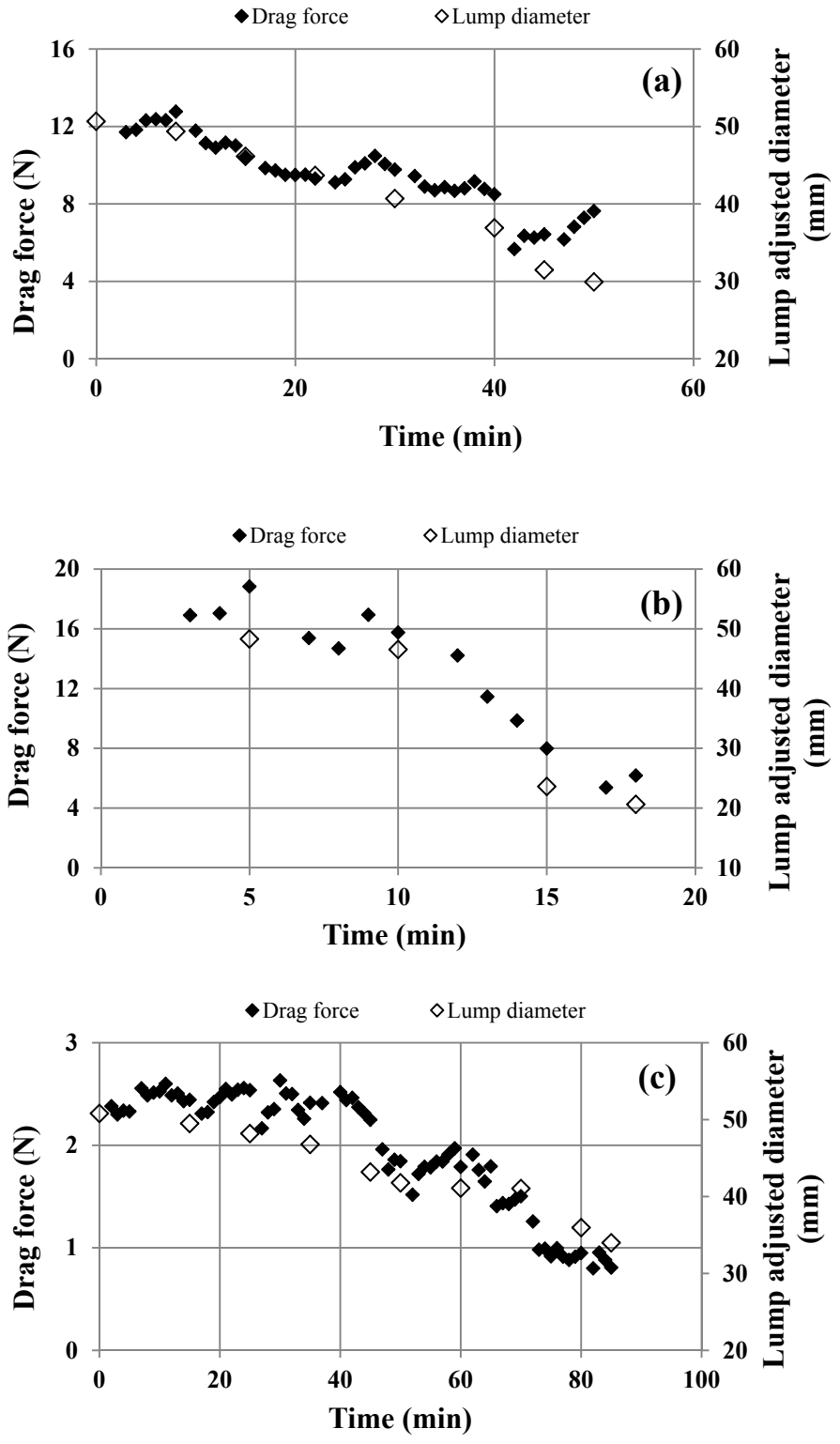

Figure 4.41 Measured drag force acting on ablating lump in comparison with lump adjusted diameter in water: (a) Run R-W4: V=2.5m/s; T=30°C; (b) Run R-W5: V=3m/s; T=30°C; (c) Run R-W6: V=1m/s; T=45°C

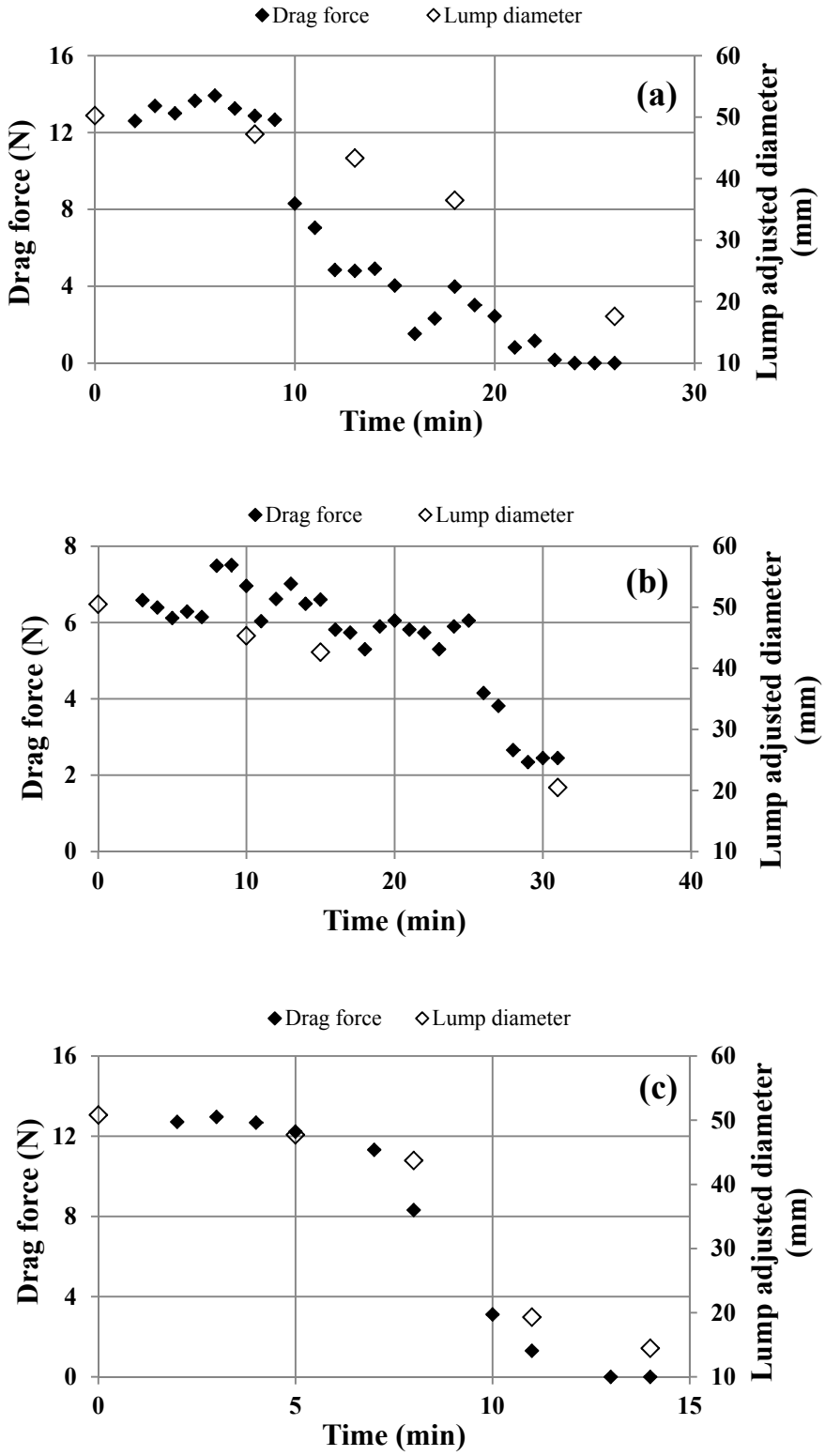

Figure 4.42 Measured drag force acting on ablating lump in comparison with lump adjusted diameter in slurry (C=0.15): (a) Run R-15-3: V=2m/s; T=30°C; (b) Run R-15-7: V=1.5m/s; T=45°C; (c) Run R-15-8: V=2m/s; T=45°C

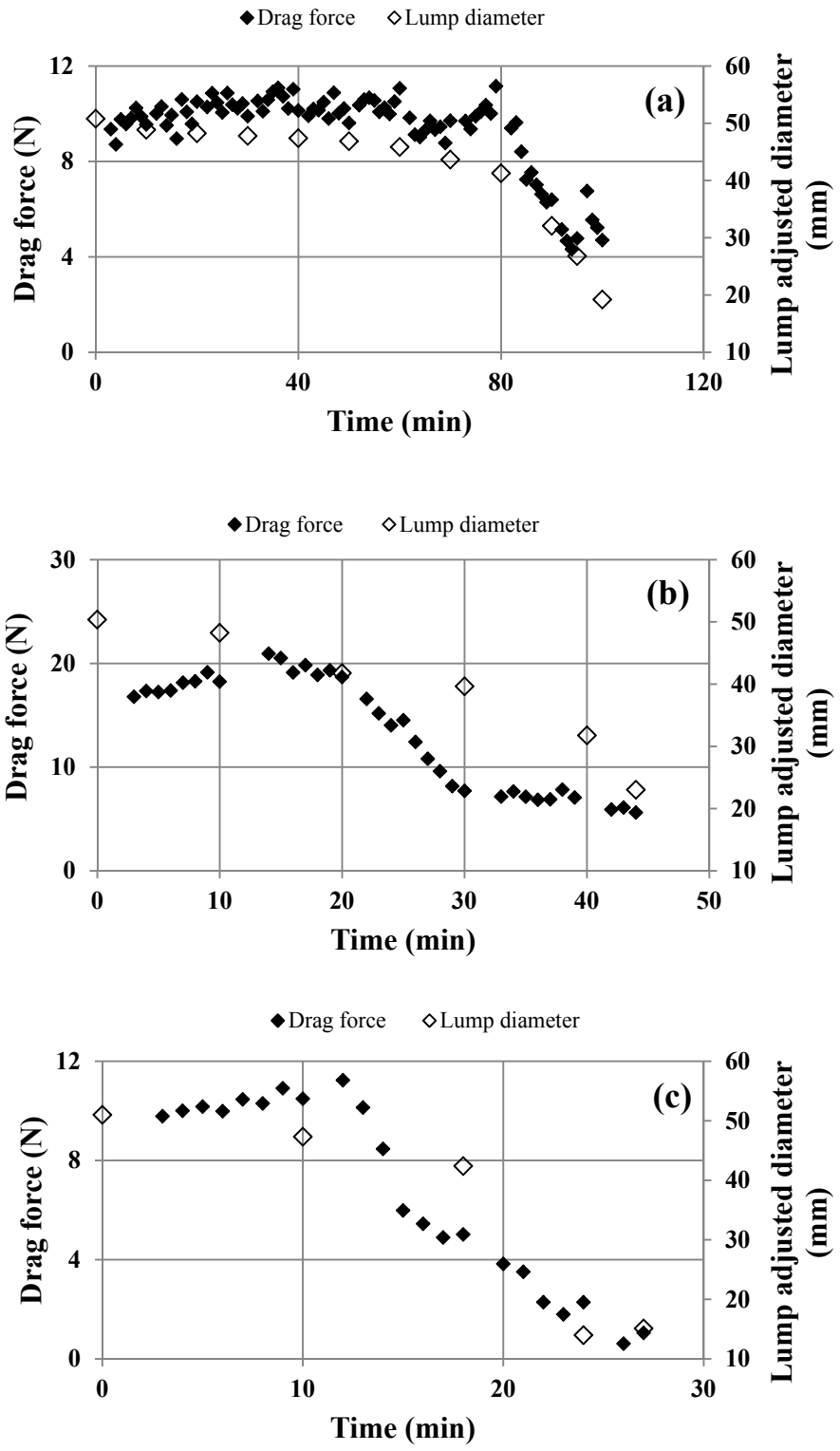

Figure 4.43 Measured drag force acting on ablating lump in slurry (C=0.30); (a) Run R-30-2: V=1.5m/s; T=30°C; (b) Run R-30-3: V=2m/s; T=30°C; (c) Run R-30-6: V=1.5m/s; T=45°C

4.10. Comparing lump ablation results with existing SRC (1996) experimental results

Recall that in Chapter 2, lump ablation studies conducted at the Saskatchewan Research Council Pipe Flow Technology Centre™ in 1996 were reviewed. In this study, they introduced a certain number of actual oil sand lumps into a 264mm pipeline loop and measured the mass loss by trapping the lumps and measuring their mass at certain time intervals. These tests were conducted at two initial lump temperatures, T_{0L} = 10 and -7°C and different slurry temperatures (Masliyah, 2008).

Prior to the present study, the results of the SRC (1996) experiments were the only available experimental data on the ablation of oil sand lumps. Additionally, the Bara and Masliyah (1997) model was validated using these data thus these results are very well known among engineers and scientists in the oil sand industry. However, one must be very cautious when comparing the results of those experiments with the results of the current study because the two studies are different in number of ways:

- The slurry velocity and concentration used for the SRC (1996) experiments are not publically available; therefore, it is difficult to compare the two sets of data in this regard.
- The actual oil sand lumps used by SRC (1996) were shoveled and transferred to the lab; because of these processes the internal structure of the lumps changes from that of the core samples. However, the artificial oil sand lumps, used here, were freshly made and no external force has impacted their structure. Therefore, at identical operating conditions the artificial oil sand lumps may be more resistant to ablation or breakage.
- The artificial oil sand lump is individually anchored in a pipe so its contact with pipe wall and other lumps is eliminated. On the other hand, a certain amount of actual oil sand ore, which was introduced into the pipeline by SRC (1996) contained several lumps; these lumps would frequently

contact with the pipe wall and each other. Additionally, the actual oil sand lumps tested in 1996 passed through a centrifugal pump many times. These differences would lead to higher ablation rates.

- The artificial oil sand lump used for the current study was anchored so its slip velocity remained unchanged and equal to the slurry bulk velocity. However, for freely-moving lumps, the slip velocity should be expected to decrease as lump size decreases. However, one might argue that, for an anchored lump, as the lump size decreases pipe cross section increases, thus, the flow velocity decreases and this causes reduction of lump slip velocity. It is believed that the effect of basket in the reduction of pipe cross section is dominant, i.e. the basket size is larger than that of a lump at different ablation stages, and because the basket size remains unchanged the bulk velocity where a lump is anchored remains constant.

5. Model development

Recall that heat is transferred to the lump from the slurry so the viscosity of the surface layer decreases, causing the layer to soften and shear away. A new layer, which is then exposed to the slurry, softens and ablates the same way. This process repeats until the entire lump is ablated (Masliyah, 2008). Therefore, heat transfer and shear forces are the two critical factors in oil sand lump ablation. Any predictive model must consider the heat transfer and surface shear forces. In this chapter, a model that is capable of predicting the ablation rate as a function of bitumen viscosity and surface shear stress is developed. The model originates from Newton's Law of Viscosity and is developed based on the following assumptions:

- The oil sand lump remains cylindrical during the ablation;
- The lump ablates in thin layers, removed from cylinder circumference and its sides as shown in Figure 5.1;
- The thin softened layer of the lump, Δh, which is ablated away, contains only bitumen;
- The velocity within the thin layer varies from zero at the surface of the cylinder to u_b at the lump interface, where u_b is smaller than flow bulk velocity and can be calculated using momentum equations considered for both fluids.

Heat transfer to the oil sand lump was modelled to obtain a temperature profile within the lump, from which the bitumen viscosity profile could be determined. To simplify the analysis and ease of modelling, it was assumed that the temperature profile was constant along each vertical and horizontal line within the geometry. Thus two cut-lines (shown in Figure 5.2), one in the horizontal and one in the vertical direction, with the following orientations were determined for obtaining temperature profiles:

Line1: [(0, 0.0254), (0.0254, 0.0254)]; Line2: [(0.0127, 0), (0.0127, 0.0508)]

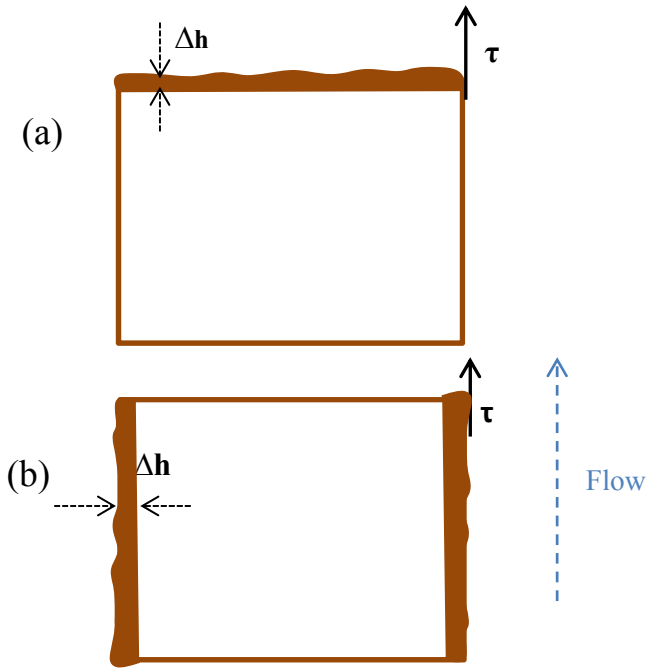

Figure 5.1 Side view of oil sands lump: (a) ablation from circumference and (b) ablation from two ends

Ultimately, the model was validated using the current experimental measurements. It was found that the proposed model is capable of predicting ablation rates at high temperature (T = 45°C) but less accurate at lower temperature (T = 30°C). This might be because of the fact that lump ablation at 30°C is more shear stress driven; therefore, a more accurate estimation of shear stress on the lump in slurry is necessary to predict the ablation rate. Since no exact method of calculating shear stress on the solid object in a slurry flow exists at this time, a method used to estimate the shear stress from drag force acting on a cylinder in water was used for both water and slurries.

5.1. Heat transfer

With the application of COMSOL Multiphysics 4.2a, it was possible to simulate heat transfer to and within the cylindrical oil sand lump. The temperature profile within the lump was obtained using the simulations.

5.1.1. Model definition

Simulations were based on the "2D heat transfer in solid" module. In 2D, a cylindrical oil sand lump was assumed to be a square.

5.1.2. Domain equation

The following heat transfer equation is solved by COMSOL to calculate temperature profile in a solid:

$$\rho C_p \frac{\partial T}{\partial t} - \nabla(k_t \nabla T) = Q_q \qquad (5.1)$$

In this study, transient heat transfer was solved with initial time of zero, time interval 0.1. No heat is consumed or created so $Q_q = 0$.

5.1.3. Modelling geometry

As seen in Figure 5.2, a rectangle in *r* and *y* directions with corner point at (0, 0) was defined as the geometry. The rectangle length was set at 0.0508m (cylindrical lump length) with the width equal to 0.0254m, i.e. cylindrical lump radius.

5.1.4. Boundary conditions

Symmetry boundary conditions were applied along boundaries 4 and 5. Convection boundary conditions were applied for boundaries 1, 2 and 3.

For the convection boundary condition, COMSOL allows one to define the flow condition on the boundaries or to manually set the heat transfer coefficient. In the first case, in 2D geometry, COMSOL calculates the heat transfer coefficient for a 2D plate; for the current study, however, the actual geometry is a cylinder. Therefore, to limit the errors and assumptions, the heat transfer coefficient for a cylinder was separately calculated and entered into the model as a user defined input.

Heat transfer coefficients for both free (in air) and forced (in water) convection were determined based on equations given in Chapter 4. As no literature exists for

estimating heat transfer coefficient by convection from slurries to a large object, a simplified method had to be applied. More details about this approach are given in the following pages.

The laboratory temperature was assumed to be 20°C and for forced convection in flow, the temperature was assumed to be that of the ablation test in question.

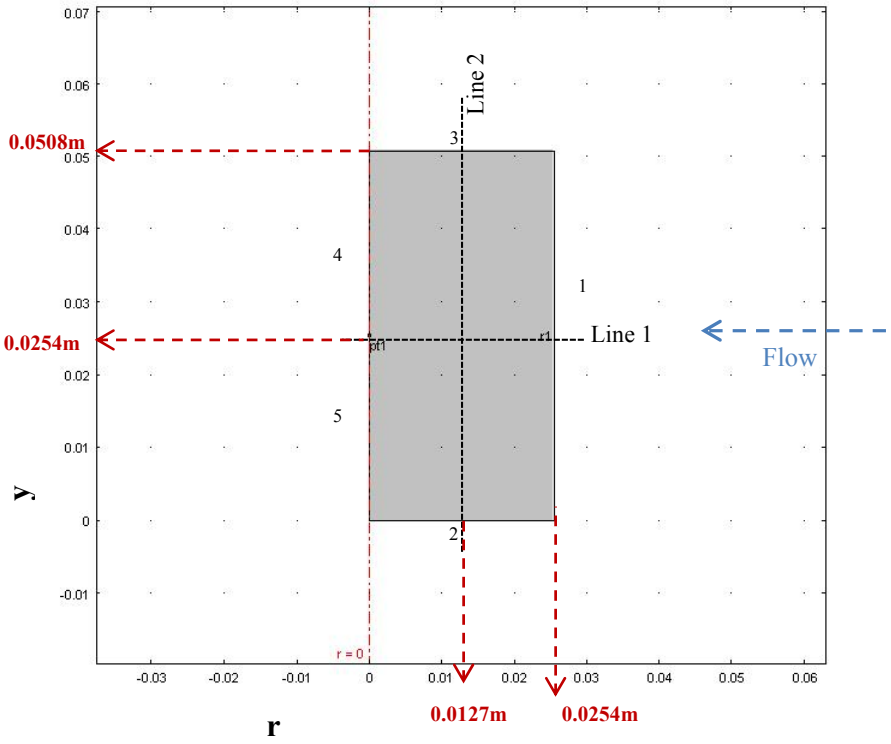

Figure 5.2 COMSOL geometry of oil sand lump for heat transfer simulation

Heat transfer coefficient for lump in air

Data given in Table 5.1 were substituted into Equation 4.27 to calculate the Nusselt number, here: $Nu = 36$.

$$\boldsymbol{Nu = 0.125\ (Gr\ Pr)^{1/3}} \qquad (4.27)$$

Heat transfer coefficient was then calculated: $h = 18$ W/m^{2}K.

Heat transfer coefficient for lump in water

Recall from Chapter 4, Equation 4.28 can be used to calculate the Nusselt number for convection to a cylinder in water:

$$\boldsymbol{Nu = 0.3 + \frac{0.62\,Re^{1/2}Pr^{1/3}}{\left[1+\left(\frac{0.4}{Pr}\right)^{2/3}\right]^{1/4}}\left[1+\left(\frac{Re}{282000}\right)\right]^{4/5}} \qquad (4.28)$$

Data given in Table 5.1 were used to calculate Reynolds numbers and the heat transfer coefficients presented in Table 5.2.

Table 5.1 Input parameters used to calculate heat transfer coefficients

Parameter	Value
d (m)	0.0508
T_f (°C)	6
Pr (air)*	0.7
Gr (air)	3.55×10^{7}
ϑ (air) (m^2/s)*	1.3×10^{-5}
k_t (air) (W/mK)*	0.025
k_t (water) (W/mK)*	0.63
C_p (water) (J/kgK)*	4174
k_t (oil sand) (W/mK)**	1.5
C_p (oil sand) (J/kgK)**	900

* (Holman, 2010)
** (Cervenan et al., 1981)

With the assumption of the analogy between heat transfer from the slurry to the pipe wall and heat transfer from the slurry to a solid object, heat transfer coefficients for slurries were estimated. For this purpose, Equations 4.29 to 4.32 were used:

$$\boldsymbol{Nu = 0.00567\,Re^{0.987}Pr^{0.4}} \qquad (4.29)$$

where: $Nu = \frac{Dh_m}{k_{t_m}}$, $Pr = \frac{C_{pm}\mu_m}{k_{tm}}$, $Re = \frac{VD\rho_m}{\mu_m}$

$$C_{pm} = C_{mass}C_{ps} + (1 - C_{mass})C_{pf} \quad (4.30)$$

$$\mu_m = \mu_f(1 + 22.4\,C) \quad (4.31)$$

$$k_{tm} = \frac{2k_{tf}+k_{ts}-2C\,(k_{tf}-k_{ts})}{2k_{tf}+k_{ts}+C\,(k_{tf}-k_{ts})} \quad (4.32)$$

Table 5.2 Nusselt number and heat transfer coefficients: water

Water bulk velocity (m/s)	Water actual velocity (m/s)	T = 30°C		T = 45°C	
		Cylinder Reynolds Number	h (W/m^2K)	Cylinder Reynolds Number	h (W/m^2K)
1	1.5	9.6×10^3	4785	1.2×10^5	5302
1.5	2.3	1.4×10^5	6448	1.9×10^5	7290
2	3.0	1.9×10^5	8108	2.5×10^5	9313
2.5	3.8	2.4×10^5	9792	3.2×10^5	11390

Heat transfer coefficients calculated using these equations are given in Table 4.6. Slurry heat transfer coefficients were found to be slightly different than those calculated for water.

Water heat transfer coefficients were used for simulations because: (i) once these coefficients were used in simulations, slight differences in temperature profiles were observed and (ii) the slurry heat transfer coefficients were calculated using correlations which were not developed for the purpose of predicting heat transfer from slurry to a solid object. The temperature profile obtained using water heat transfer coefficient was also used for modelling lump ablation in slurries.

5.1.5. Mesh sizing

The geometry was meshed using the COMSOL normal triangular mesh option (maximum element size = 0.0034m and minimum element size = 1.52×10^{-5}m). No refining was done because the geometry is a simple rectangle with no complicated

edges or attached parts. An image of the meshed geometry is presented as Figure 5.3.

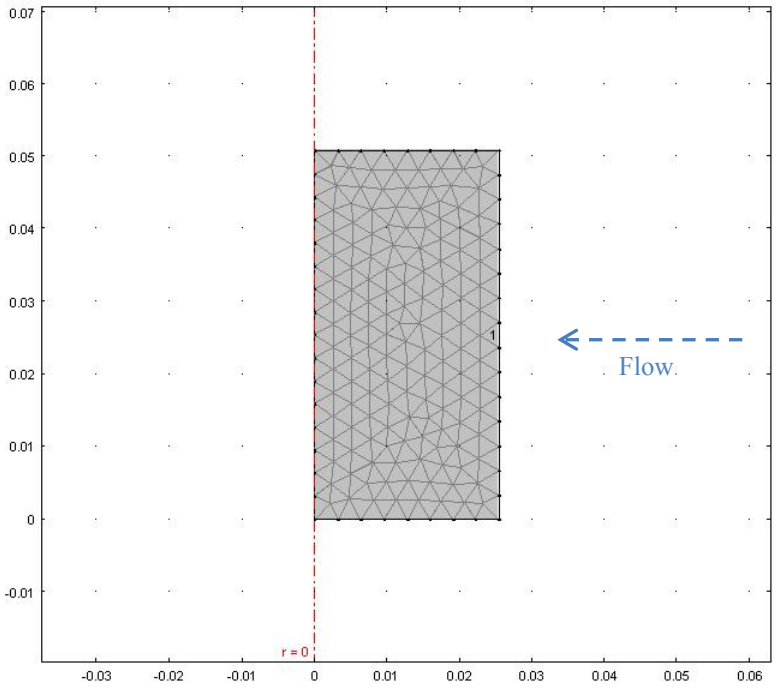

Figure 5.3 Distribution of mess elements for simulating heat transfer using COMSOL

5.1.6. Post processing and visualization

The temperature profiles along the two predetermined lines (shown in Figure 5.2) were calculated as outputs of the model. The temperature profiles were then used to calculate the bitumen viscosity profiles within the lump.

5.1.7. Simulation results

Heat transfer in air

It normally takes about 10min to place the oil sand lump in the gauged spool. A COMSOL simulation was used to determine the temperature profile of the oil sand lump prior to the start of flow, i.e. after 10min exposure to air. Figure 5.4 depicts the temperature profile of the oil sand lump after being exposed to room temperature (T = 20°C) for a period of 10min. Based on the temperature profile,

the local temperature within the lump varies between T = 275K (1.85°C) and T = 278.7K (3.75°C). The average of the maximum and minimum temperatures (2.8°C) of the lump was assumed as the lump initial temperature for simulating forced convection in water or slurry flow.

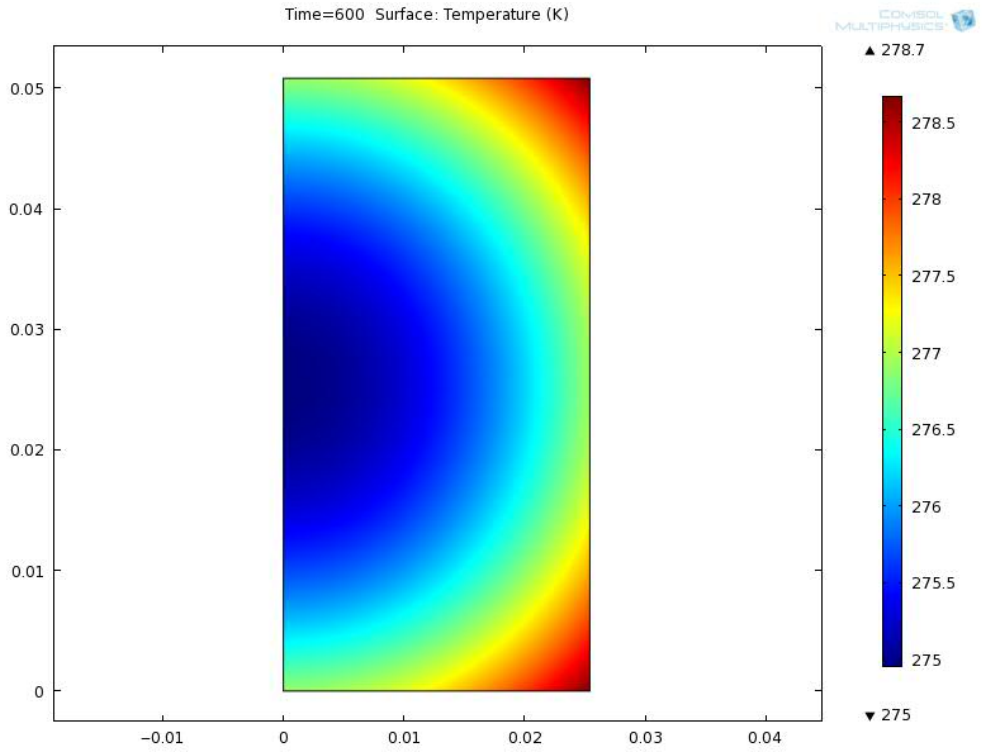

Figure 5.4 Oil sand lump temperature profile after10min exposure to air at room temperature (20°C)

Heat transfer with flow at T = 30°C

The temperature profiles of a lump after 5min exposure to water or slurry flow at T = 30°C at different velocities are illustrated in Figures 5.5 to 5.7. It can be seen that with a 1m/s increase in velocity (from 1 to 2m/s) at T = 30°C, the heat transfer to the lump increases somewhat.

Each temperature profile shows that heat transfer to the edges of the lump occurs considerably more rapidly than that within the central portion. In other words, the

edges of the lump heat more rapidly, leading to a lower bitumen viscosity in these regions. This fact, along with the fact that shearing on the edges of the lump is higher, leads to faster ablation of the lumps from the edges. These consequently result in the observed change in lump shape from cylindrical to spherical. These results agree with observations made during the visualization tests (refer to Figures 4.1 and 4.2).

Simulations show that for most of operating conditions studied during this project, the lump reaches a uniform temperature after about 10min. Figure 5.8 provides an illustration of the temperature profile within the lump after 10min exposure to flow (water or slurry) at V = 1m/s and T = 30°C.

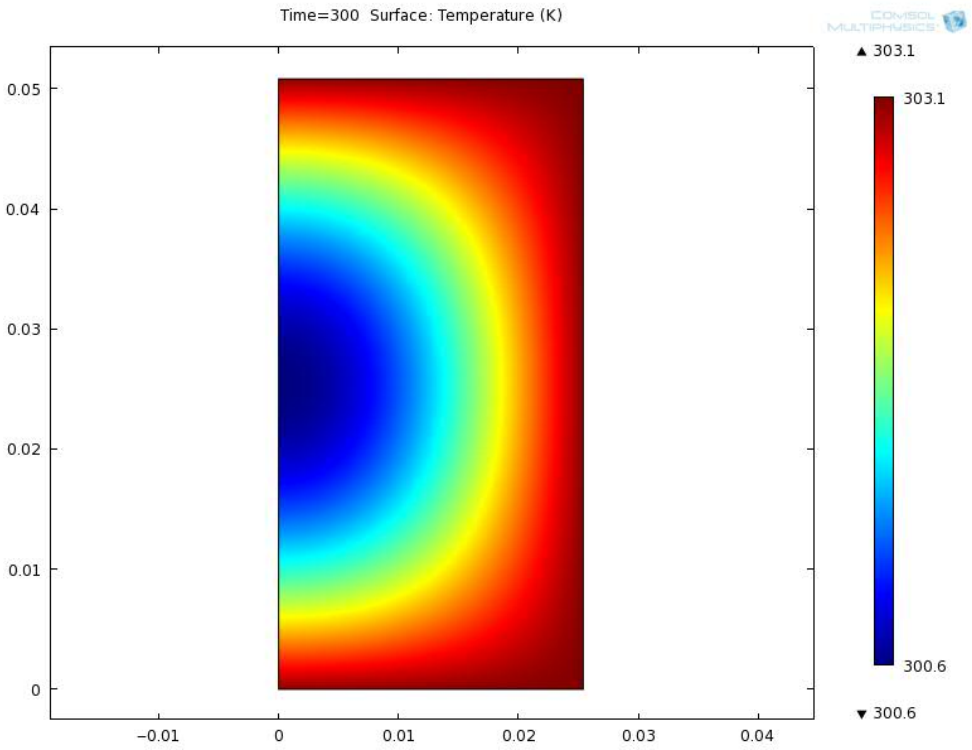

Figure 5.5 Lump temperature profile after 5 min heat transfer in water or slurry flow at V=1m/s and T=30°C

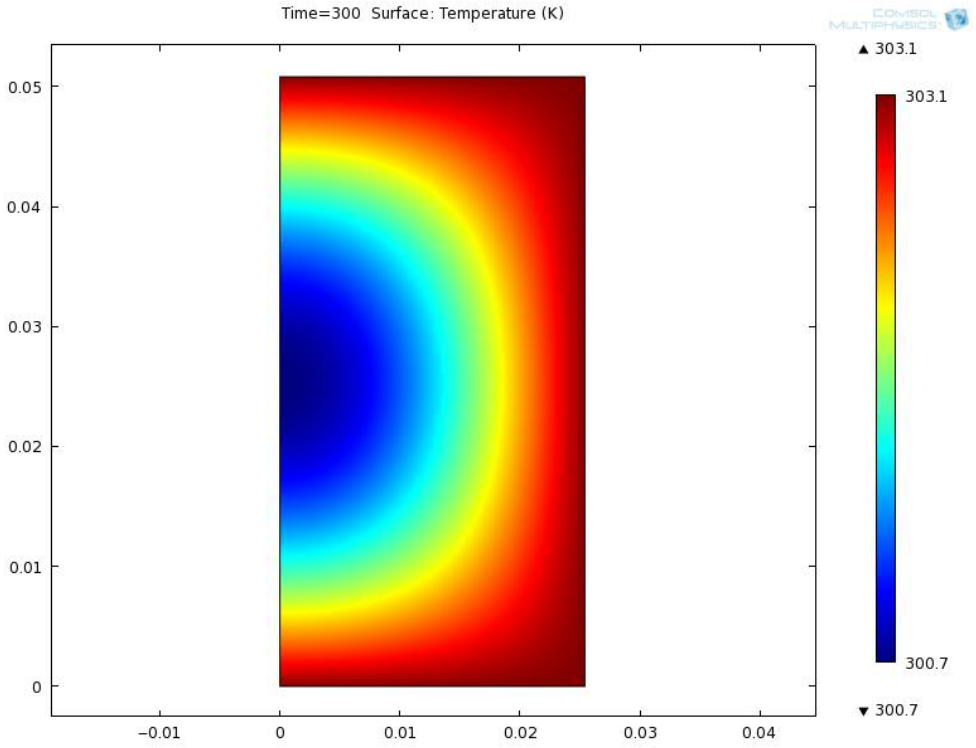

Figure 5.6 Lump temperature profile after 5 min heat transfer for water or slurry flow at V=2m/s and T=30°C

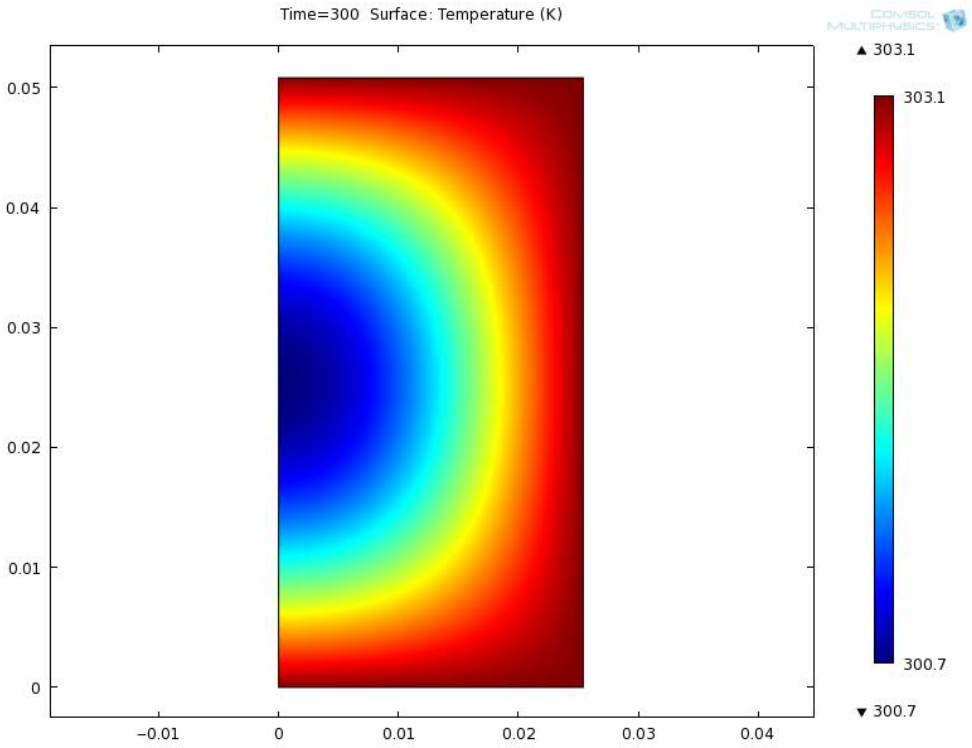

Figure 5.7 Lump temperature profile after 5 min heat transfer for water or slurry flow at V=2.5m/s and T=30°C

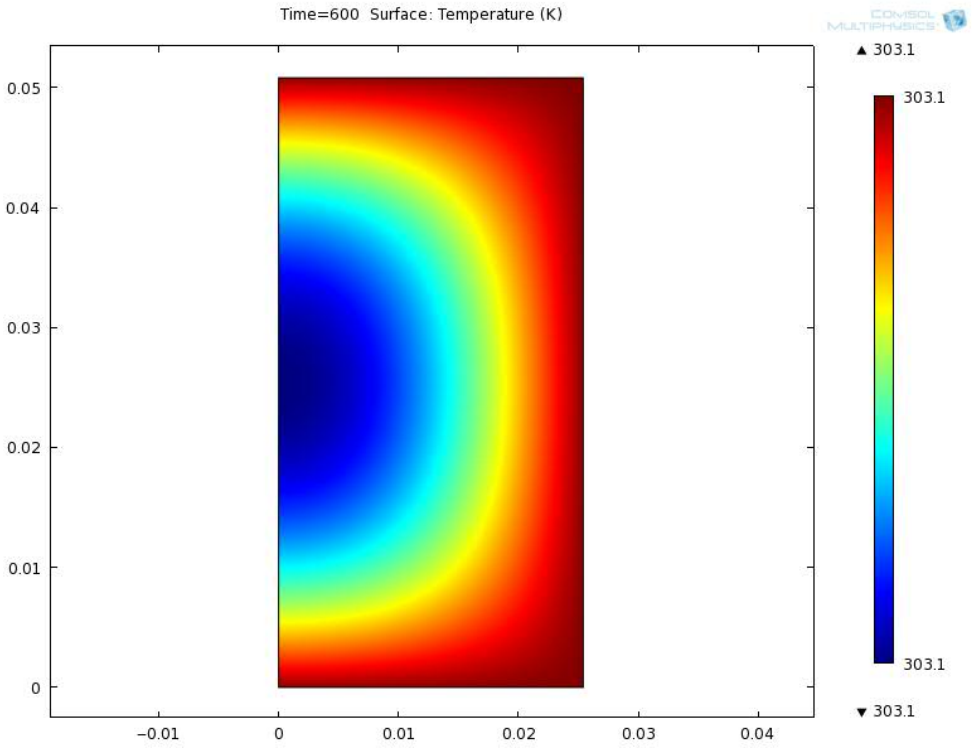

Figure 5.8 Lump temperature profile after 10 min heat transfer for water or slurry flow at V=1m/s and T=30°C

The temperature profiles within the lump during ablation were also evaluated along the two cut-lines shown in Figure 5.2. It was found that the local temperature changes significantly with time. Figure 5.9 presents the temperature profile of the lump (along Line 1) at different times of exposure to flow at V = 1m/s and T = 30°C. As shown in this figure, the heat transfer from the flow to the lump occurs relatively rapidly.

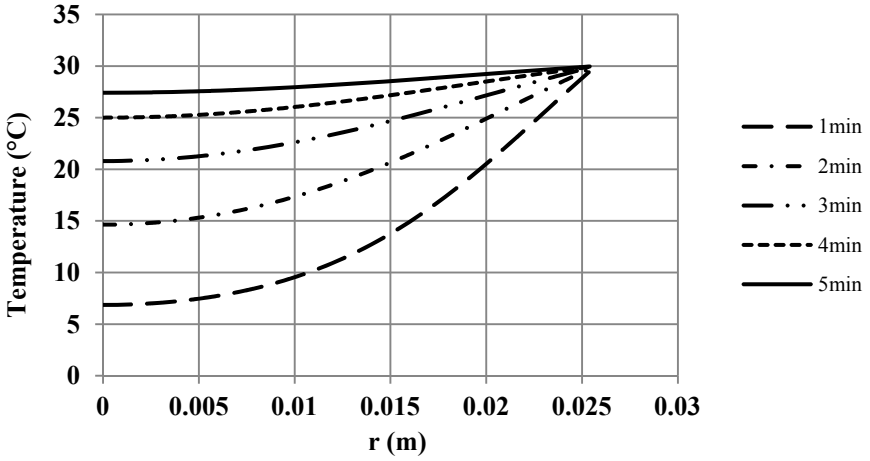

Figure 5.9 Lump temperature profile (along Line 1) for water or slurry flow at V=1m/s and T=30°C

The viscosity distribution within the oil sand lump was determined using Equation 3.2:

$$Ln(\mu_B) = 111.96 \left(\frac{1}{T}\right)^{0.62} \qquad (3.2)$$

Since ablation typically began after about 5min exposure to the flow, the viscosity profile for each lump was determined at t = 5min. The lump temperature and viscosity profiles along Lines 1 and 2 at V = 1m/s and T = 30°C are plotted in Figures 5.10 and 5.11. According to Figure 5.10, a temperature change of about 2.6°C from the core of the lump to the surface causes about one order of magnitude decrease in the viscosity. It again emphasizes that the huge viscosity difference between the surface and core of the lump results in the gradual ablation of the lumps. Similar observations hold for the plot presented here as Figure 5.11.

Figure 5.12 shows the comparisons of the lump temperature and viscosity profiles at t = 5min and V = 1 and 2m/s. Although the 1m/s velocity increase (from 1 to 2m/s) changes slightly the heat transfer to the lump, when ablation is considered, small absolute differences in viscosity matter a great deal.

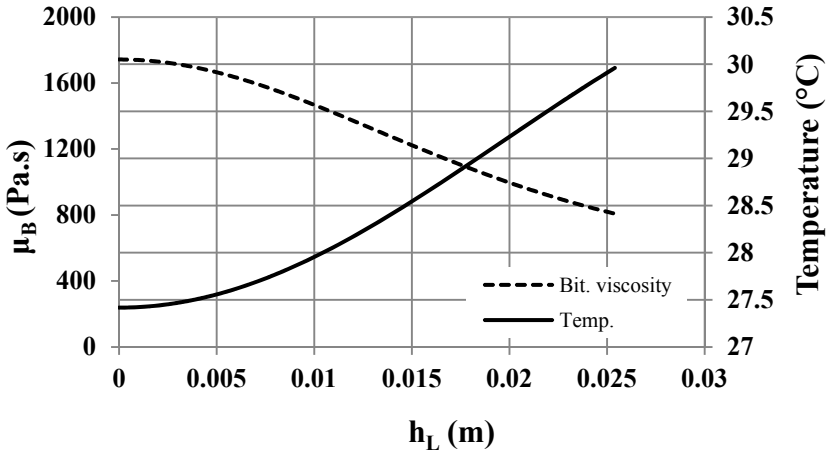

Figure 5.10 Lump temperature and viscosity profile (along Line 1) at t =5min for water or slurry flow at V=1m/s and T=30°C

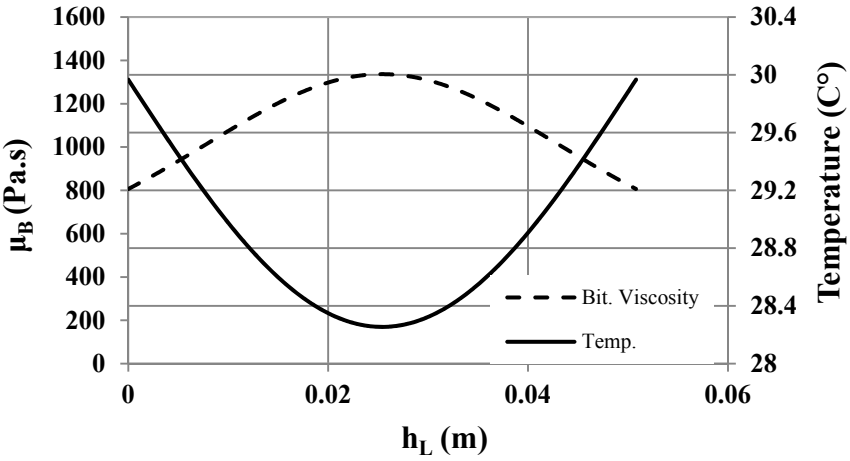

Figure 5.11 Lump temperature and viscosity profile (along Line 2) at t =5min for water or slurry flow at V=1m/s and T=30°C

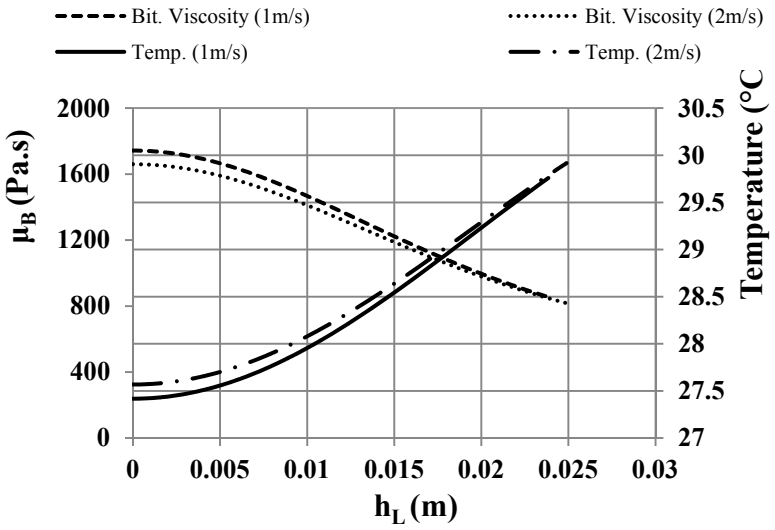

Figure 5.12 Effect of water or slurry velocity on lump local temperature and bitumen viscosity: T=30°C

Heat transfer with flow at T = 45°C

The lump temperature profiles in flows at 45°C and different velocities at t = 5min were obtained. The results are presented in Figures 5.13 to 5.15. Temperature at the edges of the lump was higher than that at the core of the lump and this was independent of velocity. The temperature and bitumen viscosity profiles (along Lines 1 and 2) for flow at V = 1m/s were plotted (Figures 5.16 and 5.17). It is important to note that bitumen viscosity is almost one order of magnitude smaller at T = 45°C, as clearly shown by comparing Figures 5.10 and 5.11 (30°C) with Figures 5.16 and 5.17 (45°C). In this case, the temperature at the lump surface is 4°C higher than that at its core. The bitumen viscosity differs at these two temperatures by about a factor of seven. Therefore, the surface layer, whose viscosity is significantly lower, ablates while the remainder of the lump stays intact.

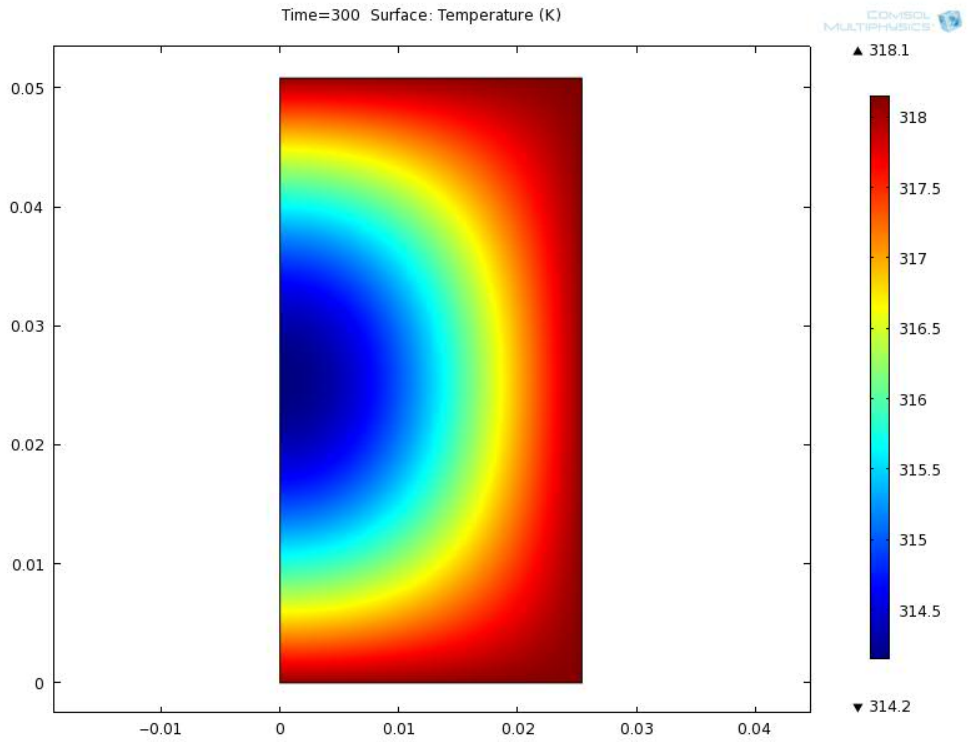

Figure 5.13 Lump temperature profile after 5 min heat transfer for water or slurry flow at V=1m/s and T=45°C

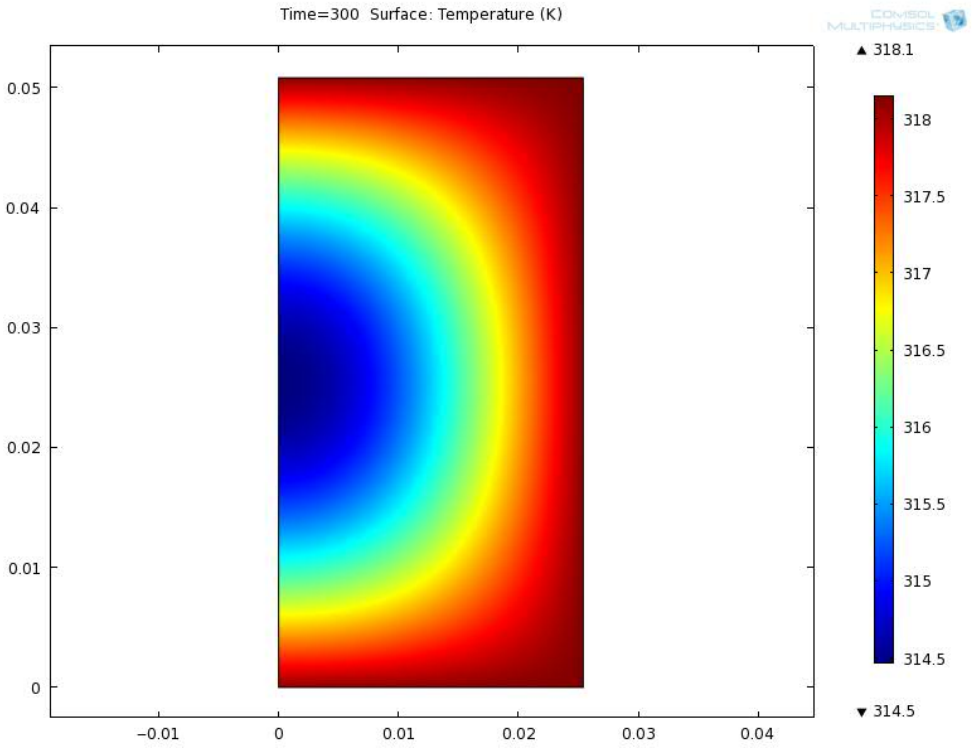

Figure 5.14 Lump temperature profile after 5min heat transfer for water or slurry flow at V=1.5m/s and T=45°C

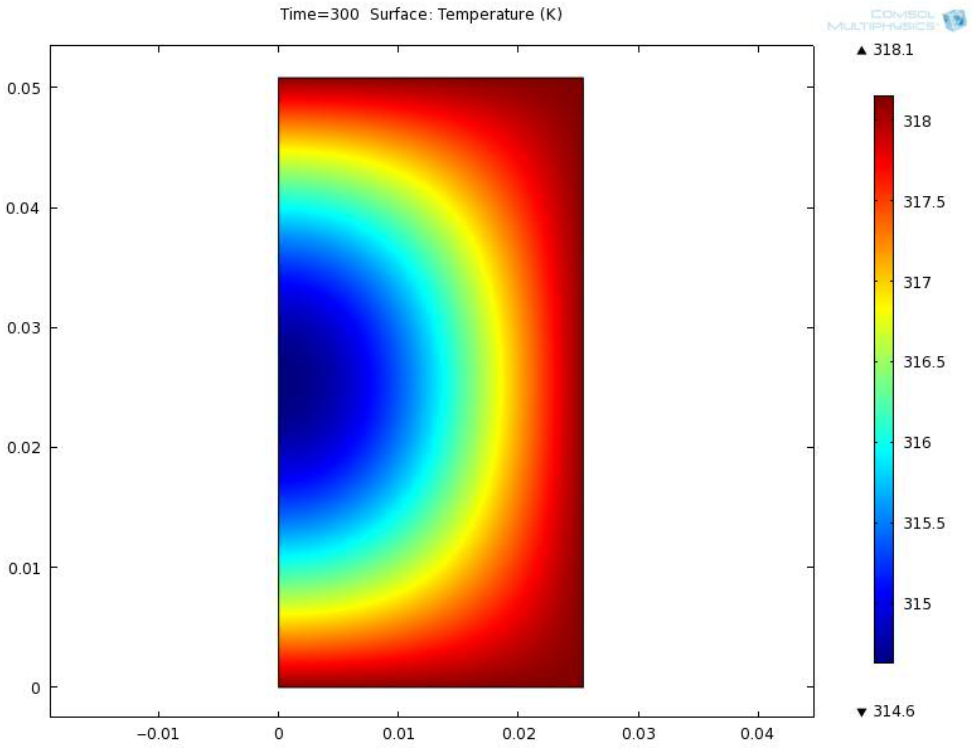

Figure 5.15 Lump temperature profile after 10 min heat transfer for water or slurry flow at V=2m/s and T=45°C

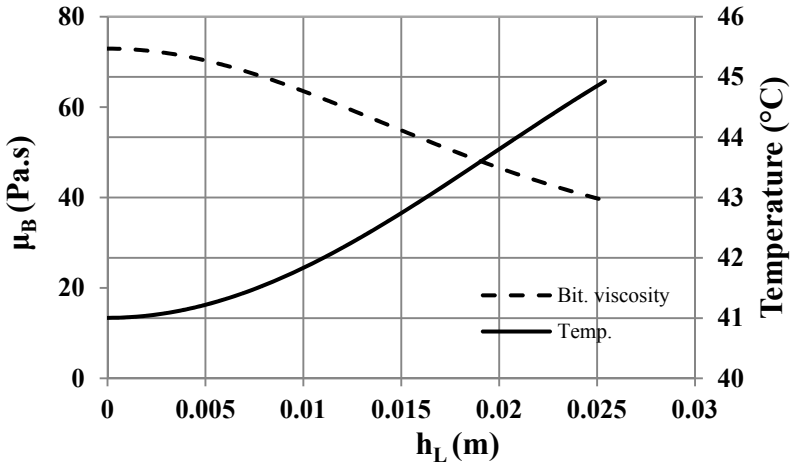

Figure 5.16 Lump temperature and viscosity profile (along Line 1) at t =5min for water or slurry flow at V=1m/s and T=45°C

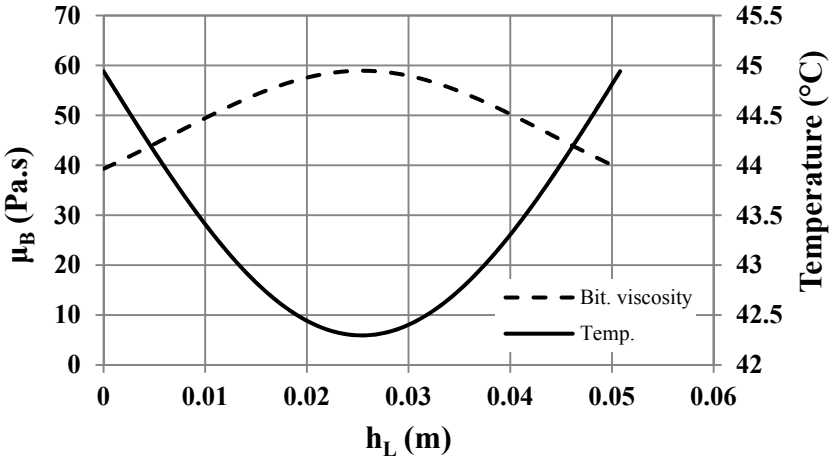

Figure 5.17 Temperature and viscosity profile of lump (along Line 2) at t =5min for water or slurry flow at V=1m/s and T=45°C

5.2. Mass loss of oil sand lump

The assumptions given earlier were used to develop a model for predicting oil sand lump mass loss. Newton's Law of Viscosity for the lump viscous surface layer can be written as:

$$\boldsymbol{\tau_{wp} = \mu_B \frac{du_b}{dh_L}} \qquad (5.2)$$

this equation can be solved for u_b:

$$\boldsymbol{u_b = \frac{\tau_{wp}}{\mu_B} h_L + B} \qquad (5.3)$$

where h_L varies from zero to Δh. The constant B has a value of 0 based on the boundary condition: $u_b = 0$ at $h_L = 0$. Equation 5.3 is therefore written as:

$$\boldsymbol{u_b = \frac{\tau_{wp}}{\mu_B} h_L} \qquad (5.4)$$

The volume flow rate of the viscous liquid, removed because of the shear stress τ_{wp}, can be calculated as:

$$\boldsymbol{Q = \int_0^{\Delta h} u_b dA} \quad \text{or} \quad \boldsymbol{Q = \int_0^{\Delta h} u_b\, w\, dh_L} \qquad (5.5)$$

where w is equal to $(2\pi R)$ and R denotes the radius of the lump. Equation 5.4 is then substituted in to Equation 5.5 and integrated:

$$\boldsymbol{Q = \frac{\tau_{wp}}{\mu_B}\left(\frac{\Delta h^2}{2}\right) w} \qquad (5.6)$$

Mass flow rate of the viscous liquid from the circumference of the cylinder can be calculated from:

$$\boldsymbol{\dot{m} = \rho_{lum}\left(\frac{\tau_{wp}}{\mu_B}\right)\left(\frac{\Delta h^2}{2}\right) w} \qquad (5.7)$$

A similar approach is taken for ablation from the two ends of the cylindrical oil sand lump. An equation similar to Equation 5.2 must be solved for mass loss from the two ends. In this case, however, $w = 2R$.

The total mass loss is equal to sum of the mass loss from the circumference and the mass loss from the two ends. Thus the model to calculate total lump mass loss can be written as:

$$\boldsymbol{\dot{m} = \rho_{lum}\tau_{wp}\left[(2\pi R)(\Delta h^2/(2\,\mu_B))_{circum} + (2R)(\Delta h^2/(2\,\mu_B))_{ends}\right]} \qquad (5.8)$$

which can be simplified to:

$$\boldsymbol{\dot{m} = \frac{\rho_{lum}\tau_{wp}\,R}{\mu_B}\left[\pi\,(\Delta h^2)_{circum} + (\Delta h^2)_{ends}\right]} \qquad (5.9)$$

This equation shows that the rate of mass loss ($\dot{m}$) is a function of surface shear stress (τ_{wp}) and bitumen viscosity (μ_B), which itself is a function of temperature. Lump density (ρ_{lum}), lump radius (R) and bitumen viscosity (μ_B) are known and surface shear stress (τ_{wp}) and the thickness of softened layer $(\Delta h)_{circum}$ and $(\Delta h)_{ends}$ must be determined using the experimental data.

It must be noted that this model was developed with the assumption that lump is cylindrical so the results will be more reliable for the first stages of the ablation

process; however, in this study the ablation rate remained almost identical throughout the ablation process.

5.3. Ablation model validation

It is very well understood that in order for an oil sand lump to ablate, thermal energy is needed to heat the lump and mechanical energy is required to remove the softened layer(s). Bitumen viscosity decreases significantly once temperature increases and it leads to faster lump ablation. Larger values of surface shear stress also result in accelerated removal of the softened layers of the lump. These effects are implemented in the model developed here. In this model, lump mass loss is proportional to the lump surface shear stress and inversely changes with the bitumen viscosity.

Once an oil sand lump is exposed to the hot slurry medium, it heats up and, as shown earlier, the temperature of the surface layer quickly reaches the slurry temperature. Therefore, the viscosity of the surface layer decreases. However, if one considers a lump to be a collection of thin layers, the viscosity of the next layers of the lump are much higher because the temperature decreases towards the centre of the lump. Although the layer next to the surface layer might not be hard like a solid, its viscosity is high relative to the surface layer so it can be assumed to be "solid-like" with zero velocity. It is also known that the thin surface layer contains sand grains, small amount of water and bitumen. However, the amount of water is very small thus its effect on the viscosity of the layer can easily be ignored. Sand grains in the softened layer would increase the viscosity of the layer and therefore increase the energy requirement for removal of that layer; however, they may also increase the removal of the thin layer based on the observations of Law et al. (1987) in the ablation of wax-sand samples, i.e. removal as clusters.

The model was validated using experimental data from the present study and heat transfer simulations from COMSOL. The procedure for validation was:

- Surface shear stress on the cylindrical oil sand lump was calculated using the experimental data. Details about the calculation of shear stress from drag force measurements are given on the following page.
- Temperature profiles on cut-lines 1 and 2 were determined.
- Bitumen viscosity profiles on Lines 1 and 2 were defined using Equation 3.2.
- The $(\Delta h)_{circum}$ and $(\Delta h)_{ends}$ were determined using bitumen viscosity profile along Lines 1 and 2; $(\Delta h)_{circum}$ was the distance from point (0.0254, 0.0254) whose viscosity was the lowest and $(\Delta h)_{ends}$ was the distance from (0.0127, 0.0508) with the lowest viscosity. The thickness of the layers of the lump ($(\Delta h)_{circum}$ and $(\Delta h)_{ends}$) which are ablated at V = 1, was decided to be the layer whose viscosity is 4% lower than the bitumen viscosity at the corresponding slurry temperature. The percent increase of the viscosity of the layers was considered to be 6.5%, 11% and 16% for V = 1.5, 2 and 2.5m/s, respectively.
- The average bitumen viscosity (μ_B) at $(\Delta h)_{circum}$ and $(\Delta h)_{ends}$ was used as the input to Equation 5.9.
- Ablation rate was calculated using Equation 5.9.
- Measured ablation rate was determined, using the method given in Chapter 4, for each experimental run. It was found that the ablation rate remained relatively constant during ablation.

The density of the oil sand lump and its initial radius were assumed to be constant at 1944kg/m^3 and 0.0254m, respectively.

5.3.1. Surface shear stress

It is assumed that the skin friction component of the drag force is responsible for lump mass loss. In order to estimate the ablation rate of an oil sand lump using the

model developed here, shear stress related to the skin friction that acts on the lump must be estimated.

In the current study, the drag force acting on an ablating lump at different operating conditions was measured. In order to represent both the pressure drag and skin drag, the drag coefficient can be written as:

$$\mathbf{C_D} = \mathbf{C_P} + \mathbf{C_f} \qquad (5.10)$$

where C_P and C_f are the pressure drag coefficient and skin drag coefficient, respectively. The ratio of the skin friction coefficient to the total drag coefficient for a smooth cylinder may be approximated using the experimental findings of Achenbach (1968). He measured the distribution of the local pressure and skin friction for different cylinders in two different wind tunnels, and presented a graph that shows the ratio of the skin friction coefficient to the total drag coefficient, shown here as Figure 5.18.

According to Figure 5.18, the ratio of the skin friction to the drag force (C_f/C_D) for cylinder in water ($Re = \frac{D\,(V-V_s)\rho_f}{\mu_f} = 10^5\ to\ 3\times10^5$) is:

$$\boldsymbol{C_f/C_D = K} \qquad (5.11)$$

where the constant $K \approx 0.007$ to 0.015.

When the total drag force is known, the surface shear stress can be calculated using Equation 5.11 and:

$$\boldsymbol{\tau_{wp} = \frac{K}{A} F_D} \qquad (5.12)$$

Although Figure 5.18 is obtained for a cylinder in water, it was assumed that Equation 5.11 also holds for a cylinder in slurry flow.

Using Equations 5.11 and 5.12, the surface shear stress on the lump in water at V = 1m/s and T = 45°C (measured F_D = 2.19N) is 1.89Pa.

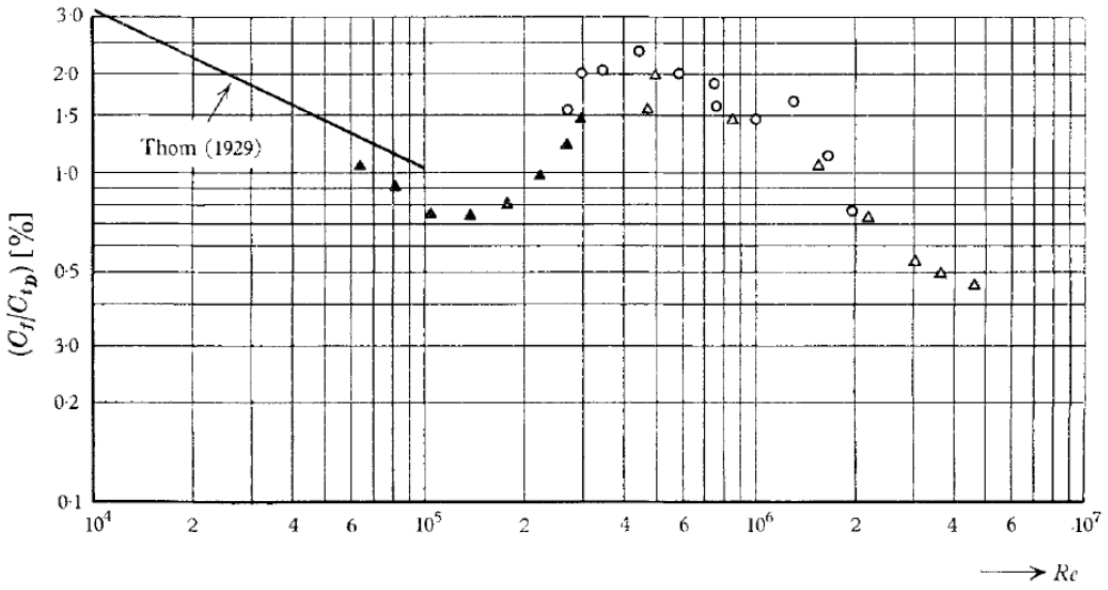

Figure 5.18 Ratio of friction coefficient to total drag coefficient on a smooth cylinder
Δ (L/d= 3.33 low pressure wind channel): ▲ (L/d=3.33 high pressure wind channel): ○ (L/d=6.66 high pressure wind channel) (Achenbach, 1968)

5.3.2. Model validation results

The steps mentioned earlier were applied for each of the water runs and the slurry (C = 0.15 and 0.30) runs. Recall that, oil sand lump ablation rate changed in two steps and the second step seemed to be shear stress driven. In this section, the ablation rate for the second step of ablation was considered.

Here is an example:

The ablation rate for a lump ablated with water flowing at V = 1m/s and T = 45°C, was found experimentally to be 2.2g/min. Table 5.3 presents the inputs to the ablation model, developed here. The inputs were obtained from COMSOL modelling and drag force measurements. By substituting the inputs into the model (Equation 5.9), the ablation rate was calculated to be:

$$\dot{m}_{tot} = 0.8\ \frac{g}{min}$$

In this case, model prediction was smaller than the measurement. Comparisons for all the water and slurry runs are presented as parity plots in Figures 5.19 (a, b and c) and 5.20 (a, b and c) for T = 30 and 45°C.

Table 5.3 Input parameters used for model validation: V=1m/s and T=45°C

Drag force on cylinder	**Shear stress on cylinder**	**Bit. Viscosity (circumference)**	**Bit. Viscosity (ends)**	$(\Delta h)_{circum}$	$(\Delta h)_{ends}$
(N)	(Pa)	(Pa.s)	(Pa.s)	(m)	(m)
2.19	1.89	40.56	40.76	1.04×10^{-3}	1.54×10^{-3}

It appears that the model developed here is reasonably accurate for ablation in water and slurries (C = 0.15 and 0.30) at T = 45°C but the disagreement is significant for ablation in water and slurries (C = 0.15 and 0.30) at T = 30°C. The error for the model prediction is the largest for ablation in slurry (C = 0.15) at T = 30°C.

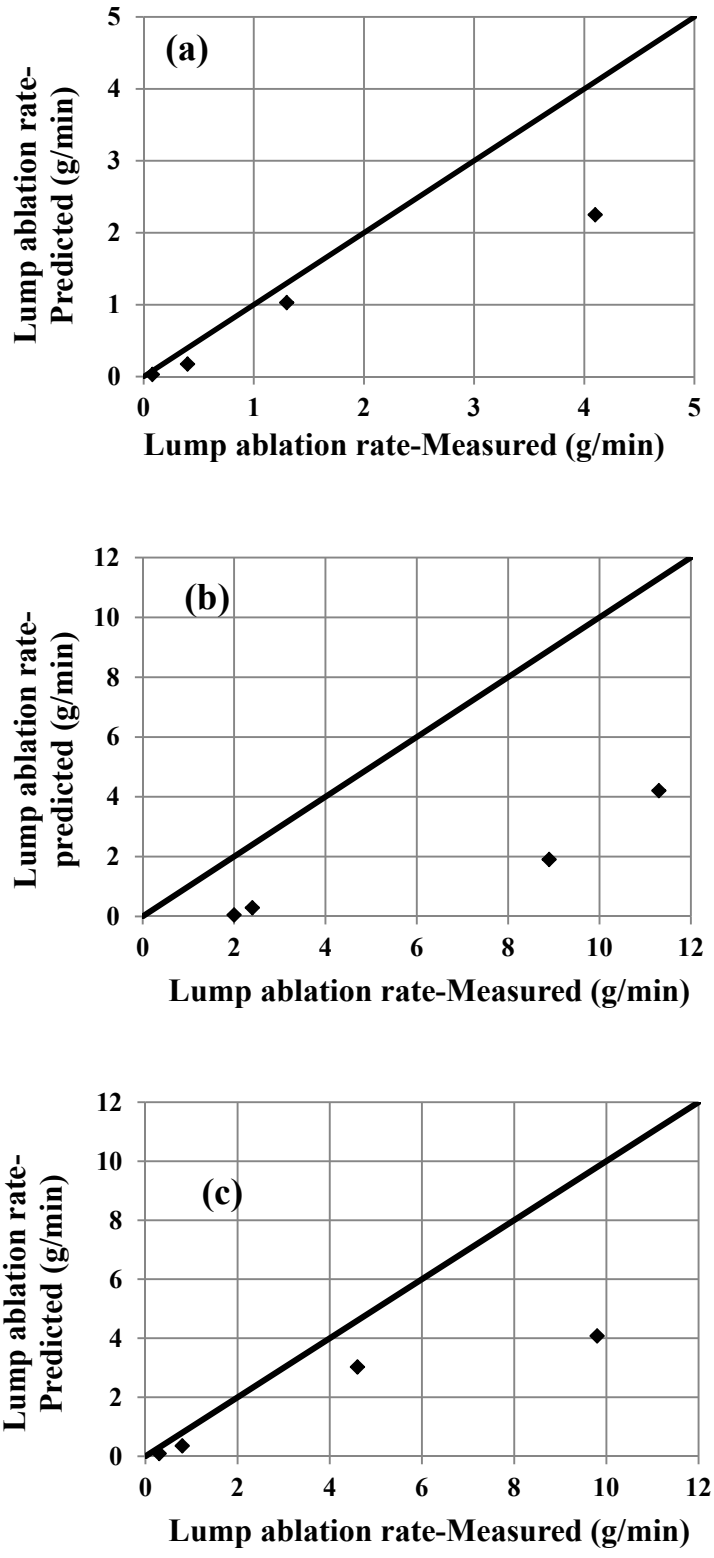

Figure 5.19 Comparison of measured and calculated lump ablation rate: (a) water, (b) slurry (C=0.15) and (c) slurry (C=0.30) at T=30°C

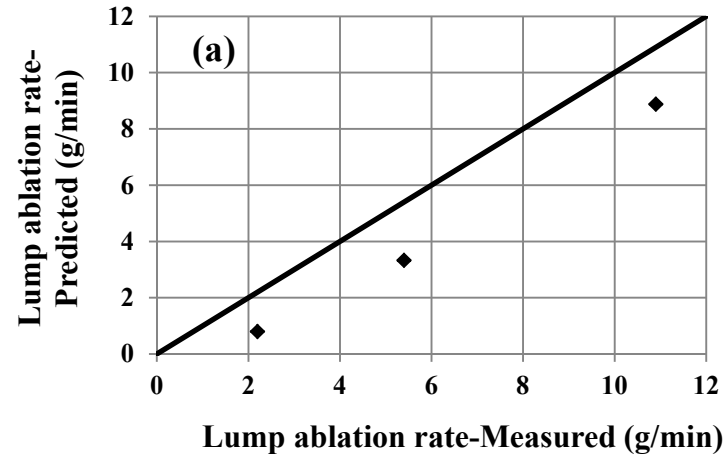

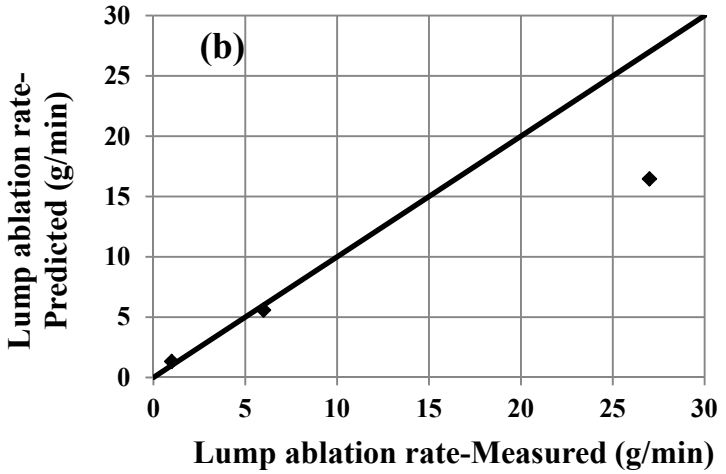

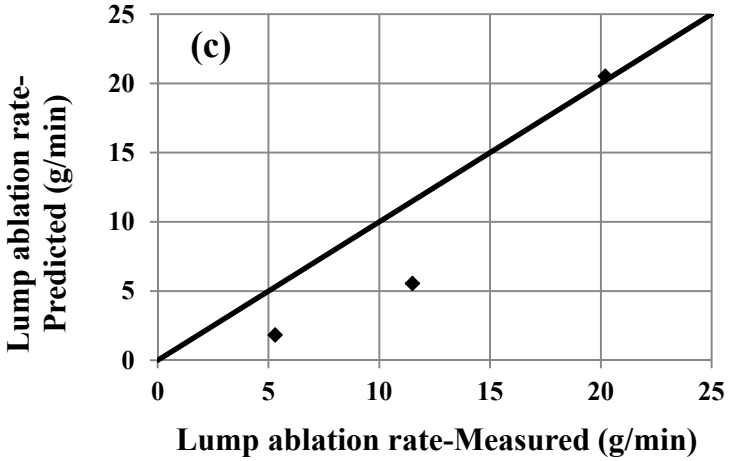

Figure 5.20 Comparison of measured and calculated lump ablation rate: (a) water (b) slurry (C=0.15) and (c) slurry (C=0.30) at T=45°C

5.3.3. Limitations of the validation method

As shown, the model is better capable of predicting lump ablation at T = 45°C. The following reasons can be given for this observation:

- The method used here to calculate skin friction, using the ratio of skin coefficient to drag coefficient, is limited to one study conducted with single-phase flow. Therefore, applying it to the objects in slurries undoubtedly creates some error in calculating surface shear stress. Recall that ablation at T = 30°C is more shear stress dependent than ablation at T = 45°C, as heat transfer is the dominant factor in the latter case. If any error exists in the calculation of the surface shear stress acting on the lump, it will more significantly affect the predictions made for the low temperature cases.
- Turbulence modulation, described in Chapter 4, affects the shear stress in slurries; however, there is no evidence of how it affects the shear stress in highly concentrated slurries. As discussed in Chapter 4, the effect of turbulence modulation on ablation is more pronounced in slurries at T = 30°C and therefore it affects ablation at this temperature. Lack of information required to accurately calculate the surface shear stress under conditions where turbulence modulation is expected to be important is another reason for the poorer model predictions of ablation at T = 30°C.

6. Possible industrial implications

This research represents an initial step of a much larger program to improve and expedite the in-pipe conditioning of oil sand. For environmental and economic reasons, oil sand mine operators wish to obtain complete oil sand conditioning in short pipelines. In order to achieve this goal, the existing conditioning process must be modified.

While it is far too early in the process to recommend concrete changes to the existing pipeline conditioning systems, the limited results obtained thus far can be used to make some qualitative comments on the commercial-scale ablation process. Some of the suggestions are provided in this chapter.

- Oil sand ablation is primarily dependent on temperature, so an increase in the slurry temperature will increase the ablation rate. However, it is known that because of the effect of temperature increases on greenhouse gas emissions, companies are reluctant to increase the temperature of the conditioning process.
- The other important parameter in oil sand lump ablation is slurry velocity. The present study shows that ablation rate is proportional to V^2 so even a slight increase in the slurry velocity causes a significant increase in the ablation rate. Recall that in the present study, the oil sand lump was anchored so the velocity of the lump was zero. In reality, though, the lump moves inside the hydrotransport pipeline and its velocity is roughly 0.9V (Gillies and McKibben, 2011). It must also be noted that residence time is inversely proportional to the slurry velocity for freely moving lumps: the higher the velocity the lower the residence time. When a lump is moving with a slip velocity, the ablation rate is proportional to $(V-V_{lum})^2$. This means that in order to increase the ablation rate of oil sand lump, modifications must be made to increase lump slip velocity. One way to increase the slip velocity is to use vertical sections within hydrotransport pipeline. This way, the lump velocity is equal to its hindered settling velocity. Assuming that one individual

large particle exists in a slurry of smaller particles flowing in a vertical pipe, settling velocity of the large particle in a homogeneous slurry can be determined using Equation 6.1 (Shook and Roco, 1992):

$$\boldsymbol{V_{\infty}} = \left(\frac{\boldsymbol{4gd(\rho_s - \rho_m)}}{\boldsymbol{3C_D\rho_m}}\right)^{\boldsymbol{0.5}} \qquad (6.1)$$

where ρ_s and ρ_m denote the solid particle and slurry flow density and d indicates the solid particle diameter. The density of slurry flow can be calculated using Equation 4.10 (Shook and Roco, 1992):

$$\boldsymbol{\rho_m = \rho_s C + \rho_f(1 - C)} \qquad (4.10)$$

The settling velocity of an individual spherical particle (d = 0.0508m and ρ_s = 2650kg/m^3) in slurry (C = 0.30) of d_{50} = 0.090mm particles flowing at V = 3.5m/s and T = 45°C is 1m/s, when assuming C_D = 0.44. The lump slip velocity then would be 2.5m/s. On the other hand, when the slurry flows, given above, in a horizontal pipe at the same velocity, the particle slip velocity would be 0.35m/s. Reid (2012) also calculated the slip velocity of a 70mm oil sand lump in a vertical tailings (D = 610mm) pipeline operating at V = 4.1m/s equal to 2.94m/s (Reid, 2012).

According to Paradis (2012), Canadian Natural Resources Limited operates their hydrotransport pipeline (D = 711mm, L = 3km) with minimum operating problems (Paradis, 2012) in spite of having vertical sections. In fact, they seem to observe lower erosion inside the vertical hydrotransport pipe compared to the horizontal or inclined lines. Thus, using vertical risers in hydrotransport pipelines seems to be beneficial in different ways.

- Other methods such as using horizontal pipes with wavy bottom (Gillies, 2012) or frequent addition of reducer sections in the hydrotransport pipeline (Sanders, 2012) can be suggested. Using pipes with wavy bottom causes the large oil sand lumps to slow down while moving through the pipe and this increases

their slip velocity compared to the lumps moving in a smooth pipe with an identical bulk velocity.

It is noteworthy that these methods are given based on findings of this study which were obtained for anchored oil sand lumps. In reality, several oil sand lumps move inside the pipes and also pass through the pumps. The methods recommended here must be experimentally and theoretically evaluated before application. Additionally, the effect of these modifications on the pipe erosion and wear of the pipe must be studied.

7. Summary and conclusions

7.1. Summary

Currently, trucks and shovels are used to mine and transfer oil sands ore to the slurry preparation plant. Oil sand slurry is then conditioned and simultaneously transported to the extraction plant using hydrotransport pipelines. Oil sand conditioning includes oil sand lump ablation, bitumen liberation and air attachment. Oil sand production companies wish to eliminate the use of trucks and run the extraction at the mine face. The "At-face" method requires considerably shorter hydrotransport pipelines. One potential issue with using shorter hydrotransport pipelines will be incomplete ablation of oil sand lumps. In order to achieve complete ablation in short hydrotransport pipelines, the existing conditioning process must be modified. Because of the desire to keep greenhouse gas emission as low as possible, conditioning at higher slurry temperatures is not an acceptable option. One way to increase the ablation of oil sand lump is using high-shear short duration conditioning. However, before any fundamental changes are applied to the process, a better understanding of oil sand lump ablation must be obtained. Unfortunately, not many studies have been done on oil sand lump ablation; thus, the current study was focused on the oil sand lump ablation. During this study, an experimental method and apparatus was designed and built for investigating the ablation of oil sand lumps. The effect of slurry temperature, velocity and concentration on the lump ablation was studied. This study aimed to develop a model that predicts the ablation of oil sand lump in different operating conditions as a function of surface shear stress and slurry temperature.

A series of preliminary tests were completed at University of Alberta to identify an idealized oil sand lump with repeatable properties and enough strength to use in ablation tests. These tests were done to develop a plan for the actual experiments and designing the experimental apparatus. A 104mm pipeline loop, with pumping capacity up to 60L/s of highly concentrated slurries was then built at Saskatchewan Research Council PipeFlow Technology Centre™. In this study the maximum tested flow rate was 25L/s. An innovative measurement technique

using strain gauge technology was established for on-line tracking of the mass loss of the anchored oil sand lumps. Four small strain gauges looped in a full-bridge circuit were used for the measurements. The new method also allowed measuring the drag force on ablating and non-ablating objects. The accuracy of the drag force measurement technique was evaluated with comparison of the measured drag force with the calculated drag force on a number of smooth spheres in water.

An oil sand lump was anchored in a basket at the height of 40D. The artificial cylindrical oil sand lumps, manufactured by a time-consuming method and based on similar dry density to the actual oil sand lumps, were used for the experiments. Slurries (C = 0.15 and 0.30) were prepared by mixing pre-weighed industrial quartz (d_{50} = 0.190mm) with water. The flow temperature was adjusted using a double-pipe heat exchanger located in the vertical section of the pipeline loop. The strain gauges, temperature and flow meter readings were collected using Dasylab 10.0 software.

Flow velocity varied from 1 to 3m/s and lump ablation experiments were completed at two different temperatures (T = 30 and 45°C). Mass of the oil sand lump was measured with time at different operating conditions. The effects of slurry velocity, concentration and slurry temperature, on the ablation of oil sand lump were investigated. Ablation of a cylindrical oil sand lump at initial ablation steps was modeled using Newton's Law of Viscosity written for the surface softened layer of the lump. The heat transfer to the lump was simulated using COMSOL Multiphysics software. The results of the COMSOL simulation and the experimental data, collected here, were used to validate the model.

7.2. Conclusions

The present study showed that:

- The innovative on-line measurement method and the experimental apparatus built at SRC provide the opportunity to test oil sand lump ablation at many different operating conditions. The strain gauge measurement method also enables one to measure the drag force on the ablating oil sand lump or for non-ablating objects.
- The artificial oil sand lumps can be used for studying oil sand lump ablation. The data produced using these lumps are repeatable.
- The ablation of oil sand lump is enhanced significantly with increase of the flow temperature. It was observed that the increase of ablation rate because of increasing water and slurry (C = 0.30) temperature by 15°C is equal to the increase of ablation rate associated with a velocity increase of 1m/s. However, a 15°C increase in slurry (C = 0.15) temperature results in the same amount of the increase of ablation rate because of the velocity increase of 0.5m/s. Therefore, heat transfer plays a more important role for ablation in water and slurry (C = 0.30) where surface shear stresses are suggested to be lower.
- Velocity significantly affects oil sand lump ablation. The lump ablation rate changes in two steps: the first step is heat transfer related and the second step is shear stress related. Oil sand lump ablation rate, for the shear stress related step, increases with V^n where n = 2-4.7. Velocity has a much stronger effect on lump ablation at the lower slurry temperature tested here (30°C).
- Ablation in water occurs considerably more slowly than that in the slurry. However, an increase of slurry concentration from 15% to 30% at T = 30°C reduces the ablation rate. This reduction may be related to the turbulence modulation in slurries which affects shears forces and heat transfer.

- For the range of concentrations studied here, slurry concentration does not have a significant influence on the ablation of oil sand lumps at T = 45°C.
- The ablation rate of an oil sand lump at certain operating conditions remains constant during ablation because it is anchored in a basket.
- The drag force acting on a lump depends on the slurry concentration. The drag force acting on the lump is the greatest in slurry (C = 0.30).
- The equivalent fluid model was found to be appropriate for simulating the drag force acting on the large objects in slurry flow in a vertical pipe. In the equivalent fluid model, the slurry is treated like a single-phase fluid with density and viscosity related to the slurry concentration.
- The ablation model developed here shows that ablation rate is a function of surface shear force and temperature. In the model, the effect of temperature is implemented as the change in the bitumen viscosity.
- Validation of the ablation model shows that the model better predicts ablation at T = 45°C. This may be related to the assumptions made to calculate the surface shear stress on a lump.

7.3. Major contributions of this study

The major contributions of the current study can be summarized as:

- During this study, an innovative on-line mass and force measurement method using strain gauges was developed. This method not only allowed measuring the drag force on the ablating oil sand lump, it also was used to measure the drag force on different non-ablating objects in various operating conditions. These measurements were used to model the drag force in slurries.
- For the first time, an artificial oil sand lump was successfully used for studying lump ablation.
- The effect of slurry velocity and concentration on the oil sand lump, with characteristics very similar to those of an actual oil sand lump, was experimentally studied for the first time.

- The ablation of an individual oil sand lump was visualized and recorded.

7.4. Shortcomings of this study

These are the shortcomings of this work:

- Use of a basket to hold an oil sand sample in place eliminated lump surface area exposed for ablation and prevented it from freely moving along the pipe.
- The experiments were completed at two different temperatures and one sand size. This study was also limited to one lump size and shape.
- During the current study, attempts to apply a method of mass measurement for a freely-moving oil sand lump did not provide any practical results. By anchoring the lump in vertical slurry flow, forces caused by wall-lump interactions, lump-lump interactions and Coloumbic force are eliminated. The reduction or elimination of these forces probably results in lower ablation rates. When a lump is fixed in place, the effect of velocity on its residence time is also eliminated.
- In order to develop the model many assumptions had to be made; in areas such as heat transfer to the large objects and estimating skin friction using drag force measurements in slurry flows.

8. Recommendations for future work

The effect of shear exposure on the oil sand lump ablation was studied here. This research will be a basis for further investigations of oil sand lump ablation. Many questions must be answered before an ablation model capable of accurately predicting the ablation rate of any type of oil sand lump in different operating conditions is developed.

A number of different studies must be done to be able to generalize some of the results of this study. The recommendations resulting from this project include the following:

- Conduct ablation tests in slurries with lower and higher concentrations than those examined here to gain a better understanding of the effect of slurry concentration on lump ablation and on the way turbulence modulation affects the experiments. It is envisioned that tests in slurries ($C < 0.30$) can easily be completed using the existing SRC apparatus but in order to run tests in slurries ($C > 0.30$), some modifications must be made. Most importantly, the strain gauge measurement becomes impossible as the maximum voltage was nearly achieved when tests were done using slurry ($C = 0.30$) at $V = 2.5$m/s. It is suggested to use strain gauges with smaller surface area and larger resistance or replace the membrane with a thinner membrane to increase its deformation reaction.
- Investigate the oil sand lump ablation in slurries with larger particle size (e.g. 0.300mm). This investigation will help to determine oil sand lump ablation for different ore grades. When this sand size is used, a higher range of slurry velocity must be considered to avoid settling of sand in the horizontal section of the pipe. In this case, the range of slurry concentration may be limited because of limitations of the current strain gauge measurement. Similar solutions as given above can be applied to modify the measurement system.

- Repeat a number of experiments in a temperature between 30 and 45°C; say 37°C or 40°C. This is to examine if turbulence modulation affects ablation differently at different temperatures.
- Study ablation of freely-moving oil sand lump inside the pipeline loop and compare the results with the current study. One way to prevent the lumps from entering the pump might be to trap them at the end of the pipe before they enter the storage tank. The lumps can again be dropped into the loop at the pump discharge using a conical feeder. These experiments can be done by introducing more than one lump to the system. One simple way to measure lump(s) mass is to use a spring scale connected to the trapping tool. The limitation of this method is that at high velocities, frequent trapping and dropping of the lump(s) is required. One way to reduce the trapping and dropping exercise is to increase the pipe length; in this case replacing the loop with a horizontal pipeline will be more practical. Another possibility is to simply let the lumps circulate in the loop through the pump and at the end attempt to account for the shearing or breakage caused by the pump.
- Plan and conduct experiments that provide knowledge about heat transfer from slurries to large non-ablating objects. If a correlation for the heat transfer coefficient is developed, a significant improvement in the ablation model will be observed. These experiments need a new experimental apparatus.
- Conduct lump ablation tests using oil sand lumps of different compositions (bitumen/sand/water) and sizes. It is noteworthy that the process of manufacturing an artificial oil sand lump is very sensitive to the type of material which is used. The amount of fine particles, sand particle size distribution, its particle shape and bitumen viscosity, used for injection, significantly affect the lump production process and its characteristics. It is suggested to apply the changes in the materials in a step- by-step fashion in order to more easily resolve the potential issues. Smaller and larger oil sand lumps can be produced by manufacturing new moulds.

- Measure drag force on non-ablating objects (different shapes and sizes) in different slurry concentrations to develop a drag coefficient correlation applicable to all objects. This also can be done in a way that one correlation is developed for each object depending on its shape. These experiments are easily done using the SRC experimental apparatus as a continuation to the drag force measurements done in this study. It is recommended to conduct these tests for objects with spherical equivalent diameter smaller or equal to 50.8mm to avoid significant wall effects.
- Measure the slip velocity of large non-ablating particles in different slurry velocities and concentrations. It is suggested to use the SRC study in this area as the start point. This study is proprietary and legal actions must be taken to obtain permission to use it.
- Use findings of ongoing research currently being conducted in the Pipeline Transport Processes group on turbulence modulation in concentrated slurries to interpret the effect of concentration on ablation at low slurry temperatures.
- Manually measure temperature of lump at different internal points by introducing thermometers inside the lump while it is placed in the room temperature. Compare the measurements with the predictions of the COMSOL simulation and determine how different they are and how this difference affects the model validation.
- Update the ablation model developed in this study using additional information obtained by running experiments mentioned above. The updated model is expected to provide capability of predicting oil sand lump ablation rate in any desired operating conditions.

References

Achenbach, E. (1968). Distribution of local pressure and skin friction around a circular cylinder in cross-flow up to Re=5*10^6. *Journal of Fluid Mechanics, 34*, 625-639.

Adane, K. F. K., Sumner, R. J., McKibben, M. J., and Sanders, R. S. (2012). Modelling vertical slurry flows. *Powder Technology, To be submitted*

Bird, R. B., Stewart, W. E., and Lightfoot, E. N. (1960). *Transport phenomena* John Wiley & Sons.

Cervenan, M. R., Vermeulen, F. E., and Chute, F. S. (1981). Thermal conductivity and specific heat of oil sand samples. *Canadian Journal of Earth Sciences, 18*, 926-931.

Chalaturnyk, R. J. (January 2009). *Personal communication*

Crowe, C. T. (2000). On models for turbulence modulation in fluid-particle flows. *International Journal of Multiphase Flow, 26*(5), 719-727.

Doroodchi, E., Evans, G. M., Schwarz, M. P., Lane, G. L., Shah, N. and Nguyen, A. (2008). Influence of turbulence intensity on particle drag coefficients. *Chemical Engineering Journal, 135*(1–2), 129-134.

El-Behery, S. M., El-Askary, W. A., Hamed, M. H., and Ibrahim, K. A. (2011). Hydrodynamic and thermal fields analysis in gas-solid two-phase flow. *International Journal of Heat and Fluid Flow, 32*(3), 740-754.

Eskin, D., Leonenko, Y., Lezhnin, S., and Vinogradov, O. (2002). A model of oil sand lump digestion. *Minerals Engineering, 15*(6), 469-472.

Flint, L. (2005). Bitumen recovery Technology–A review of long-term R&D opportunities. LENEF Consulting (1994) Limited.

Friesen, W. I., Dabros, T., and Kwong, T. (2004). A bench-scale study of conditioning behaviour in oil sands slurries. *The Canadian Journal of Chemical Engineering, 82*(4), 743-751.

Gillies, D. P. (2012), Particle contributions to kinematic friction in slurry pipeline flow, *Masters of Science Thesis*. Chemical and Material Engineering Department, University of Alberta, Edmonton, Alberta, Canada.

Gillies, R. G., and McKibben, M. M. (2011). *Personal communication.*

Gillies, R. G., and Shook, C. A. (2000). Modelling high concentration settling slurry flows. *The Canadian Journal of Chemical Engineering, 78*, 709-715.

Gillies, R. G., Shook, C. A., and Xu, J. H. (2004). Modelling heterogeneous slurry flows at high velocities. *Canadian Journal of Chemical Engineering, 82*(5), 1060-1065.

Gore, R. A., and Crowe, C. T. (1989). Effect of particle size on modulating turbulent intensity. *International Journal of Multiphase Flow, 15*(2), 279-285.

Hesketh, R. P., Fraser Russell, T. W., and Etchells, A. W. (1987). Bubble size in horizontal pipelines. *AIChE Journal, 33*(4), 663.

Holman, J. P. (2010). *Heat transfer* (10th ed.) McGraw Hill-Higher Education.

Kawanisi, K., & Shiozaki, R. (2008). Turbulent effects on the settling velocity of suspended sediment. *Journal of Hydraulic Engineering*, 134 (2) 261-266.

Kim, S., Lee, K. B., and Lee, C. G. (2005). Theoretical approach on the turbulence intensity of the carrier fluid in dilute two-phase flows. *International Communications in Heat and Mass Transfer, 32*(3-4), 435-444.

Kiyohashi, H., Kawashima, T., and Ishihama, W. (1974). On heat transfer and pressure drop of pipeline slurries for prevention of freezing.

Law, H. S., Masliyah, J. H., and Nandakumar, K. (1987). Ablation of ice-solids and wax-solids mixtures in turbulent axisymmetrical water jets. *Canadian Journal of Chemical Engineering, 65*(3), 420-429.

Masliyah, J. H. (2008). Fundamentals of oil sand extraction. University of Alberta

Masliyah, J. H., Czarnecki, J., and Xu, Z. (2011). Handbook on theory and practice of bitumen recovery from Athabasca oil sands. Canada: Kingsley Knowledge Publishing.

Masliyah, J. H., Zhou, Z. J., Xu, Z. H., Czarnecki, J., and Hamza, H. (2004). Understanding water-based bitumen extraction from Athabasca oil sands. *Canadian Journal of Chemical Engineering, 82*(4), 628-654.

Paradis, T. (2012). Vertical hydrotransport riser. *1st Pipeline Transport Processes (PTP) Workshop,* Edmonton, AB, Canada.

Perry, C. C., and Lissner, H. R. (1962). *The strain gauge premier* (2nd ed.) New York: McGraw-Hill.

Qiu, L. (2010). Effect of oil sands slurry conditioning on bitumen recovery from oil sands ores. (M.S. Thesis, University of Alberta (Canada)).

Reid, K. (2012). Vertical versus inclined transport: Oil sand lumps. *1st Pipeline Transport Processes (PTP) Workshop,* Edmonton, AB, Canada.

Sanders, R. S. (2008, 2011 and 2012). *Personal communication.*

Sanders, R. S., Ferre, A. L., Maciejewski, W., Gillies, R. G., and Shook, C. A. (2000). Bitumen effects on pipeline hydraulics during oil sand hydrotransport. *The Canadian Journal of Chemical Engineering, 78*(4), 731-742.

Sanders, R. S., Schaan, J., Hughes, R., and Shook, C. A. (2004). Performance of sand slurry pipelines in the oil sands industry. *Canadian Journal of Chemical Engineering, 82*(4), 850-857.

Sanders, R. S., Schaan, J., and McKibben, M. M. (2007). Oil sand slurry conditioning tests in a 100 mm pipeline loop. *Canadian Journal of Chemical Engineering, 85*(5), 756-764.

Schaan, J., Cook, N., and Sanders, R. S. (2007). On-line wear measurements for commercial-scale, coarse-particle slurry pipelines. *HYDROTRANSPORT 17 - the 17th International Conference on the Hydraulic Transport of Solids,* 291-300.

Scott, J. D., Chalaturnyk, R. J., and Wong, Y. K. (August, 2001). Manual of artificial oil sands sample preparation. Unpublished manuscript.

Shook, C. A., Gillies, R. G., and Sanders, R. S. (2002). Pipeline hydrotransport with application in the oil sand industry. (No. 11508-1E02). SRC Pipe Flow Technology Centre:

Shook, C. A., and Roco, M. C. (1992). Slurry flows: Principles and practice

Speight, J. G. (2005). Handbook of coal analysis. John Whiley & Sons.

Traynis, V. V. (1970). Parameters and flow regimes for hydraulic transport of coal by pipelines. Terraspace*, INC.*

Versteeg, H. K., and Malalasekera, W. (1995). An introduction to computational fluid dynamics, the finite volume method. Prentice Hall.

Wallwork, V., Xu, Z. H., and Masliyah, J. H. (2004). Processibility of Athabasca oil sand using a laboratory hydrotransport extraction system (LHES). *Canadian Journal of Chemical Engineering, 82*(4), 687-695.

Window,A.L. and Holister,G.S. (1982). Strain gauge technology (1st ed.). London and New York: Elsevier Applied Science.

Young, D., Munson, B. R., and Okiishi, T. H. (2004). A brief introduction to fluid mechanics. John Wiley & Sons.

Zhao, L. H., Andersson, H. I., and Gillissen, J. J. J. (2010). Turbulence modulation and drag reduction by spherical particles. *Physics of Fluids, 22*(8) .

Zhou, Q., and Cheng, N. (2009). Experimental investigation of single particle settling in turbulence generated by oscillating grid. *Chemical Engineering Journal,* 149(1–3), 289-300.

Appendix 1: Strain gauge installations

All the information given here is taken directly from Micro-Measurements division for Measurements Group, Inc. (www.measurementsgroup.com)

1. Introduction

Because the strain gauge is an extremely sensitive device capable of registering the smallest effects of an imperfect bond, considerable attention to details must be taken to assure stable, creep-free installations. However, the techniques involved are very simple, and readily mastered.

2. Strain gauge adhesive

Micro-measurements M-LINE adhesives undergo extensive laboratory testing to ensure reliability and consistency of those properties required in strain gauge bonding. To assure accurate and reliable strain gauge measurements, a certified adhesive such as M-Bond 200 methyl-2-cyanoacrylate or M-Bond AE-10 epoxy adhesive is selected for most general laboratory installations.

2.1 M-Bond 200

Micro-measurements certified M-Bond 200 is an excellent general-purpose laboratory adhesive because of its fast room temperature cure and ease of application. It is compatible with all Micro-measurements strain gauges and all common structural materials. M-Bond 200 adhesive can be used for high-elongation tests (+60000με), for fatigue studies, and for one-cycle proof tests within a normal operating temperature range of -25° to +150°F (-32° to +65°C).

The catalyst supplied with M-Bond 200 is specially formulated to control the reactivity rate. For best results, the catalyst should be used sparingly. Since M-Bonds are weakened by exposure to high humidity, adequate protective coatings are essential.

3. Surface preparation

Strain gauges can be bonded satisfactorily to almost any solid material if the material surface is properly prepared. The purpose of surface preparation is to develop a chemically clean surface having a roughness appropriate to the gauge installation requirements, a surface alkalinity of the correct pH, and visible gauge lay out lines for locating and orienting the strain gauge. The Micro-measurements system of surface preparation will accomplish these objectives for aluminum alloys and steels in fine basic operations:

- Solvent degreasing
- Surface abrading
- Application of gauge layout lines
- Surface conditioning
- Neutralizing

To ensure maximum cleanliness and best results, the following should be avoided in all steps:

- Touching the surface with the fingers
- Wiping back and forth and reusing swaps or sponges
- Dragging contaminants into the cleaned area from the uncleaned boundary of that area
- Allowing a cleaning solution to evaporate on the surface
- Allowing partially prepared surface to sit between steps in preparation process or a prepared surface to sit before bonding

3.1 Solvent degreasing

Degreasing is performed to remove oils, greases, organic contaminants, and soluble chemical residues. Degreasing should always be the first operation. Degreasing can be accomplished using a solvent such as CSM-1 degreaser or acetone. Use a clean gauze sponge to clean the entire specimen, if possible, or an area covering 4 to 6 in on all sides of the gauge location.

3.2 Surface abrading

The surface is abraded to remove any loosely bonded adherents (scale, rust, paint, coatings, oxides, etc.), and to develop a surface texture suitable for bonding. For rough or coarse surfaces it may be necessary to start with a grinder, disc sander, or file; but, for most specimens a suitable surface can be produced with only silicon-carbide paper of the appropriate grit.

Place a liberal amount of M-Prep conditioner A in the gauging area and wet-lab with clean 320-grit silicon-carbide paper for aluminum, or 220-grit for steel. Add conditioner A as necessary to keep the surface wet during the palling process. When a bridge surface is produced, wipe the surface dry with a clean gauze sponge. A clean surface of the gauze should be used with each wiping stroke. A sufficiently large area should be cleaned to ensure that contaminants will not be dragged back in to the gauging area during the steps to follow. Repeat the above step, using 400-grit silicon-carbide paper for aluminum, or 300-grit for steel.

3.3 Layout lines

The desired location and orientation of the strain gauge on the test surface should be marked with a pair of crossed, perpendicular reference lines. The reference layout lines should be burnished, rather than scored or scribed, on the surface. For aluminum, a medium hard drafting pencil is satisfactory. For most steels, a ball-point pen or a tapered brass rod may be used. All residues from the burnishing operations should be removed in the following step.

3.4 Surface conditioning

After the layout lined are marked, conditioner A should be applied repeatedly, and the surface scrubbed with cotton-tipped applicators until a clean tip is no longer discolored by scrubbing. The surface should be kept constantly wet with conditioner A until the cleaning is completed. When clean the surface should be dried by wiping through the cleaned area with a single slow stroke of a gauze sponge. The stroke should begin inside the cleaned area to avoid dragging contaminants in from the surrounding area. Throw the used gauze away and, with

fresh gauze, make a single slow stroke in the opposite direction. Throw the second gauze away.

3.5 Neutralizing

To provide optimum alkalinity for Micro-measurements strain gauge adhesives, the cleaned surface must be neutralized. This can be done by applying M-Prep Neutralizer 5A liberally to the cleaned surface, and scrubbing the surface with a clean cotton-tipped applicator. The cleaned surface should be kept completely wet with Neutralizer 5A throughout this operation. When neutralized, the surface should be dried by wiping through the clean area with a single slow stroke of a clean gauze sponge. Throw the used gauze away and, with fresh gauze, make a single stroke in the opposite direction. Always begin within the cleaned area to avoid recontamination from the un-cleaned boundary. The surface is now properly prepared for gauge bonding. The gauges should be installed within 30 minutes on aluminum or 40 minutes on steel.

4. Strain gauge bonding

The electrical resistance strain gauge is capable of making accurate and sensitive indications of strain on the surface of the test part. Its performance is absolutely dependent on the bond between itself and the test part. The procedures outlined below will help ensure satisfactory bonds when using M-Bond 200 or AE-10 adhesives. The steps shown assume that a terminal strip will be used.

4.1 Handling and preparation

Micro-measurements strain gauges are specially treated for optimum bond formation with all appropriate gauge adhesives. No further cleaning is necessary if contamination of the prepared bonding surface is avoided during handling. Gauges should never be touched with hands. Remove strain gauge from its acetate envelope by grasping the edge of the gauge backing with tweezers, and place on a chemically clean glass plate with the bonding side of the gauge down. Place the

appropriate terminal (if any) next to the strain gauge solder tabs, leaving a space of approximately 1/16 (1mm) between the gauge backing and terminal.

Using a 4-to-6-in length of M-LINE PCT-2A cellophane tape, anchor one end of the tape to the glass plate behind the gauge and terminal. Wipe the tape firmly down over the gauge and terminals. Pick the gauge and terminals up by carefully lifting the tape at a shallow angle (30 to 45 degrees) until the tape comes free with the gauge and terminal attached. (The shallow angle is important to avoid over-stressing the gauge and causing permanent resistance changes.)

The stain gauge is now prepared for positioning on the test specimen. Position the gauge/tape assembly so the triangle alignment marks on the gauge are over the layout lines on the specimen. Holding the tape at a shallow angle, wipe the assembly onto the specimen surface. If the assembly is misaligned, lift the tape again at a shallow angle until the assembly is free of the specimen. Reposition and wipe the assembly again with a shallow angle.

In preparation for applying the adhesive, lift the end of the tape opposite the solder tabs at a shallow angle until the gauge and terminal are free of the specimen. Tack the loose end of the tape under and press to the surface so the gauge lies flat with the bonding side exposed.

The appropriate adhesive may now be applied. The procedure for M-Bond 200 is described in the section that follows.

4.2 Bonding with M-Bond 200

M-Bond 200 should be applied sparingly in a thin uniform coat. Wipe the brush against the lip of the bottle approximately ten times to remove most of the catalyst. Set the brush down on the gauge and swab the gauge backing by sliding the brush over the entire gauge surface. Move the brush to an adjacent tape prior to lifting from the surface. Allow the catalyst to dry at least one minute under laboratory conditions.

The next three steps must be completed in sequence within three to five seconds.

Lift the tucked-under tae. Holding the gauge/ tape assembly in a fixed position, apply one or two drops of M-Bond 200 adhesive at the junction of the tape and specimen surface, about ½in outside the actual gauge installation area. Immediately rotate the tape to approximately a 30-degree angle so that the gauge is bridged over the installation area. Holding the tape slightly taut and beginning from the tab end of the gauge, slowly and firmly make a single wiping stroke over the gauge/ tape assembly with a clean gauze sponge to bring the gauge back down over the alignment marks on the specimen. Release the tape. Immediately apply firm thumb pressure to the gauge and terminal area. This pressure should be held for at least one minute. Wait two minutes before the next step (tape removal).

The gauge and terminal should now be bonded to the specimen. To remove the tape, pull it back directly over itself, peeling it slowly and steadily off the surface.

Appendix 2: Manufacturing artificial oil sand lump

1. Equipment

The following equipment was used:

O-rings	Four ,OD = 50.8mm, Thickness = 3mm
Latex membrane	L = 50mm, ID = 50.8mm- HM-4180.20
Porous stones	Two: D = 63.2mm, One: D = 58.8mm Product of Mott Corporation
Sample cell	Split mould parts, Bottom pedestal, Top cab, Top plate, Cooling blanket
Heating blanket & Temperature controller	Tubular blanket ID = 12.7cm, OD = 17.78cm, L = 17.78cm, Heater rate: 100W, 120 VAC, 1 phase, 60 Hz, 0.84 AMPS, custom-built by Briskheat
Triaxial load frame	HM398 Proloader II (Max capacity: 45N), product of Gilson company Inc.
Vibrating table	Syntron Vibrating table, Model VP-51-D1, 115V, 60Cy
Vacuum pump	Oil-less diaphragm, Model No. DAA-V715A-EB
Hot plate	Temperature adjustable
Hot- air gun	Varitemp®
Dry ice	3kg per day
Bitumen storage tank	Piston cylinder with volume = 1*L*

The following images present the split mould and different equipment used for lump manufacturing.

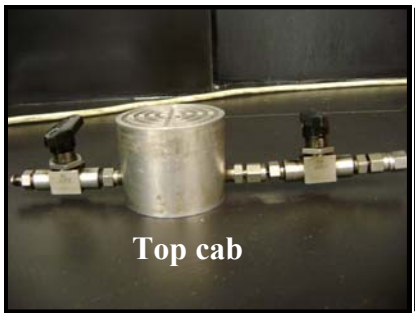

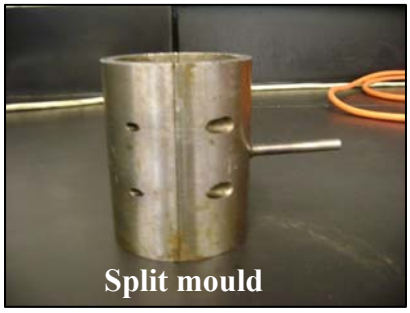

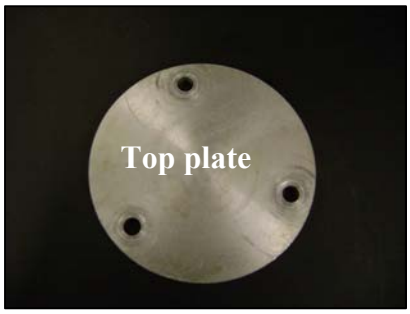

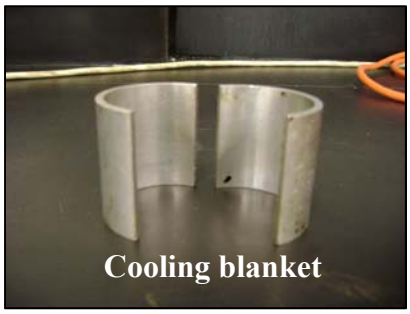

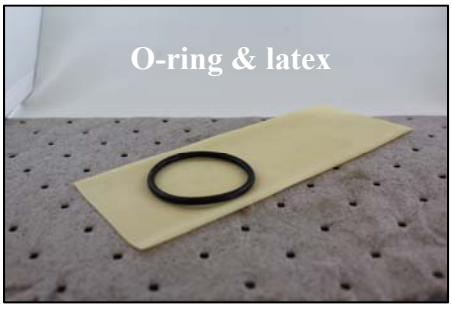

The image of piston-cylinder for bitumen storage and its dimension are given here.

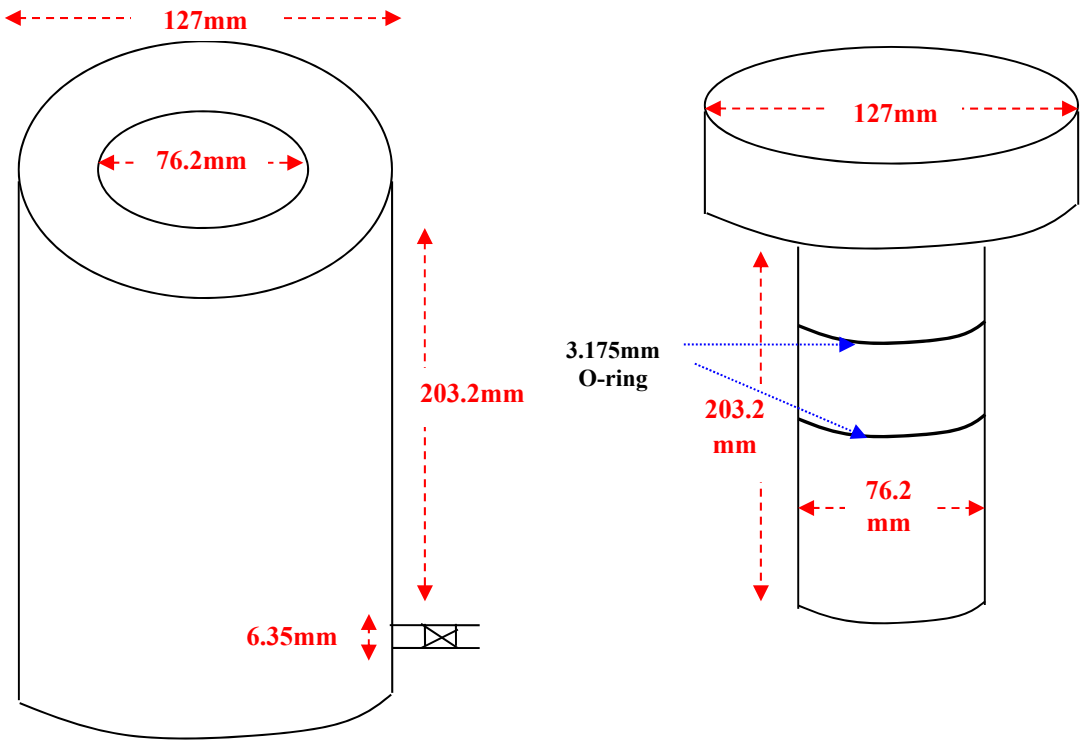
127mm
76.2mm
203.2mm
6.35mm
127mm
3.175mm
O-ring
203.2
mm
76.2
mm

2. Preliminary preparation

All the information given here is given from (Scott et al., 2001).
A series of preparations must be completed before making artificial oil sand lump. Pictures of different steps are given for further information.

1) Suitable amount of sand, method of calculation given in 3.1.3 is weighed and boiled for 30min in a beaker of half full of water. Boiling seizes the aeration, saturation and cleaning of the sand. Cleaning is more meant for tailings sand.
2) Porous stones are boiled in a beaker for 20min. This way, stone pores become clean and saturated with water.
3) Stored bitumen is warmed up to 80°C using the heating blanket.
4) Latex membrane is checked for tiny holes and obvious leaks.

3. Sand densification

Following steps should be taken to prepare a stack of dense sand:

1) Latex membrane is put on the smaller cylindrical part of the pedestal and is sealed with two O-rings.
2) Saturation valves are opened and water is flown through until 5mm of water is stored on top of the pedestal. Valves should be closed at this point.
3) A saturated 63.5mm porous stone is placed on the bottom pedestal and again water is flown through the valves. It is to make sure the gap between porous stone and pedestal is air-free.
4) Split mould is now assembled on the pedestal using four screws. The top portion of the membrane is then folded down over the mould and is sealed with O-rings.
5) The assembled mould should now be attached to a vacuum outlet which applies 80kPa.
6) Saturated sand is then transferred to the mould using a scoop.

7) Once all the sand was transferred into the mould, a saturated 50.8mm diameter porous stone is placed on top of the sand; and then a surcharge weight of about 2.8kg (steel cylinder with d = 50.8mm) is positioned on top of it.
8) At this point, the assembly is transferred on the vibrating table and is vibrated at the speed of 60 out of 100 for 1-3min. The vibration is done to reach the appropriate level of sand compaction. Desired level of compaction was obtained experimentally; it reaches when 36mm of the surcharge weight is down into the split mould. If the vibrating table is close to the vacuum pump, vibrating can be started before step 6 at a lower rate. Vibration can then be increased to reach the desired level.
9) After removing the surcharge and porous stone, the membrane is unfolded and then top section is removed.
10) Membrane is folded down over the mould and is held with O-rings. Second saturated 63.5mm porous stone is positioned on the dense sand. At this moment, about 2mm water must be seen on top of the porous stone.

4. Bitumen flushing

1) Top cap is placed on the porous stone; water pushes out of the valves and makes them air-free. Valves should be closed now.
2) The membrane should now be unfolded onto the top cap and be sealed with O-rings.
3) Disconnect the vacuum from the split mould and connect it to the top cap. Inside the cell must now be vacuumed for 30s. Water stored on top of the porous stone is being taken out.
4) The assembly is disconnected from the vacuum. Cell must be opened very cautiously. The vacuum formed inside the cell prevents the pack of sand to change shape.
5) O-rings are moved down to the appropriate level. If they are not set on the right place, assembling the split mould without damaging the stack of sand is very difficult and extra care must be taken.

6) The cell is assembled once again by tightening the screws.
7) Three treaded rods which are bolted on the bottom pedestal tightly hold the top plate over the top cap. This prevents any up lift action during freezing or bitumen flushing process.
8) The whole set-up should now be transferred to a hot plate in order to warm up the dense sand and mould assembly to 80°C. The heating helps to reduce the viscosity of bitumen to aid in flushing it through the sand. This process takes about 45min with hot plate set at 80°C.
9) Bitumen storage tank, now at about 80°C, is attached to one of the drainage valves of the top cap. Stainless steel tubing with ID = 6.35mm was used for this purpose.
10) Bitumen flushing with the flow rate of 15 mL/h is started. The piston of the storage piston-cylinder is pushed at the appropriate speed (in this case 20-22) using a load frame to provide the required bitumen flow rate.
11) One of the pedestal's drainage valves remains open during flushing. About 30-35 mL of water is normally replaced with bitumen over a period of 4-5 hours bitumen flushing.
12) After bitumen starts to discharge from the pedestal's drainage valve, meaning that sand is bitumen saturated, bitumen flushing is stopped. The whole assembly is then transferred to a freezing box with dry ice and remains for about 30min. All the valves should be closed at this point.

5. Mould Disassembling

Once the whole set-up is completely frozen, it is taken out from the dry ice and:

1) The top plate is first removed, and then the split mould is disassembled and removed. The cool jacket (previously cooled with dry ice) is put around the lump.
2) The pedestal is heated with hot plate and removed. Before each step the set-up is placed back in the ice to refreeze, this prevents the lump from falling apart or losing its shape.
3) The top cap is also heated and detached with the same procedure.

4) Porous stones are then quickly heated and removed using the hot gun.
5) Latex membrane is then taken away.
6) The artificial oil sands lump is now wrapped with plastic and aluminum wraps. It is properly labeled and kept frozen in a freezer.

Pictures of the major steps of manufacturing of the oil sand lump are given below:

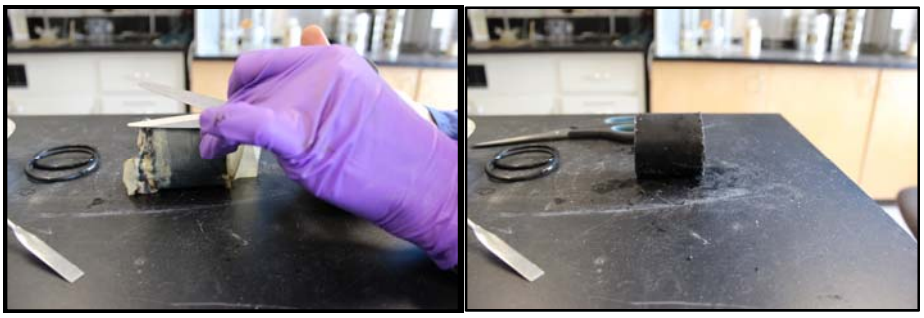

To speed up the production of lump, at times two split mould were prepared with similar method. Both assemblies were then individually placed on top of the hot plates at identical height for bitumen flushing. Bitumen flushing was still completed with identical piston-cylinder, this time a tee connection and two sets of steel tubing were used. One pressure gauge (ASHCROFT, Model No.15W 1005PH 01L) was used right at the discharge valve to ensure pressure does not increase when the two cells are injected.

Appendix 3: Carrier fluid and bitumen viscosity measurement

Samples of carrier fluid were taken from a ball valve positioned downstream the pump discharge on a ½ inch pipe. A fluid sample was first screened with a 45μm sieve to eliminate large particles and then was poured into the cup for the measurement. Viscosity was measured at 25°C using HAAKE RS150 (RheoStress RS150) viscometer with applying Z41 Ti sensor ($OD_{spindle}$ = 20.71mm, ID_{cup} = 21.7mm and L = 55mm). Table 3A.1 presents the data of viscometer output for different dates.

Table 3A.1. Viscometer output for carrier flow viscosity measurements at different times

Jul-14		Jul-25		Jul-27		Jul-29		Aug-17		Aug-18	
Spindle speed (1/min)	Torque (μN/m)	Spindle speed (1/min)	Torque (μN/m)	Spindle speed (1/min)	Torque (μN/m)	Spindle speed (1/min)	Torque (μN/m)	Spindle speed (1/min)	Torque (μN/m)	Spindle speed (1/min)	Torque (μN/m)
5.00	2.311	5.00	2.693	5.00	2.647	5.00	2.647	5.00	2.395	5.00	2.37
15.55	6.540	15.55	6.600	15.55	6.858	15.55	6.858	15.55	6.328	15.55	6.34
26.11	10.942	26.11	10.809	26.11	10.895	26.11	10.895	26.11	10.574	26.11	10.58
36.67	15.397	36.67	14.818	36.67	14.855	36.67	14.855	36.67	14.815	36.67	14.94
47.22	19.966	47.22	18.965	47.22	18.805	47.22	18.805	47.22	19.225	47.22	18.88
57.78	24.766	57.78	23.357	57.78	22.876	57.78	22.876	57.78	23.661	57.78	23.06
68.34	29.601	68.34	27.949	68.34	26.948	68.34	26.948	68.34	28.150	68.34	27.51
78.89	34.531	78.89	32.294	78.89	31.287	78.89	31.287	78.89	32.661	78.89	32.20
89.45	39.411	89.45	37.135	89.45	35.680	89.45	35.680	89.45	37.345	89.45	36.85
100.00	47.735	100.00	46.195	100.00	43.530	100.00	43.530	100.00	46.118	100.00	46.34
100.00	47.671	100.00	46.271	100.00	43.583	100.00	43.583	100.00	46.257	100.00	46.31
89.45	38.483	89.45	37.035	89.45	35.182	89.45	35.182	89.45	37.227	89.45	36.80
78.89	33.501	78.89	32.139	78.89	30.677	78.89	30.677	78.89	32.420	78.89	32.02
68.34	28.666	68.34	27.652	68.34	26.274	68.34	26.274	68.34	27.844	68.34	27.39
57.78	23.977	57.78	23.163	57.78	22.107	57.78	22.107	57.78	23.282	57.78	22.95
47.22	19.343	47.22	18.757	47.22	17.913	47.22	17.913	47.22	18.781	47.22	18.52
36.67	14.868	36.67	14.447	36.67	13.842	36.67	13.842	36.67	14.449	36.67	14.28
26.11	10.495	26.11	10.237	26.11	9.813	26.11	9.813	26.11	10.290	26.11	10.09
15.55	6.238	15.55	6.137	15.55	5.806	15.55	5.806	15.55	6.176	15.55	6.00
5.00	2.218	5.00	2.209	5.00	2.064	5.00	2.064	5.00	2.323	5.00	2.20

The same viscometer was used to measure the viscosity of bitumen. This time Z38 Ti sensor ($OD_{spindle}$ = 19.01mm, ID_{cup} = 21.7mm and L = 55mm) was used. Bitumen was pre-heated in a container whose lid is closed, to avoid water loss, using an oven before pouring into the cup; this was to facilitate the process of pouring a small sample into the cup. Bitumen was also heated with a stepwise procedure before the actual viscosity measurement at a certain temperature. It was to ensure that temperature is uniform within the sample before measuring the viscosity. This process was done in three steps, for each step the stirring speed increased gradually. Table 3A.2 gives the time period and spindle speed of each step. Tables 3A.3 and 3A.4 illustrate the spindle speeds and the torques measured for each bitumen sample. These numbers belong to the viscosity measurement period which happens after heating.

Table 3A.2. Heating steps for bitumen viscosity measurements

Temperature (°C)	Step No.	Time (s)	Spindle speed (1/min)
40	1	1800	0.000
	2	900	3.000
	3	900	9.006
60	1	1800	0.000
	2	900	9.006
	3	900	27.02
80	1	1800	0.000
	2	900	9.006
	3	900	90.06

Table 3A.3. Viscometer output for ATB-2

Temperature (°C)					
40		60		80	
Spindle speed (1/min)	Torque (μN/m)	Spindle speed (1/min)	Torque (μN/m)	Spindle speed (1/min)	Torque (μN/m)
1.03	10047	1.00	998	1.00	189
2.29	22434	13.71	13825	37.44	7038
3.55	34941	26.43	26842	73.87	13902
4.84	47658	39.14	39776	110.30	20748
6.12	60228	51.86	52395	146.70	27471
7.41	72784	64.58	64671	183.20	34076
8.70	85102	77.30	76338	219.60	40430
9.99	97201	90.01	87474	256.10	46415
10.0	97041	90.00	86581	256.10	45848
8.74	84919	77.28	74471	219.60	39265
7.44	72487	64.56	62816	183.20	32902
6.16	60175	51.85	51005	146.70	26590
4.87	47696	39.14	38917	110.30	20221
3.59	35166	26.43	26515	73.87	13627
2.30	22600	13.71	13851	37.44	6960
1.02	9977	1.00	1020	1.00	189

Table 3A.4. Viscometer output for ATB-1

Temperature (°C)					
40		60		80	
Spindle speed (1/min)	Torque (μN/m)	Spindle speed (1/min)	Torque (μN/m)	Spindle speed (1/min)	Torque (μN/m)
1.01	7227	1.00	616	1.00	113
2.28	16377	13.71	8497	37.44	4220
3.57	25704	26.43	16438	73.87	8313
4.86	35037	39.14	24369	110.30	12365
6.14	44249	51.86	32162	146.70	16342
7.42	53466	64.57	39796	183.20	20702
8.71	62622	77.28	47187	219.60	26426
9.99	71724	90.00	54286	256.10	32082
10.0	71702	90.00	53903	256.10	31612
8.72	62542	77.29	46400	219.60	26994
7.44	53362	64.57	39019	183.20	22627
6.15	44184	51.85	31543	146.70	18264
4.86	34977	39.14	24081	110.30	13841
3.58	25760	26.43	16343	73.87	9352
2.29	16502	13.71	8528	37.44	4772
1.01	7234	1.00	627	1.00	129

Appendix 4: Measuring maximum sand volume concentration

A pre-weighted amount of sand was poured into a graduated cylinder and its total volume was determined ($\forall_{tot}$). The actual volume of sand (i.e. assuming no pore exists) was then calculated using its density (2650kg/m^3). Then C_{max} was calculated using:

$$C_{max} = \frac{\forall_{tot} - \forall_{Act}}{\forall_{tot}} \qquad (4A.1)$$

Appendix 5: Prototype experimental data

Ablation of 25.4mm hand-formed spherical lumps

Time (min)	Fraction Digested (MA-Run2)	Fraction Digested (MA-Run8)	Fraction Digested (MA-Run10)	Fraction Digested (MA-Run17)	Fraction Digested (MA-Run18)
2	0.058	0.053	0.055	0.059	0.0215
4	0.19	0.169	o.247	0.317	0.215
6	0.259	0.275	0.455	0.462	0.333
8	0.349	0.376	0.559	0.553	0.446
10	0.439	0.450	0.464	0.634	0.516
12	0.550	0.508	0.720	0.693	0.586
14	0.624	0.566	0.821	0.779	0.666
16	0.677	0.619	--	0.860	0.736
18	0.730	0.651	--	--	0.801
20	0.825	0.693	--	--	0.838
22	0.862	0.730	--	--	--
24	--	0.757	--	--	--
26	--	0.783	--	--	--
28	--	0.810	--	--	--
30	--	0.831	--	--	--
32	--	0.862	--	--	--

Ablation of 19mm hand-formed spherical lumps

Time (min)	Fraction Digested (MA-Run1)	Fraction Digested (MA-Run6)	Fraction Digested (MA-Run7)	Fraction Digested (MA-Run14)	Fraction Digested (MA-Run16)
2	0.099	0.021	0.063	0.00	0.115
4	0.277	0.144	0.252	0.216	0.208
6	0.416	0.268	0.431	0.371	0.417
8	0.495	0.361	0.600	0.474	0.583
10	0.564	0.536	0.789	0.618	0.719
12	0.653	0.649	--	0.711	--
14	0.725	0.691	--	--	--
16	0.792	--	--	--	--

Ablation of 25.4mm octadecane- sand lumps

Time (min)	Fraction Digested (Run1)	Fraction Digested (Run2)	Fraction Digested (Run3)	Fraction Digested (Run4)
1	0.266	0.273	0.259	0.280
2	0.597	0.553	0.582	0.611
3	0.842	0.762	0.806	0.841

Ablation of artificial oil sand lump

Time (min)	Fraction Digested (Run1)	Fraction Digested (Run2)	Fraction Digested (Run2)
60	0.025	0.002	0.002
75	0.077	0.059	--
90	0.168	0.124	0.159
105	0.231	0.198	0.247
120	0.309	0.277	0.354
135	0.378	0.340	0.443
150	0.457	0.439	0.511

Effect of water flow rate on ablation of cylindrical artificial oil sands lump

Time (min)	Fraction Digested Q=1.1 L/s	Fraction Digested Q=0.7 L/s
60	0.026	--
75	0.077	--
90	0.168	0.0379
105	0.231	0.0939
120	0.309	0.164
135	0.378	0.230
150	0.457	0.299

Appendix 6: SRC test loop experimental and calculated data

Data for mass measurements by weigh scale in comparison with strain gauges

Sample No.	Mass (kg)	Mass (kg)	% Error
	(Lab bench scale)	(Strain gauge)	
98	0.20435	0.20282	0.749
91	0.20482	0.19923	2.729
71	0.20215	0.19500	3.537
80	0.20252	0.20270	-0.089
92	0.20332	0.194527	4.325
93	0.20451	0.203256	0.613
94	0.20451	0.19708	3.633
95	0.20227	0.20031	0.969
96	0.20392	0.19753	3.134
97	0.20465	0.19884	2.839
99	0.20195	0.19725	2.327
101	0.20277	0.19774	2.481
104	0.20475	0.20096	1.851
88	0.20203	0.19654	2.717
80	0.20252	0.20267	-0.074
81	0.20210	0.19771	2.172
60	0.20361	0.20166	0.958
63	0.20276	0.20671	-1.948
66	0.20320	0.19788	2.618
68	0.20453	0.19525	4.537
67	0.20387	0.20281	0.520

Data for measurement of drag force on smooth aluminum spheres in water

Drag force (calculated vs. measured):50.8mm sphere: water

Bulk velocity (m/s)	Actual velocity (m/s)	Drag force (N)	Drag force (N)
		Calculated	Measured
1.05	1.66	1.24	1.16
1.52	2.40	2.59	2.00
2.02	3.19	4.56	3.49
2.53	3.99	7.15	5.46
3.03	4.78	10.26	7.80

Drag force (calculated vs. measured):50.8mm sphere: water

Bulk velocity (m/s)	Actual velocity (m/s)	Drag force (N)	Drag force (N)
		Calculated	Measured
1.04	1.54	0.82	0.877
1.53	2.26	1.77	1.903
2.02	2.98	3.09	3.294
2.51	3.70	4.75	4.865
3.02	4.45	6.88	7.213

Drag force (calculated vs. measured):27mm sphere: water

Bulk velocity (m/s)	Actual velocity (m/s)	Drag Force (N)	Drag force (N)
		Calculated	Measured
1.06	1.48	0.28	0.30
1.53	2.13	0.57	0.62
2.03	2.83	1.01	1.03
2.51	3.50	1.55	1.44
3.02	4.21	2.24	1.98

Data for measurement of drag force on smooth aluminum spheres in slurry (C = 0.15)

Drag force (calculated vs. measured):50.8mm sphere: slurry (C=0.15)

Bulk velocity (m/s)	Actual velocity (m/s)	Drag force (N)	Drag force (N)
		Calculated	Measured
1.074	1.70	1.61	1.67
1.565	2.47	3.42	3.32
2.063	3.26	5.95	5.53
2.449	3.87	8.39	8.66
3.107	4.91	13.50	12.90

Drag force (calculated vs. measured):44.9mm sphere: slurry (C=0.15)

Bulk velocity (m/s)	Actual velocity (m/s)	Drag force (N)	Drag force (N)
		Calculated	Measured
1.09	1.60	1.12	1.37
1.51	2.22	2.15	2.38
2.05	3.02	3.96	3.87
2.55	3.76	6.14	5.87
3.00	4.42	8.48	7.82

Drag force (calculated vs. measured):35mm sphere: slurry (C=0.15)

Bulk velocity (m/s)	Actual velocity (m/s)	Drag force (N)	Drag force (N)
		Calculated	Measured
1.04	1.52	0.60	0.60
1.52	2.22	1.28	1.28
2.00	2.93	2.23	2.08
2.50	3.66	3.47	3.28
2.97	4.35	4.91	4.45

Drag force (calculated vs. measured):27mm sphere: slurry (C=0.15)

Bulk velocity (m/s)	Actual velocity (m/s)	Drag force (N)	Drag force (N)
		Calculated	Measured
1.07	1.49	0.35	0.35
1.55	2.16	0.74	0.73
2.05	2.86	1.30	1.14
2.46	3.43	1.86	1.77
2.99	4.17	2.75	2.54

Data for measurement of drag force on smooth aluminum spheres in slurry (C = 0.30)

Drag force (calculated vs. measured):50.8mm sphere: slurry (C=0.30)

Bulk velocity (m/s)	Actual velocity (m/s)	Drag Force (N)	Drag force (N)
		Calculated	Measured
1.03	1.62	1.48	1.77
1.57	2.48	3.45	3.50
2.02	3.19	5.69	6.31
2.52	3.98	8.90	8.96
3.07	4.84	13.16	12.63

Drag force (calculated vs. measured):44.9mm sphere: slurry (C=0.30)

Bulk velocity (m/s)	Actual velocity (m/s)	Drag Force (N)	Drag force (N)
		Calculated	Measured
1.14	1.67	1.22	1.74
1.54	2.27	2.24	2.96
2.01	2.96	3.80	5.00
2.52	3.71	5.97	6.91
3.01	4.43	8.52	9.20

Drag force (calculated vs. measured):34mm sphere: slurry (C=0.30)

Bulk velocity (m/s)	Actual velocity (m/s)	Drag force (N)	Drag force (N)
		Calculated	Measured
1.15	1.68	0.73	1.06
1.49	2.18	1.23	1.87
2.13	3.11	2.51	3.07
2.48	3.62	3.40	4.06
2.98	4.35	4.91	5.91

Drag force (calculated vs. measured):27mm sphere: slurry (C=0.30)

Bulk velocity (m/s)	Actual velocity (m/s)	Drag force (N)	Drag force (N)
		Calculated	Measured
1.13	1.58	0.47	0.49
1.48	2.07	0.80	1.08
2.08	2.90	1.58	2.00
2.47	3.44	2.23	2.46
3.14	4.38	3.63	4.01

Data for measurement of drag force on basket in water

Basket effect in drag force measurement: 50.8mm cylinder: water

Bulk velocity (m/s)	Drag force (N)	Drag force (N)	Drag force (N)
	50.8mm cylinder in basket	50.8mm cylinder	basket effect
1.05	6.74	1.86	4.88
1.51	13.78	3.10	10.68
2.03	24.46	5.29	19.17
2.53	35.24	8.06	27.18
3.03	51.85	11.48	40.37

Basket effect in drag force measurement: 50.8mm sphere: water

Bulk velocity (m/s)	Drag force (N)	Drag force (N)	Drag force (N)
	50.8mm sphere in basket	50.8mm sphere only	basket effect
1.03	5.92	1.51	4.41
1.53	12.70	2.71	9.99
2.03	21.54	4.45	17.08
2.52	30.75	6.80	23.94
3.02	44.02	9.44	34.57

Basket effect in drag force measurement: 44.9mm sphere: water

Bulk velocity (m/s)	Drag force (N)	Drag force (N)	Drag force (N)
	44.9mm sphere in basket	44.9mm sphere only	basket effect
1.04	5.47	0.88	4.59
1.51	10.60	1.90	8.69
2.02	18.32	3.29	15.03
2.53	28.42	4.86	23.55
3.01	39.85	7.21	32.64

Basket effect in drag force measurement: 27mm sphere: water

Bulk velocity (m/s)	Drag force (N)	Drag force (N)	Drag force (N)
	27mm sphere in basket	27mm sphere only	basket effect
1.02	4.33	0.301	4.03
1.51	8.65	0.618	8.03
2.00	14.84	1.028	13.81
2.51	23.11	1.438	21.67
3.01	32.60	1.984	30.62

Measured drag force on empty basket: water

Bulk velocity (m/s)	Drag force measured on empty basket (N)
1.04	4.66
1.50	10.15
2.05	18.48
2.53	27.15
3.03	36.15

Data for measurement of drag force on basket in slurry (C = 0.15)

Basket effect in drag force measurement: 50.8mm cylinder: slurry (C=0.15)

Bulk velocity (m/s)	Drag force (N)	Drag force (N)	Drag force (N)
	50.8mm cylinder in basket	50.8mm cylinder	basket effect
1.10	9.71	2.87	6.84
1.58	18.14	5.37	12.77
2.06	30.55	9.31	21.25
2.51	43.79	13.54	30.25
3.07	66.24	19.57	46.67

Basket effect in drag force measurement: 44.9mm sphere: slurry (C=0.15)

Bulk velocity (m/s)	Drag force (N)	Drag force (N)	Drag force (N)
	44.9mm sphere in basket	44.9mm sphere only	basket effect
0.99	7.52	1.37	6.15
1.55	16.29	2.38	13.90
2.01	23.95	3.87	20.07
2.56	38.65	5.67	32.98
2.93	45.61	7.80	37.81

Basket effect in drag force measurement: 35mm sphere: slurry (C=0.15)

Bulk velocity (m/s)	Drag force (N)	Drag force (N)	Drag force (N)
	34mm sphere in basket	34mm sphere only	basket effect
1.02	5.90	0.597	5.30
1.54	14.05	1.284	12.77
2.01	24.08	2.081	22.00
2.52	37.80	3.281	34.52
3.00	54.17	4.449	49.72

Data for measurement of drag force on basket in slurry (C = 0.30)

Basket effect in drag force measurement: 50.8mm cylinder: slurry (C=0.30)

Bulk velocity (m/s)	Drag force (N)	Drag force (N)	Drag force (N)
	50.8mm cylinder in basket	50.8mm cylinder	basket effect
1.05	9.53	5.11	4.88
1.54	18.44	8.25	10.64
2.02	31.74	12.01	20.19
2.47	48.53	17.36	31.63

Basket effect in drag force measurement: 50.8mm sphere: slurry (C=0.30)

Bulk velocity (m/s)	Drag force (N)	Drag force (N)	Drag force (N)
	50.8mm sphere in basket	50.8mm sphere only	basket effect
1.10	10.52	2.41	8.58
1.55	19.89	4.58	15.79
2.05	35.77	7.77	28.48
2.48	53.76	11.12	43.11

Basket effect in drag force measurement: 44.8mm sphere: slurry (C=0.30)

Bulk velocity (m/s)	Drag force (N)	Drag force (N)	Drag force (N)
	44.8mm sphere in basket	44.9mm sphere only	basket effect
1.08	9.46	1.74	7.72
1.55	17.72	2.96	14.76
2.01	32.40	5.00	27.39
2.50	44.19	6.91	37.29

Basket effect in drag force measurement: 35mm sphere: slurry (C=0.30)

Bulk velocity (m/s)	Drag force (N)	Drag force (N)	Drag force (N)
	34mm sphere in basket	34mm sphere only	basket effect
1.04	7.63	1.068	6.56
1.49	16.08	1.874	14.21
2.01	25.13	3.079	22.05
2.50	39.75	4.061	35.69

Basket effect in drag force measurement: 27mm sphere: slurry (C=0.30)

Bulk velocity (m/s)	Drag force (N)	Drag force (N)	Drag force (N)
	27mm sphere in basket	27mm sphere only	basket effect
1.05	7.28	0.490	6.79
1.54	15.78	1.086	14.69
2.02	25.46	2.003	23.46
2.47	40.35	2.460	37.89

Measured drag force on empty basket: slurry (C=0.30)

Bulk velocity (m/s)	Drag force measured on empty basket (N)
1.09	7.95
1.53	15.04
2.05	26.04
2.49	40.2

Difference between drag force on basket, measured using solid object-basket assembly and empty basket: water

Basket effect on drag force measurement using solid object-basket assembly (N)				Drag force on empty basket (N)	%Difference between two measurements	%Difference between two measurements	%Difference between two measurements	%Difference between two measurements
cylinder (d=50.8mm)	sphere (d=50.8mm)	sphere (44.9mm)	sphere (d=27mm)	Empty basket	cylinder (d=50.8mm)	sphere (d=50.8mm)	sphere (44.9mms)	sphere (d=27mm)
4.88	4.41	4.59	4.03	4.66	1.15	-1.38	-0.38	-3.62
10.68	9.99	8.69	8.03	10.15	1.27	-0.40	-3.87	-5.83
19.17	17.08	15.03	13.81	18.48	0.92	-1.97	-5.15	-7.23
27.18	23.94	23.55	21.67	27.15	0.03	-3.14	-3.55	-5.61
40.37	34.57	32.64	30.62	36.15	2.76	-1.12	-2.55	-4.14

Difference between drag force on basket, measured using solid object-basket assembly and empty basket: slurry (C = 0.15)

Basket effect on drag force measurement using solid object-basket assembly (N)				Drag force on empty basket (N)	%Difference between two measurements	%Difference between two measurements	%Difference between two measurements	%Difference between two measurements
cylinder (d=50.8mm)	sphere (d=50.8mm)	sphere (44.9mms)	sphere (d=27mm)	Empty basket	cylinder (d=50.8mm)	sphere (d=50.8mm)	sphere (44.9mms)	sphere (d=27mm)
6.84	7.46	6.15	5.3	8.65	-5.84	-3.69	-8.45	-12.01
12.77	12.07	13.9	12.77	15.36	-4.60	-6.00	-2.49	-4.60
21.25	23.61	20.07	22	26.2	-5.22	-2.60	-6.62	-4.36
30.25	36.84	32.98	34.52	33.59	-2.61	2.31	-0.46	0.68
46.67	48.13	37.81	49.72	44.4	1.25	2.02	-4.01	2.83

Difference between drag force on basket, measured using solid object-basket assembly and empty basket: slurry (C=0.30)

Basket effect on drag force measurement using solid object-basket assembly (N)					**Drag force on empty basket (N)**	**%Diff. between two measurements**	**%Diff. between two measurements**	**%Diff. between two measurements**	**%Diff. between two measurements**	**%Diff. between two measurements**
cylinder (d=50.8mm)	sphere (d=50.8mm)	sphere (d=44.9mm)	sphere (d=35mm)	sphere (d=27mm)	Empty basket	cylinder (d=50.8mm)	sphere (d=50.8mm)	sphere (d=44.9mm)	sphere (d=35mm)	sphere (d=27mm)
4.88	8.58	7.72	6.56	6.79	7.95	-11.96	1.91	-0.73	-4.79	-3.93
10.64	15.79	14.76	14.21	14.69	15.04	-8.57	1.22	-0.47	-1.42	-0.59
20.19	28.48	27.39	22.05	23.46	26.04	-6.33	2.24	1.26	-4.15	-2.61
31.63	43.11	37.29	35.69	37.89	40.2	-5.97	1.75	-1.88	-2.97	-1.48

Data for fluctuation of drag force measurement on aluminum cylinder-basket and bulk velocity measurements in water and slurries

V=1m/s: water

Time (min)	Slurry bulk velocity (m/s)	Strain gauge reading (v)	Drag force (N)
1	1.04	0.1150	7.80
2	1.04	0.1144	7.79
3	1.04	0.1174	7.88
4	1.04	0.1157	7.83
5	1.04	0.1132	7.75
6	1.04	0.1098	7.64
7	1.04	0.1087	7.61
8	1.04	0.1120	7.71
9	1.04	0.1135	7.76
10	1.04	0.1152	7.81

Drag force measurement fluctuation:V=1.5m/s: water

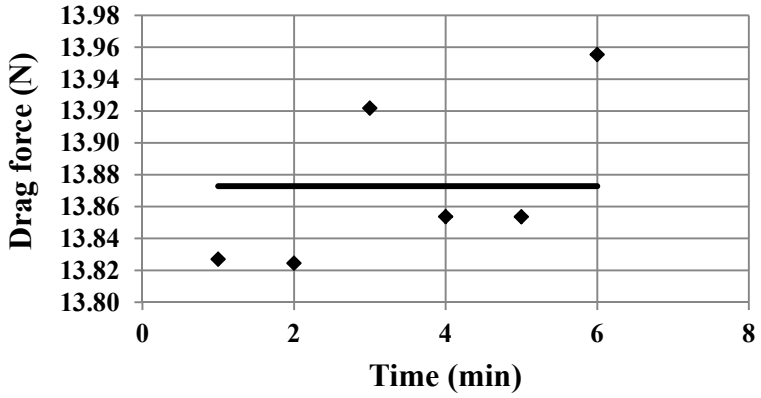

Bulk velocity fluctuation:V=1.5m/s:water

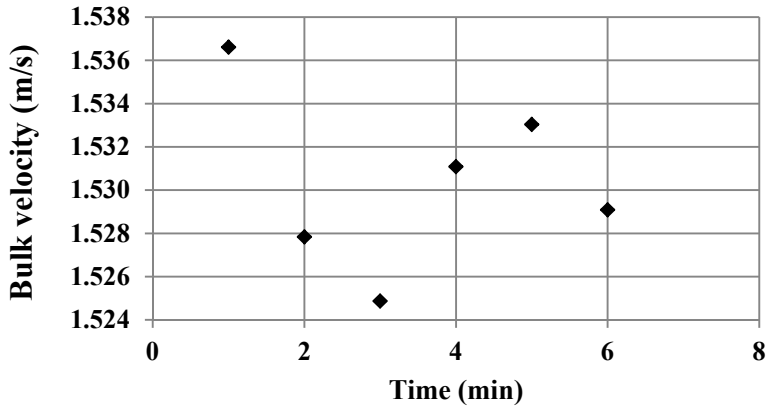

Time (min)	Slurry bulk velocity (m/s)	Strain gauge reading (v)	Drag force (N)
1	1.54	0.3399	0.1334
2	1.53	0.3398	0.1334
3	1.52	0.3429	0.1334
4	1.53	0.3407	0.1334
5	1.53	0.3407	0.1334
6	1.53	0.3440	0.1334

Drag force measurement fluctuation:V=2m/s:water

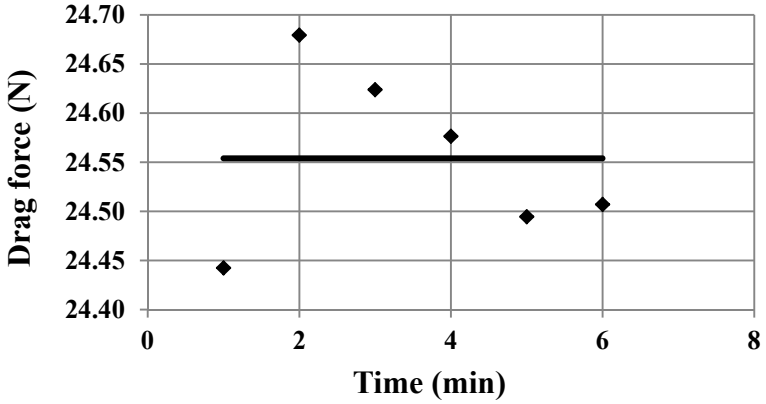

Bulk velocity fluctuation:V=2m/s:water

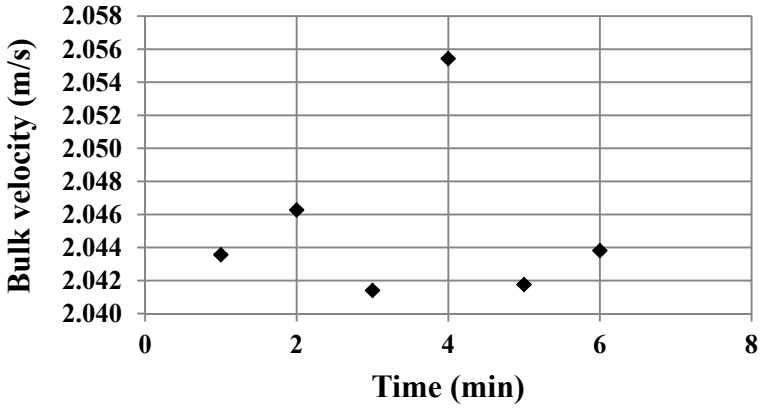

Time (min)	Slurry bulk velocity (m/s)	Strain gauge reading (v)	Drag force (N)
1	2.0436	0.6789	24.44
2	2.0463	0.6864	24.68
3	2.0414	0.6847	24.62
4	2.0554	0.6832	24.58
5	2.0418	0.6805	24.49
6	2.0438	0.6809	24.51

Drag force measurement fluctuation:V=2.5m/s:water

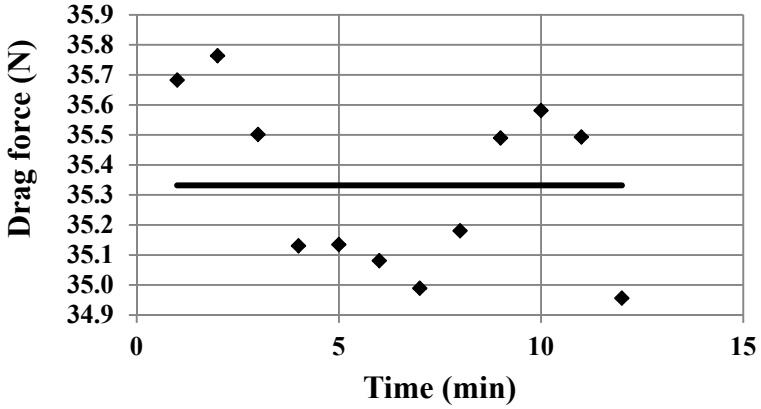

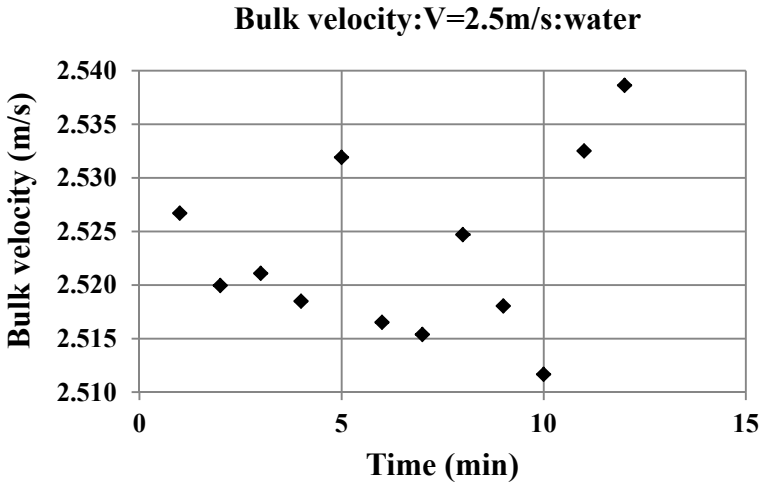

Time (min)	Slurry bulk velocity (m/s)	Strain gauge reading (v)	Drag force (N)
1	2.527	1.038	35.68
2	2.520	1.040	35.76
3	2.521	1.032	35.50
4	2.519	1.020	35.13
5	2.532	1.020	35.13
6	2.517	1.019	35.08
7	2.515	1.016	34.99
8	2.525	1.022	35.18
9	2.518	1.032	35.49
10	2.512	1.035	35.58
11	2.533	1.032	35.49
12	2.539	1.015	34.96

Drag force measurement fluctuation:V=3m/s:water

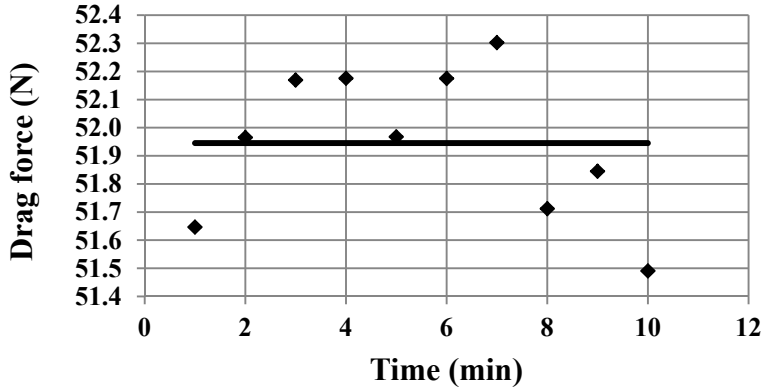

Bulk velocity fluctuation:V=3m/s:water

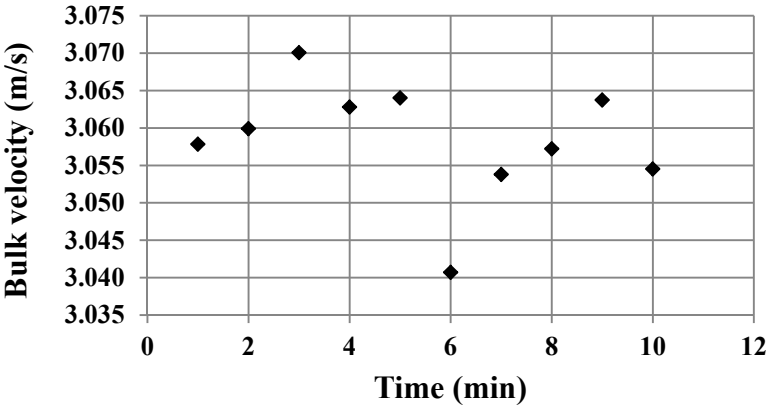

Time (min)	Slurry bulk velocity (m/s)	Strain gauge reading (v)	Drag force (N)
1	3.058	1.548	51.65
2	3.060	1.558	51.96
3	3.070	1.564	52.17
4	3.063	1.565	52.18
5	3.064	1.558	51.97
6	3.041	1.565	52.18
7	3.054	1.569	52.30
8	3.057	1.550	51.71
9	3.064	1.554	51.84
10	3.055	1.543	51.49

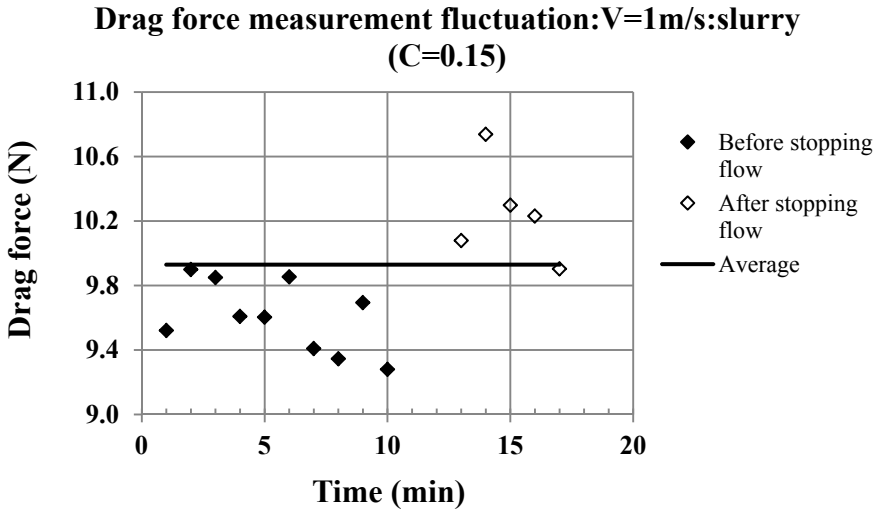

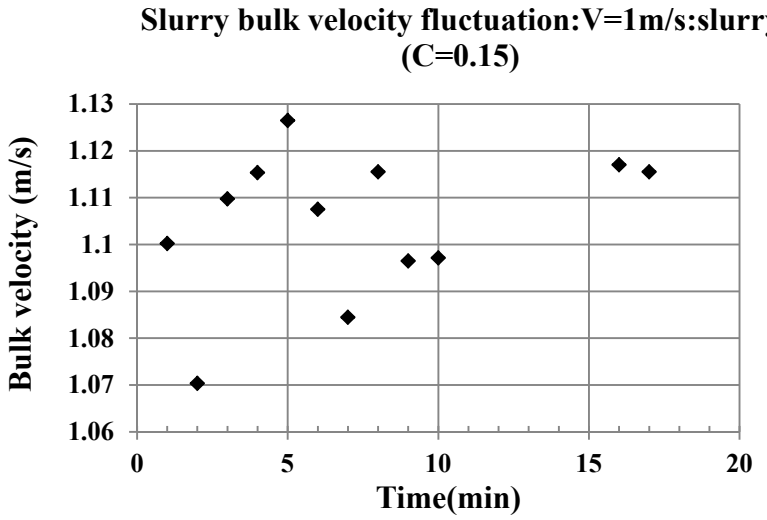

Time (min)	Slurry bulk velocity (m/s)	Strain gauge reading (v)	Drag force (N)
1	1.10	0.9706	9.52
2	1.07	1.0091	9.90
3	1.11	1.0041	9.85
4	1.12	0.9795	9.61
5	1.13	0.9790	9.60
6	1.11	1.0045	9.85
7	1.08	0.9591	9.41
8	1.12	0.9527	9.35
9	1.10	0.9882	9.69

10	1.10	0.9460	9.28
13	1.08	1.0274	10.08
14	1.18	1.0946	10.74
15	1.16	1.0498	10.30
16	1.12	1.0429	10.23
17	1.12	1.0096	9.90

V=1.5m/s: slurry (C=0.15)

Time (min)	Slurry bulk velocity (m/s)	Strain gauge reading (v)	Drag force (N)
1	1.60	0.5010	18.28
2	1.59	0.4842	17.76
3	1.59	0.4877	17.86
4	1.51	0.4968	18.15
5	1.58	0.4922	18.01
6	1.61	0.5003	18.26
7	1.59	0.4878	17.87
8	1.55	0.4918	17.99
9	1.61	0.4984	18.20
10	1.57	0.4904	17.95
11	1.62	0.5141	18.69
12	1.59	0.5148	18.71
13	1.58	0.5201	18.88
14	1.59	0.5184	18.83
15	1.60	0.5225	18.96

V=2m/s: slurry (C=0.15)

Time (min)	Slurry bulk velocity (m/s)	Strain gauge reading (v)	Drag force (N)
1	2.02	0.8874	30.38
2	2.06	0.8950	30.62
3	2.04	0.9022	30.84
4	2.08	0.8841	30.28
5	2.08	0.9046	30.92
6	2.10	0.8812	30.18
7	2.02	0.8912	30.50
8	2.10	0.8970	30.68
9	2.05	0.8788	30.11

10	2.08	0.8750	29.99
11	2.00	0.9134	31.19
12	1.96	0.9066	30.98
13	1.98	0.8943	30.59
14	1.98	0.8968	30.67
15	2.01	0.9083	31.03
16	1.96	0.9059	30.96

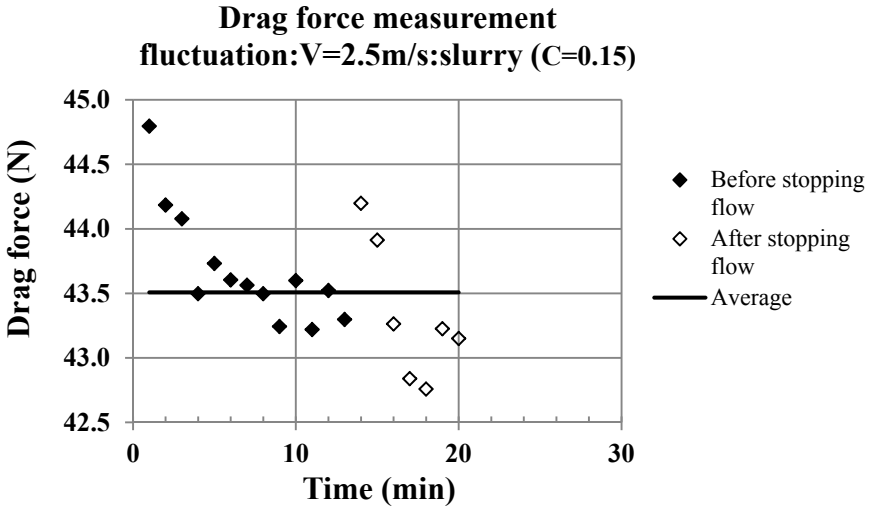

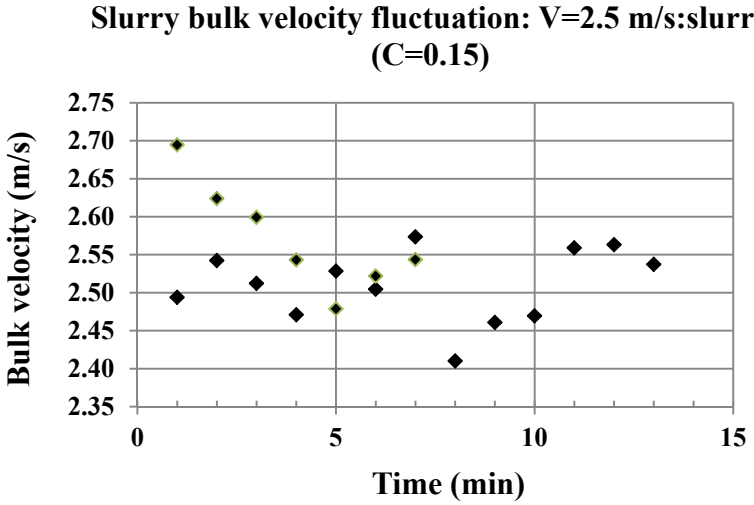

Time (min)	Slurry bulk velocity (m/s)	Strain gauge reading (v)	Drag force (N)
1	2.49	1.3480	44.80
2	2.54	1.3285	44.18
3	2.51	1.3251	44.08
4	2.47	1.3065	43.50
5	2.53	1.3140	43.73
6	2.50	1.3099	43.60
7	2.57	1.3086	43.56
8	2.41	1.3065	43.50
9	2.46	1.2984	43.24
10	2.47	1.3098	43.60
11	2.56	1.2976	43.22
12	2.56	1.3073	43.52
13	2.54	1.3001	43.30
14	2.69	1.3289	44.20
15	2.62	1.3198	43.91
16	2.60	1.2990	43.26
17	2.54	1.2855	42.84
18	2.48	1.2829	42.76
19	2.52	1.2978	43.23
20	2.54	1.2954	43.15

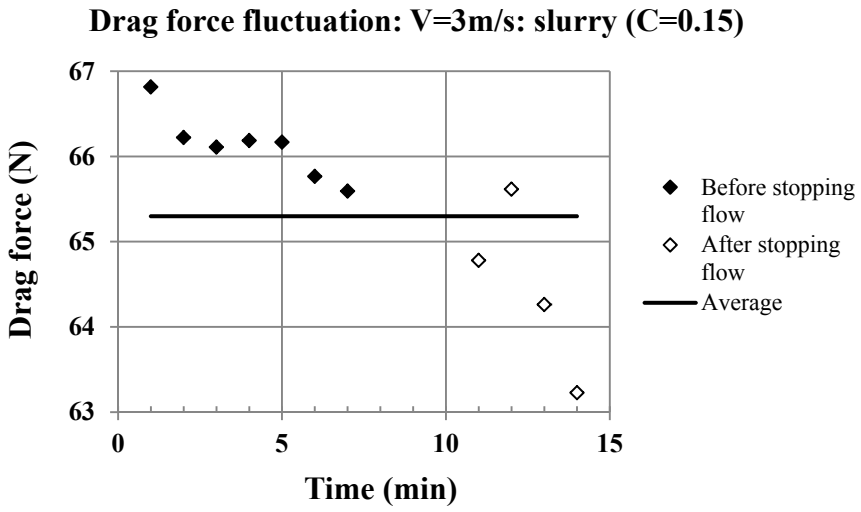

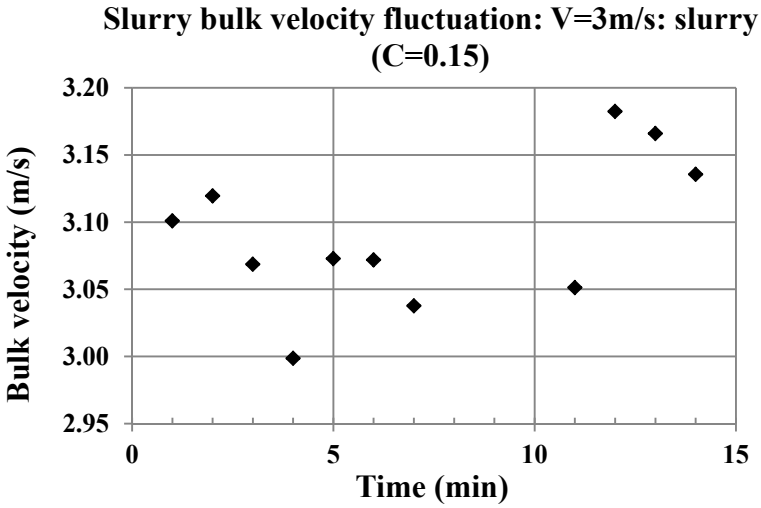

Time (min)	Slurry bulk velocity (m/s)	Strain gauge reading (v)	Drag force (N)
1	3.10	2.0514	66.82
2	3.12	2.0324	66.22
3	3.07	2.0288	66.11
4	3.00	2.0313	66.19
5	3.07	2.0307	66.17
6	3.07	2.0178	65.77
7	3.04	2.0124	65.59
8	3.50	2.0514	59.21
11	3.05	1.8085	64.78
12	3.18	1.9864	65.62
13	3.17	2.0131	64.26
14	3.14	1.9699	63.23

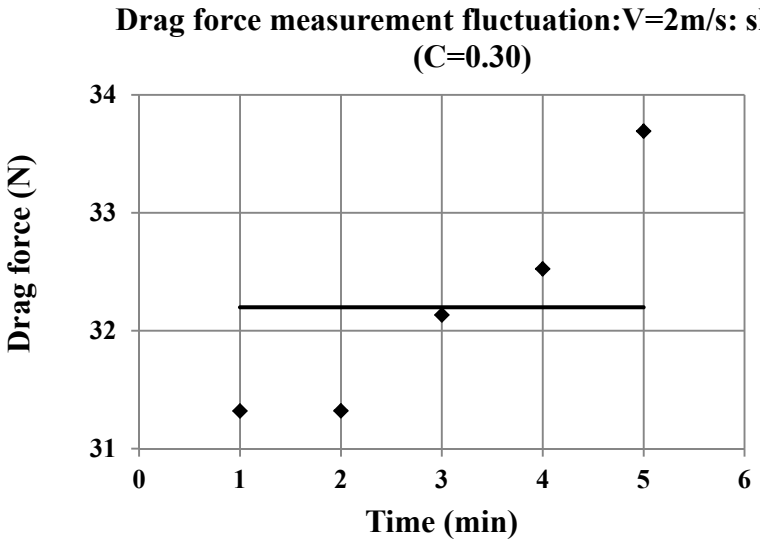

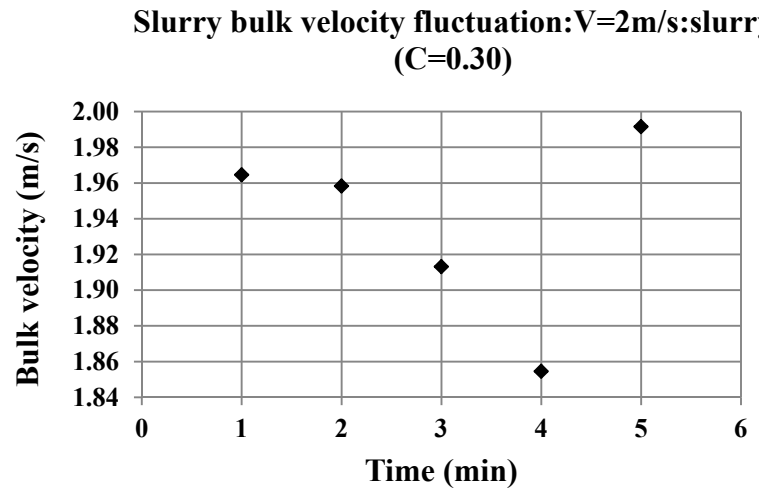

Time (min)	Slurry bulk velocity (m/s)	Strain gauge reading (v)	Drag force (N)
1	1.96	0.9108	31.32
2	1.96	0.9109	31.32
3	1.91	0.9368	32.13
4	1.85	0.9493	32.52
5	1.99	0.9866	33.69

Data for Strain gauge calibration

Positive voltage (large weights)	
Reading (volts)	**Force (kg)**
0.0000	0.000
0.0410	0.147
0.0884	0.295
0.1358	0.442
0.1978	0.644
0.2441	0.791
0.2901	0.939
0.3364	1.086
0.4293	1.381
0.5527	1.772
0.6441	2.067
0.7391	2.362
0.8266	2.657
0.9202	2.952
1.0141	3.247
1.1110	3.553
1.2539	4.006
1.3946	4.456
1.5340	4.909
1.8313	5.845
1.9203	6.140
1.1492	3.710
0.8641	2.804
0.5387	1.772
0.0000	0.000

Positive voltage (small weights)	
Reading (volts)	**Force (kg)**
-0.0016	0.000
0.0110	0.040
0.0240	0.080
0.0370	0.120
0.0495	0.160
0.0621	0.200
0.0369	0.120
0.0110	0.040

-0.0015	0.000

Negative voltage (large weights)	
Reading (volts)	**Force (kg)**
-0.0013	0.000
-0.0491	0.147
-0.0962	0.295
-0.1456	0.442
-0.2094	0.644
-0.2572	0.791
-0.3048	0.939
-0.3526	1.086
-0.4490	1.381
-0.5694	1.772
-0.6644	2.067
-0.7558	2.362
-0.8509	2.657
-0.9458	2.952
-1.0398	3.247
-1.1355	3.553
-1.2782	4.006
-1.4184	4.456
-1.5641	4.909
-1.8551	5.845
-1.9493	6.140
-1.4126	4.456
-1.0324	3.258
-0.8421	2.657
-0.5594	1.772
0.0022	0.000

Negative voltage (small weights)	
Reading (volts)	**Force (kg)**
-0.0017	0.000
-0.0140	0.040
-0.0203	0.060
-0.0268	0.080
-0.0326	0.100
-0.0459	0.140
-0.0514	0.160

-0.0649	0.200
-0.0458	0.140
-0.0265	0.080
-0.0007	0.000

Data for lump ablation tests in Basket#2: (AT, ATB-2) lumps

water: V=1.5m/s: T=30°C

Time (min)	Strain gauge reading (v)	Strain gauge reading (v)	Lump mass (kg)	Fraction digested
	Plus basket	Minus basket		
0	-0.1190	-0.0640	0.1977	0.000
10	-0.1163	-0.0613	0.1892	0.043
20	-0.1145	-0.0595	0.1836	0.071
41	-0.1111	-0.0561	0.1731	0.125
61	-0.1080	-0.0530	0.1631	0.175
81	-0.1008	-0.0458	0.1405	0.290
101	-0.0984	-0.0433	0.1328	0.328
121	-0.0665	-0.0115	0.0325	0.836

water: V=2m/s: T=30°C

Time (min)	Strain gauge reading (v)	Strain gauge reading (v)	Lump mass (kg)	Fraction digested
	Plus basket	Minus basket		
0	-0.1194	-0.0638	0.1973	0.000
5	-0.1081	-0.0525	0.1616	0.181
10	-0.1053	-0.0497	0.1528	0.225
20	-0.0907	-0.0351	0.1068	0.459
30	-0.0762	-0.0206	0.0611	0.690
35	-0.0694	-0.0138	0.0397	0.799
40	-0.0646	-0.009	0.0246	0.875

C=30% slurry: V=1.5m/s: T=30°C

Time (min)	Strain gauge reading (v)	Strain gauge reading (v)	Lump mass (kg)	Fraction digested
	Plus basket	Minus basket		
0	-0.1171	-0.0639	0.1977	0.000
11	-0.1135	-0.0604	0.1864	0.057
20	-0.1118	-0.0587	0.1811	0.084
30	-0.1116	-0.0584	0.1802	0.088
40	-0.1103	-0.0572	0.1763	0.108
50	-0.1089	-0.0557	0.1717	0.131
60	-0.1085	-0.0553	0.1706	0.137
70	-0.0996	-0.0465	0.1427	0.278
80	-0.0933	-0.0401	0.1226	0.380
90	-0.0748	-0.0217	0.0645	0.674
95	-0.0738	-0.0206	0.0611	0.691
100	-0.0698	-0.0167	0.0487	0.753

Data for repeatability tests

Repeatability test: water: V=2m/s: T=30°C

Time (min)	Fraction digested		
	sample#1	sample#2	sample#3
0	0.000	0.000	0.000
5	0.059	---	---
10	0.159	0.066	0.043
20	0.211	0.105	0.150
30	0.250	0.160	0.198
40	0.332	0.223	0.262
50	0.404	0.314	0.325
60	0.487	0.375	0.384
70	0.556	0.450	0.442

Repeatability test: water: V=2m/s: T=45°C

Time (min)	Fraction digested		
	sample#1	sample#2	sample#3
0	0.000	0.000	0.000
5	0.201	0.240	0.232
10	0.384	0.554	0.424
13	0.612	0.881	0.737
18	0.988	---	0.983

Repeatability test: slurry (C=0.15): V=2m/s: T=45°C

Time (min)	Fraction digested		
	sample#1	sample#2	sample#3
0	0.000	0.000	0.000
5	0.553	0.133	0.247
8	0.976	0.555	0.957
11	0.997	0.962	0.967
14	---	0.984	---

Repeatability test: slurry (C=0.15): V=2.5m/s: T=30°C

Time (min)	Fraction digested		
	sample#1	sample#2	sample#3
0	0.000	0.000	0.000
5	0.000	---	---
8	---	0.233	0.019
10	0.153	---	---
14	---	0.633	0.607
19	---	0.779	0.752
20	0.557	---	---
24	---	0.954	0.976
25	0.918	---	---

Repeatability test: slurry (C=0.30): V=1.5m/s: T=30°C

Time (min)	Fraction digested		
	sample#1	sample#2	sample#3
0	0.000	0.000	0
10	0.084	0.066	0.101
20	0.116	0.100	0.131
30	0.147	0.126	0.184
40	0.151	0.148	0.204

50	0.182	0.175	0.254
60	0.230	0.228	0.305
70	0.354	0.334	0.452
80	0.467	0.438	0.643
90	0.851	0.824	0.894
95	0.903	0.897	0.952
100	0.990	0.962	---

Repeatability test: slurry (C=0.30): V=2m/s: T=30°C

Time (min)	Fraction digested		
	sample#1	sample#2	sample#3
0	0.000	0.000	0.000
5	0.053	0.084	0.121
10	0.100	0.117	0.430
20	0.208	0.248	0.675
30	0.326	0.363	0.833
40	0.840	0.750	0.936
44	0.929	---	---
50	---	0.900	---

Repeatability test: slurry (C=0.30): V=1m/s: T=45°C

Time (min)	Fraction digested		
	sample#1	sample#2	sample#3
0	0.000	0.000	0.000
5	0.036	0.092	0.050
15	0.053	0.197	0.122
26	0.331	---	---
27	---	0.265	0.268
35	0.514	---	---
36	---	0.367	0.421
41	0.678	---	---
42	---	0.415	0.553
45	0.857	---	---
46	---	0.469	---
48	0.926	---	0.748
49	---	0.503	---
55	---	0.690	0.874
60	---	0.872	---

Repeatability test: T=45°C:V=1m/s: slurry (C=0.30)

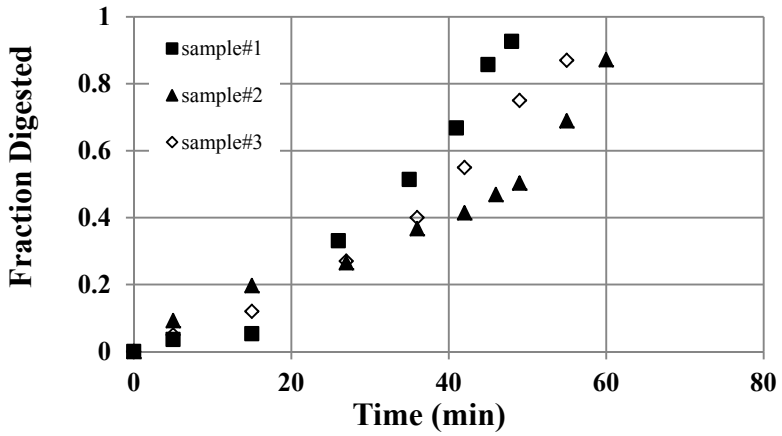

Repeatability test: slurry (C=0.30): V=1.5m/s: T=45°C

Time (min)	Fraction digested		
	sample#1	sample#2	sample#3
0	0.000	0.000	0.000
5	---	0.026	---
10	0.201	0.277	0.232
18	0.617	0.703	0.593
22	---	0.944	---
24	0.986	---	0.975
27	0.983	1.000	0.994

Repeatability test: slurry (C=0.30): V=2m/s: T=45°C

Time (min)	Fraction digested		
	sample#1	sample#2	sample#3
0	0.000	0.000	0.000
5	0.250	0.542	0.350
10	---	0.998	0.606
13	0.893	---	0.984
15	1.000	---	---

Data for different runs of oil sands lump ablation and ablation rate calculation

R-W1 (water-V=1m/s-T=30°C)

Time (min)	Strain gauge reading (v)	Strain gauge reading (v)	Lump mass (kg)	Fraction digested
	Plus basket	Minus basket		
0	-0.11927	-0.06557	0.20281	0.0000
10	-0.11517	-0.06147	0.18989	0.0637
20	-0.11426	-0.06056	0.18704	0.0777
40	-0.11446	-0.06076	0.18765	0.0747
60	-0.1136	-0.05990	0.18496	0.0880
70	-0.11328	-0.05958	0.18393	0.0930

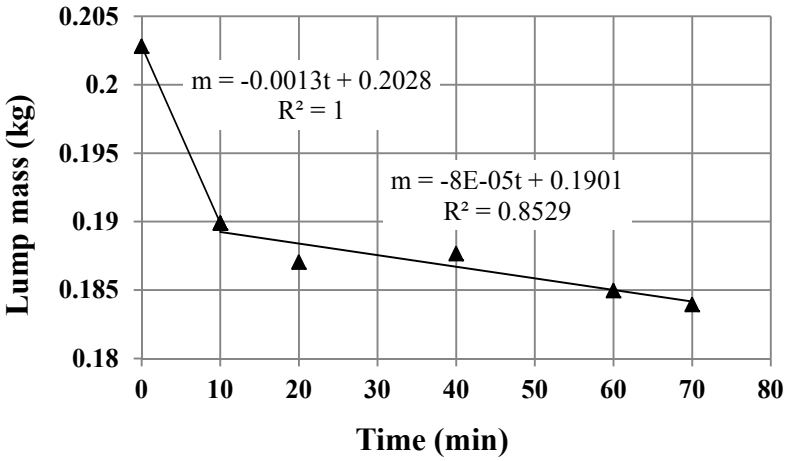

R-W2 (water-V=1.5m/s-T=30°C)

Time (min)	Strain gauge reading (v)	Strain gauge reading (v)	Lump mass (kg)	Fraction digested
	Plus basket	Minus basket		
0	-0.11820	-0.06431	0.198844	0.0000
10	-0.11080	-0.05691	0.17554	0.1172
20	-0.10909	-0.05521	0.17016	0.1442
30	-0.1077	-0.05389	0.16602	0.1650
40	-0.10796	-0.05408	0.16660	0.1621
50	-0.10686	-0.05298	0.16314	0.1795
60	-0.10421	-0.05033	0.15478	0.2215
70	-0.10362	-0.04974	0.15293	0.2309
80	-0.10335	-0.04946	0.15206	0.2352
90	-0.10160	-0.04772	0.14656	0.2629
101	-0.09645	-0.04256	0.13031	0.3446
111	-0.09240	-0.03852	0.11757	0.4087
120	-0.08942	-0.03553	0.10816	0.4560

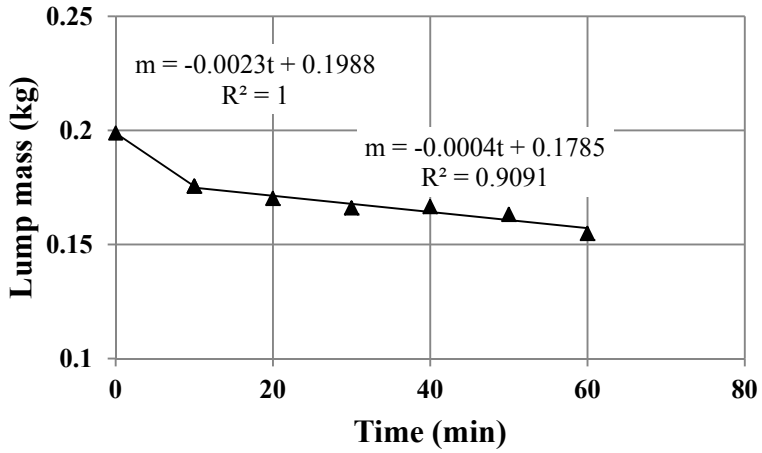

R-W3 (water-V=2m/s-T=30°C)

Time (min)	Strain gauge reading (v)	Strain gauge reading (v)	Lump mass (kg)	Fraction digested
	Plus basket	Minus basket		
0	-0.11667	-0.06375	0.19708	0.0000
5	-0.11296	-0.06003	0.185373	0.0594
10	-0.10676	-0.05383	0.16583	0.1585
20	-0.10346	-0.05053	0.15543	0.2113
30	-0.10103	-0.04811	0.14779	0.2501
40	-0.09592	-0.04299	0.13167	0.3319
50	-0.09143	-0.03851	0.11754	0.4036
60	-0.08621	-0.03328	0.10107	0.4871
70	-0.08192	-0.02899	0.08755	0.5557

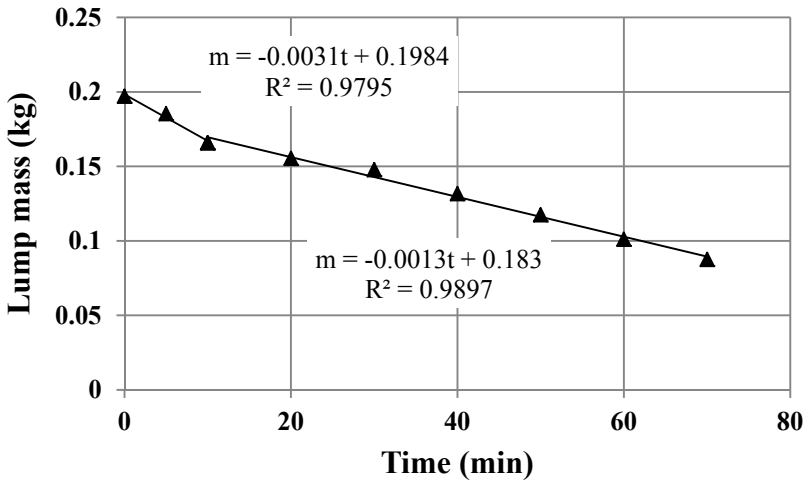

R-W4 (water-V=2.5m/s-T=30°C)

Time (min)	Strain gauge reading (v)	Strain gauge reading (v)	Lump mass (kg)	Fraction digested
	Plus basket	Minus basket		
0	-0.11761	-0.06477	0.20031	0.0000
8	-0.11283	-0.05999	0.18525	0.0752
15	-0.10207	-0.04924	0.15135	0.2444
22	-0.09478	-0.04194	0.12837	0.3592
30	-0.08698	-0.03415	0.10380	0.4818
40	-0.07043	-0.01760	0.05165	0.7422
45	-0.06420	-0.01136	0.03200	0.8403
50	-0.06277	-0.00993	0.02749	0.8628

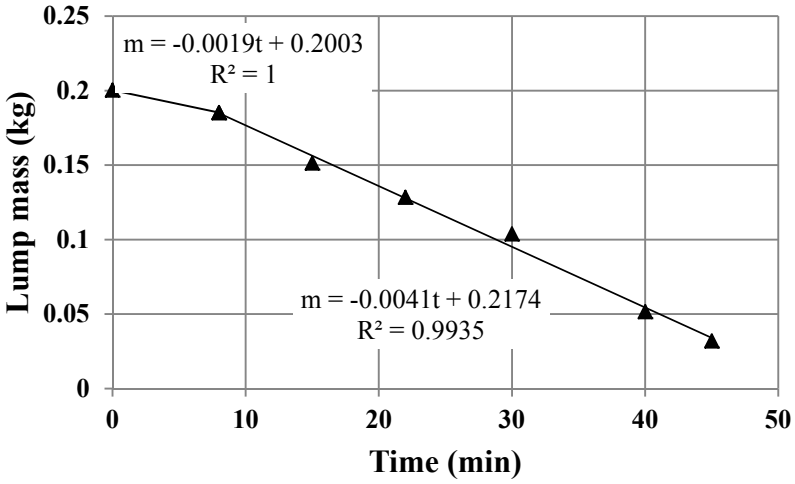

R-W5 (water-V=3m/s-T=30°C)

Time (min)	Strain gauge reading (v)	Strain gauge reading (v)	Lump mass (kg)	Fraction digested
	Plus basket	Minus basket		
0	-0.11843	-0.06389	0.197537	0.0000
5	-0.11133	-0.05679	0.175162	0.1133
10	-0.08889	-0.03435	0.104447	0.4713
15	-0.06007	-0.00553	0.013627	0.9310
18	-0.05863	-0.00409	0.009089	0.9540

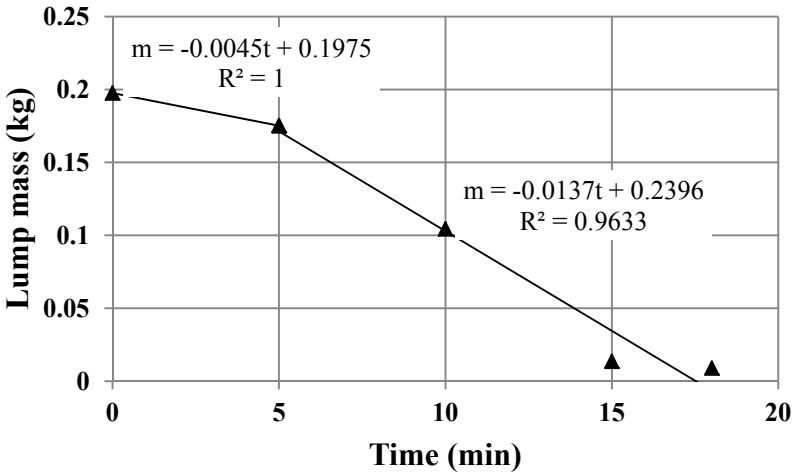

R-W6 (water-V=1m/s-T=45°C)

Time (min)	Strain gauge reading (v)	Strain gauge reading (v)	Lump mass (kg)	Fraction digested
	Plus basket	Minus basket		
0	-0.11459	-0.06163	0.190415	0.0000
15	-0.1134	-0.06044	0.186665	0.0197
25	-0.10882	-0.05586	0.172232	0.0955
35	-0.10419	-0.05123	0.157641	0.1721
45	-0.09351	-0.04055	0.123985	0.3489
70	-0.07667	-0.02371	0.070917	0.6276
80	-0.06931	-0.01635	0.047724	0.7494
85	-0.06694	-0.01398	0.040255	0.7886

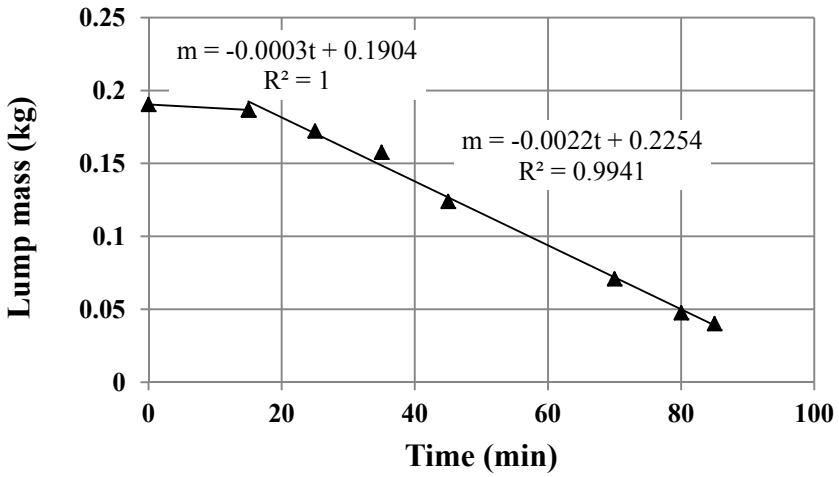

R-W7 (water-V=1.5m/s-T=45°C)

Time (min)	Strain gauge reading (v)	Strain gauge reading (v)	Lump mass (kg)	Fraction digested
	Plus basket	Minus basket		
0	-0.11816	-0.06443	0.19922	0.0000
10	-0.11414	-0.0604	0.18653	0.0637
20	-0.09471	-0.04098	0.12532	0.3709
30	-0.07697	-0.02324	0.06942	0.6515
35	-0.07328	-0.01955	0.05779	0.7099
40	-0.06183	-0.00810	0.02171	0.8910
43	-0.05560	-0.00186	0.00206	0.9897

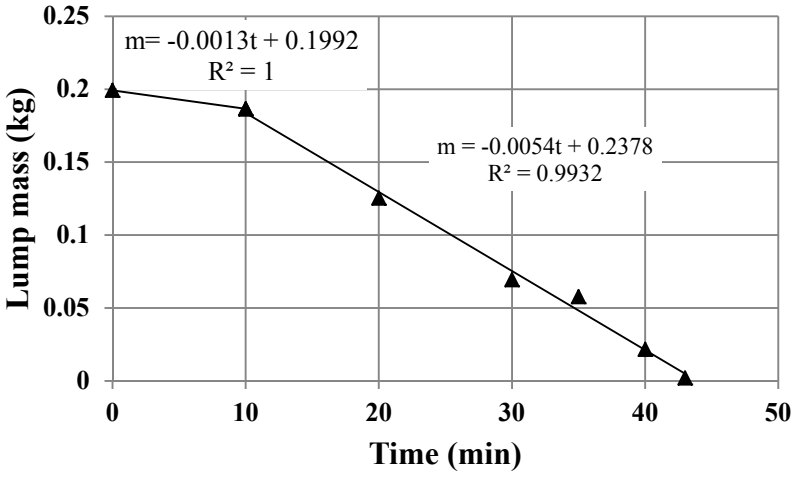

R-W8 (water-V=2m/s-T=45°C)

Time (min)	Strain gauge reading (v)	Strain gauge reading (v)	Lump mass (kg)	Fraction digested
	Plus basket	Minus basket		
0	-0.11830	-0.06571	0.20325	0.0000
5	-0.10532	-0.05273	0.16235	0.2012
10	-0.09355	-0.04096	0.12527	0.3836
13	-0.07885	-0.02626	0.07893	0.6116
18	-0.05458	-0.00199	0.00245	0.9879

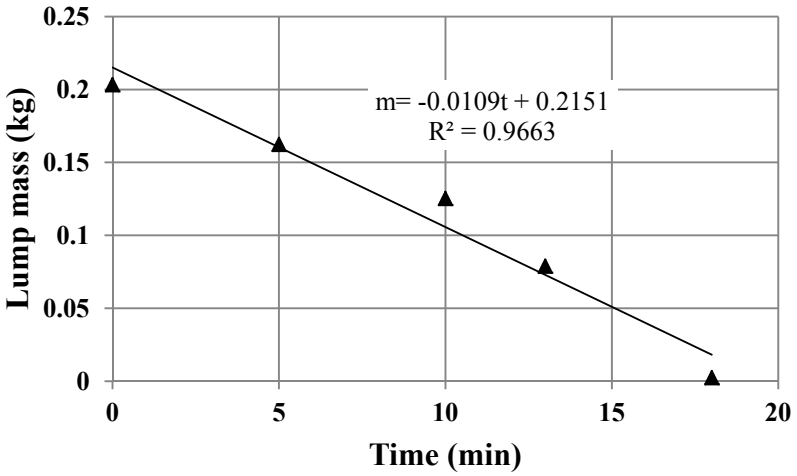

R-15-1 (slurry (C=0.15)-V=1m/s-T=30°C)

Time (min)	Strain gauge reading (v)	Strain gauge reading (v)	Lump mass (kg)	Fraction digested
	Plus basket	Minus basket		
0	-0.11737	-0.06237	0.19275	0.0000
5	-0.11521	-0.06021	0.18593	0.0354
11	-0.11290	-0.05790	0.17865	0.0731
21	-0.10798	-0.05298	0.16316	0.1535
31	-0.10168	-0.04668	0.14330	0.2565
37	-0.09655	-0.04155	0.12713	0.3404

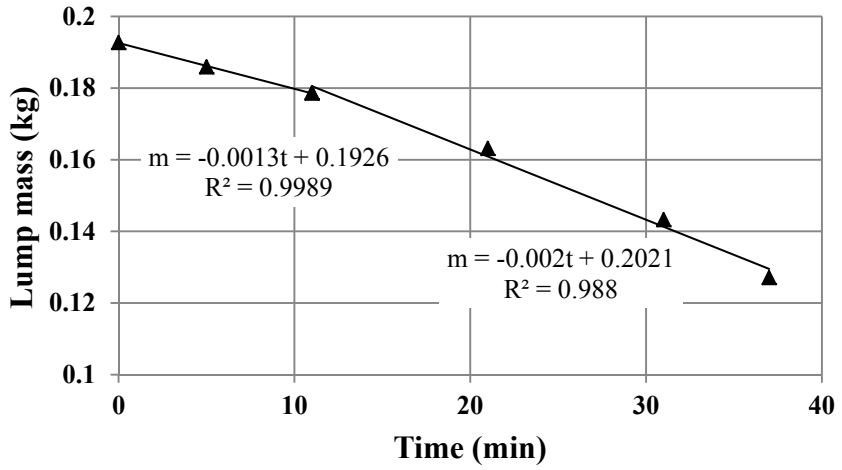

R-15-2 (slurry (C=0.15)-V=1.5m/s-T=30°C)

Time (min)	Strain gauge reading (v)	Strain gauge reading (v)	Lump mass (kg)	Fraction digested
	Plus basket	Minus basket		
0	-0.11563	-0.06273	0.19388	0.0000
10	-0.11072	-0.05782	0.17841	0.0797
20	-0.10163	-0.04874	0.14977	0.2274
30	-0.09609	-0.04319	0.13230	0.3176
40	-0.09176	-0.03887	0.11867	0.3879
50	-0.08595	-0.03306	0.10037	0.4823
60	-0.07702	-0.02412	0.07220	0.6276
71	-0.06488	-0.01198	0.03396	0.8248
76	-0.05764	-0.00474	0.01113	0.9426
80	-0.05417	-0.00128	0.00022	0.9988

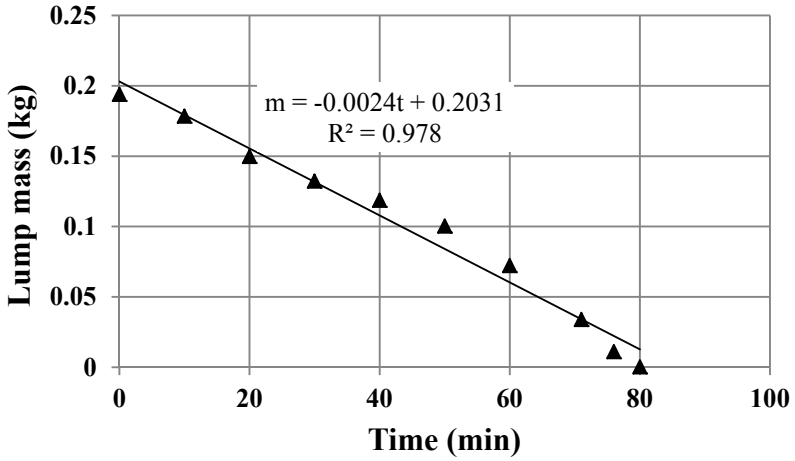

R-15-3 (slurry (C=0.15)-V=2m/s-T=30°C)

Time (min)	Strain gauge reading (v)	Strain gauge reading (v)	Lump mass (kg)	Fraction digested
	Plus basket	Minus basket		
0	-0.11890	-0.06390	0.197568	0.0000
8	-0.10820	-0.05320	0.163849	0.1707
13	-0.09640	-0.04140	0.126664	0.3589
18	-0.08020	-0.02520	0.075613	0.6173
26	-0.05800	-0.00300	0.005654	0.9714

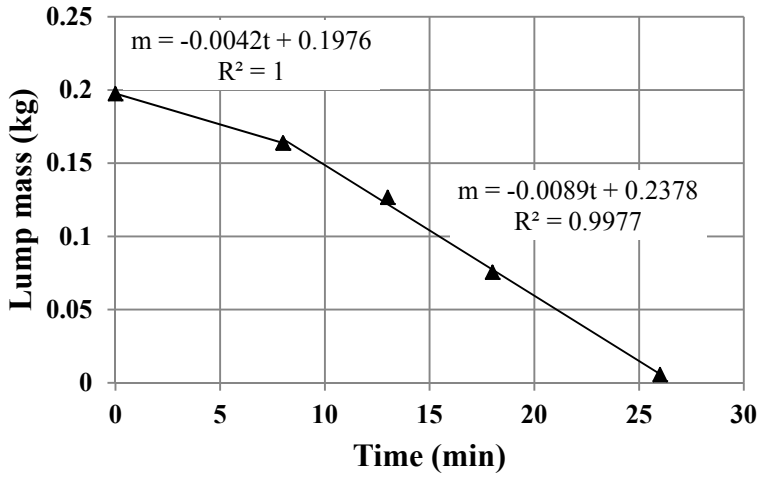

R-15-4 (slurry (C=0.15)-V=2.5m/s-T=30°C)

Time (min)	Strain gauge reading (v)	Strain gauge reading (v)	Lump mass (kg)	Fraction digested
	Plus basket	Minus basket		
0	-0.11641	-0.06343	0.19607	0.0000
8	-0.11521	-0.06222	0.19228	0.0194
14	-0.07867	-0.02568	0.07712	0.6067
19	-0.06962	-0.01664	0.04862	0.7520
24	-0.05569	-0.00271	0.00473	0.9759

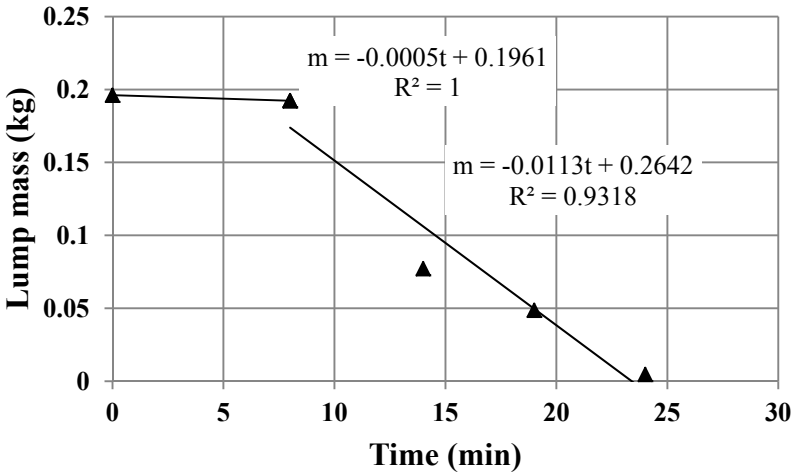

R-15-6 (slurry (C=0.15)-V=1m/s-T=45°C)

Time (min)	Strain gauge reading (v)	Strain gauge reading (v)	Lump mass (kg)	Fraction digested
	Plus basket	Minus basket		
0	-0.11489	-0.06289	0.19438	0.0000
9	-0.11394	-0.06194	0.19140	0.0153
15	-0.11036	-0.05836	0.18012	0.0734
21	-0.10866	-0.05666	0.17475	0.1010
35	-0.08043	-0.02144	0.06376	0.6720

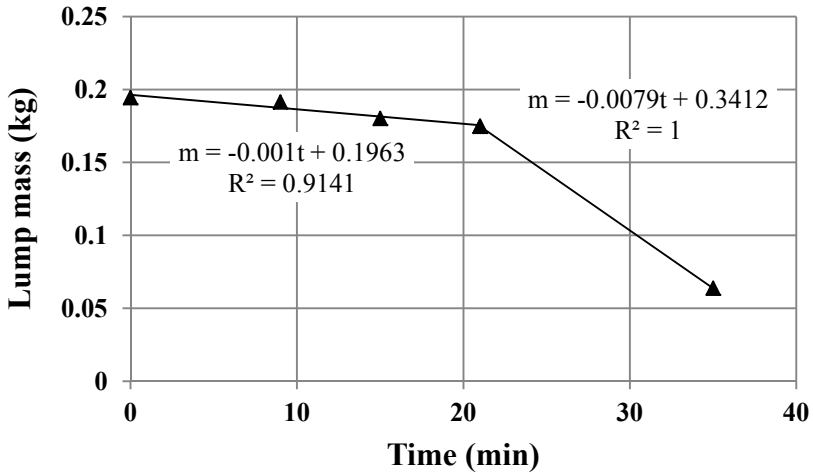

R-15-7 (slurry (C=0.15)-V=1.5m/s-T=45°C)

Time (min)	Strain gauge reading (v)	Strain gauge reading (v)	Lump mass (kg)	Fraction digested
	Plus basket	Minus basket		
0	-0.11654	-0.06454	0.199593	0.0000
10	-0.09907	-0.04707	0.14454	0.2758
15	-0.09138	-0.03938	0.120298	0.3973
31	-0.05745	-0.00545	0.013375	0.9330

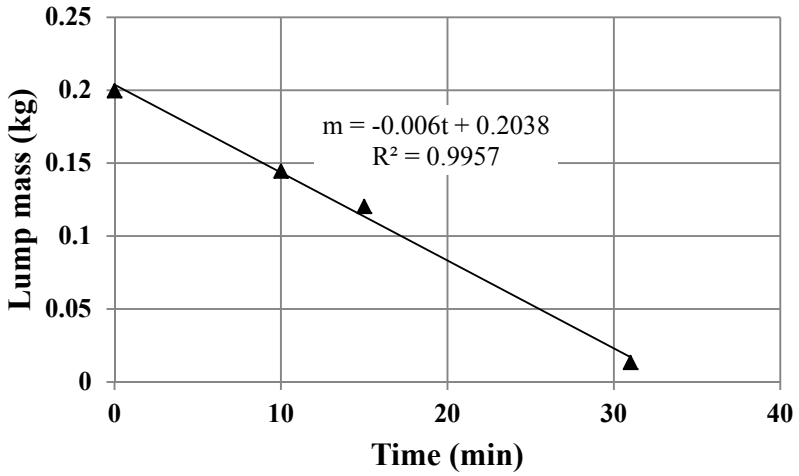

R-15-8 (slurry(C=0.15)-V=2m/s-T=45°C)

Time (min)	Strain gauge reading (v)	Strain gauge reading (v)	Lump mass (kg)	Fraction digested
	Plus basket	Minus basket		
0	-0.11651	-0.06337	0.19589	0.0000
5	-0.10822	-0.05508	0.169766	0.1334
8	-0.08199	-0.02885	0.087107	0.5553
11	-0.05672	-0.00358	0.007497	0.9617
14	-0.05600	-0.00221	0.003149	0.9839

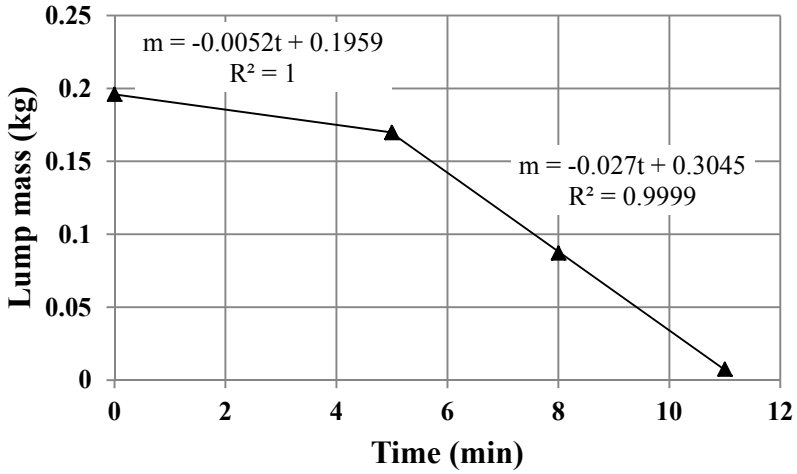

R-30-1 (slurry (C=0.30)-V=1m/s-T=30°C)

Time (min)	Strain gauge reading (v)	Strain gauge reading (v)	Lump mass (kg)	Fraction digested
	Plus basket	Minus basket		
0	-0.11514	-0.06258	0.193393	0.0000
8	-0.11358	-0.06101	0.188461	0.0255
18	-0.11332	-0.06075	0.187641	0.0297
24	-0.11160	-0.05903	0.182221	0.0578
32	-0.11183	-0.05926	0.182946	0.0540
37	-0.11143	-0.05886	0.181686	0.0605
42	-0.11100	-0.05844	0.180346	0.0675

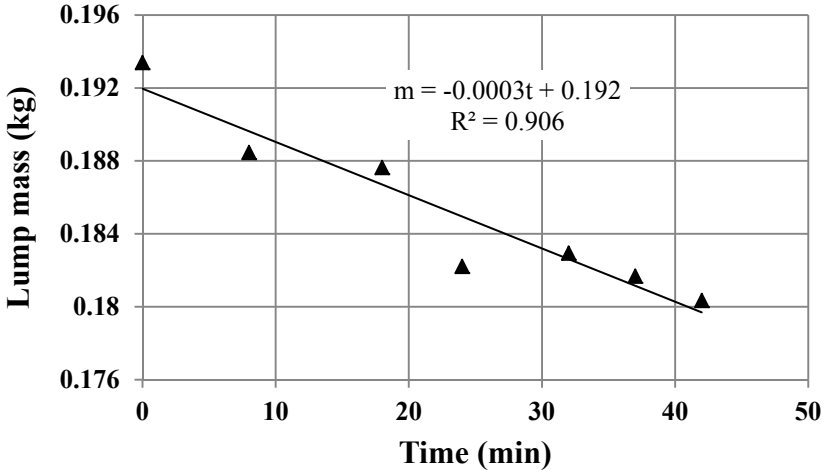

R-30-2 (slurry (C=0.30)-V=1.5m/s-T=30°C)

Time (min)	Strain gauge reading (v)	Strain gauge reading (v)	Lump mass (kg)	Fraction digested
	Plus basket	Minus basket		
0	-0.11676	-0.06317	0.19525	0.0000
10	-0.11266	-0.05907	0.18233	0.0662
20	-0.11054	-0.05695	0.17565	0.1004
30	-0.10896	-0.05536	0.17066	0.1260
40	-0.10758	-0.05399	0.16632	0.1482
50	-0.10590	-0.05231	0.16103	0.1753
60	-0.10265	-0.04905	0.15077	0.2278
70	-0.09608	-0.04248	0.13007	0.3338
80	-0.08965	-0.03605	0.10980	0.4376
90	-0.06571	-0.01212	0.03438	0.8239
95	-0.06116	-0.00757	0.02004	0.8974
100	-0.05714	-0.00354	0.00737	0.9622

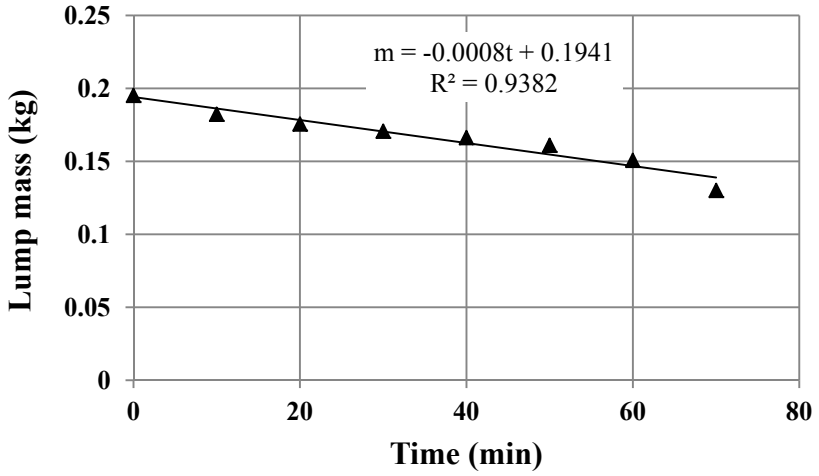

R-30-3 (slurry ((C=0.30)-V=2m/s-T=30°C)

Time (min)	Strain gauge reading (v)	Strain gauge reading (v)	Lump mass (kg)	Fraction digested
	Plus basket	Minus basket		
0	-0.11580	-0.0640	0.19788	0.0000
10	-0.10820	-0.0564	0.17393	0.1210
20	-0.08880	-0.0370	0.11280	0.4300
30	-0.07340	-0.0216	0.06427	0.6752
40	-0.06350	-0.0117	0.03307	0.8329
44	-0.05700	-0.0052	0.01259	0.9364

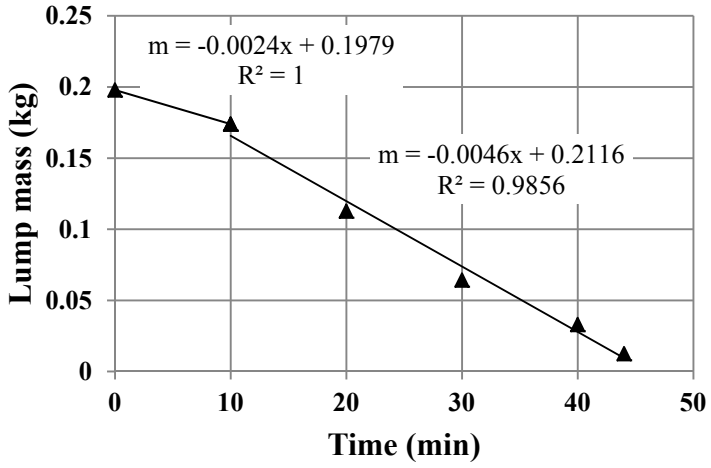

R-30-4 (slurry ((C=0.30)-V=2.5m/s-T=30°C)

Time (min)	Strain gauge reading (v)	Strain gauge reading (v)	Lump mass (kg)	Fraction digested
	Plus basket	Minus basket		
0	-0.11597	-0.06557	0.202815	0.0000
5	-0.09363	-0.04323	0.132415	0.3471
10	-0.08193	-0.03153	0.09556	0.5288
16	-0.06385	-0.01345	0.038585	0.8098
20	-0.05116	-0.00075	-0.00142	0.9990

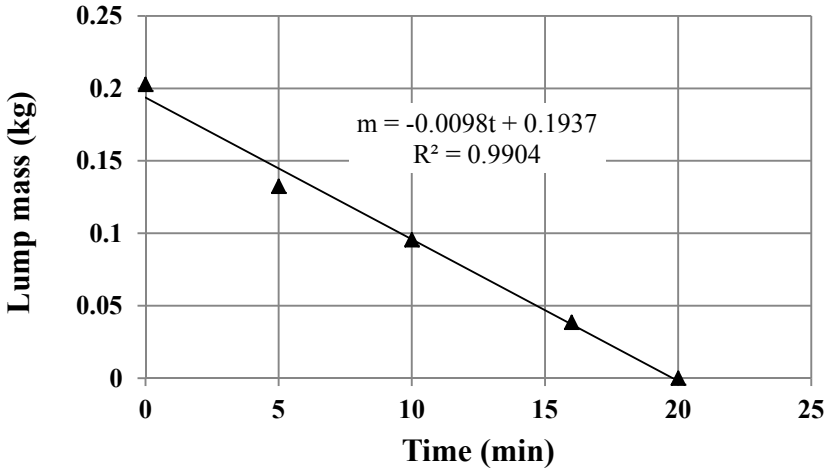

R-30-5 (slurry ((C=0.30)-V=1m/s-T=45°C)

Time (min)	Strain gauge reading (v)	Strain gauge reading (v)	Lump mass (kg)	Fraction digested
	Plus basket	Minus basket		
0	-0.11459	-0.06163	0.190415	0.0000
15	-0.1134	-0.06044	0.186665	0.0197
25	-0.10882	-0.05586	0.172232	0.0955
35	-0.10419	-0.05123	0.157641	0.1721
45	-0.09351	-0.04055	0.123985	0.3489
70	-0.07667	-0.02371	0.070917	0.6276
80	-0.06931	-0.01635	0.047724	0.7494
85	-0.06694	-0.01398	0.040255	0.7886

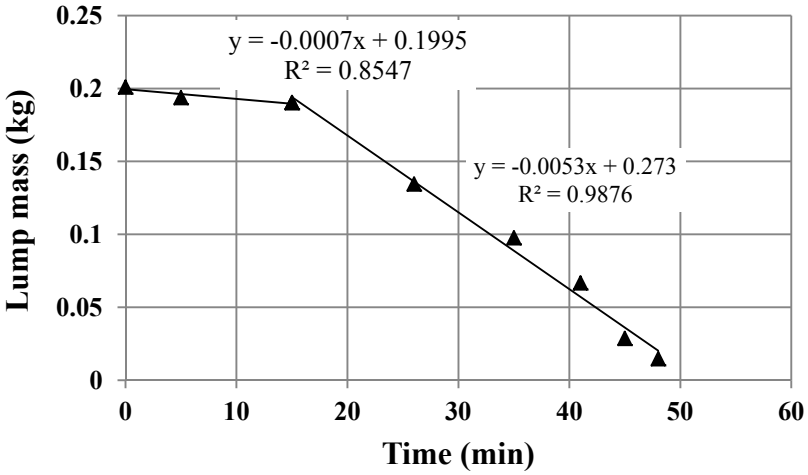

R-30-6 (slurry (C=0.30)-V=1.5m/s-T=45°C)

Time (min)	Strain gauge reading (v)	Strain gauge reading (v)	Lump mass (kg)	Fraction digested
	Plus basket	Minus basket		
0	-0.11816	-0.06443	0.199223	0.0000
10	-0.11414	-0.0604	0.186539	0.0637
20	-0.09471	-0.04098	0.125325	0.3709
30	-0.07697	-0.02324	0.06942	0.6515
35	-0.07328	-0.01955	0.057792	0.7099
40	-0.06183	-0.00810	0.02171	0.8910
43	-0.05560	-0.00186	0.002061	0.9897

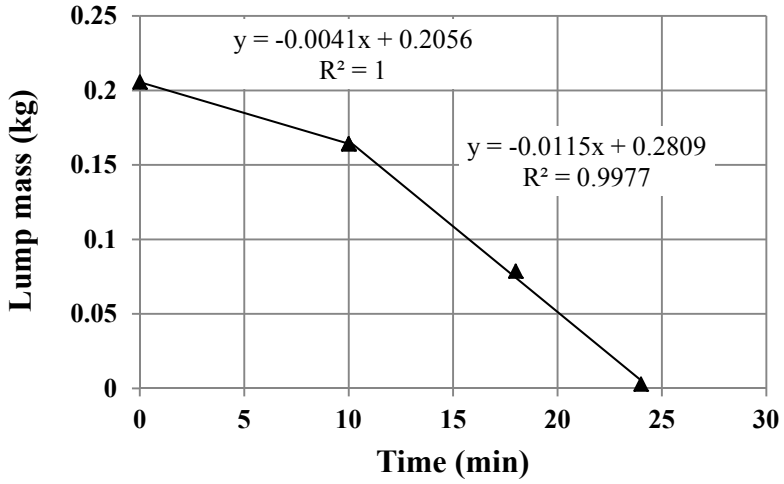

R-30-7 (slurry ((C=0.30)-V=2m/s-T=45°C)

Time (min)	Strain gauge reading (v)	Strain gauge reading (v)	Lump mass (kg)	Fraction digested
	Plus basket	Minus basket		
0	-0.1183	-0.06571	0.203256	0.0000
5	-0.10532	-0.05273	0.162352	0.2012
10	-0.09355	-0.04096	0.125277	0.3836
13	-0.07885	-0.02626	0.078937	0.6116
18	-0.05458	-0.00199	0.002455	0.9879

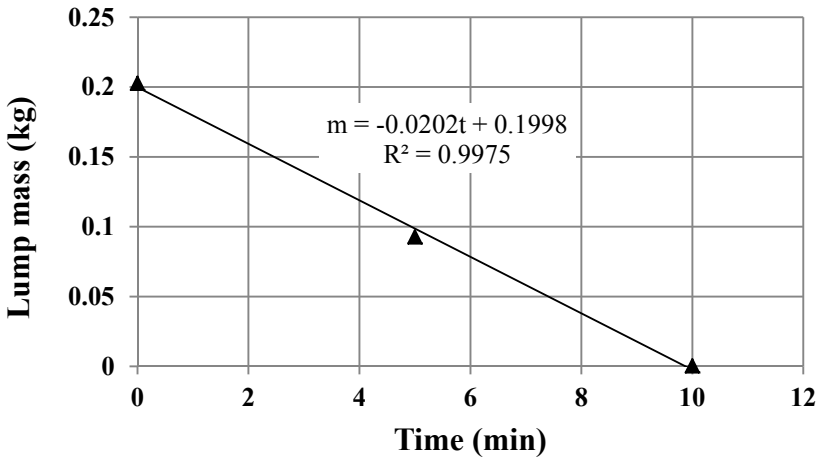

Effect of slurry velocity on oil sand lump ablation- slurry (C = 0.15)

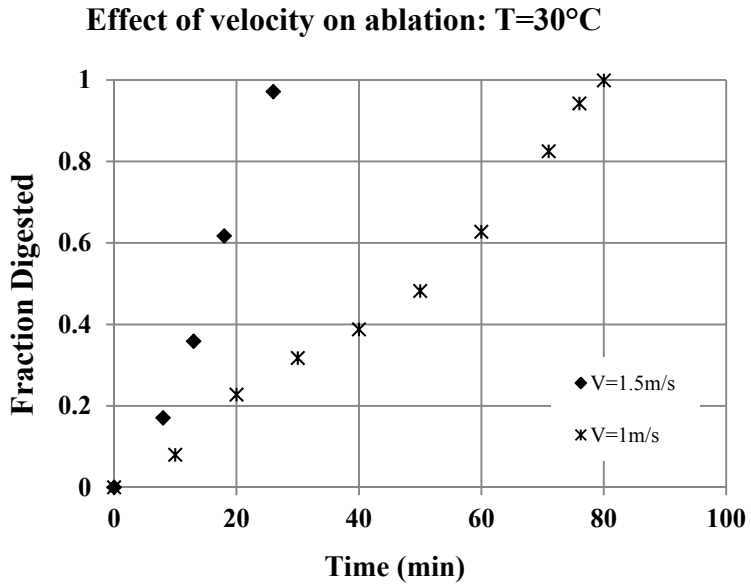

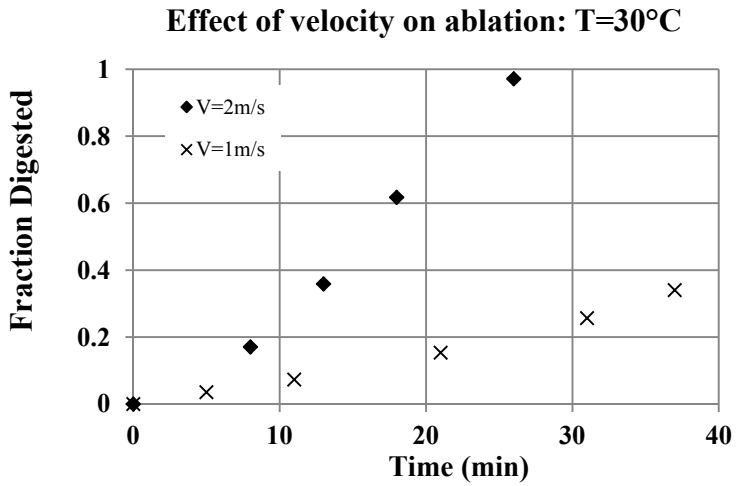

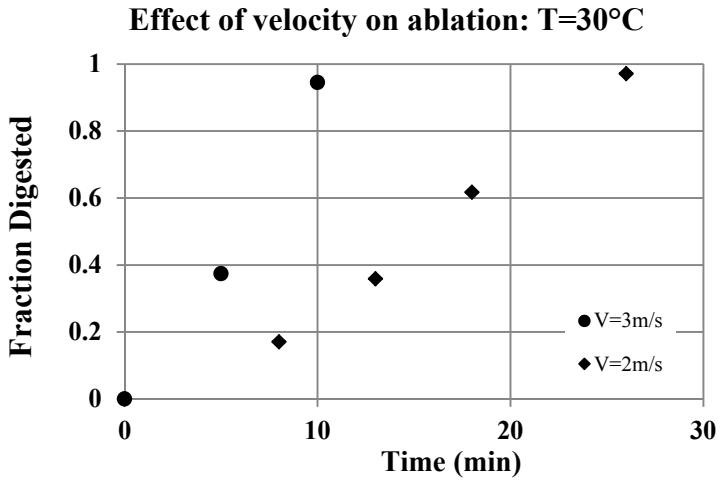

Effect of slurry velocity on oil sand lump ablation- slurry (C = 0.30)

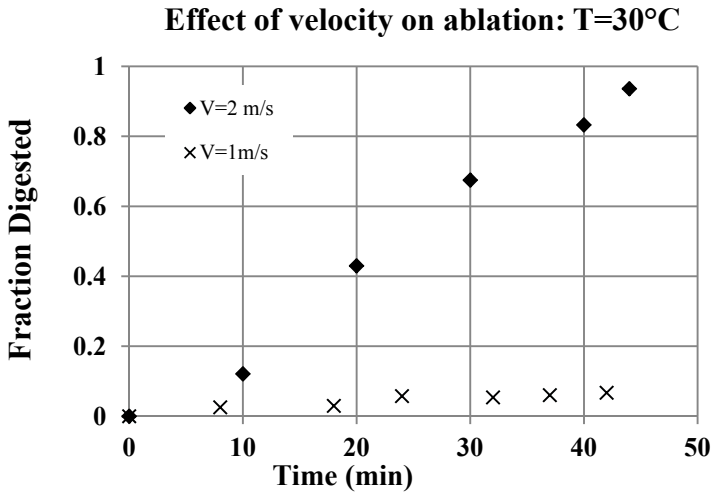

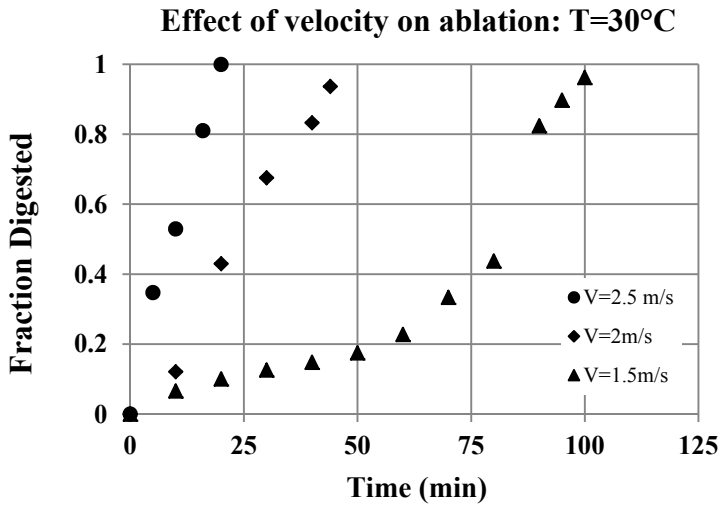

Online drag force measurement for ablation in water

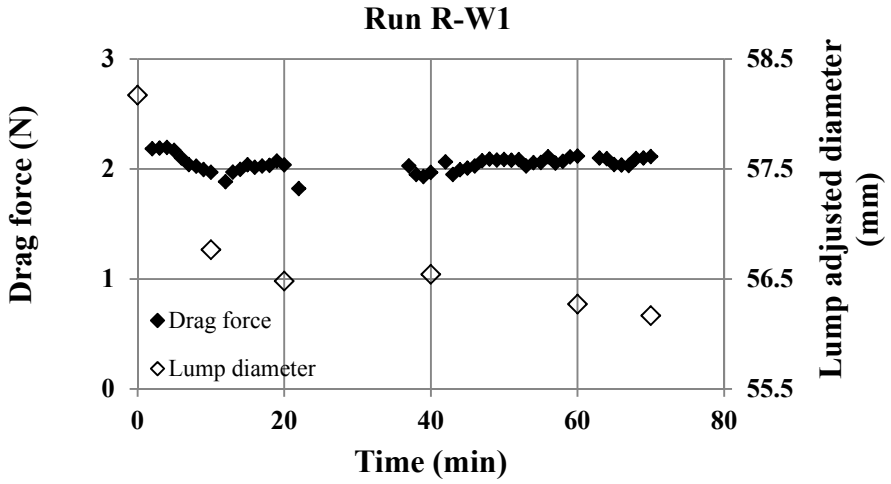

Time (min)	Strain gauge reading (v)	Total force (kg)	Drag force (kg)	Drag force (N)
		Lump in basket	Lump in basket	Lump only
2	0.1385	0.4558	0.6982	2.185
3	0.1387	0.4563	0.6987	2.190
4	0.1389	0.4569	0.6993	2.196
5	0.1381	0.4543	0.6968	2.171
6	0.1358	0.4472	0.6896	2.101
7	0.1339	0.4411	0.6835	2.041
8	0.1334	0.4396	0.6820	2.026
9	0.1325	0.4365	0.6789	1.995
10	0.1317	0.4339	0.6763	1.970
12	0.1309	0.4315	0.6677	1.885
13	0.1337	0.4404	0.6765	1.972
14	0.1345	0.4430	0.6791	1.997
15	0.1358	0.4472	0.6833	2.038
16	0.1351	0.4448	0.6809	2.015
17	0.1355	0.4460	0.6821	2.027
18	0.1357	0.4466	0.6827	2.033
19	0.1369	0.4507	0.6868	2.073
20	0.1358	0.4471	0.6833	2.038
22	0.1293	0.4265	0.6612	1.822
37	0.1360	0.4477	0.6824	2.030
38	0.1335	0.4396	0.6744	1.951

39	0.1328	0.4376	0.6723	1.931
40	0.1341	0.4415	0.6763	1.970
42	0.1370	0.4510	0.6860	2.065
43	0.1334	0.4393	0.6743	1.951
44	0.1348	0.4438	0.6788	1.994
45	0.1352	0.4452	0.6802	2.009
46	0.1358	0.4471	0.6821	2.027
47	0.1374	0.4521	0.6871	2.076
48	0.1378	0.4536	0.6886	2.091
49	0.1375	0.4526	0.6876	2.081
50	0.1377	0.4532	0.6882	2.087
51	0.1375	0.4525	0.6875	2.080
52	0.1377	0.4531	0.6881	2.086
53	0.1358	0.4471	0.6821	2.027
54	0.1368	0.4502	0.6852	2.058
55	0.1368	0.4504	0.6854	2.060
56	0.1385	0.4558	0.6908	2.113
57	0.1367	0.4498	0.6848	2.053
58	0.1372	0.4514	0.6864	2.069
59	0.1385	0.4557	0.6907	2.111
60	0.1387	0.4563	0.6913	2.117
63	0.1385	0.4558	0.6895	2.100
64	0.1383	0.4552	0.6889	2.094
65	0.1366	0.4497	0.6834	2.040
66	0.1365	0.4494	0.6831	2.036
67	0.1364	0.4488	0.6825	2.031
68	0.1384	0.4555	0.6892	2.096
69	0.1385	0.4558	0.6895	2.100
70	0.1390	0.4572	0.6909	2.113

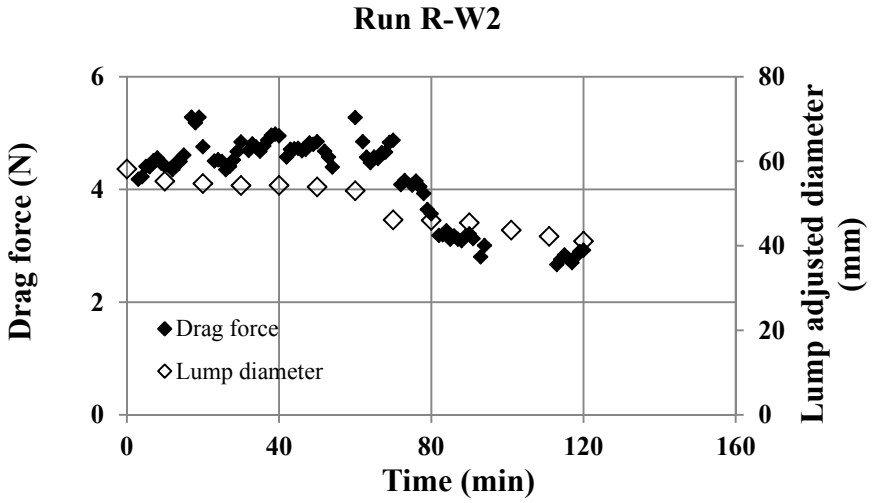

Time (min)	Strain gauge reading (v)	Total force (kg)	Drag force (kg)	Drag force (N)
		Lump in basket	Lump in basket	Lump only
3	0.3780	1.220	1.461	4.182
4	0.3794	1.225	1.466	4.227
5	0.3852	1.243	1.484	4.407
6	0.3850	1.242	1.483	4.401
7	0.3885	1.254	1.495	4.511
8	0.3900	1.259	1.500	4.560
9	0.3871	1.249	1.490	4.469
10	0.3855	1.244	1.485	4.419
12	0.3869	1.249	1.478	4.351
13	0.3908	1.261	1.491	4.472
14	0.3916	1.263	1.493	4.496
15	0.3952	1.275	1.505	4.610
17	0.4167	1.344	1.573	5.283
18	0.4135	1.333	1.563	5.183
19	0.4167	1.344	1.573	5.284
20	0.3999	1.290	1.520	4.758
23	0.3926	1.267	1.494	4.503
24	0.3934	1.269	1.496	4.527
25	0.3924	1.266	1.493	4.495
26	0.3878	1.251	1.478	4.351

27	0.3896	1.257	1.484	4.409
28	0.3933	1.269	1.496	4.523
29	0.3980	1.284	1.511	4.673
30	0.4034	1.301	1.528	4.842
32	0.3993	1.288	1.513	4.692
33	0.4030	1.300	1.525	4.808
34	0.4013	1.294	1.519	4.754
35	0.3988	1.287	1.512	4.678
36	0.4018	1.296	1.521	4.772
37	0.4052	1.307	1.532	4.876
38	0.4079	1.316	1.541	4.962
39	0.4085	1.318	1.543	4.982
40	0.4076	1.315	1.540	4.951
42	0.3955	1.276	1.501	4.576
43	0.3998	1.290	1.515	4.712
44	0.4001	1.291	1.516	4.721
45	0.4004	1.292	1.517	4.729
46	0.3990	1.287	1.512	4.685
47	0.3998	1.290	1.515	4.710
48	0.4034	1.301	1.527	4.825
49	0.4027	1.299	1.524	4.800
50	0.4042	1.304	1.529	4.848
52	0.3993	1.288	1.512	4.678
53	0.3960	1.278	1.501	4.574
54	0.3903	1.260	1.483	4.398
60	0.4184	1.349	1.573	5.276
62	0.4060	1.310	1.529	4.849
63	0.3972	1.281	1.501	4.573
64	0.3941	1.271	1.491	4.475
65	0.3973	1.282	1.501	4.575
66	0.3965	1.279	1.499	4.551
67	0.3997	1.289	1.509	4.652
68	0.4001	1.291	1.510	4.665
69	0.4055	1.308	1.528	4.834
70	0.4068	1.312	1.532	4.873
72	0.3820	1.233	1.451	4.087
73	0.3842	1.240	1.459	4.158
75	0.3816	1.232	1.450	4.075
76	0.3840	1.239	1.458	4.151

77	0.3808	1.229	1.448	4.050
78	0.3769	1.217	1.435	3.930
79	0.3678	1.188	1.406	3.643
80	0.3654	1.180	1.399	3.568
82	0.3533	1.141	1.359	3.185
83	0.3536	1.142	1.360	3.195
84	0.3559	1.150	1.368	3.266
85	0.3511	1.134	1.353	3.117
86	0.3530	1.140	1.359	3.176
87	0.3511	1.134	1.353	3.118
88	0.3503	1.132	1.350	3.091
89	0.3528	1.140	1.358	3.169
90	0.3542	1.144	1.362	3.213
91	0.3515	1.135	1.354	3.128
93	0.3420	1.105	1.321	2.805
94	0.3484	1.126	1.341	3.006
113	0.3420	1.105	1.307	2.668
114	0.3449	1.115	1.316	2.757
115	0.3475	1.123	1.324	2.839
116	0.3454	1.116	1.318	2.773
117	0.3431	1.109	1.310	2.702
118	0.3467	1.120	1.322	2.813
119	0.3494	1.129	1.330	2.898
120	0.3502	1.131	1.333	2.924

Run R-W4

Time (min)	**Strain gauge reading (v)**	**Total force (kg)**	**Drag force (kg)**	**Drag force (N)**
		Lump in basket	Lump in basket	Lump only
3	1.162	3.722	3.961	11.702
4	1.166	3.735	3.973	11.826
5	1.181	3.783	4.022	12.303
6	1.183	3.790	4.028	12.365
7	1.181	3.784	4.023	12.310
8	1.196	3.830	4.069	12.759
10	1.164	3.730	3.969	11.780

11	1.144	3.664	3.903	11.132
12	1.136	3.640	3.879	10.898
13	1.144	3.666	3.905	11.154
14	1.140	3.652	3.891	11.012
15	1.121	3.592	3.830	10.422
17	1.105	3.541	3.773	9.856
18	1.101	3.529	3.760	9.733
19	1.094	3.505	3.737	9.505
20	1.094	3.505	3.736	9.497
21	1.094	3.506	3.738	9.511
22	1.088	3.486	3.717	9.313
24	1.081	3.465	3.697	9.113
25	1.086	3.482	3.713	9.272
26	1.106	3.545	3.776	9.892
27	1.113	3.566	3.797	10.096
28	1.125	3.605	3.836	10.480
29	1.112	3.563	3.794	10.067
30	1.103	3.533	3.765	9.777
32	1.092	3.499	3.730	9.442
33	1.075	3.444	3.676	8.903
34	1.068	3.424	3.656	8.709
35	1.074	3.441	3.672	8.871
36	1.067	3.421	3.652	8.674
37	1.072	3.435	3.666	8.810
38	1.083	3.471	3.702	9.167
39	1.071	3.431	3.663	8.779
40	1.062	3.403	3.635	8.504
42	0.972	3.115	3.346	5.672
43	0.993	3.184	3.416	6.356
44	0.990	3.175	3.406	6.263
45	0.996	3.192	3.424	6.432
47	0.987	3.165	3.397	6.169
48	1.008	3.232	3.463	6.821
49	1.023	3.279	3.511	7.285
50	1.034	3.314	3.546	7.631

Run R-W5

Time (min)	Strain gauge reading (v)	Total force (kg)	Drag force (kg)	Drag force (N)
		Lump in basket	Lump in basket	Lump only
2	1.622	5.191	5.433	17.141
3	1.613	5.164	5.406	16.879
4	1.618	5.177	5.419	17.012
5	1.675	5.360	5.602	18.800
7	1.565	5.008	5.250	15.351
8	1.542	4.937	5.179	14.657
9	1.614	5.167	5.409	16.908
10	1.577	5.046	5.289	15.728
12	1.527	4.889	5.131	14.183
13	1.439	4.608	4.851	11.431
14	1.388	4.445	4.687	9.830
15	1.329	4.254	4.497	7.958
17	1.250	4.002	4.233	5.377
18	1.275	4.084	4.315	6.175

Run R-W6

Time (min)	Strain gauge reading (v)	Total force (kg)	Drag force (kg)	Drag force (N)
		Lump in basket	Lump in basket	Lump only
2	0.1453	0.4775	0.7125	2.325
3	0.1428	0.4694	0.7044	2.245
4	0.1440	0.4731	0.7081	2.282
5	0.1437	0.4723	0.7073	2.274
7	0.1509	0.4953	0.7302	2.499
8	0.1487	0.4883	0.7233	2.431
9	0.1496	0.4910	0.7260	2.458
10	0.1500	0.4923	0.7273	2.470
11	0.1523	0.4998	0.7348	2.544
12	0.1487	0.4883	0.7233	2.431
13	0.1493	0.4903	0.7253	2.450

14	0.1469	0.4826	0.7176	2.375
15	0.1473	0.4839	0.7189	2.388
17	0.1454	0.4777	0.7109	2.309
18	0.1459	0.4793	0.7124	2.324
19	0.1490	0.4892	0.7224	2.422
20	0.1506	0.4942	0.7273	2.471
21	0.1531	0.5023	0.7354	2.550
22	0.1513	0.4967	0.7298	2.495
23	0.1529	0.5015	0.7346	2.542
24	0.1533	0.5030	0.7362	2.558
25	0.1527	0.5010	0.7341	2.537
27	0.1430	0.4701	0.6962	2.165
28	0.1480	0.4859	0.7120	2.320
29	0.1490	0.4893	0.7153	2.353
30	0.1580	0.5178	0.7438	2.633
31	0.1539	0.5048	0.7309	2.506
32	0.1537	0.5042	0.7303	2.500
33	0.1487	0.4884	0.7144	2.344
34	0.1460	0.4797	0.7058	2.259
35	0.1510	0.4956	0.7216	2.415
37	0.1531	0.5024	0.7213	2.411
40	0.1565	0.5133	0.7322	2.518
41	0.1541	0.5054	0.7243	2.441
42	0.1548	0.5076	0.7265	2.463
43	0.1519	0.4984	0.7173	2.372
44	0.1500	0.4924	0.7113	2.314
45	0.1479	0.4858	0.7048	2.249
47	0.1439	0.4730	0.6754	1.961
48	0.1376	0.4529	0.6552	1.763
49	0.1406	0.4626	0.6649	1.859
50	0.1402	0.4612	0.6636	1.845
52	0.1316	0.4336	0.6302	1.518
53	0.1380	0.4542	0.6509	1.721
54	0.1403	0.4613	0.6580	1.790
55	0.1401	0.4607	0.6573	1.784
56	0.1419	0.4666	0.6632	1.842
57	0.1419	0.4666	0.6633	1.842
58	0.1442	0.4738	0.6705	1.913
59	0.1460	0.4797	0.6764	1.971

60	0.1402	0.4612	0.6578	1.789
62	0.1449	0.4761	0.6700	1.909
63	0.1401	0.4609	0.6549	1.760
64	0.1365	0.4494	0.6434	1.647
65	0.1412	0.4644	0.6584	1.795
66	0.1288	0.4248	0.6188	1.406
67	0.1298	0.4278	0.6218	1.435
68	0.1295	0.4270	0.6210	1.427
69	0.1309	0.4315	0.6254	1.471
70	0.1319	0.4347	0.6287	1.503
72	0.1296	0.4273	0.6037	1.258
73	0.1208	0.3992	0.5755	0.981
74	0.1212	0.4003	0.5767	0.993
75	0.1187	0.3926	0.5689	0.917
76	0.1213	0.4007	0.5770	0.996
77	0.1187	0.3924	0.5687	0.915
78	0.1176	0.3890	0.5654	0.882
79	0.1186	0.3922	0.5686	0.913
80	0.1198	0.3960	0.5724	0.950
82	0.1186	0.3920	0.5570	0.800
83	0.1235	0.4078	0.5728	0.954
84	0.1212	0.4004	0.5653	0.882
85	0.1188	0.3929	0.5579	0.808

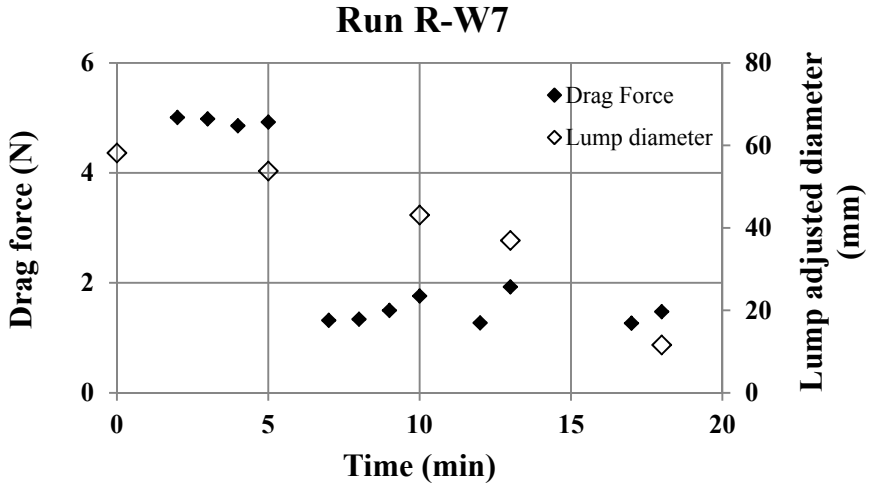

Time (min)	Strain gauge reading (v)	Total force (kg)	Drag force (kg)	Drag force (N)
		Lump in basket	Lump in basket	Lump only
2	0.6708	2.155	2.395	5.010
3	0.6699	2.152	2.392	4.983
4	0.6659	2.139	2.379	4.857
5	0.6681	2.146	2.386	4.925
7	0.5592	1.798	2.019	1.318
8	0.5598	1.801	2.021	1.339
9	0.5649	1.817	2.037	1.498
10	0.5733	1.844	2.064	1.760
12	0.5634	1.812	2.014	1.272
13	0.5843	1.879	2.081	1.927
17	0.5632	1.811	2.013	1.268
18	0.5770	1.855	2.035	1.475

Online drag force measurement for ablation in slurry (C = 0.15)

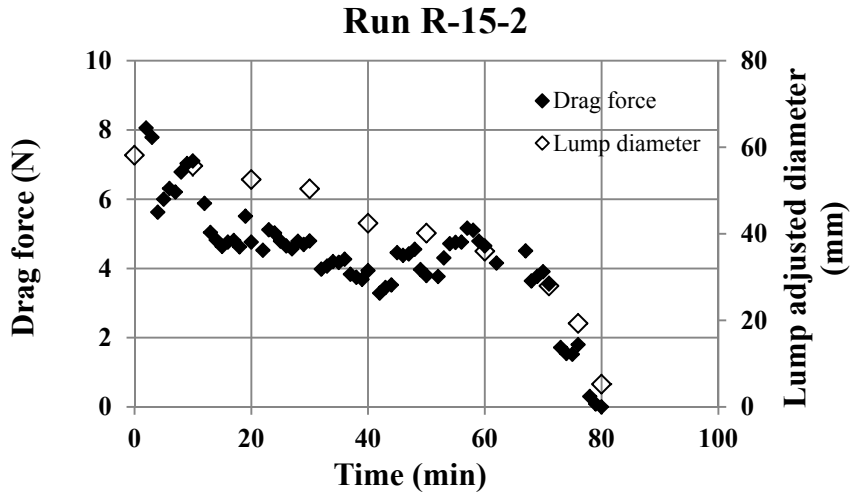

Time (min)	Strain gauge reading (v)	Total force (kg)	Drag force (kg)	Drag force (N)
		Lump in basket	Lump in basket	Lump only
2	0.6096	1.960	2.165	8.059
3	0.6010	1.932	2.138	7.788
4	0.5319	1.712	1.917	5.626
5	0.5439	1.750	1.955	6.000
6	0.5556	1.787	1.987	6.312
7	0.5523	1.777	1.977	6.209
8	0.5708	1.836	2.036	6.789
9	0.5786	1.860	2.061	7.032
10	0.5809	1.868	2.068	7.106
12	0.5418	1.743	1.943	5.881
13	0.5149	1.657	1.857	5.038
14	0.5080	1.635	1.835	4.822
15	0.5022	1.617	1.817	4.640
16	0.5093	1.639	1.829	4.761
17	0.5109	1.644	1.834	4.810
18	0.5050	1.626	1.815	4.626
19	0.5333	1.716	1.906	5.511
20	0.5093	1.639	1.829	4.762
22	0.5018	1.615	1.805	4.526
23	0.5207	1.676	1.865	5.117

24	0.5178	1.666	1.856	5.027
25	0.5103	1.642	1.832	4.791
26	0.5077	1.634	1.818	4.651
27	0.5051	1.626	1.809	4.569
28	0.5120	1.648	1.831	4.784
29	0.5092	1.639	1.822	4.695
30	0.5123	1.649	1.832	4.794
32	0.4864	1.566	1.750	3.982
33	0.4892	1.575	1.759	4.071
34	0.4933	1.588	1.772	4.199
35	0.4926	1.586	1.770	4.176
36	0.4970	1.600	1.779	4.267
37	0.4833	1.556	1.735	3.836
38	0.4804	1.547	1.726	3.747
39	0.4785	1.541	1.720	3.687
40	0.4865	1.567	1.745	3.938
42	0.4658	1.500	1.679	3.290
43	0.4710	1.517	1.696	3.451
44	0.4733	1.524	1.703	3.525
45	0.5031	1.620	1.798	4.458
46	0.5026	1.618	1.790	4.377
47	0.5039	1.622	1.794	4.419
48	0.5083	1.636	1.808	4.554
49	0.4895	1.576	1.748	3.967
50	0.4841	1.559	1.731	3.797
52	0.4833	1.556	1.728	3.771
53	0.5002	1.610	1.782	4.303
54	0.5134	1.652	1.824	4.715
55	0.5146	1.656	1.828	4.754
56	0.5181	1.667	1.829	4.763
57	0.5309	1.708	1.870	5.164
58	0.5290	1.702	1.864	5.105
59	0.5189	1.670	1.832	4.789
60	0.5145	1.656	1.818	4.651
62	0.4987	1.606	1.767	4.156
67	0.5143	1.655	1.804	4.510
68	0.4865	1.567	1.715	3.639
69	0.4908	1.580	1.728	3.773
70	0.4951	1.594	1.742	3.906

71	0.4838	1.558	1.706	3.553
73	0.4252	1.371	1.519	1.718
74	0.4196	1.353	1.501	1.545
75	0.4215	1.359	1.499	1.521
76	0.4304	1.387	1.527	1.799
78	0.3826	1.235	1.375	0.305
79	0.3763	1.215	1.353	0.087
80	0.3715	1.200	1.337	0.000

Run R-15-3

Time (min)	Strain gauge reading (v)	Total force (kg)	Drag force (kg)	Drag force (N)
		Lump in basket	Lump in basket	Lump only
2	1.169	3.743	3.956	12.603
3	1.193	3.823	4.036	13.383
4	1.181	3.784	3.997	13.001
5	1.206	3.862	4.062	13.646
6	1.214	3.890	4.090	13.922
7	1.193	3.821	4.022	13.248
8	1.181	3.782	3.983	12.866
9	1.174	3.762	3.962	12.663
10	1.035	3.317	3.517	8.301
11	0.995	3.189	3.389	7.042
12	0.929	2.979	3.166	4.850
13	0.927	2.974	3.161	4.800
14	0.931	2.985	3.172	4.910
15	0.903	2.895	3.082	4.033
16	0.829	2.658	2.827	1.529
17	0.854	2.740	2.909	2.327
18	0.907	2.909	3.077	3.984
19	0.876	2.810	2.979	3.019
20	0.858	2.752	2.920	2.443
21	0.806	2.586	2.755	0.818
22	0.817	2.621	2.789	1.159
23	0.793	2.545	2.689	0.170
24	0.780	2.505	2.648	0.000
25	0.790	2.536	2.679	0.000
26	0.773	2.481	2.624	0.000

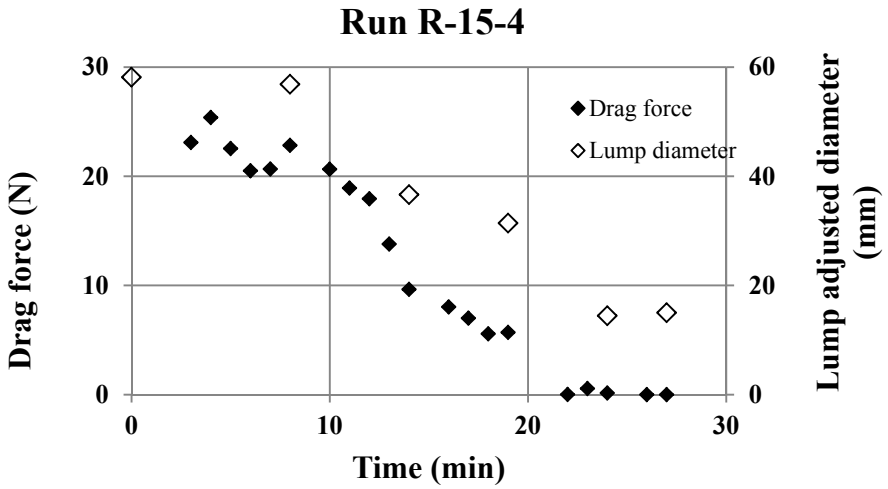

Time (min)	Strain gauge reading (v)	Total force (kg)	Drag force (kg)	Drag force (N)
		Lump in basket	Lump in basket	Lump only
3	1.742	5.573	5.779	23.107
4	1.815	5.806	6.012	25.390
5	1.724	5.516	5.722	22.546
6	1.659	5.309	5.515	20.516
7	1.664	5.325	5.531	20.674
8	1.733	5.546	5.752	22.841
10	1.664	5.324	5.529	20.655
11	1.609	5.148	5.354	18.931
12	1.590	5.089	5.253	17.941
13	1.458	4.666	4.830	13.794
14	1.325	4.244	4.408	9.652
16	1.274	4.079	4.243	8.037
17	1.241	3.974	4.138	7.008
18	1.198	3.838	3.992	5.573
19	1.203	3.852	4.006	5.711
22	1.021	3.272	3.426	0.017
23	1.043	3.343	3.481	0.558
24	1.030	3.301	3.438	0.142
26	0.956	3.064	3.201	0.000
27	0.967	3.099	3.237	0.000

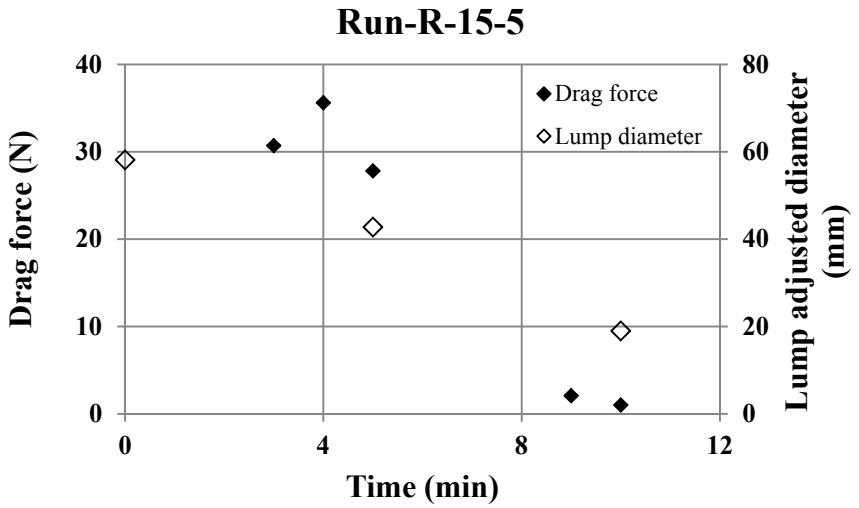

Time (min)	Strain gauge reading (v)	Total force (kg)	Drag force (kg)	Drag force (N)
		Lump in basket	Lump in basket	Lump only
3	2.395	7.659	7.865	30.718
4	2.551	8.158	8.364	35.609
5	2.311	7.390	7.570	27.823
9	1.495	4.786	4.946	2.082
10	1.461	4.678	4.838	1.017

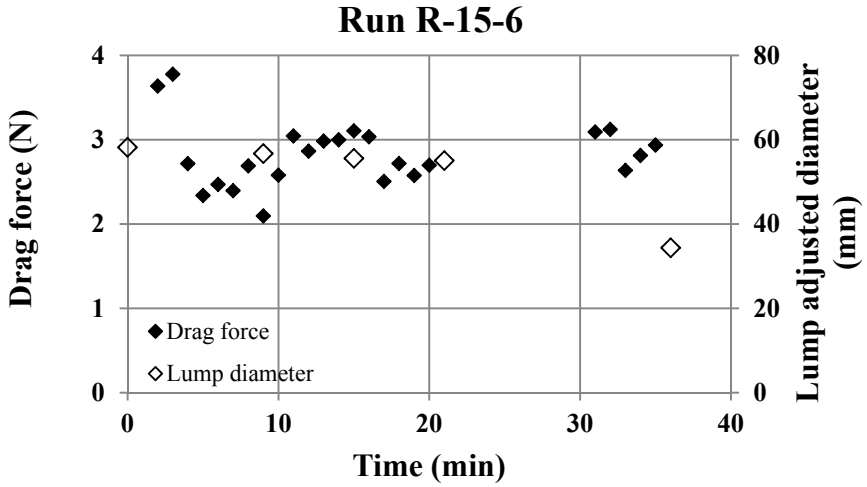

Time (min)	Strain gauge reading (v)	Total force (kg)	Drag force (kg)	Drag force (N)
		Lump in basket	Lump in basket	Lump only
2	0.3242	1.048	1.253	3.636
3	0.3287	1.063	1.267	3.776
4	0.2951	0.956	1.159	2.716
5	0.2831	0.917	1.120	2.338
6	0.2886	0.935	1.134	2.469
7	0.2868	0.929	1.126	2.395
8	0.2950	0.955	1.156	2.690
9	0.2750	0.891	1.095	2.094
10	0.2908	0.942	1.145	2.579
11	0.3056	0.989	1.192	3.044
12	0.2999	0.971	1.174	2.865
13	0.3037	0.983	1.186	2.983
14	0.3042	0.985	1.188	3.000
15	0.3075	0.995	1.198	3.104
16	0.3066	0.992	1.191	3.036
17	0.2897	0.938	1.137	2.505
18	0.2965	0.960	1.159	2.719
19	0.2919	0.945	1.144	2.575
20	0.2958	0.958	1.157	2.698
31	0.3217	1.040	1.197	3.093
32	0.3226	1.043	1.200	3.123
33	0.3071	0.994	1.151	2.636

34	0.3127	1.012	1.169	2.812

Run R-15-7

Time (min)	Strain gauge reading (v)	Total force (kg)	Drag force (kg)	Drag force (N)
		Lump in basket	Lump in basket	Lump only
3	0.5616	1.806	2.015	6.589
4	0.5555	1.787	1.996	6.396
5	0.5466	1.758	1.967	6.119
6	0.5584	1.796	1.985	6.291
7	0.5538	1.781	1.971	6.149
8	0.5966	1.918	2.107	7.488
9	0.5973	1.920	2.109	7.511
10	0.5798	1.864	2.053	6.962
11	0.5503	1.770	1.959	6.038
12	0.5688	1.829	2.018	6.619
13	0.5816	1.870	2.059	7.018
14	0.5676	1.825	2.006	6.494
15	0.5711	1.837	2.017	6.604
16	0.5460	1.756	1.937	5.817
17	0.5435	1.748	1.929	5.739
18	0.5295	1.704	1.884	5.302
19	0.5486	1.765	1.945	5.900
20	0.5535	1.780	1.961	6.052
21	0.5460	1.756	1.937	5.817
22	0.5435	1.748	1.929	5.739
23	0.5295	1.704	1.884	5.302
24	0.5486	1.765	1.945	5.900
25	0.5535	1.780	1.961	6.052
26	0.5052	1.626	1.768	4.158
27	0.4942	1.591	1.733	3.817
28	0.4574	1.474	1.615	2.662
29	0.4472	1.441	1.583	2.344
30	0.4507	1.452	1.594	2.454
31	0.4507	1.452	1.594	2.454

Run R-15-8

Time (min)	Strain gauge reading (v)	Total force (kg)	Drag force (kg)	Drag force (N)
		Lump in basket	Lump in basket	Lump only
2	1.049	3.361	3.569	12.720
3	1.057	3.386	3.594	12.963
4	1.050	3.366	3.565	12.677
5	1.036	3.321	3.519	12.233
7	1.012	3.243	3.426	11.322
8	0.916	2.937	3.120	8.321
10	0.763	2.450	2.590	3.112
11	0.706	2.266	2.405	1.303
13	0.652	2.094	2.231	0.000
14	0.658	2.113	2.251	0.000

Online drag force measurement for ablation in slurry (C = 0.30)

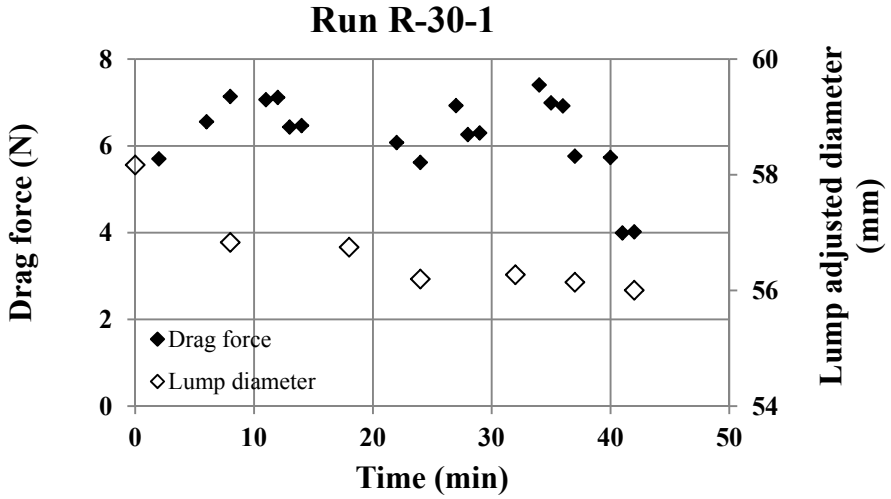

Time (min)	Strain gauge reading (v)	Total force (kg)	Drag force (kg)	Drag force (N)
		Lump in basket	Lump in basket	Lump only
2	0.3714	1.199	1.374	5.701
6	0.3991	1.288	1.461	6.557
8	0.4177	1.347	1.520	7.140
11	0.4154	1.339	1.513	7.067
12	0.4171	1.345	1.518	7.120
13	0.3952	1.275	1.449	6.436
14	0.3963	1.279	1.452	6.468
22	0.3843	1.240	1.412	6.078
24	0.3696	1.193	1.366	5.620
27	0.4114	1.327	1.499	6.929
28	0.3901	1.259	1.431	6.262
29	0.3913	1.263	1.435	6.300
34	0.4266	1.375	1.548	7.407
35	0.4135	1.333	1.505	6.992
36	0.4112	1.326	1.498	6.922
37	0.3743	1.208	1.380	5.764
40	0.3734	1.205	1.377	5.734
41	0.3179	1.028	1.200	3.996
42	0.3186	1.031	1.202	4.019

Run R-30-2

Time (min)	Strain gauge reading (v)	Total force (kg)	Drag force (kg)	Drag force (N)
		Lump in basket	Lump in basket	Lump only
3	0.6956	2.234	2.412	9.330
4	0.6753	2.169	2.347	8.692
5	0.7089	2.276	2.454	9.744
6	0.7042	2.261	2.436	9.568
7	0.7120	2.286	2.461	9.813
8	0.7258	2.330	2.505	10.246
9	0.7142	2.293	2.468	9.882
10	0.7037	2.260	2.434	9.551
12	0.7183	2.307	2.481	10.011
13	0.7276	2.336	2.511	10.301
14	0.7024	2.256	2.430	9.511
15	0.7163	2.300	2.475	9.946
16	0.6853	2.201	2.374	8.961
17	0.7377	2.368	2.541	10.602
18	0.7211	2.315	2.488	10.082
19	0.7049	2.264	2.437	9.577
20	0.7347	2.359	2.532	10.509
22	0.7276	2.336	2.509	10.284
23	0.7460	2.395	2.568	10.862
24	0.7335	2.355	2.528	10.470
25	0.7203	2.313	2.486	10.056
26	0.7465	2.396	2.568	10.867
27	0.7309	2.347	2.519	10.377
28	0.7260	2.331	2.503	10.225
29	0.7326	2.352	2.524	10.431
30	0.7156	2.298	2.470	9.899
32	0.7359	2.363	2.535	10.535
33	0.7222	2.319	2.491	10.106
34	0.7377	2.368	2.540	10.590
35	0.7483	2.402	2.574	10.924
36	0.7539	2.420	2.591	11.087
37	0.7424	2.383	2.554	10.728
38	0.7262	2.332	2.502	10.220

39	0.7521	2.414	2.585	11.030
40	0.7234	2.323	2.494	10.134
42	0.7163	2.300	2.471	9.912
43	0.7255	2.329	2.500	10.198
44	0.7240	2.325	2.496	10.152
45	0.7347	2.359	2.530	10.487
46	0.7131	2.290	2.459	9.798
47	0.7478	2.400	2.570	10.884
48	0.7202	2.312	2.482	10.021
49	0.7266	2.333	2.503	10.221
50	0.7072	2.271	2.441	9.614
52	0.7310	2.347	2.517	10.360
53	0.7385	2.371	2.541	10.593
54	0.7411	2.379	2.549	10.674
55	0.7373	2.367	2.537	10.555
56	0.7229	2.321	2.488	10.081
57	0.7285	2.339	2.506	10.256
58	0.7199	2.311	2.479	9.987
59	0.7366	2.365	2.532	10.511
60	0.7544	2.422	2.589	11.067
62	0.7149	2.296	2.463	9.832
63	0.6924	2.224	2.391	9.126
64	0.6890	2.213	2.380	9.020
65	0.6979	2.241	2.408	9.298
66	0.7123	2.287	2.450	9.702
67	0.7006	2.250	2.412	9.335
68	0.7044	2.262	2.424	9.454
69	0.6826	2.192	2.355	8.773
70	0.7125	2.288	2.450	9.709
73	0.7122	2.287	2.449	9.698
74	0.7014	2.253	2.415	9.363
75	0.7183	2.307	2.469	9.892
76	0.7260	2.331	2.489	10.086
77	0.7348	2.359	2.517	10.360
78	0.7236	2.323	2.481	10.011
79	0.7602	2.440	2.598	11.155
82	0.7039	2.261	2.418	9.395
83	0.7115	2.285	2.443	9.632
84	0.6725	2.160	2.318	8.412

85	0.6352	2.041	2.199	7.241
86	0.6501	2.089	2.229	7.537
87	0.6337	2.036	2.177	7.022
88	0.6209	1.996	2.136	6.624
89	0.6103	1.962	2.102	6.291
90	0.6137	1.973	2.113	6.398
92	0.5737	1.845	1.985	5.145
93	0.5585	1.796	1.937	4.670
94	0.5484	1.764	1.901	4.319
95	0.5628	1.810	1.947	4.770
97	0.6263	2.013	2.150	6.759
98	0.5877	1.889	2.026	5.549
99	0.5782	1.859	1.993	5.223
100	0.5615	1.806	1.940	4.700

Run R-30-3

Time (min)	**Strain gauge reading (v)**	**Total force (kg)**	**Drag force (kg)**	**Drag force (N)**
		Lump in basket	Lump in basket	Lump only
3	1.268	4.062	4.235	16.778
4	1.286	4.119	4.293	17.339
5	1.283	4.108	4.282	17.235
6	1.289	4.128	4.297	17.378
7	1.313	4.205	4.374	18.133
8	1.318	4.219	4.387	18.267
9	1.345	4.307	4.475	19.132
10	1.317	4.216	4.384	18.236
14	1.403	4.492	4.660	20.942
15	1.389	4.448	4.616	20.509
16	1.349	4.321	4.475	19.124
17	1.372	4.392	4.546	19.822
18	1.342	4.297	4.451	18.892
19	1.356	4.342	4.496	19.333
20	1.335	4.276	4.430	18.685
22	1.268	4.061	4.215	16.578
23	1.223	3.918	4.072	15.175
24	1.187	3.801	3.955	14.026

25	1.202	3.852	4.006	14.524
26	1.139	3.649	3.792	12.424
27	1.087	3.484	3.627	10.806
28	1.049	3.361	3.503	9.597
29	1.003	3.215	3.358	8.166
30	0.989	3.169	3.312	7.715
33	0.970	3.111	3.254	7.148
34	0.987	3.163	3.305	7.652
35	0.970	3.110	3.253	7.139
36	0.963	3.088	3.224	6.852
37	0.965	3.093	3.228	6.895
38	0.994	3.187	3.323	7.825
39	0.970	3.110	3.246	7.071
42	0.935	2.997	3.128	5.912
43	0.941	3.017	3.147	6.103
44	0.925	2.967	3.097	5.612

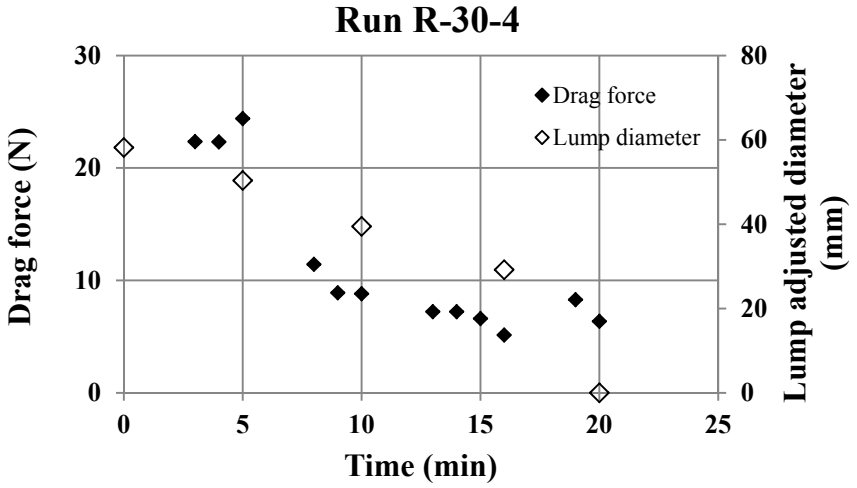

Time (min)	Strain gauge reading (v)	Total force (kg)	Drag force (kg)	Drag force (N)
		Lump in basket	Lump in basket	Lump only
3	1.938	6.201	6.377	22.350
4	1.940	6.206	6.374	22.322
5	2.009	6.427	6.586	24.405
8	1.598	5.113	5.264	11.435
9	1.516	4.854	5.005	8.893
10	1.514	4.846	4.997	8.815
13	1.463	4.684	4.835	7.224
14	1.463	4.684	4.835	7.225
15	1.447	4.634	4.772	6.601
16	1.401	4.484	4.622	5.135
19	1.504	4.815	4.944	8.292
20	1.443	4.619	4.748	6.369

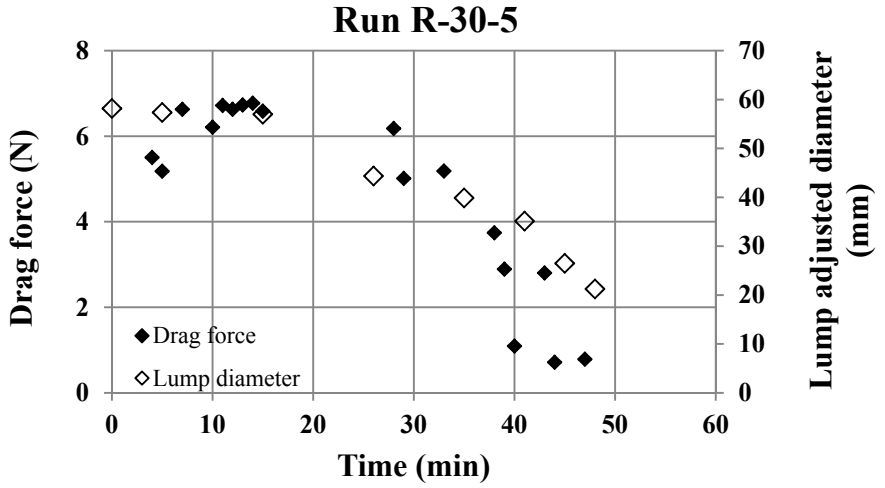

Time (min)	Strain gauge reading (v)	Total force (kg)	Drag force (kg)	Drag force (N)
		Lump in basket	Lump in basket	Lump only
4	0.3663	1.183	1.353	5.502
5	0.3561	1.150	1.321	5.183
7	0.4028	1.299	1.468	6.629
10	0.3895	1.257	1.426	6.212
11	0.4057	1.309	1.478	6.720
12	0.4028	1.299	1.468	6.629
13	0.4063	1.311	1.479	6.730
14	0.4076	1.315	1.483	6.771
15	0.4017	1.296	1.464	6.586
28	0.3929	1.268	1.423	6.182
29	0.3556	1.149	1.304	5.014
33	0.3638	1.175	1.321	5.186
38	0.3177	1.028	1.174	3.743
39	0.2928	0.948	1.087	2.892
40	0.2353	0.765	0.904	1.092
43	0.2899	0.939	1.078	2.801
44	0.2261	0.735	0.866	0.716
47	0.2294	0.746	0.873	0.787

Run R-30-6

Time (min)	Strain gauge reading (v)	Total force (kg)	Drag force (kg)	Drag force (N)
		Lump in basket	Lump in basket	Lump only
3	0.7115	2.285	2.458	9.786
4	0.7186	2.307	2.481	10.007
5	0.7238	2.324	2.497	10.170
6	0.7210	2.315	2.479	9.989
7	0.7363	2.364	2.527	10.465
8	0.7309	2.347	2.511	10.299
9	0.7506	2.410	2.573	10.915
10	0.7371	2.366	2.530	10.491
12	0.7609	2.442	2.606	11.235
13	0.7257	2.330	2.494	10.133
14	0.6726	2.161	2.324	8.471
15	0.5995	1.927	2.071	5.986
16	0.5822	1.872	2.016	5.445
17	0.5647	1.816	1.960	4.896
18	0.5686	1.828	1.972	5.017
20	0.5307	1.708	1.851	3.831
21	0.5205	1.675	1.819	3.512
22	0.4869	1.568	1.694	2.284
23	0.4713	1.518	1.644	1.798
24	0.4869	1.568	1.694	2.284
26	0.4334	1.397	1.523	0.612
27	0.4474	1.442	1.568	1.051

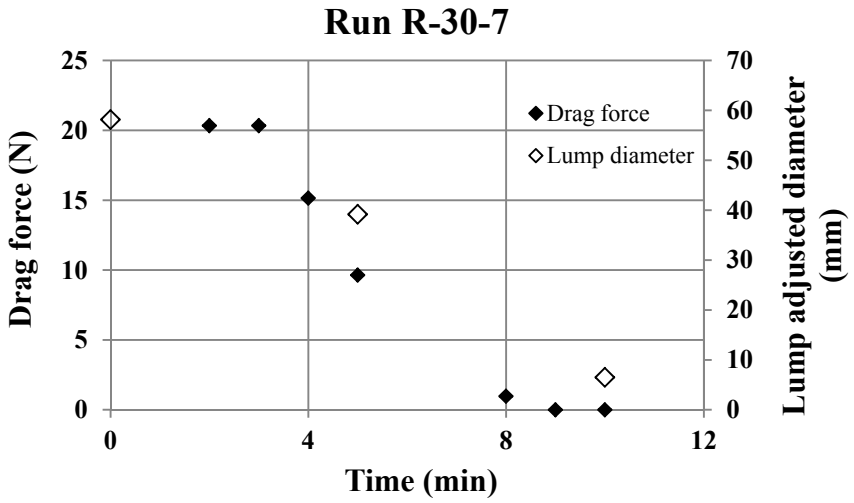

Time (min)	Strain gauge reading (v)	Total force (kg)	Drag force (kg)	Drag force (N)
		Lump in basket	Lump in basket	Lump only
2	1.383	4.428	4.598	20.334
3	1.383	4.428	4.598	20.334
4	1.225	3.925	4.069	15.151
5	1.050	3.364	3.508	9.647
8	0.686	2.202	2.347	0.975
9	0.648	2.082	2.205	0.000
10	0.608	1.956	2.078	0.000

Simulation result

Lump temperature and bitumen viscosity along Line1: V=1m/s: T=30°C: t=5min

r(m)	Temperature (°C)	Bitumen viscosity (Pa.s)
0	27.42	1742.92
0.000509	27.42	1742.07
0.000517	27.42	1742.04
0.000525	27.42	1742.01
0.001033	27.42	1739.47
0.001526	27.43	1735.44
0.001550	27.43	1735.20
0.001575	27.43	1734.96
0.002066	27.44	1729.26
0.002543	27.45	1722.31
0.002583	27.45	1721.66
0.002623	27.46	1721.00
0.003100	27.47	1712.39
0.003567	27.49	1702.70
0.003616	27.49	1701.60
0.003667	27.49	1700.47
0.004133	27.51	1689.35
0.004590	27.54	1677.31
0.004650	27.54	1675.66
0.004711	27.54	1673.96
0.005167	27.57	1660.58
0.005623	27.59	1646.17
0.005674	27.60	1644.51
0.005721	27.60	1642.93
0.006181	27.63	1627.29
0.006668	27.66	1609.71
0.006688	27.67	1608.96
0.006707	27.67	1608.26
0.007195	27.70	1589.59
0.007692	27.74	1569.62
0.007702	27.74	1569.21
0.007712	27.74	1568.76
0.008207	27.79	1548.00
0.008668	27.83	1528.07
0.008712	27.83	1526.12

0.008760	27.84	1524.02
0.009218	27.88	1503.61
0.009644	27.92	1484.15
0.009723	27.93	1480.51
0.009808	27.94	1476.59
0.010228	27.98	1456.87
0.010615	28.02	1438.48
0.010728	28.03	1433.09
0.010849	28.04	1427.26
0.011227	28.08	1409.00
0.011577	28.12	1391.94
0.011726	28.14	1384.65
0.011887	28.16	1376.77
0.012226	28.20	1360.06
0.012540	28.24	1344.48
0.012726	28.26	1335.21
0.012923	28.28	1325.42
0.013220	28.32	1310.63
0.013502	28.35	1296.61
0.013715	28.38	1286.10
0.013938	28.41	1275.07
0.014209	28.44	1261.69
0.014467	28.47	1249.01
0.014704	28.50	1237.41
0.014953	28.54	1225.24
0.015198	28.57	1213.27
0.015448	28.60	1201.19
0.015701	28.64	1188.97
0.015943	28.67	1177.40
0.016204	28.70	1164.98
0.016477	28.74	1152.05
0.016706	28.77	1141.31
0.016924	28.80	1131.13
0.017209	28.84	1117.95
0.017507	28.88	1104.24
0.017710	28.91	1094.96
0.017905	28.94	1086.13
0.018217	28.98	1072.17
0.018548	29.03	1057.55
0.018723	29.05	1049.93
0.018887	29.07	1042.82

0.019229	29.12	1028.23
0.019592	29.17	1012.98
0.019735	29.19	1007.03
0.019870	29.21	1001.47
0.020241	29.26	986.34
0.020641	29.32	970.38
0.020755	29.34	965.89
0.020863	29.35	961.67
0.021269	29.41	946.04
0.021698	29.47	929.89
0.021782	29.48	926.76
0.021862	29.49	923.82
0.022296	29.55	908.05
0.022755	29.61	891.78
0.022810	29.62	889.88
0.022862	29.63	888.07
0.023328	29.69	872.16
0.023813	29.75	856.17
0.023846	29.76	855.12
0.023877	29.76	854.12
0.024364	29.83	838.73
0.024871	29.89	823.28
0.024882	29.89	822.95
0.024892	29.90	822.64
0.0254	29.96	807.77

Lump's temperature and bitumen viscosity along Line2: V=1m/s: T=30°C: t=5min

r(m)	Temperature (°C)	Bitumen viscosity (Pa.s)
0	29.97	806.30
0.000505	29.91	818.59
0.001003	29.86	830.91
0.001009	29.86	831.05
0.001015	29.86	831.19
0.001514	29.81	843.69
0.002007	29.75	856.22
0.002018	29.75	856.50
0.00203	29.75	856.80
0.002523	29.70	869.50
0.003035	29.65	882.88
0.003044	29.65	883.12
0.003054	29.65	883.36
0.003566	29.59	896.90
0.004086	29.54	910.79
0.004088	29.54	910.83
0.004089	29.54	910.87
0.00461	29.49	924.92
0.005119	29.43	938.83
0.005131	29.43	939.16
0.005145	29.43	939.53
0.005703	29.38	954.87
0.006194	29.33	968.43
0.006273	29.32	970.62
0.006363	29.31	973.12
0.006843	29.26	986.43
0.007266	29.22	998.19
0.007414	29.21	1002.29
0.007581	29.19	1006.95
0.007984	29.16	1018.19
0.008238	29.13	1025.28
0.008432	29.11	1030.68
0.008704	29.09	1038.23
0.008881	29.07	1043.14
0.009007	29.06	1046.65
0.009329	29.03	1055.57
0.009776	28.99	1067.92

0.009778	28.99	1067.99
0.009833	28.99	1069.51
0.010432	28.94	1085.99
0.010452	28.94	1086.54
0.010505	28.93	1087.98
0.010967	28.89	1100.58
0.011145	28.88	1105.38
0.011482	28.85	1114.43
0.011857	28.82	1124.39
0.011997	28.81	1128.08
0.012361	28.78	1137.61
0.012511	28.77	1141.52
0.012555	28.77	1142.66
0.012878	28.74	1150.97
0.013098	28.73	1156.59
0.013128	28.73	1157.35
0.013641	28.69	1170.29
0.013804	28.68	1174.35
0.014157	28.65	1183.00
0.01456	28.63	1192.71
0.014672	28.62	1195.38
0.014771	28.61	1197.70
0.015188	28.59	1207.41
0.015665	28.56	1218.22
0.015715	28.55	1219.34
0.015791	28.55	1221.02
0.016385	28.51	1233.85
0.016588	28.50	1238.11
0.016901	28.49	1244.52
0.017163	28.47	1249.77
0.017416	28.46	1254.71
0.017739	28.44	1260.82
0.017932	28.43	1264.41
0.018314	28.42	1271.26
0.018448	28.41	1273.60
0.018889	28.39	1281.05
0.018991	28.39	1282.72
0.019553	28.37	1291.45
0.019645	28.36	1292.82
0.020204	28.34	1300.68
0.0203	28.34	1301.95

0.020855	28.32	1308.92
0.020954	28.32	1310.08
0.021506	28.30	1316.15
0.021608	28.30	1317.18
0.022157	28.29	1322.35
0.022266	28.29	1323.28
0.022831	28.28	1327.59
0.022922	28.27	1328.20
0.023502	28.27	1331.62
0.023578	28.27	1332.00
0.024172	28.26	1334.45
0.024233	28.26	1334.65
0.024843	28.26	1336.08
0.024889	28.26	1336.14
0.025514	28.25	1336.50
0.025546	28.25	1336.48
0.026188	28.26	1335.65
0.026213	28.26	1335.60
0.026862	28.26	1333.59
0.02688	28.26	1333.52
0.027536	28.27	1330.32
0.027547	28.27	1330.25
0.028211	28.28	1325.84
0.028214	28.28	1325.81
0.028527	28.29	1323.33
0.028881	28.29	1320.20
0.028885	28.29	1320.17
0.029534	28.31	1313.60
0.029544	28.31	1313.48
0.030187	28.33	1305.97
0.030204	28.33	1305.75
0.03084	28.35	1297.33
0.030864	28.35	1296.99
0.031493	28.37	1287.71
0.031523	28.38	1287.23
0.032145	28.40	1277.13
0.032185	28.40	1276.46
0.032702	28.43	1267.41
0.032738	28.43	1266.75
0.033251	28.45	1257.23
0.033291	28.45	1256.46

0.0338	28.48	1246.50
0.033845	28.48	1245.60
0.034349	28.51	1235.22
0.034398	28.51	1234.20
0.034899	28.54	1223.43
0.034976	28.55	1221.72
0.035366	28.57	1212.99
0.035744	28.59	1204.35
0.035817	28.60	1202.66
0.035892	28.60	1200.90
0.036267	28.63	1192.06
0.03663	28.65	1183.33
0.036718	28.66	1181.21
0.036808	28.66	1179.00
0.037168	28.69	1170.11
0.037624	28.72	1158.66
0.037744	28.73	1155.61
0.037863	28.74	1152.57
0.03832	28.77	1140.79
0.038782	28.81	1128.70
0.038896	28.82	1125.70
0.039008	28.83	1122.72
0.039471	28.86	1110.33
0.03994	28.90	1097.64
0.040048	28.91	1094.72
0.040149	28.92	1091.95
0.040607	28.96	1079.40
0.041147	29.01	1064.52
0.041165	29.01	1064.02
0.04118	29.01	1063.60
0.041724	29.06	1048.57
0.042212	29.10	1035.01
0.042282	29.11	1033.06
0.042365	29.11	1030.75
0.04284	29.16	1017.50
0.043287	29.20	1005.05
0.043385	29.21	1002.32
0.043474	29.22	999.84
0.04393	29.26	987.17
0.044432	29.31	973.26
0.044475	29.31	972.07

0.044514	29.32	970.98
0.04502	29.37	957.01
0.045554	29.42	942.29
0.045565	29.42	941.99
0.045576	29.42	941.69
0.046093	29.48	927.54
0.046598	29.53	913.90
0.046622	29.53	913.25
0.046647	29.53	912.57
0.047151	29.58	899.10
0.047642	29.63	886.11
0.04768	29.64	885.12
0.047719	29.64	884.10
0.048209	29.69	871.29
0.048691	29.74	858.84
0.048727	29.75	857.92
0.048762	29.75	857.03
0.049245	29.80	844.73
0.049745	29.85	832.18
0.049763	29.86	831.73
0.049781	29.86	831.30
0.050282	29.91	818.93
0.0508	29.97	806.30

Lump temperature and bitumen viscosity along Line1: V=1m/s: T=45°C: t=5min

r(m)	Temperature (°C)	Bitumen viscosity (Pa.s)
0	41.00	72.93
0.000499	41.01	72.90
0.000977	41.01	72.82
0.000998	41.01	72.82
0.001019	41.01	72.81
0.001497	41.02	72.68
0.001954	41.04	72.51
0.001995	41.04	72.50
0.002038	41.04	72.48
0.002494	41.06	72.26
0.002936	41.08	72.00
0.002988	41.08	71.97
0.003041	41.08	71.94
0.003483	41.11	71.64
0.003923	41.14	71.30
0.003977	41.14	71.25
0.004030	41.15	71.21
0.004471	41.18	70.82
0.004910	41.21	70.41
0.004965	41.22	70.35
0.005019	41.22	70.30
0.005454	41.26	69.84
0.005905	41.30	69.33
0.005943	41.31	69.29
0.005980	41.31	69.25
0.006432	41.36	68.70
0.006902	41.41	68.11
0.006921	41.41	68.08
0.006940	41.42	68.06
0.007411	41.47	67.43
0.007857	41.53	66.81
0.007883	41.53	66.77
0.007912	41.53	66.73
0.008355	41.59	66.09
0.008732	41.64	65.52
0.008827	41.66	65.38
0.008937	41.67	65.21

0.009299	41.73	64.65
0.009607	41.77	64.16
0.009776	41.80	63.88
0.010048	41.84	63.44
0.010272	41.88	63.07
0.010441	41.90	62.79
0.010742	41.95	62.29
0.011140	42.02	61.62
0.011212	42.03	61.50
0.011266	42.04	61.41
0.011681	42.11	60.70
0.012090	42.18	59.99
0.012151	42.20	59.88
0.012664	42.29	58.99
0.012716	42.30	58.90
0.013217	42.39	58.01
0.013274	42.40	57.91
0.013418	42.43	57.66
0.013775	42.50	57.03
0.013917	42.53	56.78
0.014276	42.60	56.15
0.014617	42.66	55.55
0.014777	42.70	55.26
0.015033	42.75	54.81
0.015320	42.81	54.31
0.015588	42.86	53.84
0.015862	42.92	53.37
0.016155	42.98	52.86
0.016405	43.03	52.43
0.016639	43.08	52.03
0.016947	43.14	51.51
0.017276	43.21	50.95
0.017512	43.27	50.55
0.017717	43.31	50.21
0.018043	43.38	49.66
0.018386	43.45	49.10
0.018574	43.49	48.80
0.018752	43.53	48.51
0.019104	43.61	47.95
0.019476	43.69	47.36
0.019635	43.72	47.11

0.019786	43.76	46.88
0.020166	43.84	46.30
0.020564	43.92	45.70
0.020692	43.95	45.51
0.020812	43.98	45.33
0.021219	44.06	44.74
0.021652	44.16	44.12
0.021745	44.18	43.99
0.021832	44.20	43.86
0.022272	44.29	43.25
0.022740	44.39	42.62
0.022798	44.40	42.54
0.022854	44.41	42.47
0.023319	44.51	41.86
0.023804	44.61	41.24
0.023839	44.62	41.20
0.023872	44.62	41.16
0.024359	44.72	40.56
0.024868	44.82	39.96
0.024880	44.83	39.94
0.024891	44.83	39.93
0.025400	44.93	39.35

Lump temperature and bitumen viscosity along Line2: V=1m/s: T=45°C: t=5min

r(m)	Temperature (°C)	Bitumen viscosity (Pa.s)
0	44.94	39.28
0.0005	44.86	39.78
0.0010	44.78	40.23
0.0010	44.77	40.28
0.0011	44.76	40.33
0.0016	44.69	40.78
0.0020	44.62	41.19
0.0021	44.60	41.29
0.0022	44.58	41.41
0.0026	44.52	41.81
0.0030	44.46	42.19
0.0031	44.43	42.35
0.0033	44.40	42.54
0.0037	44.34	42.90
0.0040	44.29	43.22
0.0042	44.26	43.45
0.0045	44.22	43.72
0.0048	44.17	44.01
0.0050	44.13	44.27
0.0053	44.09	44.56
0.0056	44.04	44.87
0.0058	44.01	45.12
0.0061	43.97	45.36
0.0064	43.92	45.69
0.0067	43.87	46.04
0.0069	43.84	46.27
0.0071	43.81	46.48
0.0075	43.76	46.84
0.0078	43.71	47.21
0.0080	43.68	47.41
0.0083	43.64	47.73
0.0086	43.60	47.99
0.0087	43.59	48.10
0.0091	43.53	48.56
0.0095	43.48	48.93
0.0097	43.45	49.12
0.0101	43.39	49.56

0.0102	43.38	49.69
0.0103	43.37	49.75
0.0109	43.30	50.31
0.0111	43.27	50.51
0.0115	43.22	50.93
0.0119	43.16	51.37
0.0121	43.14	51.55
0.0126	43.08	52.00
0.0128	43.07	52.14
0.0128	43.06	52.19
0.0134	43.00	52.70
0.0136	42.97	52.93
0.0140	42.93	53.25
0.0143	42.89	53.57
0.0146	42.86	53.84
0.0150	42.83	54.13
0.0154	42.79	54.46
0.0156	42.77	54.66
0.0161	42.72	55.06
0.0163	42.71	55.17
0.0169	42.66	55.62
0.0169	42.65	55.66
0.0173	42.62	55.95
0.0176	42.60	56.12
0.0176	42.60	56.15
0.0183	42.55	56.58
0.0183	42.54	56.62
0.0190	42.50	57.00
0.0191	42.50	57.06
0.0197	42.46	57.39
0.0198	42.45	57.45
0.0204	42.42	57.73
0.0205	42.42	57.80
0.0211	42.39	58.04
0.0213	42.38	58.11
0.0217	42.36	58.29
0.0219	42.36	58.35
0.0224	42.34	58.49
0.0226	42.33	58.55
0.0230	42.32	58.66
0.0233	42.32	58.71

0.0237	42.31	58.78
0.0240	42.31	58.83
0.0243	42.30	58.87
0.0248	42.30	58.90
0.0249	42.30	58.91
0.0254	42.30	58.92
0.0254	42.30	58.92
0.0255	42.30	58.92
0.0260	42.30	58.91
0.0261	42.30	58.90
0.0265	42.30	58.87
0.0268	42.31	58.83
0.0270	42.31	58.81
0.0271	42.31	58.78
0.0275	42.32	58.72
0.0277	42.32	58.66
0.0280	42.33	58.61
0.0284	42.34	58.50
0.0284	42.34	58.48
0.0287	42.35	58.41
0.0289	42.36	58.33
0.0290	42.36	58.30
0.0296	42.38	58.10
0.0298	42.39	58.02
0.0302	42.41	57.84
0.0304	42.42	57.75
0.0308	42.44	57.56
0.0310	42.45	57.45
0.0314	42.48	57.24
0.0316	42.49	57.11
0.0320	42.51	56.89
0.0323	42.53	56.74
0.0327	42.56	56.46
0.0329	42.58	56.30
0.0332	42.60	56.10
0.0335	42.62	55.91
0.0338	42.64	55.72
0.0341	42.67	55.50
0.0343	42.69	55.33
0.0347	42.72	55.06
0.0349	42.74	54.91

0.0352	42.77	54.60
0.0355	42.79	54.41
0.0358	42.82	54.17
0.0361	42.86	53.90
0.0362	42.87	53.77
0.0364	42.88	53.66
0.0367	42.92	53.36
0.0371	42.96	53.02
0.0372	42.97	52.94
0.0373	42.98	52.87
0.0377	43.02	52.51
0.0381	43.07	52.08
0.0382	43.08	52.02
0.0382	43.09	51.97
0.0387	43.14	51.53
0.0392	43.20	51.06
0.0392	43.21	51.02
0.0393	43.21	50.98
0.0397	43.27	50.51
0.0402	43.33	50.02
0.0403	43.34	49.98
0.0403	43.34	49.95
0.0408	43.41	49.44
0.0412	43.47	49.00
0.0413	43.48	48.89
0.0415	43.50	48.75
0.0419	43.55	48.34
0.0422	43.60	48.04
0.0424	43.63	47.79
0.0427	43.68	47.45
0.0429	43.71	47.23
0.0431	43.74	47.02
0.0435	43.78	46.67
0.0437	43.82	46.39
0.0440	43.86	46.11
0.0443	43.91	45.77
0.0445	43.94	45.55
0.0447	43.97	45.38
0.0451	44.03	45.00
0.0455	44.10	44.52
0.0456	44.11	44.44

0.0457	44.12	44.37
0.0461	44.19	43.90
0.0466	44.27	43.39
0.0467	44.27	43.36
0.0467	44.28	43.34
0.0472	44.35	42.83
0.0477	44.44	42.32
0.0477	44.44	42.30
0.0477	44.44	42.28
0.0482	44.52	41.78
0.0487	44.60	41.30
0.0487	44.61	41.27
0.0488	44.61	41.24
0.0493	44.69	40.76
0.0498	44.77	40.28
0.0498	44.77	40.26
0.0498	44.77	40.25
0.0503	44.86	39.77
0.0508	44.94	39.28

Data for validating ablation model

Water-T=30°C

Slurry bulk velocity	Ablation rate (measured)	Drag force	Skin force	Shear stress	Bitumen Viscosity (circum)	Bitumen Viscosity (ends)	$(\Delta h)_{circum}$	$(\Delta h)_{ends}$	Ablation rate (calculated)
(m/s)	(g/min)	(N)	(N)	(Pa)	(Pa.s)	(Pa.s)	(m)	(m)	(g/min)
1	0.08	2.186	0.0153	1.89	838.73	832.18	0.00104	0.00105	0.03
1.5	0.60	4.67	0.0327	4.05	850.00	853.40	0.00160	0.00208	0.17
2	1.50	7.1	0.0497	6.15	897.40	892.74	0.00361	0.00310	1.03
2.5	3.70	12.3	0.0861	10.66	915.17	914.00	0.00370	0.00471	2.25

Slurry (C=0.15)-T= 30°C

Slurry bulk velocity	Ablation rate (measured)	Drag force	Skin force	Shear stress	Bitumen Viscosity (circum)	Bitumen Viscosity (ends)	$(\Delta h)_{circu}$	$(\Delta h)_{ends}$	Ablation rate (calculated)
(m/s)	(g/min)	(N)	(N)	(Pa)	(Pa.s)	(Pa.s)	(m)	(m)	(g/min)
1	1.7	3.65	0.0256	3.16	838.73	832.18	0.00104	0.00105	0.05
1.5	2.4	7.85	0.0550	6.80	850.00	853.40	0.00160	0.00208	0.29
2	7.6	13.16	0.0921	11.40	897.40	892.74	0.00361	0.00310	1.91
2.5	11.3	23	0.1610	19.93	915.17	914.00	0.00370	0.00471	4.21

Slurry (C=0.30)-T= 30°C

Slurry bulk velocity	Ablation rate (measured)	Drag force	Skin force	Shear stress	Bitumen Viscosity (circum)	Bitumen Viscosity (ends)	$(\Delta h)_{circu}$	$(\Delta h)_{ends}$	Ablation rate (calculated)
(m/s)	(g/min)	(N)	(N)	(Pa)	(Pa.s)	(Pa.s)	(m)	(m)	(g/min)
1	0.3	7.0	0.0490	6.07	838.73	832.18	0.00104	0.00105	0.10
1.5	0.9	9.5	0.0665	8.23	850.00	853.40	0.00160	0.00208	0.35
2	4.4	20.9	0.1463	18.11	897.40	892.74	0.00361	0.00310	3.03
2.5	9.8	22.3	0.1561	19.33	915.17	914.00	0.00370	0.00471	4.08

Water-T=45°C

Slurry bulk velocity	Ablation rate (measured)	Drag force	Skin force	Shear stress	Bitumen Viscosity (circum)	Bitumen Viscosity (ends)	$(\Delta h)_{circum}$	$(\Delta h)_{ends}$	Ablation rate (calculated)
(m/s)	(g/min)	(N)	(N)	(Pa)	(Pa.s)	(Pa.s)	(m)	(m)	(g/min)
1	2.0	2.186	0.0153	1.89	40.56	40.76	0.001041	0.00154	0.80
1.5	4.8	4.67	0.0327	4.05	40.88	40.97	0.00153	0.00200	3.33
2	10.9	7.1	0.0497	6.15	41.35	41.30	0.00208	0.00256	8.88

Slurry (C=0.15)-T= 45°C

Slurry bulk velocity	Ablation rate (measured)	Drag force	Skin force	Shear stress	Bitumen Viscosity (circum)	Bitumen Viscosity (ends)	$(\Delta h)_{circum}$	$(\Delta h)_{ends}$	Ablation rate (calculated)
(m/s)	(g/min)	(N)	(N)	(Pa)	(Pa.s)	(Pa.s)	(m)	(m)	(g/min)
1	3.7	3.65	0.0256	3.16	40.56	40.76	0.001041	0.00154	1.33
1.5	6.0	7.85	0.0550	6.80	40.88	40.97	0.00153	0.00200	5.59
2	15.8	13.16	0.0921	11.40	41.35	41.30	0.00208	0.00256	16.46

Slurry (C=0.30)-T= 45°C

Slurry bulk velocity	Ablation rate (measured)	Drag force	Skin force	Shear stress	Bitumen Viscosity (circum)	Bitumen Viscosity (ends)	$(\Delta h)_{circum}$	$(\Delta h)_{ends}$	Ablation rate (calculated)
(m/s)	(g/min)	(N)	(N)	(Pa)	(Pa.s)	(Pa.s)	(m)	(m)	(g/min)
1	3.7	7.0	0.0490	6.07	40.56	40.76	0.001041	0.00154	1.33
1.5	6.0	9.5	0.0665	8.23	40.88	40.97	0.00153	0.00200	5.59
2	15.8	20.9	0.1463	18.11	41.35	41.30	0.00208	0.00256	16.46